Wind-induced vibrations of a suspension bridge

A case study in full-scale

by

Etienne Cheynet

Thesis submitted in fulfilment of
the requirements for the degree of
PHILOSOPHIAE DOCTOR
(PhD)

Faculty of Science and Technology
Department of Mechanical and Structural Engineering and Materials Science
2016

University of Stavanger
N-4036 Stavanger
NORWAY
www.uis.no

ISBN: 978-82-7644-691-3
ISSN: 1890-1387
PhD Thesis UiS No. 326

To Jasna and Jónas

Preface

This thesis is submitted in partial fulfilment of the requirements for the degree of Doctor of Philosophy (PhD) at the University of Stavanger (UiS), Norway. The research work has been carried out at the Faculty of Science and Technology, Department of Mechanical and Structural Engineering and Material Science, in the period from September 2013 to October 2016. The project was funded by the University of Stavanger, i.e. Norwegian Ministry of Education and Research and supported by the Norwegian Public Road Administration. The compulsory PhD courses followed have been offered at the UiS.

Etienne Cheynet
2016

Acknowledgements

I would like to thank my main supervisor Prof. Jasna Bounović Jakobsen and my co-supervisor Prof. Jónas Snæbjörnsson, who gave me the chance to do this PhD and supported me during these three years. I also am indebted for the freedom they gave to me, which was a driving force during these three years. The content of this thesis is therefore credited to them.

My parents deserve special thanks for their unconditional love, support and encouragements, in particular before I got accepted into this PhD program. I would like to thank my "office mates" for the outstanding atmosphere they brought. I am thinking in particular of Vlada Streletskaya, Priscille Cuvillier and Shengnan Liu. I also want to thank Julien El-Sabahy, Heidi Christiansen, Lene Eliassen, Elin Andersen, Adekunle Orimolade, Mayang Kusumawardhani, Andrea Ricolfi, Charlotte Obhrai and Félicie aussi.

I am grateful to Valerie Kumer, Prof. Joachim Reuder, Benny Svardal and the research group from DTU Risø for their help during the lidar measurement campaigns and their support during these years.

Tusen takk til sprintgruppen i Skjalg som gjorde at jeg kunne forsvinne fra universitetet (nesten) hver dag før kl 17.

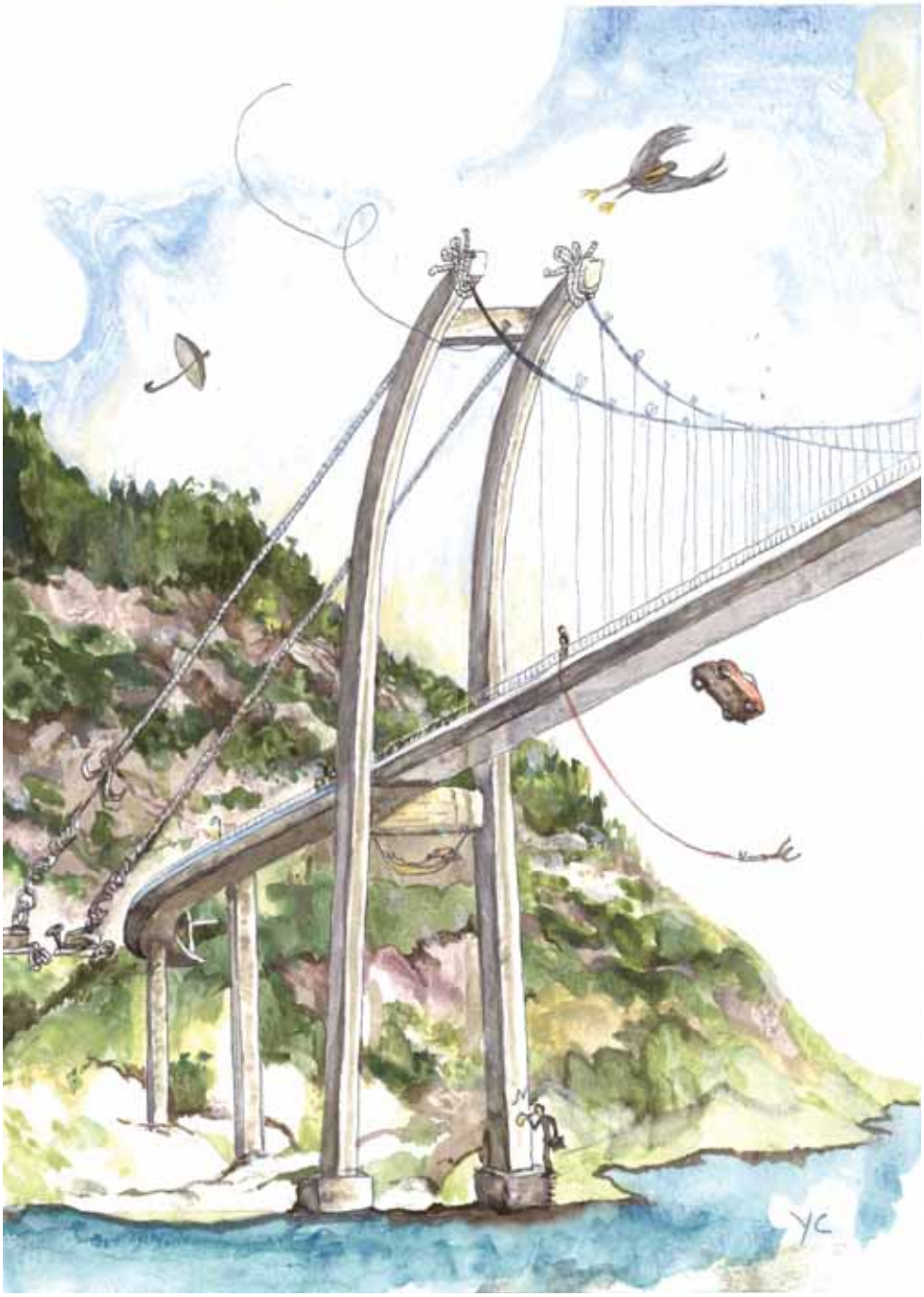

The Lysefjord Bridge seen by my dad, Yves Cheynet (2016).

Abstract

In 2013, the Norwegian government adopted an ambitious plan to cross the wide and deep-fjords of Western Norway and create a ferry-free coastal highway route. This implies the construction of multiple long-span bridges (even up to 5 km long) and in particular long-span suspension bridges. Because of their size and lightness, such structures will be particularly sensitive to environmental effects including wind turbulence. Yet, there are only relatively few studies available on wind effects on long-span bridges in full-scale and in complex terrains. Sonic anemometers fixed to a measurement mast on land are traditionally utilized to monitor wind turbulence. Recent development of remote wind sensing technologies can introduce a complementary tool for mapping the flow over several kilometres wide fjords, more representative of the future bridge exposure.

These challenges are addressed in the present thesis by studying the wind-induced vibrations of an existing suspension bridge, in full-scale. The Lysefjord Bridge, located in South-Western Norway is used as a case study. Since November 2013, it has been instrumented with multiple sonic anemometers and accelerometers. During spring 2014, two short measurement campaigns were conducted with single and dual Doppler wind lidar systems to assess their capabilities in capturing the turbulence characteristics relevant to bridge design. This thesis is structured around three main axes that are central for a systematic validation of the buffeting theory in full-scale. Firstly, a detailed investigation of the flow conditions at the bridge site is performed, by utilizing both the data from the anemometers and the Doppler Wind lidars. Secondly,

the modal parameters of the Lysefjord Bridge are identified by using an operational modal analysis. Thirdly, the buffeting response of the Lysefjord Bridge is evaluated. Discussion focuses on the sources of the discrepancies between the measured and the computed responses, selected for a detailed comparison.

Sonic anemometer records document two main wind directions (N-NE and S-SW) on the bridge site. The turbulence properties of the flow are characteristically different for these two main wind directions, so that a case-by-case approach is necessary to study the statistics of wind turbulence. The application of a single long-range pulsed wind lidar 1.75 km west of the bridge illustrated the potential of a wind lidar to capture single-point statistics of wind turbulence at distances larger than 1 km. However, a multi-lidar configuration is needed for a more complete survey of turbulence. In particular, the deployment of the short-range WindScanner system on the bridge deck demonstrated the potential of dual-wind lidar systems to measure the coherence of wind.

When it comes to structural health monitoring of the Lysefjord Bridge, a time-efficient automated covariance-driven stochastic subspace identification method was applied on six months of continuous bridge acceleration records. Results from this modal identification procedure have highlighted the dependency of the eigen-frequencies and modal damping ratios of the bridge deck on the wind velocity and temperature fluctuations. The good agreement between the measured and computed modal parameters has been identified, which allowed a detailed comparison of the measured response with the computed one in the frequency domain. Discrepancies larger than expected were observed for the standard deviation of the lateral and the vertical bridge displacement response for the N-NE exposure. The differences may be attributed to various factors, including the influence of the topography on the flow properties and the possible disturbance of the observed flow field by the bridge deck.

Table of contents

Acknowledgements **vii**

Abstract **ix**

Nomenclature **xv**

1 Introduction **1**

1.1 Research questions 3

1.2 Thesis structure 4

2 Background **9**

2.1 Full-scale analysis of suspension bridges: a review 9

2.2 Statistical description of the wind field 12

2.2.1 Coordinate systems 12

2.2.2 Single-point statistics of wind turbulence 14

2.2.3 Two-point statistics of wind turbulence 19

2.3 The buffeting theory 26

2.3.1 Assumptions 26

2.3.2 Aerodynamic forces 27

2.3.3 Equation of motion 31

2.3.4 Response in the frequency domain 32

3 Full-scale monitoring **35**
3.1 The Lysefjord Bridge 35
3.2 Long term instrumentation 35
3.3 Short term instrumentation with lidars 39
3.3.1 Overview 39
3.3.2 Applications of Doppler lidars in wind engineering . 46
3.4 Single and multi-lidars deployment 47
3.4.1 Short-range lidar configuration 48
3.4.2 Long-range lidar configuration 51
3.4.3 Flow properties investigated 54

4 Wind field characterization **57**
4.1 Introduction 57
4.2 A general description of the wind environment at the bridge site 59
4.3 Wind conditions on 22/05/2014 64
4.4 Instantaneous velocity mapping 66
4.4.1 S-SW wind case 66
4.4.2 N-NE wind case 71
4.5 Homogeneity analysis 76
4.5.1 S-SW wind case 77
4.5.2 N-NE wind case 83
4.6 Single-point wind spectra 87
4.7 Wind coherence 92
4.7.1 Co-coherence 92
4.7.2 Root-coherence 93
4.7.3 Spatial averaging effect and coherence 93
4.8 Summary 96

5 Modal Analysis **99**
5.1 Introduction 99
5.2 Free decay response from ambient vibrations 101

5.2.1 Random decrement technique 101
5.2.2 NExT 102
5.3 Automated SSI-COV procedure 104
5.3.1 Stabilization diagram 107
5.3.2 Cluster algorithm 109
5.3.3 Summary 111
5.4 Computational model estimation of modal parameters 112
5.5 Full scale measurements 113
5.5.1 Overview of the measured bridge response 114
5.5.2 Eigen-frequencies 116
5.5.3 Modes shapes 126
5.5.4 Modal damping ratios 127
5.5.5 Summary 133

6 Structural response 135
6.1 Introduction 135
6.2 Flow statistics 138
6.2.1 Single-point statistics 138
6.2.2 Two-point statistics 140
6.3 The computational bridge models 142
6.3.1 Background and resonant response 144
6.3.2 Sensitivity analysis 144
6.4 Results 149
6.4.1 Empirical approach 149
6.4.2 Buffeting response at the middle of the bridge-span for several wind records 151
6.4.3 Bridge response for multiple positions along the span 152
6.5 Summary 156

7 Challenges in the buffeting response prediction 157
7.1 Skew winds and the “cosine rule” 158

7.2 Influence of the bridge deck on the flow 161
7.3 The homogeneous flow assumption 163
7.4 Role of modal coupling 165
7.4.1 Numerical implementation of modal coupling 166
7.4.2 Modal coupling from full-scale measurements 167
7.5 Quadratic terms of the wind load 171
7.6 Non-stationarity of the flow 176
7.6.1 Directional non-stationarity 179
7.6.2 An alternative stationarity test 183
7.7 Traffic-induced vibrations 186
7.8 Other source of discrepancies 189
7.8.1 Influence of the *u*–*w* cross-spectral densities 189
7.8.2 Bridge cables and towers 189
7.9 Summary 190

8 Conclusions **191**
8.1 Summary 191
8.2 Future works 193

References **195**

Appendix A Wind-induced vibrations monitoring with satellite navigation **215**

Appendix B Hardanger Bridge properties **229**

Appendix C Publications related to the thesis **237**

Index **241**

Nomenclature

General Rules

An overline above a symbol, e.g. $\overline{a}$, indicates a time-averaged value

The superscript $\widehat{\ }$, e.g. $\widehat{a}$, indicates a normalized quantity

The superscript *, e.g. a^*, indicates the conjugate of a complex quantity

The superscript †, e.g. $a^\dagger$, indicates the pseudo inverse of a matrix

The superscript $\tilde{\ }$, e.g. $\tilde{a}$, indicates a modal quantity

The superscript $^\top$, e.g. $a^\top$, indicates the transpose of a matrix

Roman Symbols

$\mathscr{L}$	Isotropic integral length scale
$\tilde{\boldsymbol{C}}_{\boldsymbol{ae}}$	Aerodynamic modal damping matrix
$\tilde{\boldsymbol{C}}$	Structural modal damping matrix
$\tilde{\boldsymbol{K}}_{\boldsymbol{ae}}$	Aerodynamic modal stifness matrix
$\tilde{\boldsymbol{K}}$	Structural modal stifness matrix
$\tilde{\boldsymbol{M}}$	Modal mass
$\widehat{\boldsymbol{F}_{\boldsymbol{nl}}}$	Matrix of non-linear aerodynamic forces

$\widehat{\boldsymbol{F_l}}$	Matrix of linear aerodynamic forces
$\boldsymbol{A_0}$	Matrix of static wind load coefficient
$\boldsymbol{A_1}$	Matrix of dynamic buffeting load coefficients
$\boldsymbol{A_2}$	Matrix of quadratic buffeting load coefficients (without the cross-terms *uw*)
$\boldsymbol{A_{uw}}$	Matrix of quadratic buffeting load coefficient (cross-terms *uw* only)
$\boldsymbol{A}$	State Space matrix
$\boldsymbol{C}$	Damping matrix
$\boldsymbol{F}$	Matrix of aerodynamic forces
$\boldsymbol{H}$	Mechanical admittance function, Spectral transfer function
$\boldsymbol{I}$	Identity matrix
$\boldsymbol{K}$	Stiffness matrix
$\boldsymbol{M}$	Mass matrix
$\boldsymbol{O}$	Extended observability matrix
$\boldsymbol{R_i}$	Cross-correlation matrix
$\boldsymbol{r}$	Displacement vector
$\boldsymbol{S}$	Cross-spectral density matrix
$\boldsymbol{T_1}$	Block-Toeplitz matrix
$\boldsymbol{U}$,$\boldsymbol{V}$	Unitary matrices resulting from a singular value decomposition
$\overline{U}$	Along-wind mean velocity component

$\overline{V}$ Across-wind mean velocity component

$\overline{V}_r$ Along-beam mean wind velocity component

$\overline{V}_x$ Across-bridge mean wind velocity component

$\overline{V}_y$ Along-bridge mean wind velocity component

$\overline{W}$ Vertical mean wind velocity component

a, b, a_i, b_i Constant, coefficients

A_d Detector area

B Width of the deck cross-section

C_i^j Exponential decay parameter

C'_D Derivative of steady drag coefficient w.r.t. the angle of attack

C'_L Derivative of steady lift coefficient w.r.t. the angle of attack

C'_M Derivative of steady moment coefficient w.r.t. the angle of attack

C_D Steady drag coefficient

c_i Decay coefficient

C_L Steady lift coefficient

C_M Steady moment coefficient

Co Co-coherence

D Height of the deck cross-section

d_y Span-wise separation

f Frequency

F_i	Aerodynamic force
I_θ	Mass moment of inertia
I_i	Turbulence intensity
k	Wavenumber
k_θ	Horizontal distance between the aerodynamic and the shear centre as a fraction of the girder width
L	Span length
L_i	Integral length scale
L_i^y	Span-wise turbulence length scale
m_c	Lineic mass of the main cable
m_g	Lineic mass of the girder
N	Number of time step
n	Reduced frequency
Q_{uad}	Quadrature spectrum
r	Along-beam distance
R_i	Cross-correlation function
r_i	Displacement of the bridge deck
r_x, r_z, r_θ	Lateral, vertical and torsional bridge displacement response
$S_{v_r}^0$	Unfiltered along-beam wind velocity spectrum
S_i	Auto power spectral density

S_{ij} Cross power spectral density

S_{v_r} Filtered along-beam wind velocity spectrum

T Temperature

t Time

u Along-wind turbulent component

v Across-wind turbulent component

v_r Along-beam wind turbulent component

v_x Across-span wind turbulent component

v_y Along-span wind turbulent component

V_{rel} Instantaneous relative wind velocity

w Vertical-wind turbulent component

x Across-span coordinate

y Span-wise coordinate

z Vertical coordinate

Z_r Rayleigh length

Greek Symbols

α Incidence angle

β Yaw angle

$\mathbf{\Gamma}$ Reversed extended controllability matrix

Γ Gamma function

γ_i	Root-coherence
Δ_r	Range gate
ε	Error, threshold value
ζ	Modal damping ratio
η	Modal displacement
Θ	Wind direction
θ	Torsion angle
κ_i	Kurtosis
λ	Wavelength
λ_i	Eigen value for mode i
$\mathbf{\Lambda}$	Matrix of singular values
ρ	Air density
σ_i	Standard deviation
τ	Time lag
υ_i	Skewness
Φ	Azimuth angle
χ	Cross-sectional admittance functions
ϕ	Spatial averaging function
ψ, $\boldsymbol{\psi}$	mode shape, matrix of mode shapes
Ψ	Elevation angle

Ω Angle between the wind direction and the scanning beam

ω Angular frequency

Acronyms / Abbreviations

ABL Atmospheric Boundary Layer

AVT Ambient Vibrations Testing

CDTD Covariance-Driven Time-Domain

cw Continuous wave

EMD Empirical Modal Decomposition

FDR Free Decay Response

GNSS Global Navigation Satellite System

GPS Global Positioning System

IQR Inter Quartile Range

LOS Line Of Sight

MAC Modal Assurance Criterion

NPRA Norwegian Public Road Administration

OMA Operational Modal Analysis

PPI Plan Position indicator

PSD Power Spectral Density

RHI Range Height Indicator

RMS, rms Root Mean Square

SA Sonic anemometer

SBM Simplified Bridge Model

SHM Structural Health Monitoring

SI system identification

SRTM Shuttle Radar Topography Mission

SSI-COV Covariance-Driven Stochastic Subspace Identification

STD Standard Deviation

TI Turbulence intensity

WASHM Wind And Structural Health Monitoring

Chapter 1

Introduction

The number of long-span suspension bridges built with a main span over 800 m has considerably increased since the 90s (Fig. 1.1). In Europe, Norway is one of the few countries that currently still build and/or plan to build major long-span suspension bridges. In the white paper National Transport Plan 2014–2023, the Norwegian Ministry of Transport and Communication (2013) adopted a plan to improve the coastal route E39 by making it ferry-free. Until now, ferries have been used to cross wide and deep fjords, such as Haslafjorden (2 km wide and 200 m deep), Bjørnafjorden (5 km wide and 500 m deep) or Sognfjorden (3.7 km wide and 1300 m deep). To cross such fjords without ferries, a number of cable-supported bridges, floating bridges, submerged bridges or a "hybrid"-type of bridge is being considered. If suspension bridges become the first choice for some of the crossings, they will likely break the world record for the longest central span, currently held by the Akashi Kaikyō Bridge in Japan (1991 m). If other types of bridges are considered, their large dimensions and lightness will make them particularly sensitive to wind excitation.

Wind effects on large civil engineering structures have been studied as a discipline in its own right since the 60s. Harris (1975) termed this field "industrial aerodynamics" or "wind engineering". Wind engineering involves

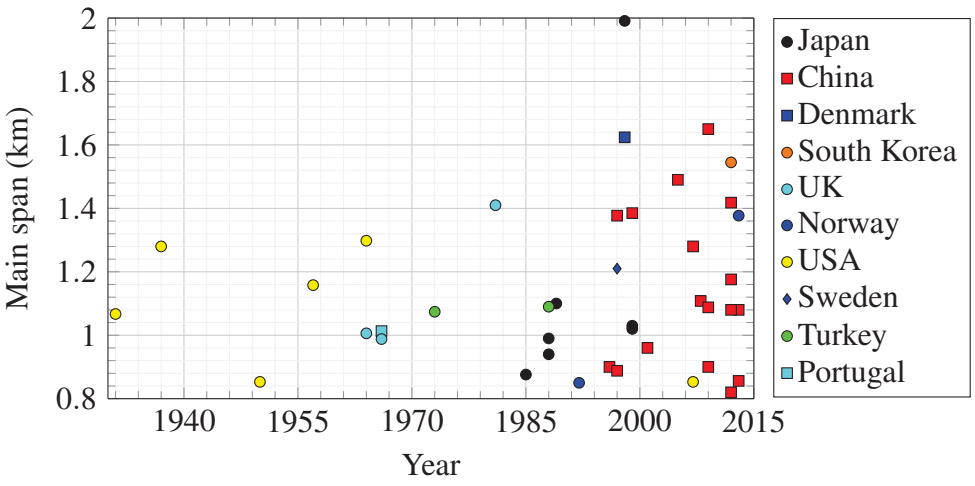

Figure 1.1 Suspension bridges with main span over 800 m.

a wide range of sub-disciplines such as meteorology, small-scale wind turbulence, measurement techniques, random signal analysis, aerodynamics and structural dynamics. All of them are called up in this thesis, which investigates the effects of wind turbulence on a suspension bridge in full-scale and in complex terrain.

As pointed out by Davenport (1975), full-scale measurements are an essential component of the scientific method to *evaluate the validity of theories for wind loading*. Full-scale measurement campaigns are usually expensive and cumbersome to carry out, and normally do not include the extreme design conditions. That can partly explain why the majority of studies on wind effects on structures are performed as experiments in wind tunnels or numerical simulations. Whereas numerical simulations and experiments may reveal details on the idealized problem studied, only the full-scale measurements provide an overview of the real in-wind structural behaviour.

This thesis presents a unique study case where wind velocity and bridge acceleration response are continuously and simultaneously monitored. Since the end of the 90s, technology improvements have facilitated simultaneous

wind measurements, the storage of large amount of wind records and their analysis. Consequently, a validation of the buffeting theory, i.e. the classical theory to estimate the displacement of a structure induced by wind turbulence, has become technically possible. In wind engineering, wind turbulence is modelled by assuming flat and homogeneous terrains. For a suspension bridge located in a Norwegian fjord, this assumption has to be re-assessed, as fjords are typically characterized by steep hills, high cliffs, islands, varying width and possible descending winds. This is particularly true for future super-long span suspension bridges which are likely to be exceptionally wind-sensitive structures. In this thesis, the term "super-long span" refers to single-span suspension bridges with a main span of at least 2 km.

1.1 Research questions

In view of the plans for construction of several super-long-span suspension bridges in Norwegian fjords, it is important to investigate *how well the buffeting theory applies to long-span suspension bridges already built in mountainous environments*. A review of the full-scale measurement campaigns available in the literature raises actually a more specific question: *How to conduct a validation of the buffeting theory in full-scale?*

The amount of full-scale wind measurements is considerably lower than its counterpart in wind tunnel experiments. Yet, wind turbulence statistics represents one of the largest uncertainties in the estimation of the buffeting response of a large civil engineering structure. To contribute in reducing the uncertainty, this thesis examines also *the performance of novel measurement techniques to study the statistics of atmospheric turbulence relevant to suspension bridges*.

1.2 Thesis structure

This thesis focuses on wind-induced vibrations of a suspension bridge in full-scale using the Lysefjord Bridge as a case study. The relatively short length of the main span of this bridge (446 m) is counterbalanced by a simpler and less costly instrumentation required for a shorter span bridge, along with its easy access, facilitating maintenance operations. Wind fluctuations and bridge acceleration responses have been simultaneously and continuously measured since November 2013 by using a set of sensors located above and inside the bridge deck, as well as on the hangers and main cables. Apart from the first chapter which is the introduction, each chapter is dedicated to one aspect of this full-scale measurement campaign (Fig 1.2).

Chapter 2: The second chapter starts with a review of the previous full-scale studies of the buffeting response of suspension bridges, and motivates a validation of the buffeting theory. The second section focuses on the statistical tools used to characterize wind turbulence. Although this chapter is mainly theoretical, it is illustrated by examples taken from the Lysefjord Bridge measurement campaign. The third part of this chapter focuses on the buffeting theory, the implementation of which has been done in the frequency domain with the software Matlab. A simplified version of the code used in the present thesis has been made freely available on The MathWorks MATLAB ® Central File Exchange website [1].

Chapter 3: The third chapter describes the instrumentation used to monitor the wind-induced vibrations of the Lysefjord Bridge. A large portion of this chapter is dedicated to the exploration of wind lidar technology to monitor wind turbulence. A review of previous scanning lidar measurements is presented to highlight that such devices have been seldom used to measure flow

[1] file id: # 51970: *Buffeting response of a suspension bridge - a frequency domain approach*

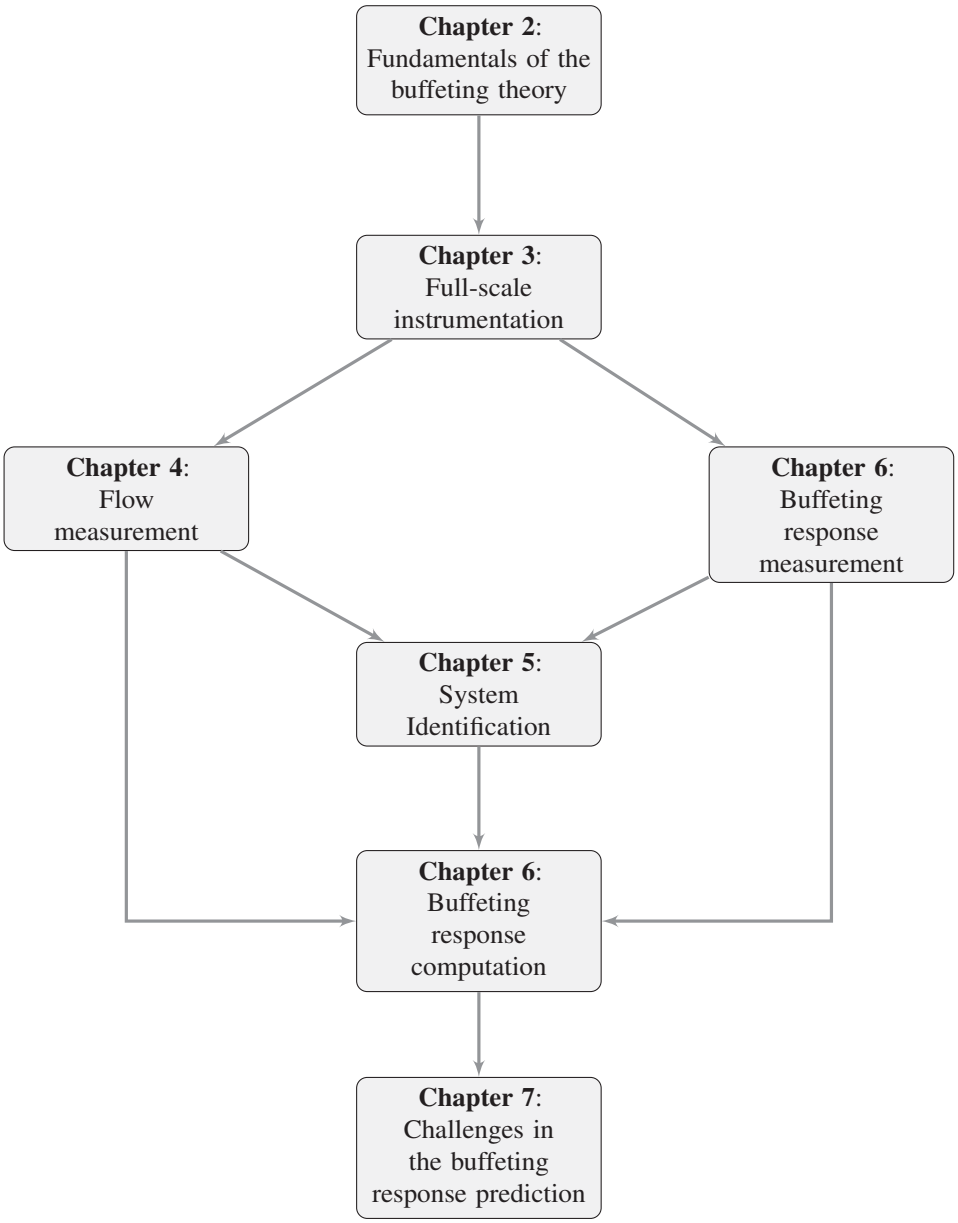

Figure 1.2 Structure of the present thesis.

at distances larger than 300 m, although that is the domain where wind lidar may become useful to bridge engineers.

Chapter 4: The fourth chapter deals with flow measurements by using the anemometers and the wind lidars presented in Chapter 3. Statistics of wind velocity data recorded during one year at the Lysefjord Bridge site by the anemometers are first briefly summarized. Two main wind directions with different statistical properties are observed. A comparison between lidar and anemometer measurements is given for these two dominant wind directions. The goal is to evaluate the potential of wind lidar for applications in bridge engineering. Two types of wind lidar are studied with focus on their complementary roles in measuring wind turbulence.

Chapter 5: The fifth chapter summarizes the results of the Operational Modal Analysis (OMA) conducted using data from the Lysefjord Bridge representing a six month period in the year 2015. The identification of the bridge modal parameters is a fundamental step to calibrate the computational bridge model used. The automated system identification procedure developed by Magalhães et al. (2009) is applied for this purpose. The influence of environmental conditions on the bridge modal properties was investigated in details. The eigen-frequencies were observed to show remarkable variations with the daily temperature fluctuations. The evolution of the modal damping ratios with the mean wind velocity was compared with the one predicted by the quasi-steady theory by using for the first time a considerable amount of samples.

Chapter 6: In the sixth chapter, the buffeting bridge response is studied based on two days that were assumed to represent well the strong wind conditions recorded at the bridge site. As a frequency domain approach is used, the bridge response is studied in terms of standard deviation and power spectral density of the bridge displacement. The bridge response is studied

first at mid-span for a wide variety of wind data and then the response along the entire span is analysed for one particular wind record.

Chapter 7: The seventh chapter investigates the different factors that may affect the bridge response but are not well-modelled or simply not taken into account by the buffeting theory. This includes the influence of the topography on the flow, the disturbance of the monitored wind by the bridge deck, the absence of wind stationarity or wind uniformity.

Chapter 2

Background

2.1 Full-scale analysis of suspension bridges: a review

The deployment of Structural Health Monitoring (SHM) systems and/or Wind And Structural Health Monitoring (WASHM) systems on long-span suspension bridges constitutes a important part of the "full-scale analysis" of such structures. One of the goals of SHM is to identify the modal parameters of a suspension bridge, i.e. its eigen-frequencies, mode shapes and modal damping ratios. Accelerometers are traditionally used to monitor the dynamic displacements (Chen et al., 2004; Macdonald and Daniell, 2005; Siringoringo and Fujino, 2008), but Global Navigation Satellite Systems (GNSS) have been increasingly used for the last 20 years for a similar purpose (Cheynet et al., 2016a; Im et al., 2011a; Meng et al., 2007; Xu et al., 2002; Yu et al., 2014). SHM systems include also the possibility to study the influence of the temperature (Xu et al., 2010) or traffic load (Brownjohn et al., 1994; Cheynet et al., 2015b; Macdonald, 2004) on the bridge displacement. A more complete review of structural health monitoring applied to suspension bridges can be find in Xu and Xia (2011). For WASHM systems, the wind field is in

Table 2.1 Review of full-scale wind and bridge vibrations monitoring, Modal Identification (MI) and data analysis (performed: ✓; not performed: ×).

Reference	MI	Buffeting response		Wind statistics	
		Computed	Measured	1-point	2-point
Present work	✓	✓	✓	✓	✓
Bietry et al. (1995)	✓	✓	✓	✓	✓
Miyata et al. (2002)	×	×	✓	✓	✓
Toriumi et al. (2000)	×	×	✓	✓	✓
Wang et al. (2013)	×	×	×	✓	✓
Hui et al. (2009a,b)	×	×	×	✓	✓
Wang et al. (2011)	×	✓	✓	✓	×
Xu and Zhu (2005)	✓	✓	✓	✓	×
Macdonald (2003)	✓	✓	✓	✓	×
Nakamura (2000)	✓	×	×	✓	×
Brownjohn et al. (1994)	✓	×	✓	✓	×
Nagayama et al. (2005)	✓	×	✓	×	×
Hay (1984)	×	×	✓	×	×

addition measured directly from the bridge deck, which allows a direct study of wind-induced vibrations. Detailed measurements of the wind-field only (Hui et al., 2009a,b; Wang et al., 2011) could be considered as a third category of full-scale measurement set-up linked to full-scale analysis of suspension bridges. Although such studies are a rarity, they provide useful information about the spatial structure of wind turbulence at the bridge site.

By combining wind and bridge displacement records, the applicability of the buffeting theory in full-scale can be assessed. This theory was introduced more than 50 years ago by Davenport (1961a) and developed by e.g. Scanlan (1975) to estimate the bridge displacement response to wind turbulence. To validate this theory, three fundamental steps must be taken: the identification of the bridge modal properties, the measurement of the bridge response and the measurement of the upstream flow. The first step requires the estimation

of the eigen-frequencies and the structural modal damping ratios as well as their evolution with the mean wind velocity. In addition, an identification of the mode shapes is necessary. The second step entails measurements of the standard deviation and the spectral density of the bridge acceleration response. The third step relies on measurements of the single and two-point statistics of wind turbulence. Table 2.1 shows that only Bietry et al. (1995) addressed these three aspects. Full-scale measurements of wind coherence were missing in the studies of Xu and Zhu (2005) or Macdonald (2003). On the other hand, Hui et al. (2009a,b) and Wang et al. (2011) provided detailed measurements of the wind field but did not relate them to the bridge vibrations analysis. Toriumi et al. (2000) and Miyata et al. (2002) monitored both the wind and the bridge response, but none of them appears to have carried out a modal-identification (MI) procedure. The studies of Toriumi et al. (2000) and Miyata et al. (2002) were actually based an measurements of the maximal deck deflection alone and the amount of data they used for this purpose was likely too small to be statistically significant.

Because the buffeting theory is based on random processes, statistical significance needs to be achieved, which can constitute a fourth aspect to be fulfilled to rigorously validate this theory in full-scale. This aspect may have not been completed by Bietry et al. (1995) whose data set was limited to 6 h. Similarly, (Xu and Zhu, 2005) focused on bridge response to winds recorded during typhoons, which are usually characterized by a short duration. In summary, there is an anomaly in the field of wind engineering, where suspension bridges are designed based on a theory that has not been thoroughly validated in full-scale.

The most challenging parameters to measure are likely to be the two-point statistics of wind turbulence and the evolution of the modal damping ratios with the mean wind velocity. This may explain why their measurement is little documented (Table 2.1). The use of an arbitrarily chosen decay parameter to estimate wind coherence is more common (Wang et al., 2011; Xu and Zhu,

2005), although a literature review from Solari (1987) suggests that the scatter of the decay parameter can be particularly large, leading to results that must be interpreted with precautions.

The present study is based on large amount of wind and acceleration data collected during the Lysefjord Bridge measurement campaign that started in November 2013. Both single and two-point statistics of wind turbulence could be obtained, which allowed for the first time a detailed study of the buffeting response of a suspension bridge in complex terrain.

2.2 Statistical description of the wind field

The atmospheric boundary layer (ABL) is limited at the bottom by the ground or water and by a stable-stratified flow at the top, but its thickness may change with meteorological conditions (Wyngaard, 2010). In the ABL, the turbulence is mechanically produced by the terrain (hills, trees, etc...) and buoyancy (convection due to temperature gradients). In the field of structural engineering, buoyancy-generated turbulence is usually disregarded because strong wind conditions are considered. In other words, the atmospheric stability is assumed to be "neutral". The reassessment of this assumption is out of the scope of the present thesis but may become pertinent for long-term measurement campaigns using WASHM systems.

2.2.1 Coordinate systems

The wind velocity is described here as a three dimensional stationary random process which is decomposed into the sum of a mean and a fluctuating part. The wind field is decomposed into three components, U, V and W called

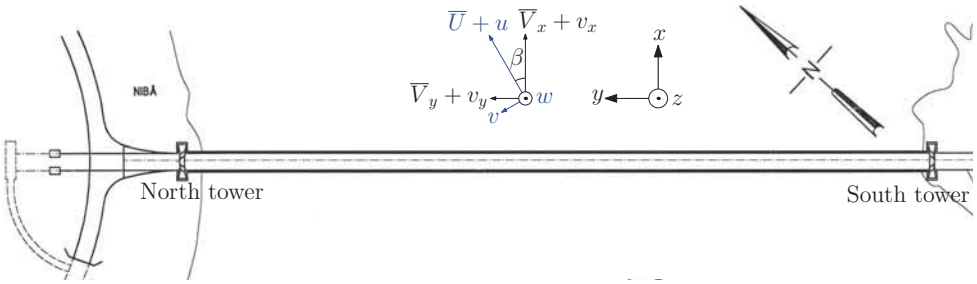

Figure 2.1 Wind-based and bridge-based coordinate system.

along-wind, across-wind and vertical wind components respectively:

$$U = \overline{U} + u \tag{2.1}$$

$$V = \overline{V} + v \tag{2.2}$$

$$W = \overline{W} + w \tag{2.3}$$

The terms $\overline{W}$ and $\overline{V}$ are per definition equal to zero under stationary wind conditions (Teunissen, 1980). The mean wind velocity is thus confined to the horizontal plane and is expressed trough the term $\overline{U}$ only. The mean wind speed is calculated here following IEC 61400-1 (2005) and EN 1991-1-4 (1991), where the 10 min averaging period is chosen. Although this is the most common averaging period, a duration of 1 h is proposed by ESDU 86010 (2001). As observed by Larsén and Mann (2006), the averaging time must be chosen wisely, as it may lead to important differences when estimating wind statistics. In addition, Wang et al. (2016) have shown that an increasing averaging time leads to an increasing number of non-stationary wind records.

For a full-scale bridge, the flow is not necessarily normal to the bridge deck. In that case, the wind is labelled as “skewed”. The angle between the along-wind and vertical wind component is called “incidence angle”. The angle between the wind direction and the normal to the bridge deck is named “yaw angle” and denoted β in Fig. 2.1. The flow can therefore be described

in two coordinate systems: one defined by the bridge orientation and one following the mean wind direction. The wind-based coordinate system has been presented in Eqs. 2.1-2.3. The wind components in the bridge-based coordinate system are obtained by projecting the along-wind and the across-wind components on the bridge axes (Fig. 2.1). The wind components normal to and along the bridge deck axis are denoted V_x and V_y respectively (Eqs. 2.4-2.5). Both V_x and V_y have a non-zero mean value in general. The vertical wind component remains the same in these two coordinate systems.

$$V_x = \overline{V}_x + v_x \tag{2.4}$$

$$V_y = \overline{V}_y + v_y \tag{2.5}$$

$$W = w \tag{2.6}$$

2.2.2 Single-point statistics of wind turbulence

Turbulence intensity

Atmospheric turbulence can be simply described in terms of the turbulence intensity (TI), which indicates the importance of wind fluctuations in relation to the mean wind velocity:

$$I_u = \frac{\sigma_u}{\overline{U}} \tag{2.7}$$

$$I_v = \frac{\sigma_v}{\overline{U}} \tag{2.8}$$

$$I_w = \frac{\sigma_w}{\overline{U}} \tag{2.9}$$

where σ_i, $i = \{u, v, w\}$ is the standard deviation of the corresponding wind velocity component. According to Holmes (2007), the ratio I_v/I_u and I_w/I_u for flat terrains is about 0.88 and 0.55 respectively. Solari and Piccardo (2001) reviewed more than 40 studies dealing with the measurement of these ratios. They found out that the ratio I_v/I_u fluctuates between 0.71 and 0.88, whereas

Table 2.2 Ratios I_v/I_u and I_w/I_u recorded on the Lysefjord Bridge site during the year 2015 for $\overline{U} > 10\ \mathrm{m\,s^{-1}}$, based on wind data recorded by the anemometers on hangers 16, 18 and 20.

Exposure	I_v/I_u	I_w/I_u
N-NE	0.86	0.41
S-SW	1.09	0.58

I_w/I_u is bounded between 0.45 and 0.6. The influence of the topography, atmospheric stability and wind stationarity on the dispersion of these ratios was however not discussed in details. For wind data recorded during typhoons, which are known to be often non-stationary, Wang et al. (2011) found for example a value of 0.90 and 0.67 for I_v/I_u and I_w/I_u respectively, i.e. higher than those reviewed by Solari and Piccardo (2001).

In the case of the Lysefjord Bridge, the average value of the ratios I_v/I_u and I_w/I_u for the year 2015, for a mean wind velocity above $10\ \mathrm{m\,s^{-1}}$, are displayed in Table 2.2. The unusual values of the ratio I_w/I_u for the N-NE exposure and the ratio I_v/I_u for the S-SW exposure may be due to the influence of the topography or the bridge deck on the recorded turbulent wind field, or the fact that the wind data are recorded at an altitude of 60 m above the sea level instead of the standard altitude of 10 m.

For flat and homogeneous terrain and neutral atmospheric stability, turbulence intensity is known to be high at low wind velocities and to decrease when the mean wind speed increases. When the mean wind velocity reaches a threshold value, the turbulence intensity remains more or less constant. Such a dependency is also observed at the Lysefjord Bridge site, where the variation in turbulence intensity is seen to be small for mean wind velocity above $10\,\mathrm{m\,s^{-1}}$ (Fig. 2.2).

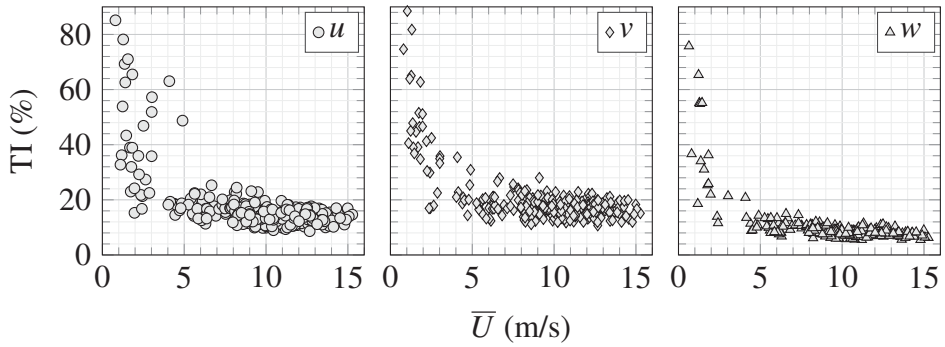

Figure 2.2 Turbulence intensity (TI) as a function of the mean wind velocity at the Lysefjord Bridge site, for winds from S-SW, from 25/10/2014 to 28/10/2014, based on wind data recorded on hangers 16, 18 and 20.

Stream-wise turbulence length scales

The integral length scales, also called stream-wise turbulence length scales, are calculated based on the integration to the first zero-crossing of the auto-covariance of the wind velocity components (Lenschow and B. Stankov, 1986):

$$L_i = \overline{U} \cdot \int_{t=0}^{t(R_i(t)=0)} R_i(t)\,\mathrm{d}t \tag{2.10}$$

where $i = \{u, v, w\}$ refers to the three wind components. $\overline{U}$ is the horizontal mean wind velocity component and R_i is the single-sided auto-covariance function of the fluctuating wind velocity. The length-scale can be computed either by a direct integration of the auto-covariance function or based on an exponential function fitted to the auto-covariance function. The later solution was used by e.g. Lothon et al. (2006) for samples with a duration too short to provide an autocorrelation function crossing the abscissa. In the present study, both methods were tested and negligible differences were observed.

The application of Eq. 2.10 to calculate accurately the integral length scales showed a high sensitivity to any non-stationary fluctuation. As a result, overestimations of the integral length scales were commonly observed. If the integral length scales have to be used to compute the von Kármán spectra, it may be preferable to directly fit a spectral formula to the measured wind spectrum, as done by e.g. Xu and Zhu (2005). Alternatively, the integral length scales can be estimated from the spectral value at zero frequency or the spectral peak. These other options require however wind records with a duration larger than 10 min to be accurate enough. As stated previously, the increase of the sample duration may unfortunately be associated with non-stationary fluctuations.

The integral length scales calculated for every sample of 10 min duration between the 25/10/2014 and 28/10/2014 (S-SW wind) are displayed in Fig. 2.3. The integral length scales seem to follow a non-linear trend with a dispersion that increases with the mean wind velocity. It goes along with the study of Solari (1987) which suggests that the evolution of the integral length scales with the mean wind velocity cannot be described in a deterministic way. Similar scatters are reported elsewhere in the literature, e.g. Cao (2013).

Single-point wind spectra

The energy content of wind turbulence in the frequency domain provides further information on the properties of the velocity fluctuations. The power spectral densities of the wind velocity, also called wind spectra can be calculated based on measurement data or approximated using semi-empirical models. In the present study, the von Kármán spectrum (Morfiadakis et al., 1996), presented in Eqs. 2.11-2.12, was found to be better suited than the Kaimal spectrum (Kaimal et al., 1972) or the Simiu & Scanlan spectrum

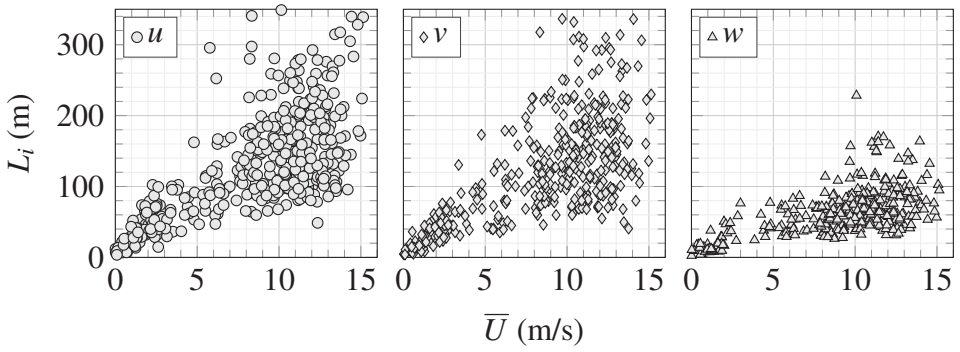

Figure 2.3 Integral length scales L_i, $i = \{u, v, w\}$, as a function of the mean wind velocity at the Lysefjord Bridge site, for winds from S-SW, from 25/10/2014 to 28/10/2014, based on wind records obtained on hangers 16, 18 and 20.

(Simiu and Scanlan, 1996) to describe the measured wind spectrum.

$$S_u(f) = \frac{4L_u\sigma_u^2}{U} \frac{1}{\left[1 + 70.7\left(\frac{fL_u}{U}\right)^2\right]^{5/6}} \tag{2.11}$$

$$S_i(f) = \frac{2L_i\sigma_i^2}{U} \frac{1 + 189\left(\frac{fL_i}{U}\right)^2}{\left[1 + 70.7\left(\frac{fL_i}{U}\right)^2\right]^{11/6}} \qquad i = \{v, w\}\,. \tag{2.12}$$

On Fig. 2.4, the measured wind spectra are calculated as the average of individual spectra for 75 wind samples of 10 min duration, recorded between the 25/10/2014 and 28/10/2014, with a mean velocity bounded between $8\,\mathrm{m\,s^{-1}}$ and $10\,\mathrm{m\,s^{-1}}$. The von Kármán spectrum is displayed for the different wind components as dashed lines in Fig. 2.4. It has been computed based on the measured standard deviation of the wind velocity components and the measured integral length scales. A good agreement is observed with the

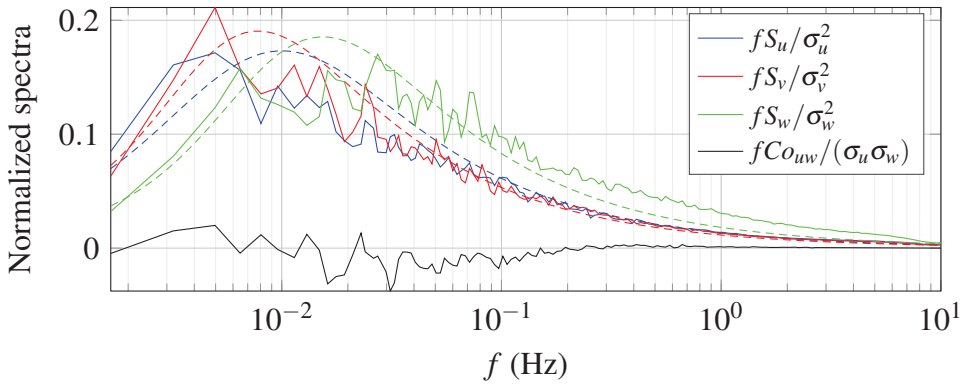

Figure 2.4 Averaged wind spectra measured for the S-SW exposure at the Lysefjord Bridge site for $8\,\mathrm{m\,s^{-1}} < \overline{U} < 10\,\mathrm{m\,s^{-1}}$ from 25/10/2014 to 28/10/2014, based on wind records obtained on hangers 16, 18 and 20. The fitted von Kármán spectrum for the different wind components is displayed as dashed lines.

von Kármán spectrum for the two horizontal components. For the vertical component, the measured spectra was on average higher than the computed one for frequency above 0.1 Hz. The possible origins of this discrepancy are discussed later in this thesis. An analytical expression of the cross-spectrum between the components u and w was proposed by Kaimal et al. (1972), and is expressed as a function of the friction velocity. To the author knowledge, there is no equivalent expression for the von Kármán spectrum. For this reason, Fig. 2.4 displays the measured cross-spectrum Co_{uw} without a corresponding analytical function fitted to the data.

2.2.3 Two-point statistics of wind turbulence

The two-point statistics of wind turbulence provides a description of the correlation of the wind velocity fluctuations along the bridge span. The cross-flow turbulence length scales are first presented here, followed by the wind coherence. The coherence of the wind load is required for accurately

estimating the dynamic bridge response. Because the properties of the flow are studied along the bridge deck which does not necessarily corresponds to cross-flow separations, the wind component V_x is used in the following instead of U.

Along-bridge turbulence length scales

The turbulence length scale along the deck span is calculated using:

$$L_i^y = \int_0^{+\infty} \boldsymbol{R_i}(\tau)\,\mathrm{d}\tau \tag{2.13}$$

where $i = \{v_x, v_y, w\}$ and $\boldsymbol{R_i}$ is the matrix of correlation coefficients at the different measurement positions. An exponential decay function is used to approximate the correlation coefficients as a function of spatial separation, the integral of which provides an estimation of the length scales along the bridge deck.

On Fig. 2.5 the mean and the standard deviation of the correlation coefficients are displayed for $8\,\mathrm{m\,s^{-1}} < \overline{V}_x < 10\,\mathrm{m\,s^{-1}}$, based on wind data recorded from 25/10/2014 to 28/10/2014 at the Lysefjord Bridge site (90 samples). The averaged value for the along-span turbulence length scale is 89 m for the v_x-component, 137 m for the v_y-component and 36 m for the w-component. The standard deviations for the v_x- and v_y-components are particularly large, about 37 m and 45 m respectively. It is only 8 m for the w-component. This is in agreement with the relatively large dispersion observed in Fig. 2.5 for the v_x- and v_y-components. This indicates that a statistical description of these turbulence length scales may be required in full-scale.

Coherence of wind velocity fluctuations

The normalized cross-spectra of the wind fluctuations, also called coherence, has been used since the 60's to take into account the spatial correlation of each

frequency component of the wind velocity fluctuations (Davenport, 1961b, 1962; Panofsky et al., 1958; Vickery, 1970). For a suspension bridge, the span-wise coherence is therefore a function of the frequency f and the along-deck spatial separation d_y . The root-coherence γ is defined as the modulus of the root-square of the coherence:

$$\gamma(d_y, f) = \frac{\left|S_{i_1 i_2}(d_y, f)\right|}{\sqrt{S_{i_1}(f) S_{i_2}(f)}} \tag{2.14}$$

where $i = \{v_x, v_y, w\}$, and S_{i_1} and S_{i_2} are the single-point wind spectra measured in two positions y_1 and y_2 respectively. The cross-spectrum for the i-component is $S_{i_1 i_2}$. The coherence is complex-valued with a real part Co named co-coherence and an imaginary part Q_{uad} called quadrature spectrum (Eq. 2.15). The root-coherence is the modulus of the coherence. As the quadrature spectrum is often small, the co-coherence is commonly approximated by the root-coherence. However, it should be noted that the

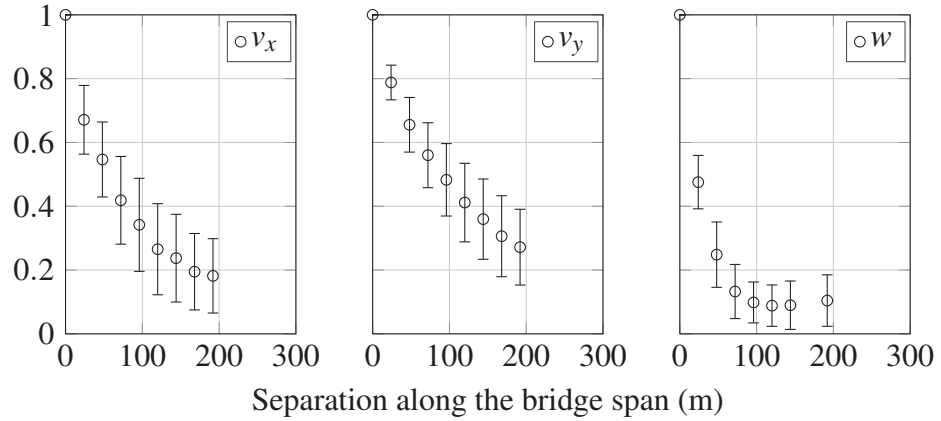

Figure 2.5 Correlation coefficients along the Lysefjord Bridge span (S-SW flow), for $8\,\mathrm{m\,s^{-1}} < \overline{V}_x < 10\,\mathrm{m\,s^{-1}}$. The data set is made of 90 samples recorded from 25/10/2014 to 28/10/2014. The total length of the error bar is equal to two standard deviations.

co-coherence can take negative values whereas the root-coherence is always positive. The co-coherence is of particular interest in wind engineering because it allows the modelling of the dynamic wind load by taking into account the in-phase correlation of the wind velocity fluctuations.

$$\gamma(d_y, f) = \left| Co(d_y, f) + i \cdot Q_{uad}(d_y, f) \right| \tag{2.15}$$

The co-coherence is approximated in the present study by a four-parameter function fitted in the least-square sense to the measured co-coherence:

$$\gamma(d_y, f) = \exp\left(- \left[\frac{d_y}{\overline{V}_x} \sqrt{(c_1 f)^2 + c_2^2} \right]^{c_3} \right) \cdot \cos\left(c_4 \frac{d_y f}{\overline{V}_x} \right) \tag{2.16}$$

The first parameter c_1 gives the slope of the exponential decay, the second one c_2 allows the co-coherence to be lower than one for a zero frequency. The third one c_3 allows an additional inflection point at low frequencies, and the last one c_4 allows the co-coherence to become negative when the frequency increases. When $c_4 = 0$, the coherence function developed by Bogunović Jakobsen (1997) is recovered. If $c_4 = 0$ and $c_3 = 1$, the 2-parameter function introduced by Hjorth-Hansen et al. (1992) is obtained. Finally, if $c_4 = 0$, $c_3 = 1$ and $c_2 = 0$, then the model from Davenport (1961b) is retrieved.

From the 25/10/2014 to 28/10/2014, the coherence for the wind component normal to the Bridge deck is computed for multiple lateral separations and mean wind velocities. The four-parameter function is fitted to the measured coherence and the fitted decay coefficients are displayed in Table 2.3. Relatively stable coefficients are obtained for the different mean wind velocities recorded. As expected, the coefficient c_2 is relatively small whereas c_3 is close to 1. The value of c_1 is significantly lower than the decay coefficient $c_1 = 7$ proposed by (Davenport, 1961b) for the 1-parameter coherence model. This difference may be explained by the existence of the parameter c_4 which affects the value of c_1 and by the use of $\overline{V}_x$ instead of $\overline{U}$. The existence of an important yaw angle may be be responsible for a reduction of the measured

Table 2.3 Coefficients found by fitting Eq. 2.16 to the measured wind coherence displayed in Fig. 2.6.

Velocity range ($\mathrm{m\,s^{-1}}$)	c_1	c_2	c_3	c_4
$8 \leq \overline{V}_x < 10$	4.14	0.03	1.09	6.34
$10 \leq \overline{V}_x < 11$	4.35	0.04	1.05	6.32
$11 \leq \overline{V}_x < 13$	4.24	0.03	1.13	5.13
$13 \leq \overline{V}_x < 14$	3.86	0.02	1.14	4.36

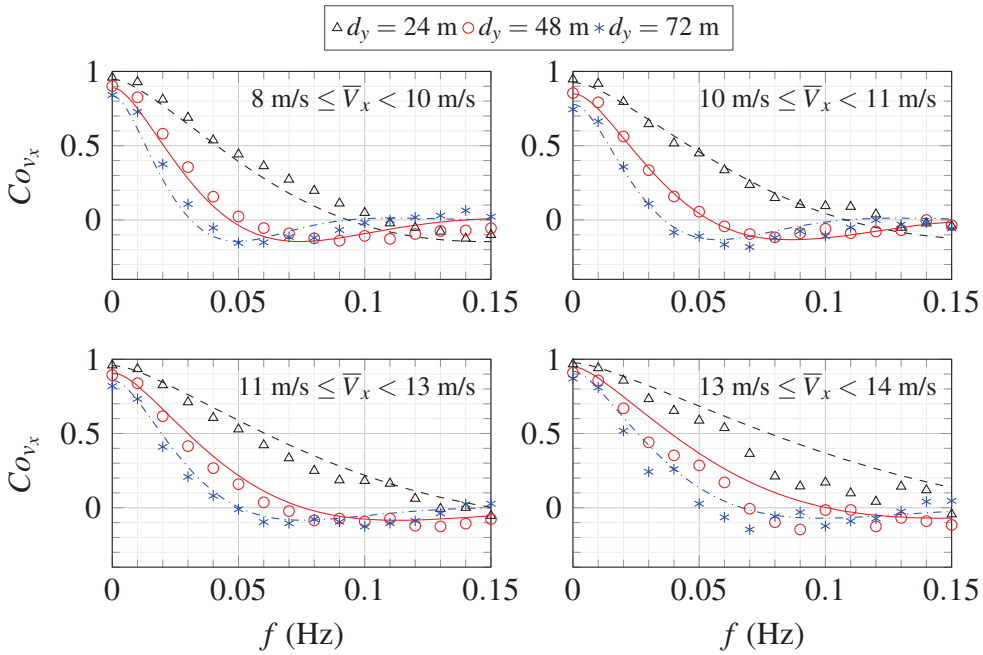

Figure 2.6 Co-coherence measured (scatter plot) and fitted (dashed lines) for the S-SW exposure at the Lysefjord Bridge site from 25/10/2014 to 28/10/2014.

coefficient c_1 and for the negative value of the coherence. The negative co-coherence is visible in Fig. 2.6 and captured by the coefficient c_4. Anyway, Fig. 2.6 shows a satisfying agreement between the fitted four-parameter function and measured coherence.

Comparison with other coherence models

Alternative coherence models are available in the literature. Among them the models by von Kármán (1948), ESDU 86010 (2001) or Krenk (1996) are quite common. The four-parameter coherence function presented in Eq. 2.16 is more general than the empirical coherence models used previously. Its versatility is highlighted in Fig. 2.7, where it is fitted to the Krenk and von Kármán coherence model.

The Krenk co-coherence model requires measurement of the integral length scale L_u:

$$Co = (1 - \frac{1}{2}a \cdot d_y)\exp(-a \cdot d_y), \quad a = \frac{1}{2}\left[\left(\frac{2\pi f}{\overline{U}}\right)^2 + \left(\frac{1}{L_u}\right)^2\right]^{0.5} \tag{2.17}$$

The von Kármán isotropic coherence model (von Kármán, 1948) is:

$$\gamma_u(f) = \frac{2^{1/6}}{\Gamma(5/6)}\left[a^{5/6}K_{5/6}(a) - \frac{1}{2}a^{11/6}K_{1/6}(a)\right] \tag{2.18}$$

$$\gamma_v(f) = b \cdot \left[\frac{4.781a^2}{(d_y/\mathscr{L})^2}a^{5/6}K_{5/6}(a) - a^{11/6}K_{11/6}(a)\right] \tag{2.19}$$

where a, the reduced frequency n and b are defined as:

$$b = \frac{0.597}{2.869a^2 \cdot (d_y/\mathscr{L})^{-2} - 1} \tag{2.20}$$

$$a = \sqrt{n^2 + (0.747D/\mathscr{L})^2} \tag{2.21}$$

$$n = \frac{2\pi fD}{\overline{U}} \tag{2.22}$$

The isotropic integral length scale $\mathscr{L}$ is defined as $\mathscr{L} = 2L_u$ (ESDU 86010, 2001), Γ is the gamma function and K_i is the modified Bessel function of the second kind (Luke, 1962). ESDU 86010 (2001) proposes a modified

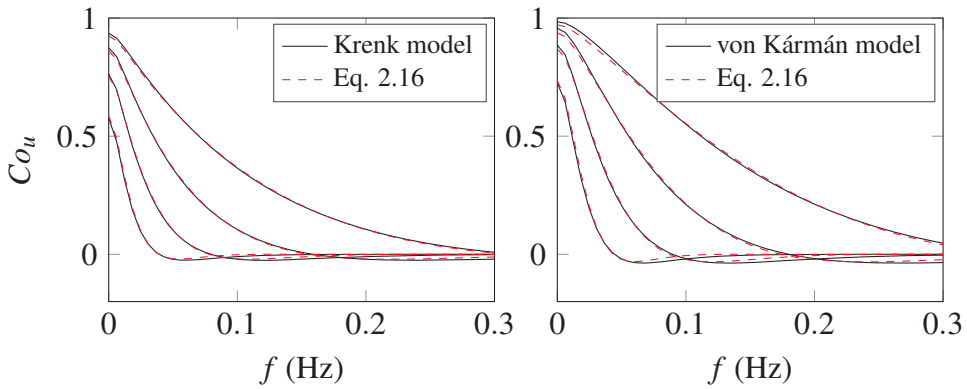

Figure 2.7 Four-parameter function fitted to the Krenk coherence model (left) and the von Kármán one (right), with $\overline{U} = 10\ \mathrm{m\,s^{-1}}$, $L_u = 75$ m and $\mathscr{L} = 150$ m, which are arbitrary chosen and used for illustrative purpose only.

von Kármán coherence model:

$$\gamma_u(f) = \exp\left(-1.15a_1^{1.5}\right) \tag{2.23}$$

$$\gamma_v(f) = \exp\left(-0.65a_1^{1.3}\right) \tag{2.24}$$

where :

$$a_1 = \sqrt{(0.747r)^2 + (cn)^2} \tag{2.25}$$

$$r = \frac{d_y}{2L_u^y} \tag{2.26}$$

$$c = \max\left(1, \frac{1.6r^{0.13}}{a^b}\right) \tag{2.27}$$

$$b = 0.35r^{0.2} \tag{2.28}$$

where L_u^y is the cross-flow turbulence length scale for the u-component at the altitude of the anemometers. The variables a and n are defined in Eq. 2.21 and Eq. 2.22 respectively.

2.3 The buffeting theory

The analysis of turbulence-induced vibrations of a suspension bridge can be conducted in the time domain or the frequency domain. For the latter, the analysis is often faster but is limited to linear loads and linear structural properties.

In the time domain, the wind load needs to be simulated in terms of time-histories, which is computationally more expensive. However, non-linearities and non-stationarity can be more easily taken into account. In the present thesis, only the frequency domain approach is presented. Possible influence of the non-linearity or non-stationarity of the wind load is discussed in Chapter 7.

2.3.1 Assumptions

Quasi-steady assumption: The quasi-steady assumption implies that the wind fluctuations instantaneously adapt to the moving bridge deck. This means that the aerodynamic coefficients and their first derivative are independent of the frequency. In the case of the Lysefjord Bridge, only the mean aerodynamic coefficients were available, making the use of the quasi-steady theory most natural.

Linearity: The aerodynamic forces calculated with the quasi-steady theory are linearised with respect to the time-dependant angle of attack, using Taylor series up to order 1. The higher order terms are assumed negligible. Similarly, the aerodynamic modal damping ratio is assumed to increase linearly with the mean wind velocity.

Modal coupling: Structural and aerodynamic modal coupling is neglected for the Lysefjord Bridge because the buffeting response is studied for wind

velocities commonly recorded on the bridge site, i.e. lower than 40 $\mathrm{m\,s^{-1}}$. The validity of this assumption is discussed in Chapter 7.

Strip assumption: The total wind load on the bridge deck can be computed by considering the wind forces on a single cross-section, and assuming that the correlation of the wind forces along the bridge deck is identical to that of the undisturbed, incoming wind fluctuations. This assumption relies on the idea that the length scale of turbulence is much larger than the deck width, so that wind gusts are not deformed when passing over the bridge. The latter produces vortices that amalgamate and grow stronger, causing an increased span-wise coherence of the wind forces (Bogunović Jakobsen, 1997; Hjorth-Hansen et al., 1992; Larose, 1997; Larose et al., 1998). This phenomenon is more pronounced for wide decks for which the ratio L_w^y/B is relatively small. The deck of the Lysefjord Bridge is 12.3 m wide. Values of L_w^y recorded along the span of this bridge were usually larger than 30 m and L_w^y/B was therefore above 2.4. Larose (1997) observed that for $L_w^y/B \leq 1.5$, the strip assumption was not valid any more.

In the case of the Lysefjord Bridge, the strip assumption seemed plausible for the horizontal and vertical resonant response whereas it was found necessary to introduce a frequency-dependent cross-sectional admittance to characterize the overturning moment. The latter is responsible for the resonant torsional response, at frequencies higher than those involved in the translational response.

2.3.2 Aerodynamic forces

The bridge is modelled as a linear system with viscous damping, where the girder cross-section and the related forces are presented in Fig. 2.8. The dynamic response of the bridge deck to wind turbulence is calculated following Scanlan (1975) and Hjorth-Hansen (1993b), based on the work of Davenport (1961a, 1962).

The dynamic lateral and vertical displacements and the deck rotation are denoted r_y, r_z, and r_θ respectively. The aerodynamic drag, lift, and pitching moment are written F_D, F_L and F_M respectively. They are transformed into the lateral wind force F_x, the vertical force F_z and pitching moment F_θ, i.e. projected between the two coordinate systems (Fig. 2.8). By using the same notations as Hjorth-Hansen (1993b), the total incidence angle α, is:

$$\alpha = \overline{\alpha} + \alpha_f \tag{2.29}$$

$$\overline{\alpha} = \overline{r_\theta} \tag{2.30}$$

$$\alpha_f = r_\theta + \arctan\left(\frac{w - \dot{r}_z - k_\theta B \dot{r}_\theta}{\overline{V}_x + v_x - \dot{r}_x}\right) \tag{2.31}$$

The fluctuating wind components and the fluctuating bridge velocity response are assumed small compared to the mean wind speed. Taylor's series up to order 1 is therefore applied to the instantaneous wind incidence angle α_f, the instantaneous wind relative velocity V_{rel}, and the quasi-steady

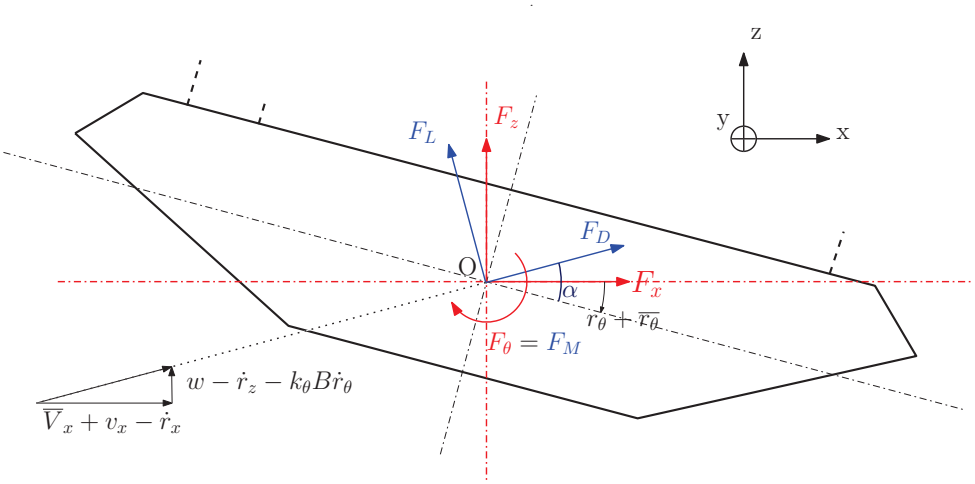

Figure 2.8 Cross-section of the bridge deck subjected to wind load.

terms of the aerodynamic coefficients C_D, C_L and C_M:

$$\alpha_f - r_\theta = \frac{w - \dot{r}_z - k_\theta B \dot{r}_\theta}{\overline{V}_x} + \mathscr{O}\left(\frac{1}{\overline{V}_x}\right)^3 \tag{2.32}$$

$$\cos(\alpha_f - r_\theta) = 1 + \mathscr{O}\left(\frac{1}{\overline{V}_x}\right)^2 \tag{2.33}$$

$$\sin(\alpha_f - r_\theta) = \alpha_f - r_\theta + \mathscr{O}\left(\frac{1}{\overline{V}_x}\right)^2 \tag{2.34}$$

$$|V_{\text{rel}}|^2 = \overline{V}_x^2 + 2\overline{V}_x v_x - 2\overline{V}_x \dot{r}_x + \mathscr{O}\left(\frac{1}{\overline{V}_x}\right)^2 \tag{2.35}$$

$$C_D(\alpha) = C_D(\overline{\alpha}) + \alpha_f \cdot C_D'(\overline{\alpha}) + \mathscr{O}\left(\overline{\alpha}^2\right) \tag{2.36}$$

$$C_L(\alpha) = C_L(\overline{\alpha}) + \alpha_f \cdot C_L'(\overline{\alpha}) + \mathscr{O}\left(\overline{\alpha}^2\right) \tag{2.37}$$

$$C_M(\alpha) = C_M(\overline{\alpha}) + \alpha_f \cdot C_M'(\overline{\alpha}) + \mathscr{O}\left(\overline{\alpha}^2\right) \tag{2.38}$$

with $\overline{\alpha}$ not explicitly shown in the following.

In its traditional format, the quasi-steady theory does not include any aerodynamic damping for the torsional deck motion (Hjorth-Hansen, 1993a). A damping term $k_\theta B \dot{r}_\theta$ was however introduced by Irwin and Wardlaw (1976). It is based on the apparent angle of attack associated with the vertical velocity at the cross section aerodynamic centre rather than the shear centre. This term is included in this thesis with $k_\theta = 0.25$, where k_θ specifies the horizontal distance between the aerodynamic and the shear centre as a fraction of the girder width. The positive k_θ value is for an aerodynamic centre located upstream of the shear centre.

In the bridge-based coordinate system, the wind load is expressed as a function of the incidence α and the aerodynamic forces:

$$\boldsymbol{F} = \begin{bmatrix} F_x \\ F_z \\ F_\theta \end{bmatrix} = \frac{1}{2}\rho V_{\text{rel}}^2 B \begin{bmatrix} \frac{D}{B} C_D \cdot \cos(\alpha_f - r_\theta) - C_L \cdot \sin(\alpha_f - r_\theta) \\ \frac{D}{B} C_D \cdot \sin(\alpha_f - r_\theta) + C_L \cdot \cos(\alpha_f - r_\theta) \\ B C_M \end{bmatrix} \tag{2.39}$$

The linearised terms from Eq. 7.5 to Eq. 7.11 are introduced into Eq. 7.12 to obtain Eq. 2.40. To simplify the calculation of the buffeting response of the Lysefjord Bridge, a modal approach is used where the equations of motion are solved in the so-called "modal base". If the bridge response is not expressed in the "modal base", then the "physical base" is used, and the displacement are calculated in a finite number of positions characterized by their spatial coordinates. The total force $\boldsymbol{F}$ applied on the cross-section of the bridge deck is expressed as the linear combination of the matrices of static wind load $\boldsymbol{A_0}$, buffeting load $\boldsymbol{A_1}$, aerodynamic damping $\boldsymbol{C}_{ae}$, and aerodynamic stiffness $\boldsymbol{K}_{ae}$:

$$\boldsymbol{F} = \boldsymbol{A_0}\left[U\right] + \boldsymbol{A_1}\begin{bmatrix} v_x \\ w \end{bmatrix} - \boldsymbol{C_{ae}}\begin{bmatrix} \dot{r}_x \\ \dot{r}_z \\ \dot{r}_\theta \end{bmatrix} - \boldsymbol{K_{ae}}\begin{bmatrix} r_x \\ r_z \\ r_\theta \end{bmatrix} \tag{2.40}$$

where:

$$\boldsymbol{A_0} = \frac{1}{2}\rho\overline{V}_x B\begin{bmatrix} D/B \cdot C_D \\ C_L \\ BC_M \end{bmatrix} \tag{2.41}$$

$$\boldsymbol{A_1} = \frac{1}{2}\rho\overline{V}_x B\begin{bmatrix} 2\frac{D}{B}C_D \cdot \chi_{v_x x} & \left(\frac{D}{B}C'_D - C_L\right)\cdot\chi_{wx} \\ 2C_L \cdot \chi_{v_x z} & \left(C'_L + \frac{D}{B}C_D\right)\cdot\chi_{wz} \\ 2BC_M \cdot \chi_{v_x\theta} & BC'_M \cdot \chi_{w\theta} \end{bmatrix} \tag{2.42}$$

$$\boldsymbol{C}_{ae} = \frac{1}{2}\rho\overline{V}_x B\begin{bmatrix} 2\frac{D}{B}C_D & \frac{D}{B}C'_D - C_L & k_\theta B(\frac{D}{B}C'_D - C_L) \\ 2C_L & C'_L + \frac{D}{B}C_D & k_\theta B(C'_L + \frac{D}{B}C_D) \\ 2BC_M & BC'_M & k_\theta B^2 C'_M \end{bmatrix} \tag{2.43}$$

$$\boldsymbol{K}_{ae} = -\frac{1}{2}\rho\overline{V}_x^2 B \begin{bmatrix} 0 & 0 & \frac{D}{B}C'_D \\ 0 & 0 & C'_L \\ 0 & 0 & BC'_M \end{bmatrix} \tag{2.44}$$

where χ_{pq} are the cross-sectional aerodynamic admittance functions. The subscript $p = \{v_x, w\}$ refers to the wind components of interest and $q = \{x, z, \theta\}$ corresponds to the lateral, vertical or torsional bridge motion respectively.

The cross-sectional aerodynamic admittance functions $\chi_{v_x x}$, χ_{wx}, $\chi_{v_x z}$ and χ_{wz} were taken as unity at all frequencies. For the torsional motion, the Liepmann's approximation of the Sears' function (Liepmann, 1952), developed for a lift slope of 2π in a fully correlated sinusoidal gust (Eq. 2.45) was chosen:

$$|\chi_{v_x\theta}(f)|^2 = |\chi_{w\theta}(f)|^2 = \frac{1}{1+\frac{2\pi f B}{\overline{V}_x}} \tag{2.45}$$

Another relevant cross-sectional aerodynamic admittance function is the one introduced by Holmes (1975) and used by e.g. by Matsuda et al. (1999) for the overturning moment. A third alternative may be to use the cross-sectional aerodynamic admittance functions developed by Larose et al. (1998) for bridge deck sections similar to the one used for the Lysefjord Bridge.

2.3.3 Equation of motion

The equations of motion for the bridge model is:

$$\boldsymbol{M}\ddot{\boldsymbol{r}} + \boldsymbol{C}\dot{\boldsymbol{r}} + \boldsymbol{K}\boldsymbol{r} = \boldsymbol{F} \tag{2.46}$$

where

$$\boldsymbol{r} = \begin{bmatrix} r_x & r_z & r_\theta \end{bmatrix}^\top \tag{2.47}$$

By combining Eq. 2.40 and Eq. 2.46, the equations of motion become:

$$\boldsymbol{M}\ddot{\boldsymbol{r}} + [\boldsymbol{C} + \boldsymbol{C_{ae}}]\dot{\boldsymbol{r}} + [\boldsymbol{K} + \boldsymbol{K_{ae}}]\boldsymbol{r} = \boldsymbol{A_0}\left[U\right] + \boldsymbol{A_1}\begin{bmatrix} v_x \\ w \end{bmatrix} \tag{2.48}$$

2.3.4 Response in the frequency domain

The matrix of static load $\boldsymbol{A_0}$ is disregarded in the following, because only the dynamic response of the bridge is studied. The real part of the cross-spectral density of the wind velocity at two points of abscissa y_i and y_j is defined using the single-point wind spectra $\boldsymbol{S}_{v_x}$ and $\boldsymbol{S}_w$, and the co-coherence functions $\boldsymbol{\gamma}_{v_x}$, $\boldsymbol{\gamma}_w$:

$$S_1(\Delta_y, f) = \sqrt{S_{v_x}(y_i, f) \cdot S_{v_x}(y_j, f)} \cdot \gamma_{v_x}(\Delta_y, f) \tag{2.49}$$

$$S_2(\Delta_y, f) = \sqrt{S_w(y_i, f) \cdot S_w(y_j, f)} \cdot \gamma_w(\Delta_y, f) \tag{2.50}$$

where $\Delta_y = \left|y_i - y_j\right|$. Thus the cross-spectrum matrix $\boldsymbol{S}_q$ of the wind velocities weighted by the matrix of buffeting load coefficients is a block matrix, where the block (i,j) is a 3 by 3 matrix defined as :

$$\boldsymbol{S}_q(i, j, f) = \boldsymbol{A_1}\begin{bmatrix} S_1(\Delta_y, f) & 0 \\ 0 & S_2(\Delta_y, f) \end{bmatrix}\boldsymbol{A_1}^{\mathsf{T}} \tag{2.51}$$

The spectrum of the modal wind load $\boldsymbol{S}_Q$ is obtained using the matrix $\boldsymbol{\psi}$ of mode shapes of the bridge deck:

$$\boldsymbol{S}_Q(f) = \int_0^L \int_0^L \boldsymbol{\psi}(y_1)\boldsymbol{S}_q(y_1, y_2, f)\boldsymbol{\psi}(y_2)\,\mathrm{d}y_1\,\mathrm{d}y_2 \tag{2.52}$$

The power spectral density of the modal bridge displacement a is:

$$\boldsymbol{S}_\eta(f) = \boldsymbol{H}(f)\boldsymbol{S}_Q(f)\boldsymbol{H}^{\mathsf{T}}(f) \tag{2.53}$$

where $\boldsymbol{H}$ is the mechanical admittance of the system modified by the modal aerodynamic damping and stiffness, defined as:

$$\boldsymbol{H}(f) = \left[-\omega^2 \tilde{\boldsymbol{M}} + i\omega\left(\tilde{\boldsymbol{C}} + \tilde{\boldsymbol{C}}_{\boldsymbol{ae}}\right) + \left(\tilde{\boldsymbol{K}}_{\boldsymbol{ae}} + \tilde{\boldsymbol{K}}\right)\right]^{-1} \tag{2.54}$$

where $\tilde{\boldsymbol{M}}, \tilde{\boldsymbol{C}}, \tilde{\boldsymbol{K}}, \tilde{\boldsymbol{C}}_{\boldsymbol{ae}}$ and $\tilde{\boldsymbol{K}}_{\boldsymbol{ae}}$ are:

$$\tilde{\boldsymbol{M}} = \int_0^L \left(\boldsymbol{\psi}^\top \boldsymbol{M} \boldsymbol{\psi}\right) \mathrm{d}y \tag{2.55}$$

$$\tilde{\boldsymbol{K}} = diag\left[\tilde{M}_i \omega_i^2\right], \quad i = \{1...\mathrm{N}_{\mathrm{modes}}\} \tag{2.56}$$

$$\tilde{\boldsymbol{C}} = diag\left[2\tilde{M}_i \omega_i \zeta_i\right], \quad i = \{1...\mathrm{N}_{\mathrm{modes}}\} \tag{2.57}$$

$$\tilde{\boldsymbol{C}}_{\boldsymbol{ae}} = \int_0^L \left(\boldsymbol{\psi}^\top \boldsymbol{C}_{\boldsymbol{ae}} \boldsymbol{\psi}\right) \mathrm{d}y \tag{2.58}$$

$$\tilde{\boldsymbol{K}}_{\boldsymbol{ae}} = \int_0^L \left(\boldsymbol{\psi}^\top \boldsymbol{K}_{\boldsymbol{ae}} \boldsymbol{\psi}\right) \mathrm{d}y \tag{2.59}$$

The PSD of the bridge response at abscissa y_r of the bridge is:

$$\boldsymbol{S}_{y_r}(f) = \boldsymbol{\psi}(y_r) \boldsymbol{S}_\eta(f) \boldsymbol{\psi}^\mathsf{T}(y_r) \tag{2.60}$$

and the standard deviation (STD) of the bridge displacement $\boldsymbol{\sigma_r}(y_r)$ at abscissa y_r is:

$$\boldsymbol{\sigma_r}(y_r) = \sqrt{\int_0^\infty \boldsymbol{S}_{y_r}(f)\, \mathrm{d}f} \tag{2.61}$$

where

$$\boldsymbol{\sigma_r}(y_r) = \left[\sigma_{r_x}(y_r) \quad \sigma_{r_z}(y_r) \quad \sigma_{r_\theta}(y_r)\right]^{\mathsf{T}} \tag{2.62}$$

The frequency domain analysis presented here is thus based on a statistical approach where the buffeting response of a suspension bridge is expressed in terms of PSD (Eq. 2.60) and STD (Eq. 2.61) of the displacement or acceleration response.

Chapter 3

Full-scale monitoring

3.1 The Lysefjord Bridge

The Lysefjord Bridge, positioned at the narrow inlet of a fjord in the South-West part of the Norwegian coast, is used as a case study. Its main span is 446 m, with the central part 55 m above the sea level (Fig. 3.1). It is oriented from North-West to South-East in a mountainous environment. By using the Shuttle Radar Topography Mission (SRTM) digital elevation data (SRTM, 2014), a detailed map of the topography around the Lysefjord can be produced as presented in Fig. 3.2. The bridge is entrenched between two steep hills with slopes ranging from 30° to 45° and a maximum altitude of 350 m to the North and 600 m to the South. As seen in Figs. 3.2-3.3, the bridge is exposed to winds that may descent from mountains nearby or follow the fjord over a longer path. The West side of the bridge is exposed to a more open and levelled area.

3.2 Long term instrumentation

Between November 2013 and June 2014, six 3D WindMaster Pro sonic anemometers from Gill Instrument Ltd have been installed on the West side

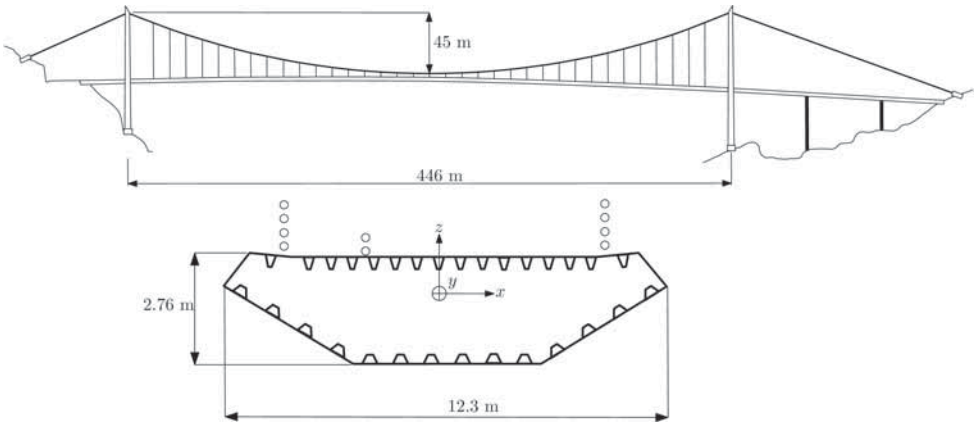

Figure 3.1 Schematic of the Lysefjord Bridge (top) and its deck cross-section (bottom).

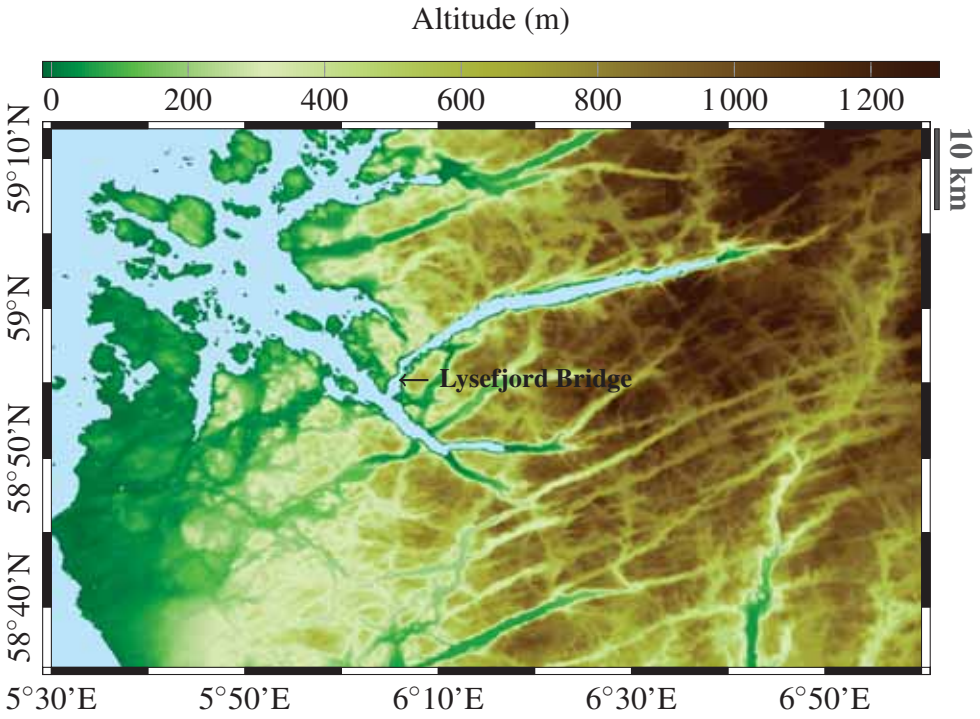

Figure 3.2 Elevation map of the Lysefjord in South-Western Norway.

Figure 3.3 Three different views from the bridge site: from the South-West (view a, top left), from the East (view b, top right), from the North-West (view c, bottom left), and the location of the viewpoints on the map (bottom right).

of the bridge deck, on hangers 08, 16, 18, 20 and 24, denoted H-08, H-16, H-18, H-20 and H-24 respectively. In addition, a Vaisala weather transmitter WXT520 has been fixed to hanger 10. The anemometers are either directly fixed to the hangers, or on the top of a vertical steel pole above the main cables (Fig. 3.5), all at ca. 6 m above the deck. At hanger H-08, an additional anemometer has been installed 10 m (H-08t) above the deck in June 2014. Four pairs of tri-axial accelerometers have also been installed inside the bridge

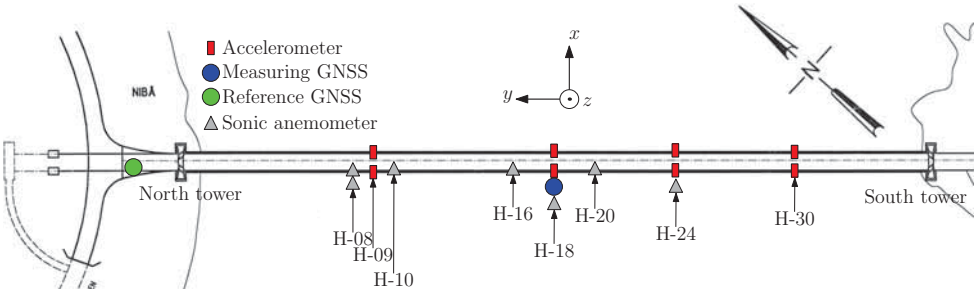

Figure 3.4 Anemometers (circles) and accelerometers (rectangles) location on the bridge.

Figure 3.5 Sonic anemometer on H-24 (left), on H-18 (middle) and weather station on H-10 (right) installed 6 m above the West side of the bridge deck.

deck, near hangers 9, 18, 24, and 30 so that both symmetric and asymmetric modes can be captured efficiently. The accelerometers used are triaxial MEMs silicon accelerometers from Canterbury Seismic Ltd. The accelerometers are placed on each side of the deck to monitor the bridge torsional response around its longitudinal axis (x), in addition to the translational response. The lateral distance between two accelerometers constituting a pair is ca. 7.15 m and the maximal sampling frequency of each accelerometer is 200 Hz. Since the distance between each hanger is 12 m, the distance between the anemometers ranges from 24 m to 168 m. A summary of the sensors installed on the bridge is shown in Fig. 3.4.

GPS timing is used to synchronize the wind and the acceleration data, acquired locally with separated data logging units. Finally, a 3G router enables wireless data access and transfer via a mobile net. The dynamic displacement

of the bridge is calculated from the acceleration data by their transformation in the frequency domain. For the analysis, the sampling frequency is reduced to 100 Hz (in 2014) or to 50 Hz (since 2015). The data are afterwards decimated to 20 Hz in post-processing.

In June 2015, a Real-Time Kinematic-Global Positioning System (RTK-GPS) was installed on the Lysefjord Bridge to directly measure its static and quasi-static displacement. The RTK-GPS consists in a base-rover combination to improve the accuracy of measurements by recording the relative displacement between a "fixed" base station and a "moving" rover station. In the present case, a set of Trimble BD930 GNSS receivers are coupled to Trimble AV33 GNSS antennas. These sensors can handle data sampling at a frequency of 20 Hz, with an accuracy of $\pm$ 8 mm $+1$ ppm for the horizontal displacements and $\pm$ 15 mm $+1$ ppm for the vertical displacements. The data recorded by the RTK-GPS are discussed in Appendix A. Sonic anemometers are used here as reference sensors for a bridge immersed in complex terrain. Prior to a bridge construction, the wind measurements are confined to locations on land, where the flow conditions are expected to differ from those above the sea surface, especially in a mountainous terrain.

3.3 Short term instrumentation with lidars

3.3.1 Overview

LIDAR is the acronym for Light Detection And Ranging. It is a remote sensing technology based on the emission of a laser beam and the analysis of the backscattered light by gas and particles in the atmosphere. A lidar is therefore made of three main components: a laser, a telescope, and the detection system. Lidars are not always used to measure the wind. The type of data that are captured by the lidar depends on the wavelength of the laser and the size of the particles that backscatter the light. For wind velocity measurements, a so-called Doppler lidar with a wavelength of ca. 1.5 µm is

commonly used. In that case, the atmospheric particles that backscatter the light are dust, pollen and aerosols. A fraction of the backscattered light is collected by the telescope and compared to the emitted light so that a Doppler shift frequency can be measured to estimate the line-of-sight (LOS) velocity of the aerosols, which is assumed identical to the wind velocity. The LOS velocity component is also called along-beam velocity, and results from the projection of the three-dimensional wind velocity vector onto the scanning beam.

Scanning modes

Some Doppler wind lidars have a rotating head allowing hemispherical scanning. In that case, multiple scanning modes are available: the Velocity Azimuth Display (VAD), the Doppler Beam Swinging (DBS), the Plan Position Indicator (PPI), the Range Height Indicator (RHI) and the Line-Of-Sight (LOS) scan. Each scan is defined in terms of three parameters: a radial distance r, an azimuth angle Φ, and an elevation angle Ψ. The azimuth angle is defined with respect to the North, and the elevation angle is defined with respect to the horizontal plane (Fig. 3.6).

The VAD scan is a conical scanning mode where the elevation angle Ψ is fixed. The azimuth angle is varying, ranging from 0 to 360° (Fig. 3.7). The measure of the along-beam velocity component V_r for multiple azimuth angles provides a relationship between Φ and V_r leading to an estimation of the horizontal wind velocity components (Weitkamp, 2005). The DBS scan is similar to the VAD scan, but the horizontal wind components are retrieved from only four azimuth angles. In that case, the azimuth-angle interval is 90°. The DBS technique leads to a better temporal resolution than the VAD mode but with a higher measurement noise. In this thesis, the DBS and VAD technique are not studied in details because they are mainly used for wind profiling, which has limited applications for suspension bridges. These scanning modes are however widely applied in the field of wind energy, and

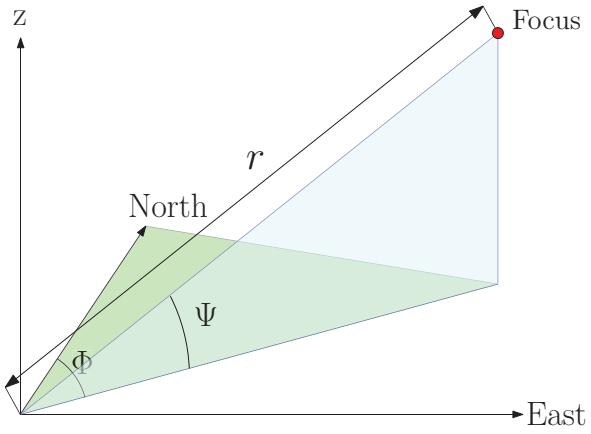

Figure 3.6 Azimuth angle Φ, elevation angle Ψ and radial distance r defined for a scanning wind lidar.

their capabilities to measure wind turbulence is well documented (Sathe et al., 2011, 2015).

The PPI, RHI and LOS scannig modes can be defined using only the pair of variables (Φ, Ψ) . The PPI mode corresponds to the case where Ψ is fixed, and the scanning head sweeps an area using multiple azimuth angles. In Fig. 3.8, a schematic of PPI scan is shown for an elevation angle of 45° and azimuth angles ranging from 0° to 90°. If only Φ is fixed, then the RHI mode is used, and the rotating head scans the flow with varying elevation angles. A schematic of a RHI scan is displayed in Fig. 3.9, where the azimuth is fixed to 20° and the elevation angles range from 0° to 90°. If both Φ and Ψ are fixed, then the LOS scanning mode is selected. If a single wind lidar is used with the PPI, RHI and LOS scan, only the along-beam wind velocity can be retrieved. The PPI scan used here is actually a "PPI sector scan" as the scanning beam does not describe a full circle. For the sake of brevity, the "PPI sector scan" is simply referred to as the "PPI scan" in the following. Although the scanning patterns displayed in Fig. 3.8 and Fig. 3.9 appear as "discrete", they are typically continuous. The wind data recorded in the points

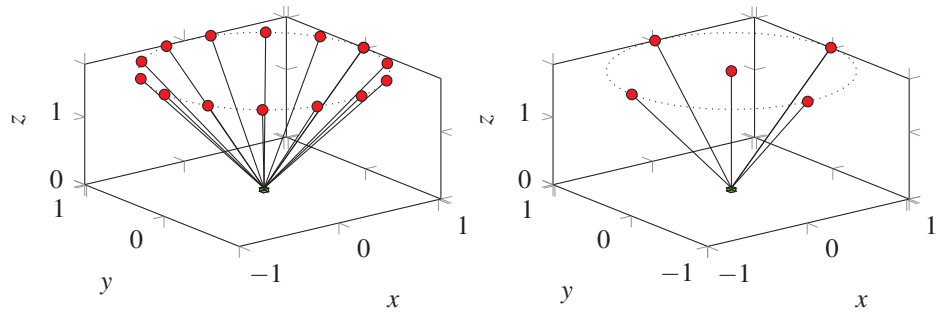

Figure 3.7 Schematic of the VAD scan (left) and DBS scan (right).

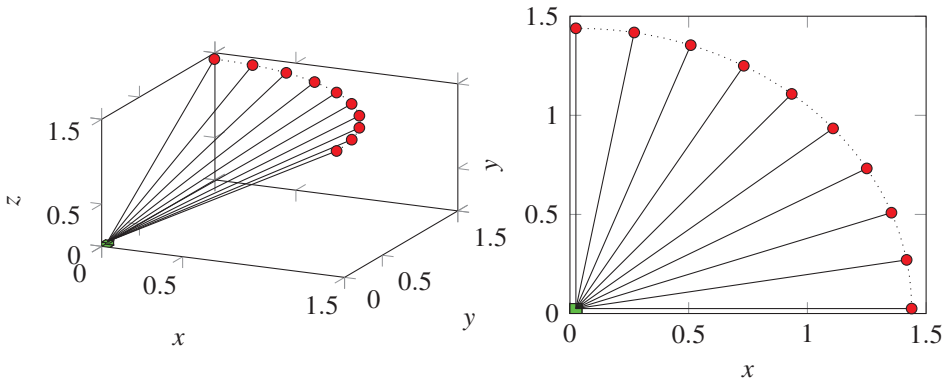

Figure 3.8 Isometric (left) and top view (right) of the schematic of a PPI scan, with multiple azimuth angles and a single elevation angle. The vertical axis is z.

drawn in Fig. 3.8 and Fig. 3.9 (symbol: •) are therefore affected by a spatial averaging due to the movement of the scanning beam.

The spatial averaging effect

There are two types of Doppler wind lidars: pulsed lidars and continuous wave (cw) lidars. For a given azimuth angle and a given elevation angle, a continuous wave lidar measures the wind velocity at a single position along the beam (right panel of Fig. 3.10). A pulsed lidar provides however simultaneous measurements in multiple positions along the beam (Fig. 3.10).

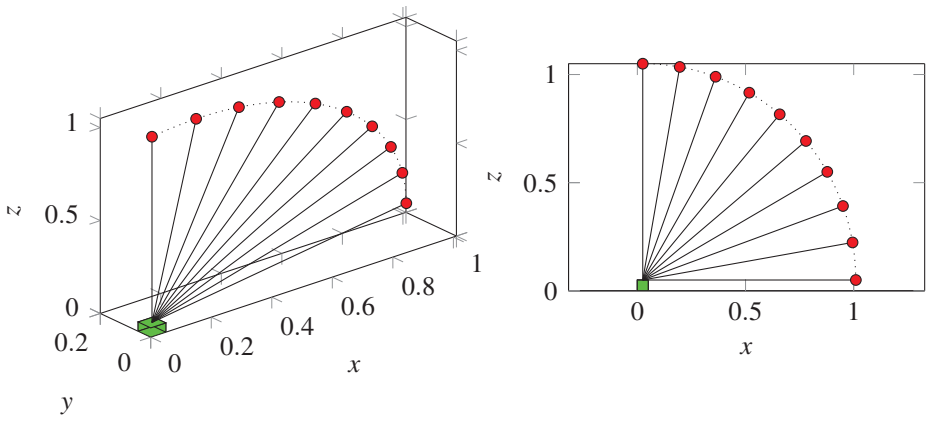

Figure 3.9 Isometric (left) and side view (right) of the schematic of a RHI scan, with multiple elevation angles and a single azimuth angle.

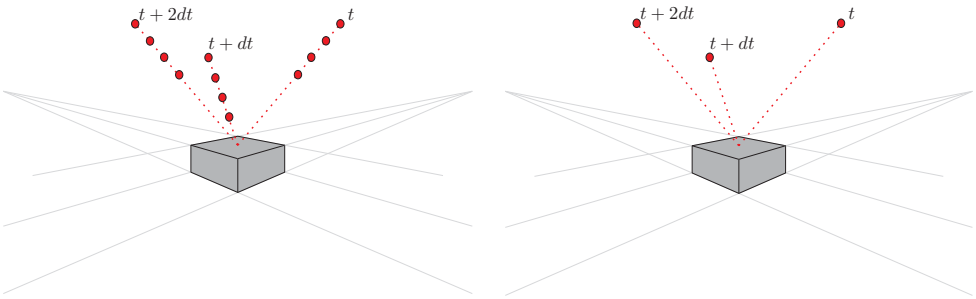

Figure 3.10 Left: Schematic of a pulsed wind lidar with simultaneous along-beam measurements, for three consecutive time steps. Right: Schematic of a cw lidar monitoring the wind field at three different consecutive time steps.

On the other hand, a cw lidar is generally able to scan the flow with a much larger sampling frequency and at shorter distances than a pulsed lidar.

Contrary to sonic anemometers that are almost single-point sensors, Doppler wind-lidars measure the wind velocity in a finite volume stretched along the scanning beam, which implies that the higher frequencies are filtered out. This is referred to as the "spatial averaging effect" in the following. This "low-pass filtering" can be observed by comparing the spectra of the

along-beam wind velocity recorded by a lidar with the one from a sonic anemometer (Angelou et al., 2012; Sjöholm et al., 2008, 2009).

The range gate is defined as the along-beam length of the stretched volume in which the line-of-sight velocity is recorded. For cw wind lidars, the range gate increases with the square of the radius. In other words, the spatial averaging effect increases for larger distances from the sensor. For a pulsed lidar on the other hand, the range gate remains constant along the beam and so the spatial averaging. According to Weitkamp (2005), the range gate Δ_r can be expressed as a function of the wavelength λ , the detector area A_d, and the distance r as :

$$\Delta_r = \frac{8r^2\lambda}{A_d} \tag{3.1}$$

For a short-range lidar, such as the WindScanner system (http://www.windscanner.dk/) which uses a wavelength of 1.5 µm and a lens area of 18 mm^2, the range gate at 100 m is only 6.7 m, whereas for a distance of 1 km, Δ_r becomes equal to 667 m. For this reason, cw lidars are often used for short-range wind monitoring, especially since the minimum working distance, also called dead-zone, is usually low. For the Zephir300, the dead-zone is 10 m whereas for a pulsed wind lidar such as the WindCube 100S, the dead zone is ca. 40 m.

Estimation of the spatial averaging effect

Following Smalikho (1995), the spatial averaging effect for a cw lidar can be expressed as a convolution between the spatial averaging function ϕ and the vector of the wind velocity $\boldsymbol{v_r^0}$ projected along the laser beam at a focus distance r from the lidar:

$$v_r(r) = \int_{-\infty}^{+\infty} \phi(s)\mathbf{n} \cdot \boldsymbol{v_r^0}(s\mathbf{n} + r\mathbf{n})\,\mathrm{d}s \tag{3.2}$$

where **n** is the along-beam unit vector and s is the along-beam distance from the light source. If the angle between the laser beam and the wind direction is zero, a scalar convolution product can be used to calculate Eq. 3.2. The function ϕ can be approximated by a Lorentzian function (Sonnenschein and Horrigan, 1971):

$$\phi(s) = \frac{1}{\pi} \frac{Z_r}{Z_r^2 + s^2} \tag{3.3}$$

where $Z_r \simeq 0.00064r^2$, in meters, for the WindScanners used in the present study. The spectral transfer function associated with Eq. 3.3 is therefore expressed as a function of the distance r and the wavenumber k:

$$|H(k,r)|^2 = e^{-2Z_r|k|} \tag{3.4}$$

If the scanning beam is aligned with the mean wind direction, the spectrum of the filtered radial velocity S_{v_r} obtained with the lidar is:

$$S_{v_r} = |H(k,r)|^2 \cdot S^0_{v_r} \tag{3.5}$$

Angelou et al. (2012) compared the theoretical and measured spectral transfer functions. A significant difference was observed, which was mainly attributed to uncorrelated measurement noise, preventing the direct application of Eq. 3.4 to correct the measured spectra. For the inertial sub-range domain, Kristensen et al. (2011), proposed an analytical expression of the spectral transfer function.

If the scanning beam is not aligned with the wind direction, Eq. 3.2 must be solved considering the three dimensional structure of wind turbulence. Then the spectral transfer function depends on three variables: the distance r, the wavenumber k and the angle Ω between the laser beam and the wind direction. To the author knowledge, no satisfying analytical, empirical or semi-empirical expression of the spectral transfer function is available in

the literature for the case where the wind direction is not aligned with the scanning beam.

3.3.2 Applications of Doppler lidars in wind engineering

Commercial wind lidars have been increasingly used since the 2000s, but mainly as wind profilers (Courtney et al., 2008; Smith et al., 2006). The configurations used by wind lidars currently available on the market target mainly the fields of wind energy and atmospheric research. A wind profiler measures the wind directly above the lidar and is therefore not adapted to monitor the flow along a bridge deck as it does not provide a better spatial resolution than an anemometer. The recent development of wind lidars equipped with a rotating scanning head has extended their versatility. A scanning wind lidar can orientate the laser beam in any direction in space or even be used as a wind profiler (Drew et al., 2013; Lane et al., 2013).

Until now, comparisons between anemometers and scanning wind lidars have been mainly limited to flat and homogeneous terrains (Table 3.1).

Table 3.1 Measurement campaigns carried out with Doppler scanning wind lidars and anemometers with focus on turbulence measurement in the atmospheric boundary layer.

Reference	Lidar type	Number of lidars	Range (m)	Terrain	Scan type
Angelou et al. (2012)	cw	1	68	flat	LOS
Sjöholm et al. (2011)	cw	1	80	flat	LOS
Sjöholm et al. (2009)	cw	1	138	flat	LOS
Kumer et al. (2015)	pulsed	1	144	flat	LOS, PPI
Newsom et al. (2015)	pulsed	2	270	flat	PPI, RHI
Schneemann et al. (2014)	pulsed	2	800	flat	LOS
Mann et al. (2009)	pulsed	3	139	flat	LOS
Fuertes et al. (2014)	pulsed	3	85	flat	LOS

Wind profilers or scanning lidars carrying out VAD or DBS mode have been disregarded from this table as they show limited applicability for bridge engineering. This table shows that the distances between the anemometers and the lidars is lower than 300 m in most cases, and in some rare cases up to 800 m. The studies by Lothon et al. (2006, 2009) are not included in Table 3.1 as they studied the wind at altitudes above the atmospheric boundary layer and the data could not be compared to anemometer measurements.

Prior to the pilot investigation at the Lysefjord Bridge, the lidar technology has not found application in bridge engineering (Sathe and Mann, 2013). Still, wind lidars may possess the capabilities to properly estimate wind properties relevant to this field, such as the statistical moments of the wind velocity, the turbulence length scales and the wind coherence.

The application of scanning wind lidars to measure atmospheric turbulence in complex terrains at distances beyond 1 km remains mostly unexplored. This brings numerous uncertainties such as a larger measurement noise and an increased flow complexity. For applications in bridge engineering, new lidar configurations need therefore to be explored.

3.4 Single and multi-lidars deployment

If a single wind lidar is used, only the along-beam velocity component is recorded at each time-step, which gives a limited information of the wind field. To retrieve the three wind components, a triple-lidar system is necessary (Fuertes et al., 2014; Mann et al., 2009; Mikkelsen et al., 2008a,b). If only two of the wind components are of interest, a dual-lidar system can be used instead (Calhoun et al., 2006; Newsom et al., 2008, 2015). Multi-lidar systems are an appealing solution to obtain more detailed wind turbulence measurements.

In this thesis, the investigation of wind turbulence by Doppler wind lidars is carried out in the vicinity of the Lysefjord Bridge during two short-term measurement campaigns. The first one is based on a single long-range

pulsed wind lidar WindCube 100S by Leosphere and the second one relies on two synchronized cw wind lidars in the so-called WindScanner system (http://www.windscanner.dk/) developed at the Department of Wind Energy at the Technical University of Denmark (DTU). The two wind lidars deployed are briefly described in the following as well as the scanning modes used. The analysis of the wind lidar data is presented in Chapter 4.

3.4.1 Short-range lidar configuration

The WindScanner system was used during the third week of May 2014 and directly installed on the bridge deck. The short-range WindScanner system is made of two or three synchronized continuous-wave (cw) wind lidars. A more detailed description of the principles of the cw lidars is given by Karlsson et al. (2000). The WindScanners are based on a modified version of the ZephIR 150 (Natural Power). The modifications of the instrument is described by Sjöholm et al. (2014) and the configuration of the instruments used in this thesis is summarized in table 3.2. The instruments used here possess a rotating head allowing a scan within a cone with a half opening angle of 60°. The laser transmitter of the lidar is eye-safe with a wavelength of 1.565 µm and an along-beam sampling frequency of 390 Hz. The short-range WindScanner system has been recently used during multiple full-scale measurement campaigns (Lange et al., 2015; Simley et al., 2016; Sjöholm et al., 2014), but this is the first time that it is applied on a suspension bridge.

The two WindScanners, denoted R2D3 and R2D1 in Fig. 3.11 aim at the same point 40 m upstream of the deck. The WindScanners are synchronized so that they can continuously scan the same volume along a 123 m line segment parallel to the bridge deck and centred on hanger 18. The measurements are continuously acquired along the line and discretized in post processing into 26 segments, with a mean spatial resolution of 5 m except at the end points where bins are 3.7 m and 4.3 m respectively.

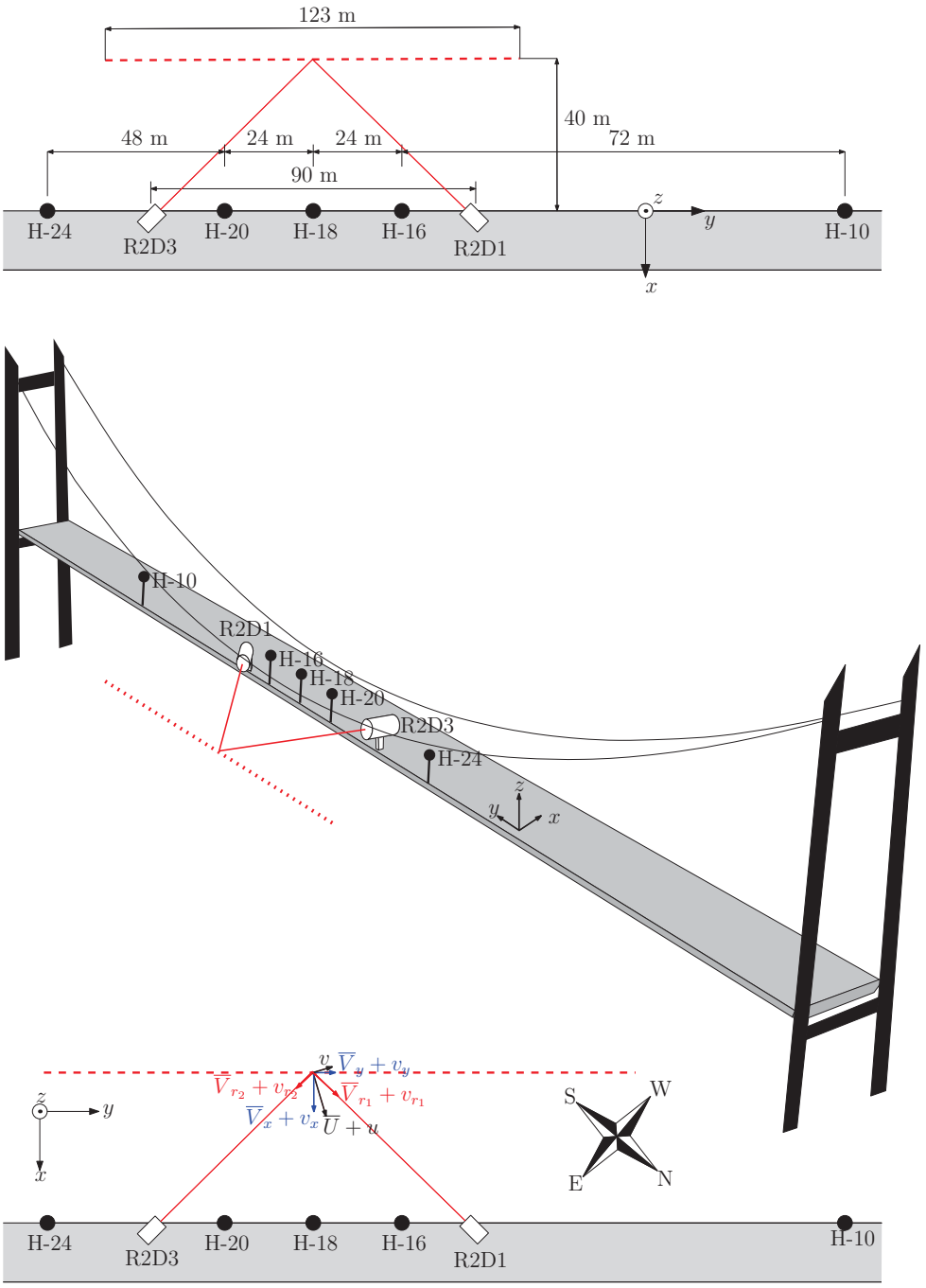

Figure 3.11 Schematic of the horizontal beam-sweeping mode carried out by the dual WindScanner system.

Table 3.2 Configuration of the lidar instruments used in the present study.

Properties	Short-range WindScanner
Wavelength	1.565 µm
Beam-width (at 40 m range)	< 1 mm
Shortest range	10 m
Longest range	< 200 m
Scan line sweep frequency	1 Hz
Scan line sweep length	123 m
Line-of-sight (LOS) sampling frequency	390 Hz
Lidars LOS detection range	$\pm$ 18 m s^{-1}

Only the horizontal beam sweeping (BS) scanning mode of the WindScanner system is presented in this thesis. The BS mode is based on a fixed elevation angle, fluctuating radial distances and fluctuating azimuth angles (Fig. 3.11), such as the trajectory of the scanned volumes looks like a triangle wave with rounded extremities (Fig. 3.12). In the bottom panel of Fig. 3.11, the along-wind and across-wind velocity components are denoted U and V respectively, the along-beam components are refereed to as V_{r_1} and V_{r_2}, and the wind components normal and along the bridge deck are called V_x and V_y respectively.

The sampling frequency of the wind velocity data retrieved with the BS mode is uniformly 1 Hz for each of the two partitions of the data set based on scanning direction. However, if the data is not partitioned based on the scanning direction the sampling frequency appears to be non-uniform (Fig. 3.12). At the centre of the scanned line, the sampling frequency is uniformly 2 Hz while towards the ends it alternates between a short and a long sampling separation. The transformation of the non-uniform sampling frequency into a uniform one is therefore a preliminary step that must be carried out before the analysis of the wind velocity data. The upper limit of the spectral analysis of the wind data is therefore fixed to 0.5 Hz. The choice of a Nyquist frequency of 0.5 Hz is governed by the largest sampling time for the lidar data, which is

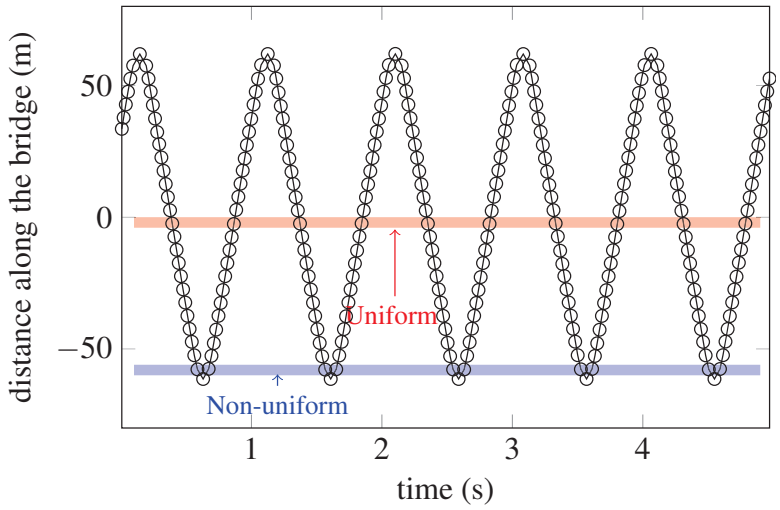

Figure 3.12 Trajectory followed by the intersection of the two scanning beams of the WindScanners. Each circle represents one volume analysed at a given time step.

1 s. In other words, the scanning beam needs 0.5 s to travel along the 123 m line segment.

The BS mode was conducted on 22/05/2014 between 16:20:00 and 16:40:00 for the S-SW flow and on 20/05/2014 between 18:10 and 18:20 for the N-NE wind case situation. The vertical BS mode, based on fixed azimuth angles but varying elevation angles, has been briefly presented in Cheynet et al. (2016c) but is out of the scope of the present thesis.

3.4.2 Long-range lidar configuration

The single pulsed Doppler wind lidar (WindCube 100S) was installed approximately 1.75 km on the West side of the Lysefjord Bridge between April and June 2014 (Fig. 3.13). The WindCube 100S recorded the wind velocity in multiple positions along the laser beam with a resolution of about 10 m that resulted from the splitting of the maximum range of 2500 m into 256

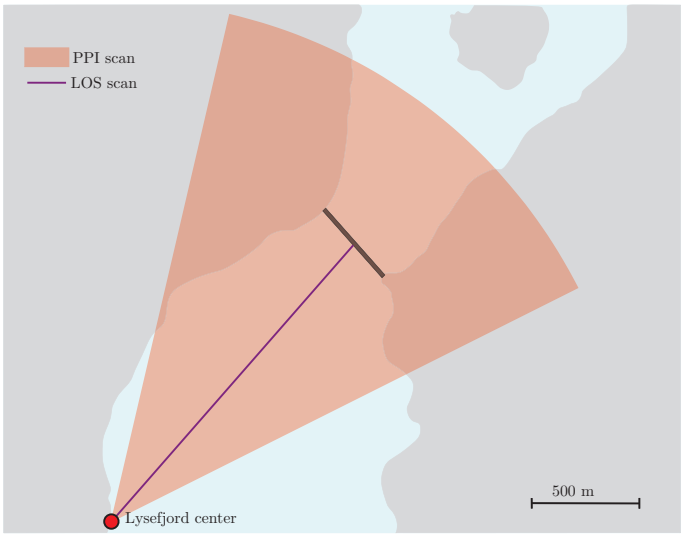

Figure 3.13 Schematic view of the Lysefjord Bridge (black line) mapped by the WindCube 100S with the PPI sector scan and the LOS scan.

equidistant overlapping range gates. Since only one long range lidar was used, the along-beam wind velocity component was the only one measured.

This lidar possesses a rotating head allowing hemispherical scanning capabilities. At relatively low distances from the lidar, a high Carrier-to-Noise Ratio (CNR) is usually obtained. The CNR is here defined as the signal to noise ratio (SNR) on the carrier frequency, and is an indicator of the quality of the data. The CNR decreases with distance and in the case of the Windcube 100S, a threshold must be fixed so that wind data with a CNR below the threshold are dismissed. The minimum threshold is fixed to -27 dB, as by Kumer et al. (2014). A threshold of -23 dB is advised by Pearson et al. (2009). In the present case, the availability of the data is drastically reduced if such a strict threshold is used. Moreover, data with a CNR between -23 dB and -27 dB showed a satisfying agreement with the anemometer records. The key parameters of the scanning pattern for both the S-SW and N-NW flows are summarized in Table 3.3.

Table 3.3 Parameters used for each scanning scenario with the WindCube 100S.

Exposure	SSW			NNE	
Scan mode	PPI 1	PPI 2	LOS	PPI	LOS
Azimuth (°)	13 to 63	13 to 63	25	30 to 46	38
Elevation (°)	3.2	0.8 and 1.8	1.8	1.8	1.8
Sampling freq. (Hz)	0.0128	0.0128	1	0.007	1
Scan speed ($°\,s^{-1}$)	2.5	5	–	1	–
Acc. time (s)	0.4	0.2	1	1	1
Duration (min)	35	35	8	30	10

S-SW exposure

By using the LOS scanning mode of the WindCube 100S, a time series recorded on 22/05/2014 from 16:12:06 to 16:20:00 was selected as representative of the flow from S-SW. This time series was made of a succession of 475 snapshots created along the laser beam. The PPI scan was run later, from 16:50:22 to 17:25:44 and consisted of 28 snapshots. Two different PPI scanning modes were actually used. For an elevation of 3.2°, the accumulation time was twice as long as for elevations angle of 0.8° and 1.8°, and a larger CNR is therefore expected for the elevation of 3.2° than for the other two elevation angles. For this reason, the PPI scan conducted with an elevation of 3.2° is studied more in details in Chapter 4. Since an elevation of 1.8° is calculated so that the scanning beam targets the bridge deck at an altitude of 55 m, a PPI sector scan conducted with an elevation of 3.2° is expected to detect the bridge towers only.

For the S-SW exposure and the PPI scan with an elevation angle of 3.2°, the lateral spatial resolution is 31 m at the position of the bridge deck, which corresponds to an azimuth increment of 1°. The LOS scan is studied by analysing a single time series obtained 1.71 km far away from the lidar, for an elevation angle of 1.8° and an azimuth angle of 38°, so that the laser beam

aims at the middle of the bridge deck. For this scan mode, the sampling frequency is 1 Hz.

N-NE exposure

For a flow coming from the inside of the fjord (N-NE exposure), the CNR is usually lower because of the area of interest is at greater distance from the lidar. To increase the CNR, the accumulation time and the scanning speed must be reduced. On 22/05/2014, the PPI scan for the flow from N-NE was made of 27 snapshots recorded between 09:30:03 and 10:13:16. The accumulation time was increased to 1 s, and the scanning speed was reduced to $0.3\,^{\circ}\,\mathrm{s}^{-1}$. The scanning head swept a much narrower area with azimuth angles ranging from 30° to 46°. The along-deck spatial resolution was therefore higher and equal to about 9 m. The sampling time was however increased to 136 s, which unfortunately did not allow a detailed analysis of the time series recorded. On 22/05/2014, between 12:00 and 12:10, i.e. one hour before the wind direction switched to S-SW, a LOS scan was in addition carried out. The mean wind speed was lower than $5\,\mathrm{m\,s}^{-1}$, which offered the occasion to evaluate the ability of the WindCube 100S to monitor accurately flows characterized by a low wind velocity.

3.4.3 Flow properties investigated

The wind field properties are studied mainly by comparing the anemometer and the lidar data. In this thesis, the anemometers are considered as the reference sensors. The abilities of Doppler wind lidar to map the instantaneous flow, to capture the flow uniformity, the wind spectra, the turbulence length scales and the wind coherence are investigated in Chapter 4.

The number of sonic anemometers available on the bridge deck is large enough to study wind coherence but not to map the instantaneous flow upstream and downstream of the bridge deck with a high spatial resolution.

On the other hand, single or dual wind lidars can be used for this purpose. Mapping the instantaneous flow is in particular useful to visualize the influence of the topography on the flow (Banta et al., 2004). To ensure that the instantaneous map of the lidar is trustworthy, a direct comparison between the time series recorded by the sonic anemometers and the lidars is also done.

The analysis of the flow homogeneity along the bridge deck requires measurement of the mean wind velocity and its standard deviation. Sonic anemometers located along the deck provide the reference data points whereas the wind lidar provides the average mean wind velocity with a higher spatial resolution. The homogeneity analysis is therefore an important step of the wind field description, in particular in mountainous terrain.

The different scanning modes used to study these properties are summarized in Table 3.4. The LOS scanning mode of the WindCube deployed at the bridge site could not be used to evaluate the flow homogeneity nor the wind coherence along the bridge deck as the azimuth angle was fixed. The along-beam wind coherence could have been measured, in a similar fashion as in Lothon et al. (2006) and Kristensen et al. (2010), but this parameter is of little relevance for estimating wind loads on structures. In the present study, the PPI scan carried out by the WindCube 100S was used with a sampling frequency too low to study wind coherence in details.

Table 3.4 Scanning scenario used for each analysis (done: ✓; not done: ×). The short-range WindScanner system allows the use of the Beam Sweeping (BS) scanning mode.

Lidars	WindCube 100S		WindScanners	
Scanning mode	PPI	LOS	BS	LOS
Instantaneous velocity map	×	✓	✓	×
Homogeneity analysis	✓	×	✓	×
Wind spectra	×	✓	✓	×
Coherence	×	×	✓	×

Chapter 4

Wind field characterization

4.1 Introduction

Detailed studies of wind conditions at bridge sites have mainly been carried out in China, Hong Kong and Japan. Equivalent studies for bridge sites in European climate hardly exist. Full-scale wind measurements can be divided into three main categories: short term records, long-term measurements for wind monitoring purposes and assessment of new measurement technologies.

Short term wind monitoring is the most documented category, in particular when it comes to studies of extreme events such as typhoon winds in Asia. For example, Xu et al. (2000b) studied the single-point statistics of wind turbulence at the Tsing Ma Bridge during Typhoon Victor using one of the first modern Wind And Structural Health Monitoring (WASHM) systems. Wang et al. (2013) performed a similar analysis during a 15 month measurement campaign at the Sutong Bridge site, although the authors only presented analysis for a limited selection of the available data. A significant amount of wind data can be obtained from short-term measurement campaigns. Based on 9 days of measurements, Macdonald (2003) gathered about 380 times series of 11 min duration with a mean wind velocity between $14.5\,\mathrm{m\,s^{-1}}$ and $15.5\,\mathrm{m\,s^{-1}}$, which allowed a detailed analysis of the turbulence intensity

and of the single-point wind spectra. Wind coherence obtained from field measurement is less commonly reported, but some examples are available in the literature (Miyata et al., 2002; Toriumi et al., 2000). In Europe, Bietry et al. (1995) studied both single and two-point statistics of wind turbulence on the Saint-Nazaire cable-stayed bridge in France. The short duration of the records (6 h) limited unfortunately the statistical significance of the data. Other short term analyses include e.g. an investigation of wind turbulence in a moderately complex terrain (Mann, 2000) and the study of cross-spectral densities between the wind components u and w on the Sotra Bridge in Norway by Øiseth et al. (2013).

Long term wind monitoring is less common. Hui et al. (2009a,b) provided a particularly well documented study for bridge engineering purpose. During 27 months, they measured the turbulence intensities, wind direction, mean wind velocity, single-point wind spectra, turbulence length scales and the wind coherence near the Stonecutter Bridge in Hong-Kong. Unfortunately, they did not measure the flow directly on the bridge structure, but on wind masts located nearby.

Since the 2000's, the application of remote sensing technology, such as wind lidars, is becoming increasingly popular to study wind turbulence. This technology initially used in atmospheric research (Reitebuch, 2012) is currently broadly used in the field of wind energy for wind profiling (Peña et al., 2009), to investigate the flow variability in complex terrain (Barkwith and Collier, 2011; Lange et al., 2015), to study wind turbulence (Sathe et al., 2011), atmospheric stability (Friedrich et al., 2012), or the flow around wind turbines (Kumer et al., 2015; Simley et al., 2016; Trabucchi et al., 2015).

One of the goals of this chapter is to investigate whether wind lidar technology can be used to complement traditional anemometers for future application in bridge engineering. The construction of large wind-sensitive civil engineering structures such as super-long span suspension bridges requires a detailed description of flow conditions. Sonic anemometers offer

limited abilities when it comes to monitoring the wind field with a high spatial resolution. In addition, remote locations such as wide fjords may be difficult to access using traditional anemometry. In this context, the use of remote sensing technology becomes an attractive option.

The present chapter is organized as follows: a short summary of the wind conditions monitored at the Lysefjord Bridge site during the year 2015 is first done, followed by a presentation of the main results from short-term measurement campaigns conducted by using long-range and short-range wind lidars at the bridge site.

4.2 A general description of the wind environment at the bridge site

The wind conditions at the bridge site are summarized here in a statistical way by using the wind records from the year 2015. The dominant wind directions were N-NE and S-SW, with a majority of wind records below 10 $\mathrm{m\,s^{-1}}$ (Fig. 4.1). The strongest winds from S-SW were recorded with a wind direction of 210° i.e. a yaw angle of 20°. For the N-NE, the largest wind velocities were recorded for a wind direction between 20° and 25°, i.e. a yaw angle ranging from 25° to 30°.

A comparison of the distribution of the first statistical moments for the three wind velocity components shows that the wind conditions for wind from S-SW and from N-NE are sensibly different. During the year 2015, the largest wind velocities were recorded for the flow from S-SW and the value of $\overline{W}$ was much larger for the S-SW exposure than for the N-NE one. More precisely, the mean vertical velocity for the N-NE exposure was most of the time close to 0 $\mathrm{m\,s^{-1}}$ whereas values ranging from 0.5 $\mathrm{m\,s^{-1}}$ to 1.5 $\mathrm{m\,s^{-1}}$ were commonly recorded for the S-SW exposure.

The standard deviation of the vertical wind velocity component is usually larger for the flow from S-SW than for the one from N-NE. However, the

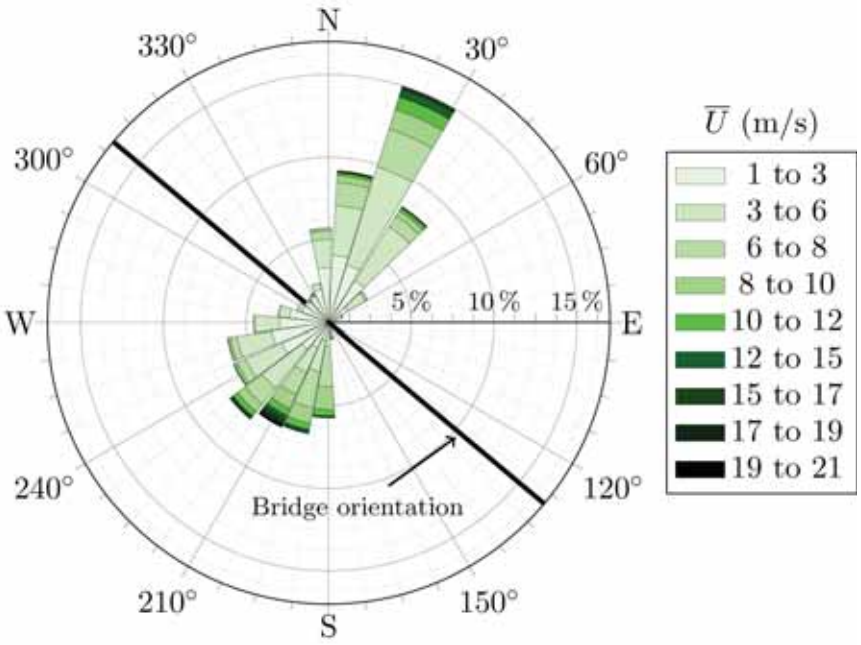

Figure 4.1 Wind rose made of 5.2×10^4 samples of 10 min duration recorded during the year 2015 at the Lysefjord bridge.

distribution of the mean and standard deviation of the wind components are not independent. This is why the turbulence intensity (TI) is usually preferred to quantify the fluctuations of the wind velocity, although the TI is not a "true" statistical moment. In general, a larger TI is recorded for the flow from N-NE, even for large wind velocities (Fig. 4.2). Atmospheric stability may have a strong influence on the turbulence intensity of the flow. For the flow from N-NE, stable atmospheric conditions correspond to turbulence intensity below 15% as opposed to more frequently observed values around e.g. 25 %.

The skewness υ of a Gaussian random process is zero. For the wind data recorded on the Lysefjord bridge, the distribution of the skewness is presented for each velocity component in the third row of Fig. 4.3. On average, a zero-valued skewness is observed for winds from S-SW, except for the vertical component where the skewness υ_w is in average equal to 0.22. For the N-NE

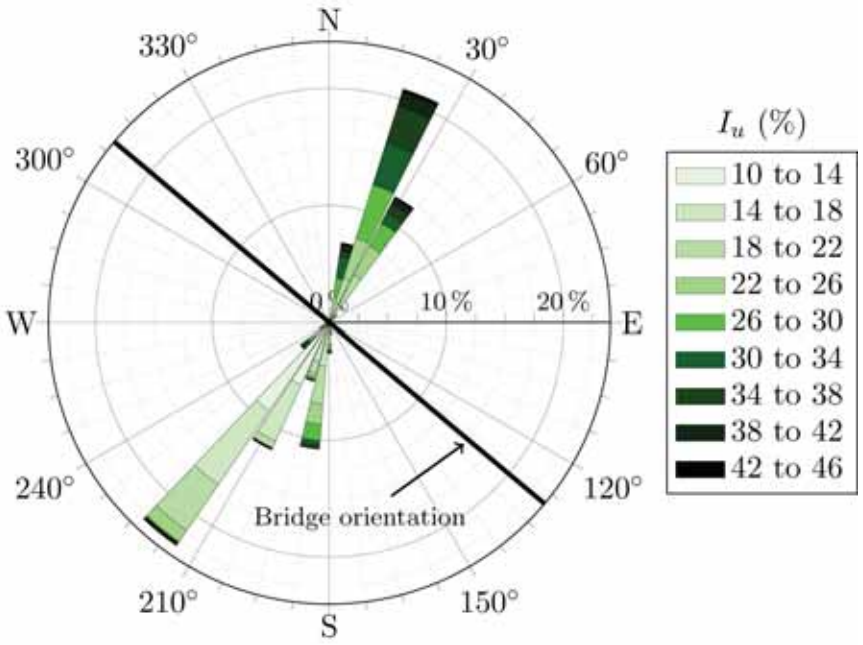

Figure 4.2 Wind rose made of 1907 samples of 10 min duration, recorded during the year 2015 on the Lysefjord bridge near hangers 16,18 and 20, with $I_u < 50$ % and $\overline{U} > 10\,\mathrm{m\,s^{-1}}$.

wind, υ_w and υ_v are close to zero, but υ_u is equal to -0.15. These unusual values are slightly visible on Fig. 4.3.

The excess coefficient of a Gaussian random process is zero. The excess coefficient is equal to $\kappa - 3$, where κ is the kurtosis of a random process. The distribution of the excess coefficient is shown in the last row of Fig. 4.3. For both the wind from S-SW and N-NE, the average excess coefficient is almost zero for the horizontal components. For the vertical velocity component, it is equal in average to 0.45 and 1.2 for S-SW and N-NE exposure respectively.

For both the S-SW and N-NE exposure, the assumption of Gaussian distribution of the wind velocity may be valid for the horizontal components, since the measured skewness and excess coefficients are close to zero in average. For the vertical component, this may not be the case for the flow from

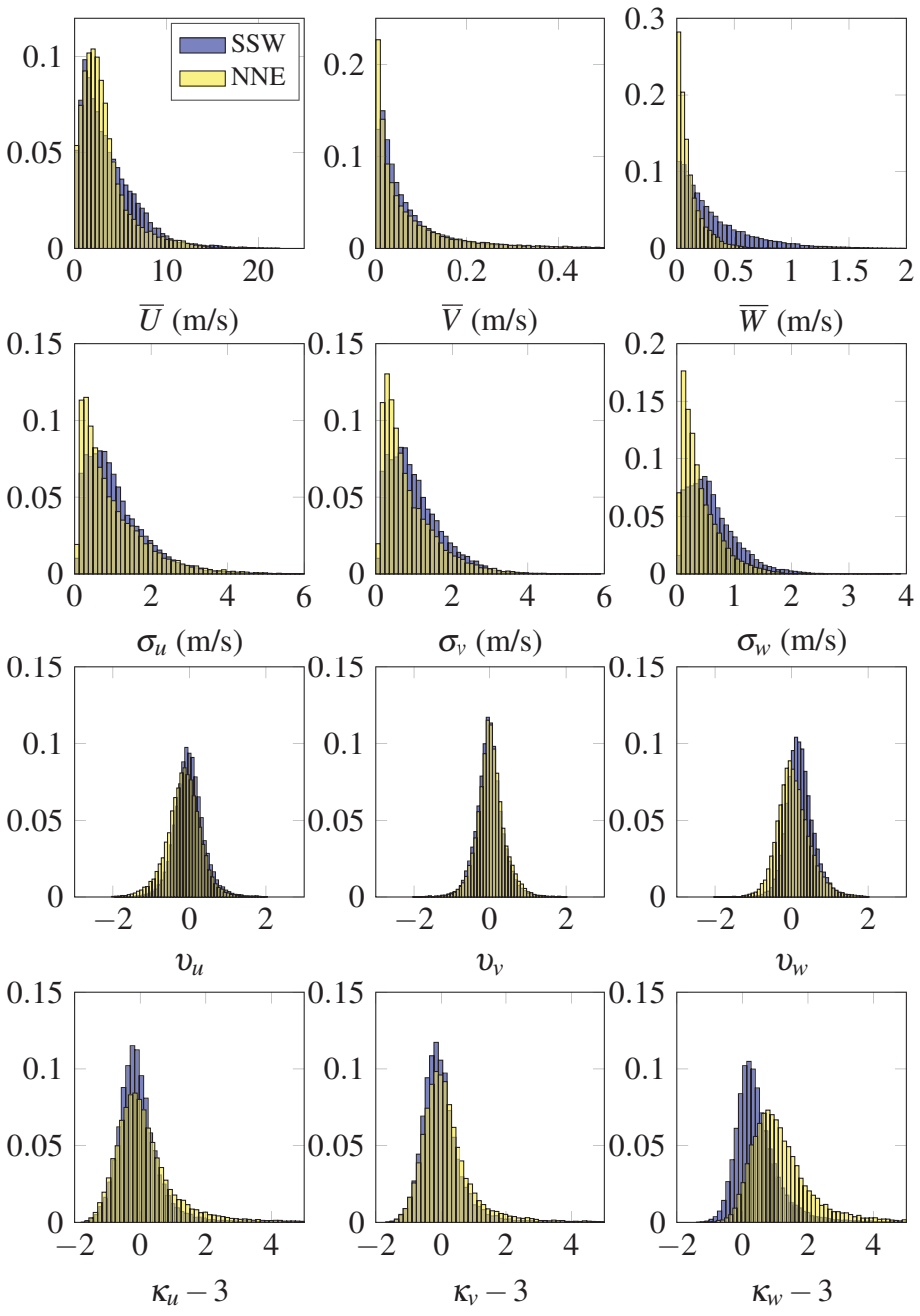

Figure 4.3 Distribution of the first four statistical moments recorded in 2015 at the bridge site.

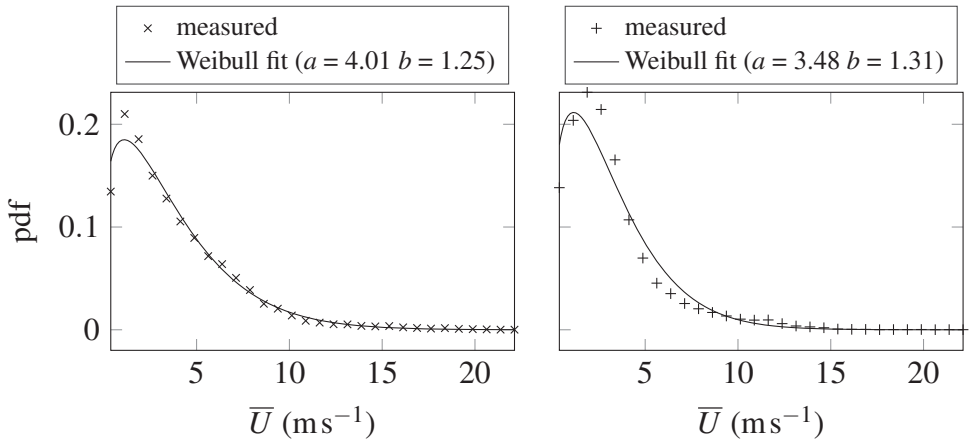

Figure 4.4 Probability density function (pdf) of the mean wind velocity for the S-SW flow (left) and the N-NE one (right) based on wind data recorded in 2015 at the Lysefjord Bridge. The scale parameter of the Weibull distribution is denoted a whereas the shape parameter is b.

N-NE. Non-Gaussian flow may also results from non-stationary fluctuations (Chen et al., 2007; Xu and Chen, 2004) or a modification of the measured flow by the bridge deck.

The distribution of the along-wind mean velocity component follows rather well a Weibull distribution (Fig. 4.4) which is commonly used to represent the distribution of the horizontal mean wind velocity (Davenport, 1963). Although a Weibull distribution indicates that the distribution of wind velocities extrema follows a Type-1 Gumbel density function, the duration of data analysed in this thesis is not large enough to estimate the design wind velocity at the bridge site. The distribution of the integral length scales has been limited to $L_u \leq 350$ m, $L_v \leq 300$ m and $L_w \leq 150$ m (Fig. 4.5). For the wind conditions recorded at the bridge site, measured integral length scales larger than these upper boundary limits usually indicate non-stationary wind conditions. For the horizontal wind components, the distribution of the integral length scales presented in Fig. 4.5 are similar for both exposures. For

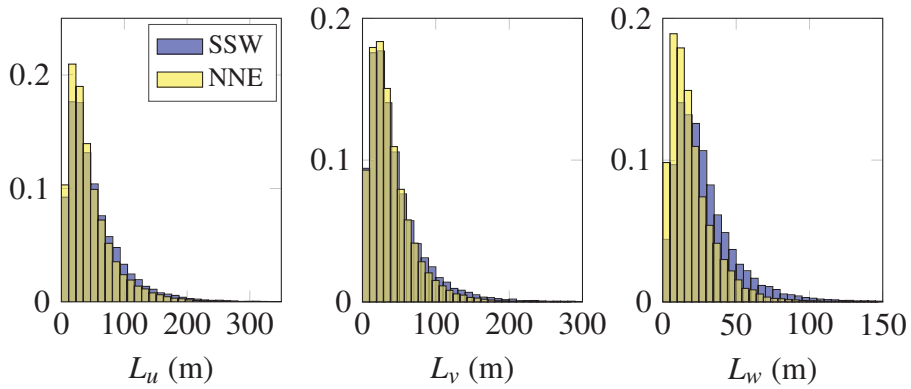

Figure 4.5 Distribution of the integral length scales recorded in 2015 at the Lysefjord Bridge for the different wind velocity components.

the vertical component, larger length scales are usually observed for the flow from S-SW (Fig. 2.3).

In summary, two dominant wind conditions are recorded at the Lysefjord Bridge site and each of them displays different wind properties. This justifies a case-by-case approach, where the wind field is studied by differentiating the N-NE flow from the S-SW flow.

4.3 Wind conditions on 22/05/2014

In this chapter, a detailed wind data analysis is based on records of 10 min to 30 min duration obtained on 22/05/2014. During this day, the sonic anemometers installed on the bridge recorded both a flow from S-SW and from N-NE (Fig. 4.6).

Fig. 4.6 is a particular wind-rose representing three variables: the wind direction, the mean wind velocity and the turbulence intensity for the along-wind component. Each dot represents one sample of 10 min duration. The five sonic anemometers are used in Fig. 4.6 so that more than 500 dots are displayed for a full day of record. This wind rose is adapted to the study

of wind turbulence in mountainous terrains because the influence of the topography on the mean wind velocity and the turbulence intensity can be clearly visualized for a large amount of data.

On 22/05/2014, the wind from N-NE was recorded in the morning, whereas the wind from S-SW was recorded in the afternoon and the evening. The flow from S-SW was characterized by a larger wind velocity than for the flow from N-NE. In addition, the turbulence intensity for the flow from S-SW was larger than usual. More precisely, the along wind turbulence intensity was larger than 20% for a mean wind velocity of 8 $\mathrm{m\,s^{-1}}$. This may be due to topographic effects and/or non-stationary wind fluctuations. When the wind direction becomes close to South, the flow crosses more hills and the change

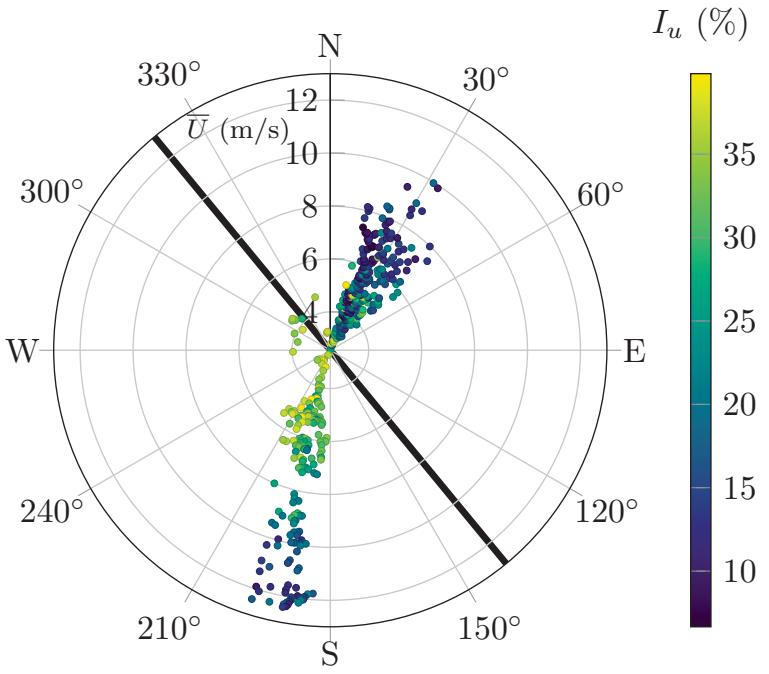

Figure 4.6 Mean wind velocity, turbulence intensity and mean wind direction from 10 min records, obtained by continuous records of all anemometers on the bridge deck on 22.5.2014 (144 samples per anemometer).

in terrain roughness due to the sea-land discontinuity (rough-to-smooth) occurs closer to the bridge deck. As pointed out by Antonia and Luxton (1972), this type of roughness change may increase the turbulence intensity if the flow is recorded close enough to the sea-land discontinuity. As underlined by Chen et al. (2007); Wang et al. (2013), an unusually large turbulence intensity may also reflect a non-stationary flow. This indicates also that under such conditions, the turbulence intensity may not be a valid descriptor for the wind characteristics.

4.4 Instantaneous velocity mapping

The pulsed lidar WindCube 100S was deployed in the LOS scanning mode to map out the instantaneous flow with a sufficiently high temporal and spatial resolution. When the short-range WindScanner system is used, the beam sweeping mode is adopted for this purpose. Flow visualization is done in two steps: First the time series obtained by the lidars and the sonic anemometers are directly compared to quickly evaluate the accuracy of the wind lidars measurements. Then the instantaneous wind velocity fluctuations are visualized in a pseudocolor plot using the Viridis color palette (Garnier, 2015).

4.4.1 S-SW wind case

Two time series are selected for the S-SW exposure. The first one corresponds to the along-beam wind component from the WindCube 100S (LOS scan) on 22/05/2014 between 16:12:06 and 16:20:00. The second one corresponds to the along-wind component recorded during the beam sweeping mode carried out by the WindScanners between 16:20:00 and 16:40:00 on 22/05/2014. The BS scanning mode carried out with the WindScanners and the LOS scan of the WindCube were unfortunately not overlapping which explains why two different time series are used in this section.

WindCube 100S

Fig. 4.7 shows that the wind velocity measured 40 m upstream of the deck by the WindCube 100S agrees well with the one measured by the anemometer on H-18. The difference, in mean and standard deviation of wind velocity, between the LOS scan and the anemometer on H-18, is 2.1% and 3.6% respectively. The synchronization procedure based on the introduction of a time lag by using the hypothesis of Taylor's frozen turbulence is validated by the good agreement between the anemometer and lidar data on Fig. 4.7.

The good agreement between the selected time series in Fig. 4.7 suggests that the 2D visualization of the flow by the lidar is reliable in the present case. On Fig. 4.8, the beam of the WindCube 100S is targeting H-18, i.e. the central part of the deck, by using an elevation angle $\Psi = 1.8°$, and an azimuth angle $\Phi = 39°$. The bridge position is clearly visible, as a thick dark line. Under neutral atmospheric stability the mean wind velocity is expected to follow a logarithmic or power law. In other words, the mean line-of-sight velocity should monotonously increase as the measured volumes are located further from the lidar. On the bottom panel of Fig. 4.8, the sudden increase of the along-beam wind velocity for radial distances between 1 km and 1.8 km

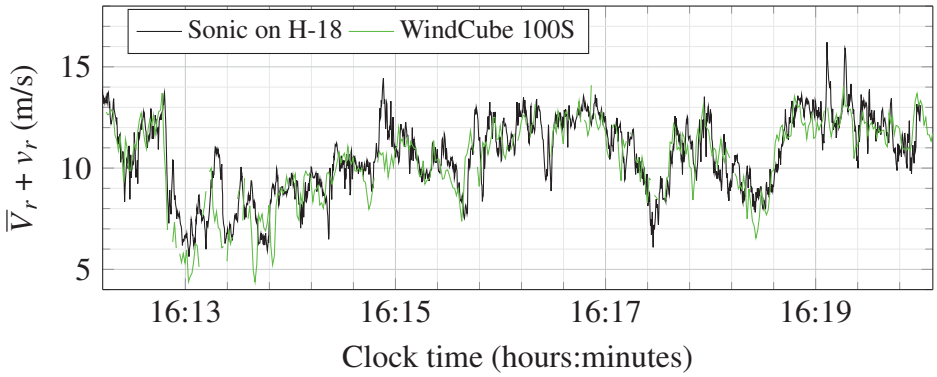

Figure 4.7 Along-beam wind component recorded on 22/05/2014 by the WindCube 100S (LOS scan) and the anemometer on H-18.

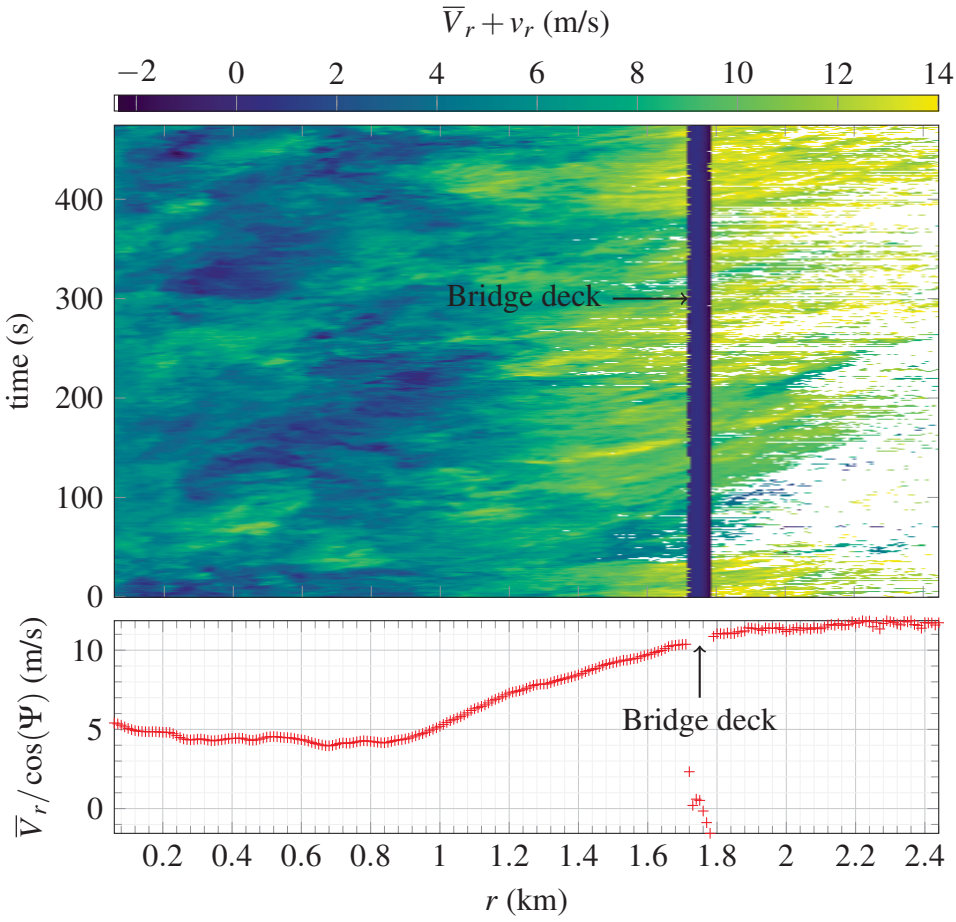

Figure 4.8 Top: LOS scan from the WindCube 100S on 22/05/2014 from 16:12:06, for $\Psi = 1.8°$ and $\Phi = 39°$. Bottom: corresponding along-beam mean wind velocity.

can not be explained by the existence of vertical wind shear alone. This increase may be due to the channelling effect of the fjord near the bridge site. A low CNR is commonly observed for distance larger than 2 km, which unfortunately limits the interpretation of the LOS wind velocity downstream of the bridge.

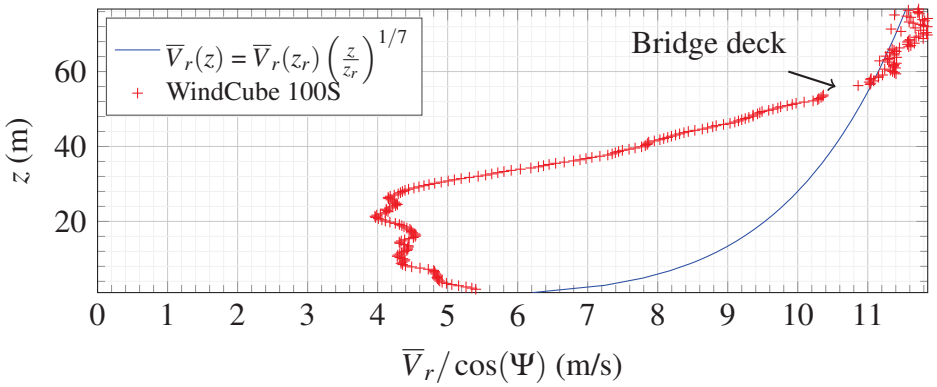

Figure 4.9 Vertical line-of-sight mean wind velocity profile for the LOS scan carried out with the WindCube 100S on 22/05/2014 from 16:12:06 to 16:20:00, for $\Psi = 1.8°$ and $\Phi = 39°$.

In Fig. 4.9, the wind velocity profile based on the power law with the coefficient of $1/7$, representative of a flat terrain, is displayed with reference to the value at the 64 m height where the sonic anemometers are installed. The mean wind profile interpreted from the measured data departs from such a general profile and indicates that the flow is strongly influenced by the fjord expansion, contraction and possible local changes in the mean wind direction. Beside its significance for the wind action of the bridge deck, proper knowledge of the local wind profile at the bridge location is also relevant to wind action on towers under construction and in possible bridge designs with towers on floating foundations.

WindScanners

On Fig. 4.10, the horizontal wind velocity components and the wind direction recorded by the anemometer on H-18 and the WindScanners show good agreement. The discrepancies are only 1.9% and 3.1% for the mean value and its standard deviation respectively. For these time series, the synchronization of the signals was done by using their cross-correlation. The WindScanner

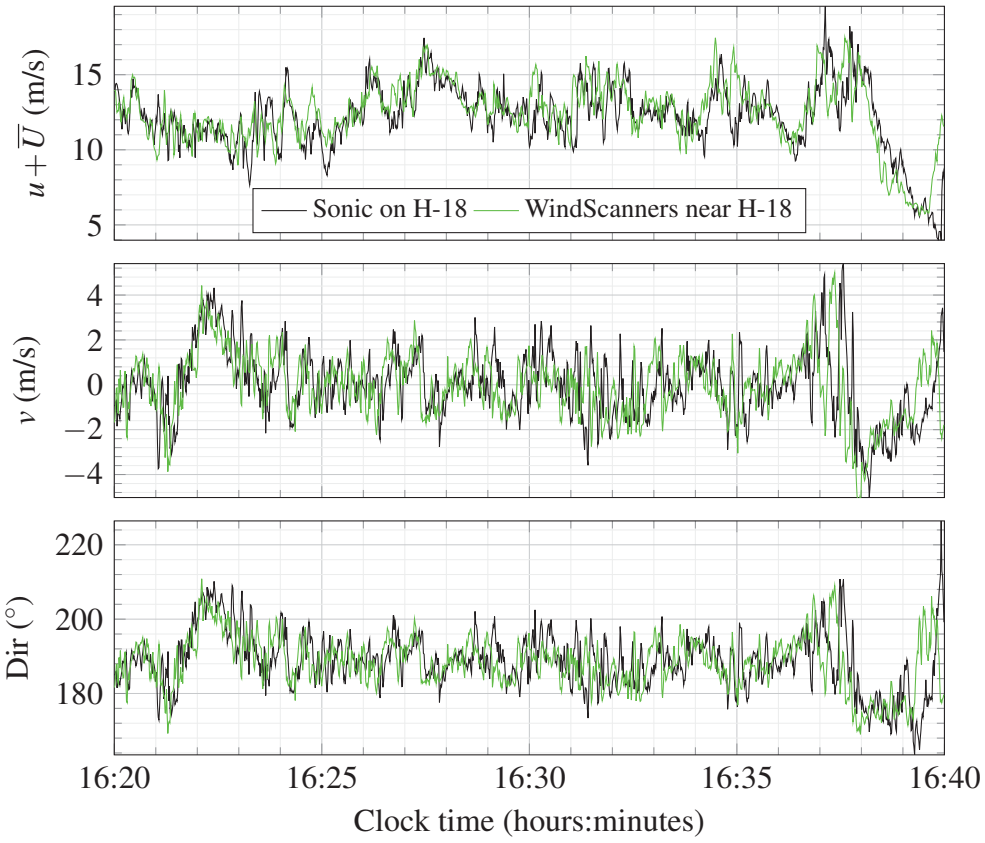

Figure 4.10 Horizontal wind components and wind direction measured by the WindScanners and the sonic anemometer on H-18 on 22/05/2014.

wind data displayed in Fig. 4.11 illustrate the wind velocity variability in time and space. The wind direction is seen to be skewed with respect to the normal to the bridge deck, as commonly observed with the anemometers. The flow was quite homogeneous along the line segment monitored, i.e. near the central part of the span. The low duration of the data sample in Fig. 4.11 facilitates the identification of a few of the correlated wind gusts in both space and time, which would not be possible by displaying the full set of 10 min duration.

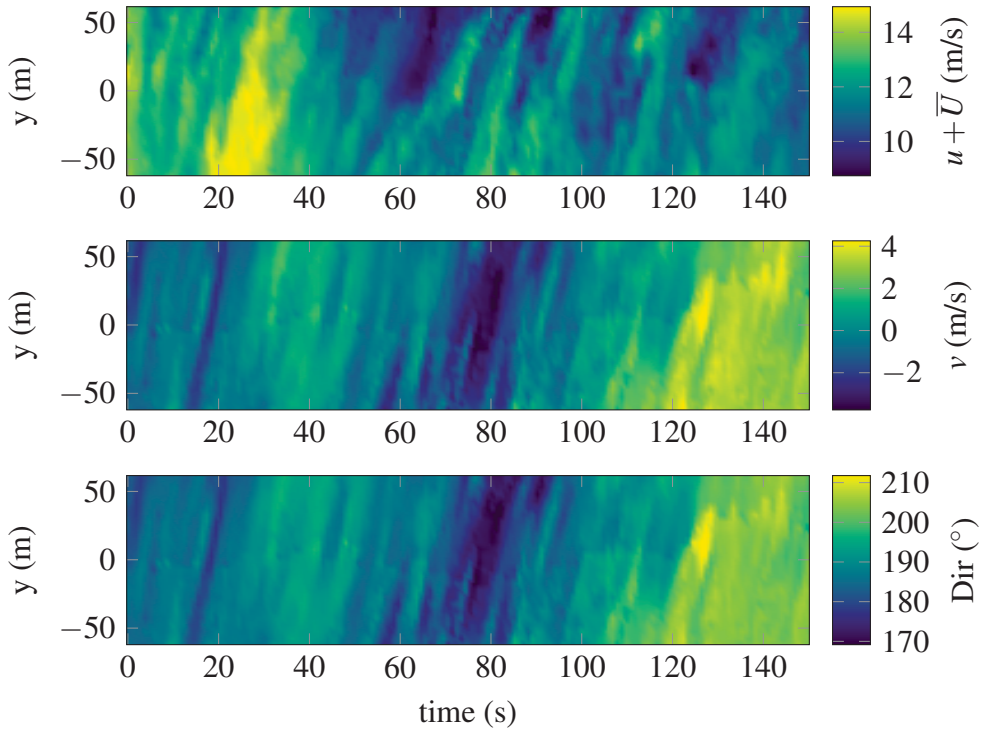

Figure 4.11 Horizontal wind components and wind direction recorded by the WindScanners on 22/05/2014 from 16:20:00 with the beam sweeping mode (S-SW flow).

4.4.2 N-NE wind case

For the N-NE flow, two time series are also selected. The first one corresponds to wind records from the WindCube 100S (LOS scan) on 22/05/2014 between 11:10 and 11:20, with an azimuth of 38° and an elevation of 1.8°. The second one comes from wind data recorded by the WindScanners (BS scan) between 18:10 and 18:20 on 20/05/2014. The WindScanner did not record any exploitable wind data on 22/05/2014 for the N-NE exposure. Consequently, a data set recorded on 20/05/2014 is used instead.

Data from the WindCube 100S

The comparison between the anemometer data on H-18 and the pulsed lidar data recorded 40 m downstream of the bridge deck is presented in Fig. 4.12. For this particular scan, the angle between the wind component V_x and the along-beam wind component U was only 12.5°. These two wind components were therefore assumed aligned. The anemometer and the lidar data agrees fairly well although the WindCube 100S does not detect any notable disturbance of the flow by the deck in the volume analysed. The mean wind velocity measured by the Lidar and the sonic on H-18 differs by only 0.78% for a value $\overline{U} = 3.4\ \mathrm{m\,s^{-1}}$. A low wind velocity is often associated with a low CNR (Mann et al., 2009), but in the present case, a good agreement was still obtained. A good agreement was also observed between the sonic and the lidar data for the standard deviation of the wind component V_x with a difference of 4.8%. The corresponding turbulence intensity for the along-beam wind component is 32%, which is rather high but realistic given the low value of the mean wind speed recorded. The sudden variation of the radial velocity near 11:17 increasing from almost 0 $\mathrm{m\,s^{-1}}$ to 6 $\mathrm{m\,s^{-1}}$ is due to an abrupt variation of the wind direction, which accounts for non-stationary wind fluctuations.

The measured along-beam wind velocity is negative if the aerosols that backscatter the emitted light move toward the lidar. The wind data displayed in Fig. 4.13 corresponds to the beginning of a transition from a N-NE flow to a S-SW one, completed within 90 min. The wind direction changes first at locations close to the lidar, which explains why the line-of-sight velocity is positive at radial distances below 300 m. Both negative and positive velocities are recorded which is expected as the mean wind velocity is particularly low. The vertical mean wind velocity profile for the along-beam wind component has therefore little significance and is not displayed in the present case for the N-NE flow.

On Fig. 4.13, the bridge deck signature is visible as a slight discontinuity in the recorded velocity near $r = 1.75$ km. Because the deck altitude is

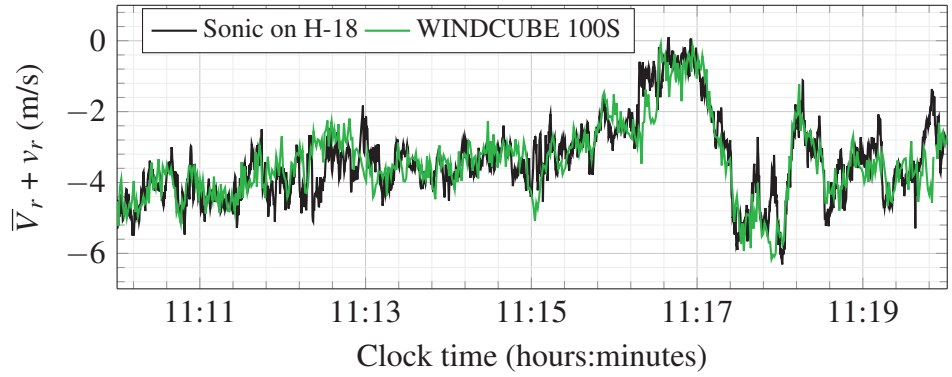

Figure 4.12 Along-beam wind velocity measured by the lidar and the sonic on H-18, on 22/05/2014. For an azimuth of 38° and an elevation of 1.8°, the beam orientation is assumed normal to the deck axis.

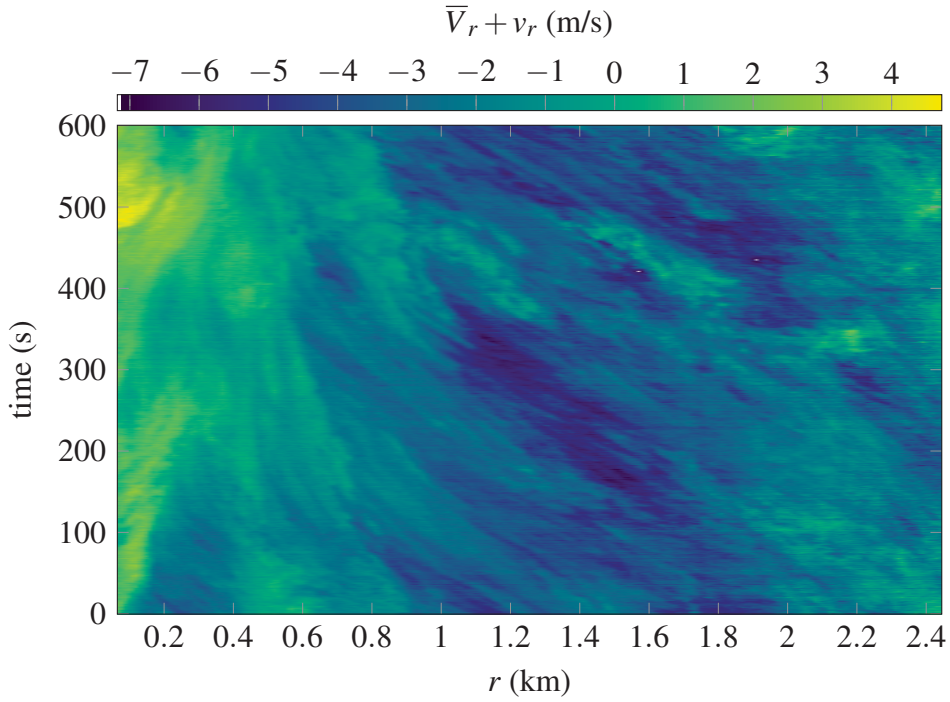

Figure 4.13 LOS scan of the WindCube 100S carried out on 22/05/2014 from 11:10:00 to 11:20:00 for a N-NE wind situation case, with an azimuth of 38° and an elevation of 1.8°.

increasing toward north, the lidar beam was probably located below the bridge deck for an azimuth of 38°, whereas the deck was clearly detected at an azimuth of 39°.

Data from the WindScanners

The particular time series selected with the WindScanners for the N-NE flow downstream of the bridge is characterized by a velocity deficit compared to the same wind record obtained with the sonic anemometer on H-18 (Fig. 4.14).

In average, this velocity deficit is about 0.4 $\mathrm{m\,s^{-1}}$ for the wind component normal to the bridge deck and about 0.2 $\mathrm{m\,s^{-1}}$ for the along-deck wind

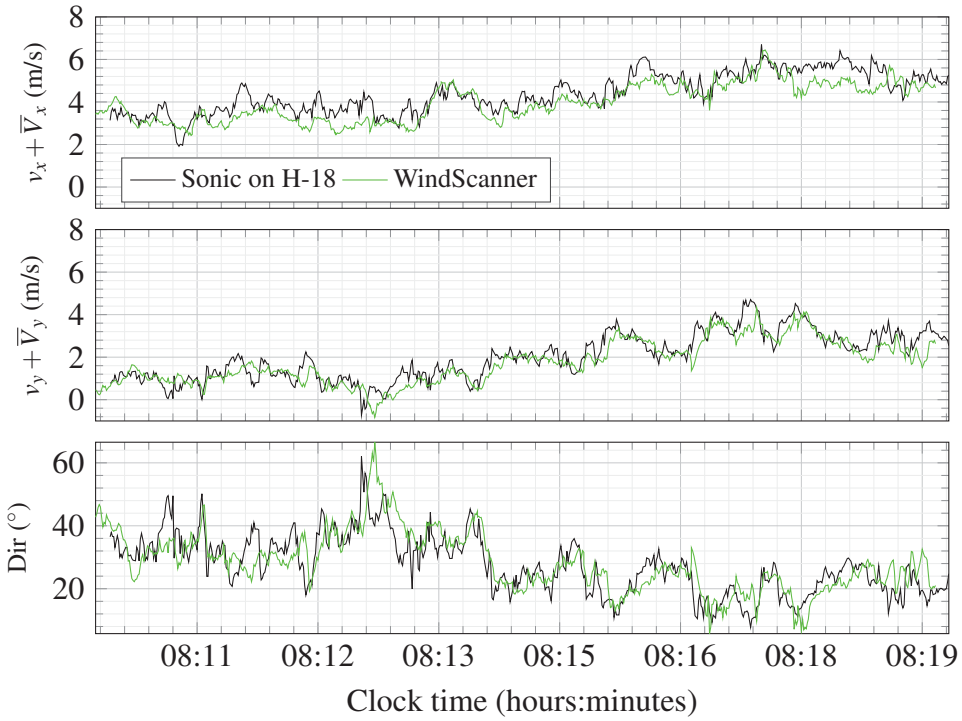

Figure 4.14 Wind components V_x and V_y recorded on 22/05/2014 by the WindScanners and the anemometer on H-18 (N-NE exposure).

component. The wind direction in the wake is also affected, but to a limited extent only (bottom panel of Fig. 4.14).

On 22/05/2014 from 08:10 to 08:20, the turbulence intensity I_u recorded by the anemometer on H-18 was ca. 0.25 which is almost twice the value of the turbulence intensity observed in Cheynet et al. (2016c) where the wake of the bridge was clearly visible. Taylor's hypothesis of frozen turbulence may no longer be valid when the velocity recorded by the WindScanners 40 m away from the deck is below 3 $\mathrm{m\,s^{-1}}$. In that case, the comparison between the anemometers and the WindsScanners data has to be done with caution. For the S-SW exposure on 22/05/2014 and a mean velocity lower than 3

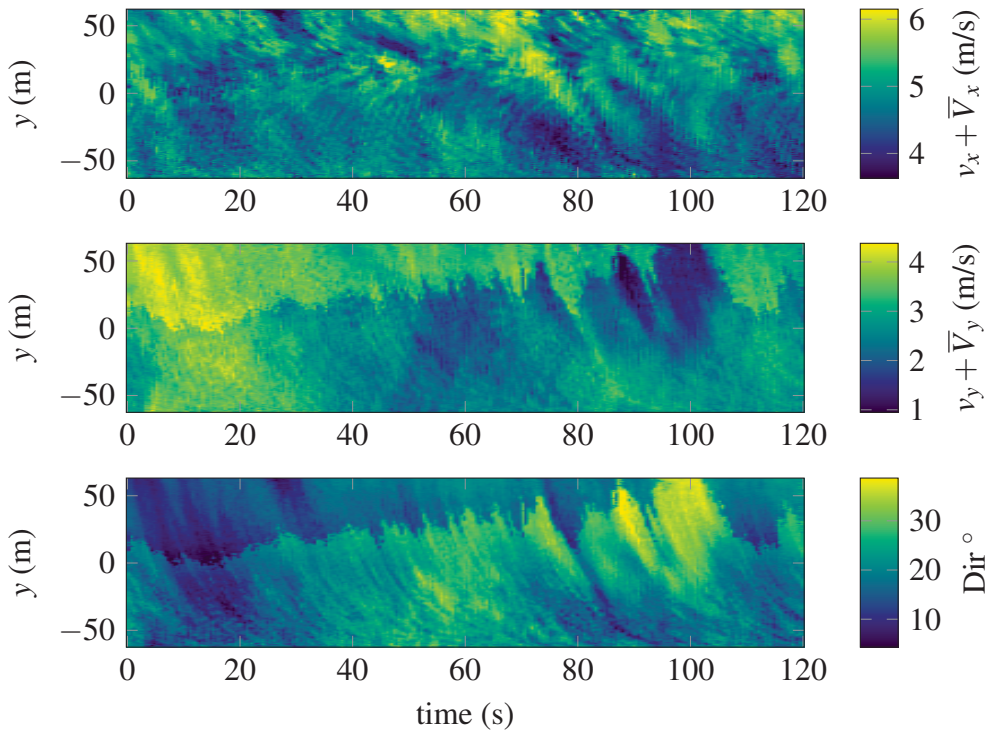

Figure 4.15 Wind components normal and parallel to the deck recorded by the WindScanners on 22/05/2014 from 08:18 with the beam sweeping mode (N-NE exposure).

$m\,s^{-1}$, it was for example common to observe a large discrepancies between the anemometer and WindScanner data.

When the instantaneous flow is mapped by the WindScanner along a 123-m long line segment parallel to the bridge deck, the gusts monitored in the direction perpendicular to the deck are significantly different from the undisturbed flow case (top panel of Fig. 4.15). The contrasted pictures in the middle and bottom panels of Fig. 4.15 may testify for the existence of a higher measurement noise in one of the two WindScanner records, which limits the interpretation of the data displayed in these two panels.

4.5 Homogeneity analysis

The monitored flow is assumed homogeneous if the mean value and standard deviation of wind velocity show limited variations along the bridge deck. Flow homogeneity is investigated first at a relative large scale, i.e. on an area of about 2.5 km^2 using the PPI scan of the WindCube 100S. The wind direction is assumed stable enough during the selected wind records to derive representative averages of the along-beam wind velocity. By using the pulsed lidar data, the flow uniformity is studied in terms of mean value and standard deviation of the wind velocity. The WindCube 100S allows a direct investigation of the influence of the topography on the flow, in particular the channelling effect of the fjord.

The uniformity assumption is studied more accurately along the bridge deck by studying the data from the different sonic anemometers and the short-range WindScanner system. By using the beam sweeping mode, the flow is investigated at a smaller scale, i.e. along the 123 m line segment parallel to the bridge span. The higher spatial and temporal resolution provided by the WindScanner system allow a direct comparison of wind statistics with those measured by the anemometers. Only the first two statistical moments are studied here. Higher moments such as skewness and kurtosis require longer

wind records to keep the random error under an acceptable level (Lenschow et al., 2012).

4.5.1 S-SW wind case

Data from the WindCube 100S

The mean value and standard deviation of the along-beam wind velocity measured with the PPI scan of the WindCube 100S are displayed for multiple azimuth angles and radial distances up to 2.4 km from the lidar in Fig. 4.16. A close-up of the nearest 300 m around the bridge is shown in Fig. 4.17. The azimuth of 0° corresponds to the North direction whereas the azimuth of 90° refers to wind from the East.

If the PPI scanning mode is used, the along-beam wind velocity depends on the azimuth angle. For small elevation angles and under the assumption of flow uniformity, the horizontal mean wind velocity component can be retrieved by dividing the along-beam velocity by $\cos(\overline{\Theta} - \Phi)$, where $\overline{\Theta}$ is the mean wind direction and Φ is the azimuth angle. In the present analysis, this operation is only relevant near the bridge deck, where the mean wind direction is known and relatively uniform. For wider azimuths angles and a larger distance to the bridge, the uncertainties related to the mean wind direction increase. The correction was therefore applied only for the case of the close-up of the bridge deck, on Fig. 4.17, where the mean wind direction is assumed uniform and equal to 190°.

On Fig. 4.16, the towers are clearly visible as dark spots corresponding to the velocity of ca. 0 $\mathrm{m\,s^{-1}}$. The South tower is visible for an azimuth angle of 46° and a distance of 1.7 km from the lidar. The North tower is visible for an azimuth angle of 32° and $r = 1.8$ km . The mountainous terrain surrounding the bridge limits the range of the observable data, as highlighted by the dark borders of the scanned region. The along-beam mean wind velocity increases as the flow approaches the bridge. Downstream of the bridge, the along-beam

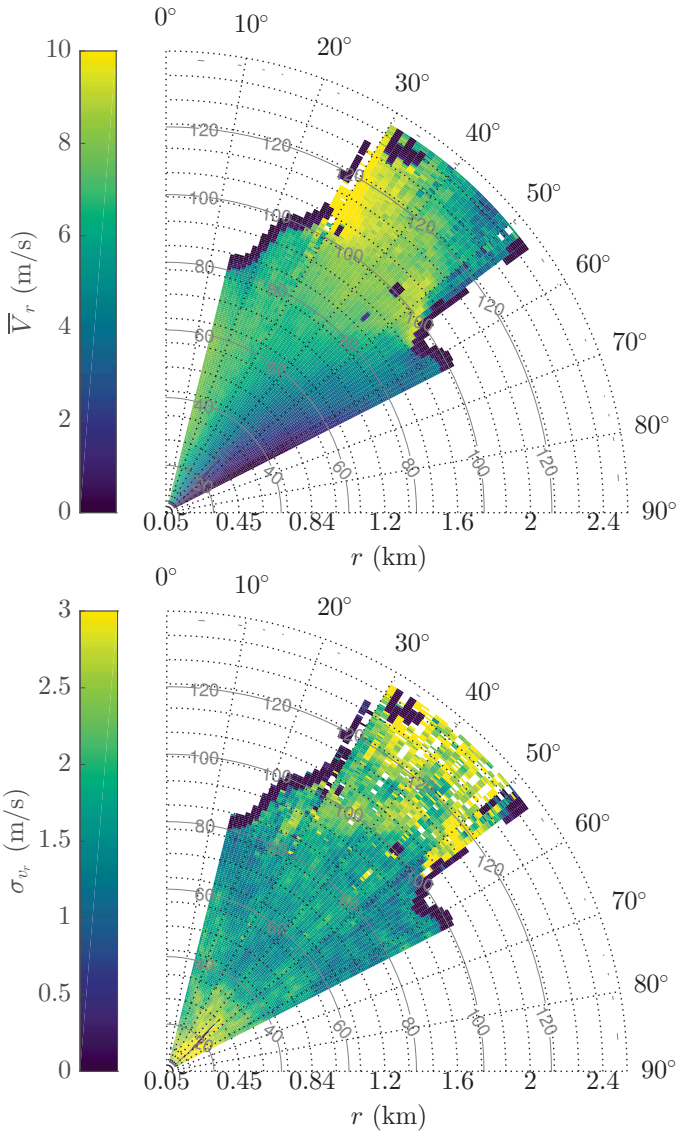

Figure 4.16 Mean (left) and standard deviation (right) of the along-beam wind velocity derived from PPI scans recorded on 22/05/2014 between 16:50:22 and 17:25:44 with an elevation of 3.2°. The wind was blowing from S-SW with $\overline{V}_x = 8.0\ \mathrm{m\,s^{-1}}$ at the bridge site. The radial grey contour indicates the altitude (in meters) above the sea level.

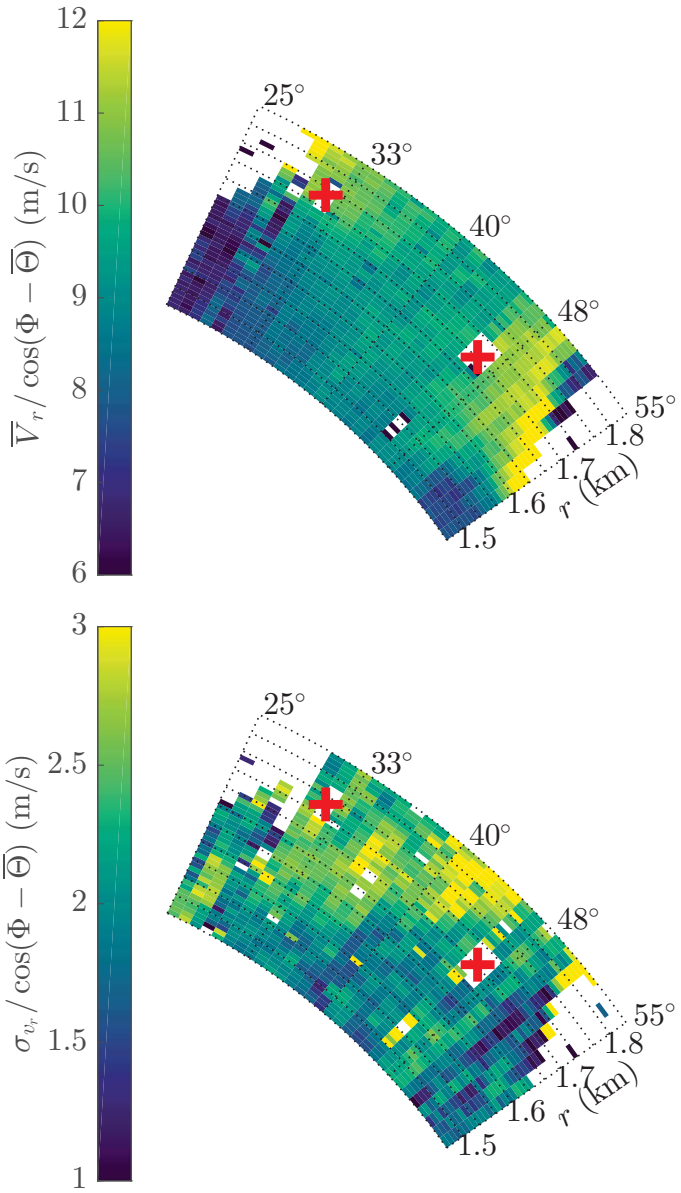

Figure 4.17 Close-up of the PPI scan with the mean (left) and standard deviation (right) of the corrected along-beam wind velocity on 22/05/2014 between 16:50:22 and 17:25:44, for an elevation angle of 3.2°. The towers are shown as thick crosses.

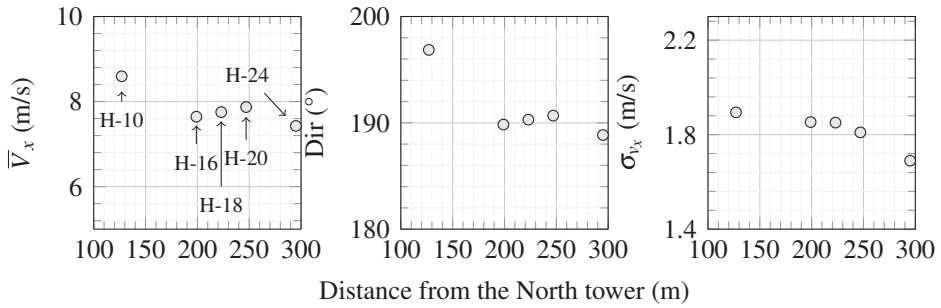

Figure 4.18 Mean wind velocity (left), mean wind direction (center) and RMS of the wind velocity (right) along the bridge, based on anemometer records between 16:50:22 and 17:25:44 on 22/05/2014.

mean wind velocity $\overline{V}_r$ is up to 30% higher near the North Tower than near the South tower. For an elevation angle of 3.2°, the scanning beam points approximatively at the tip of the tower, the height of which is 102 m. Anyway, the spatial resolution of the scan does not allow any clear visualization of the wake created by the towers. Near the South tower, a strong gradient of the along-beam wind velocity is apparent, likely indicating the flow separation around the southern hill. Additional lidar records may be required to confirm these observations.

Figs. 4.16-4.17 show that the flow is clearly affected by the topography. This motivates a further analysis of flow uniformity along the bridge span. This analysis is done by using data from the sonic anemometers (Fig. 4.18). The mean value and standard deviation of the wind velocity component $\overline{V}_x$ and the wind direction measured by the anemometers are actually almost uniform near the bridge centre, but increase toward the North Tower.

Data from the WindScanners

By using the short-range WindScanner system and the sonic anemometers on the bridge deck, single-point statistics of wind turbulence recorded on 22/05/2014 between 16:20 and 16:40 are studied. The first and the last

five minutes of this data set were not stationary according to the reverse arrangement test (Bendat and Piersol, 2011). As expected and observed by e.g. Chen et al. (2007) and Wang et al. (2016), this led to overestimation of the turbulence intensity and the integral length scales (Table 4.1).

Fig.4.19 investigates the along-deck uniformity of the measured wind statistics. The integral length scales are denoted L_u and L_v. The horizontal mean wind velocity is $\overline{U}$ and the standard deviations of the u and v components are σ_u and σ_v respectively. The abscissa has values ranging from 24 m to 168 m, corresponding to the distance between the anemometers installed between H-10 and H-24.

In Fig. 4.19, the values of L_u and L_v are particularly high for both the anemometers and the WindScanners, but the dual-lidar system seems to systematically measure larger integral length scales than those obtained with the anemometers. The beam averaging effect is likely to be at least partially

Table 4.1 Single-point statistics of wind turbulence measured by the WindScanners (WS) and the sonic anemometers (SA) at Lysefjord Bridge shown in Fig. 4.19. The duration of 20 min corresponds to wind data recorded from 16:20 to 16:40. The duration of 10 min refers to the record period ranging from 16:25 to 16:35. The relative difference is defined by using the anemometers as reference.

	Measurements				Relative difference (%)	
Duration (min)	10		20		10	20
Sensors	WS	SA	WS	SA		
L_u (m)	180	140	385	328	29	17
L_v (m)	73	60	168	152	23	10
$\overline{U}$ ($\mathrm{m\,s^{-1}}$)	13.2	12.7	12.3	12.0	3.8	2.6
σ_u ($\mathrm{m\,s^{-1}}$)	1.38	1.46	2.13	2.16	-5	-1.1
σ_v ($\mathrm{m\,s^{-1}}$)	0.99	1.16	1.43	1.56	-14	-8.3
I_u (%)	10.5	11.6	17.4	18.0	-9.1	-3.6
I_v (%)	7.6	9.2	11.6	13.0	-18	-11

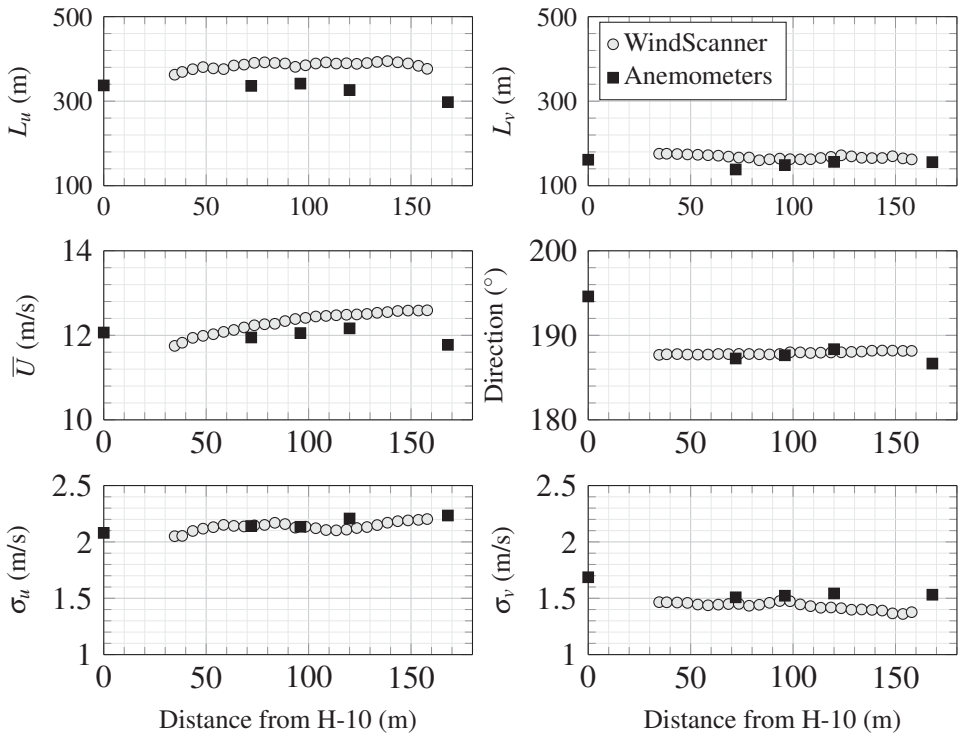

Figure 4.19 Single-point statistics of atmospheric turbulence measured by the WindScanners and the anemometers along the bridge deck on 22/05/2014 between 16:20 and 16:40.

responsible for this overestimation. The smoothing of the high frequency content of the data may lead to an auto-correlation function that decays more slowly with the time lag. Stawiarski et al. (2015) observed the same phenomenon by using large-eddy simulation data and also partially attributed this overestimation to the along-beam spatial averaging .

For the mean wind velocity $\overline{U}$, the WindScanners show a good overall agreement with the anemometers near the bridge centre (hangers 16 to 20), but a larger difference is observed with the sonic on H-24. Contrary to the anemometers, the WindScanners record a slightly increasing mean wind velocity toward the South side of the bridge. The discrepancy between the

data from the anemometers and the WindScanners is however on average lower than 3% for the mean wind velocity, which is to be expected. The uniformity of the flow is confirmed by the mean wind direction measured by the WindScanners. Larger fluctuations from the anemometers are however observed, and may be due to a slight misalignment of the sensors, or the effect of topography on the wind direction in the vicinity of the towers.

4.5.2 N-NE wind case

For the N-NE wind direction, the long-range lidar installed offers the possibility to simultaneously study the flow upstream and downstream of the bridge deck. On the other hand, the short-range lidar system offers the opportunity to investigate which properties of the flow are most affected by the bridge. Even if the wind measured by the WindScanners is perturbed by the bridge girder, the uniformity of the flow is much more affected by the complex topography.

Data from the WindCube 100s

For a wind direction from N-NE, the uniformity of the flow is investigated on Figs. 4.20-4.21 with the WindCube 100S. The flow from N-NE was more heterogeneous near the bridge than in the case of a S-SW wind. A larger along-beam velocity is captured on the North side of the bridge, which may be due to the narrowing of the fjord a couple of hundred meters upstream of the bridge, leading to a speed up of the wind velocity. The lower wind velocity toward the South side of the bridge may also be due to the wake generated by the island located 1 km to the East of the deck (Fig. 4.20). The along-beam velocity on Fig. 4.21 is corrected in a similar fashion as in Fig. 4.17 where the mean wind direction $\overline{\Theta}$ is assumed uniform and equal to 30°. As highlighted by Fig. 4.22, larger wind fluctuations are recorded near the North side of the deck and may illustrate the non-uniformity of the flow along the span.

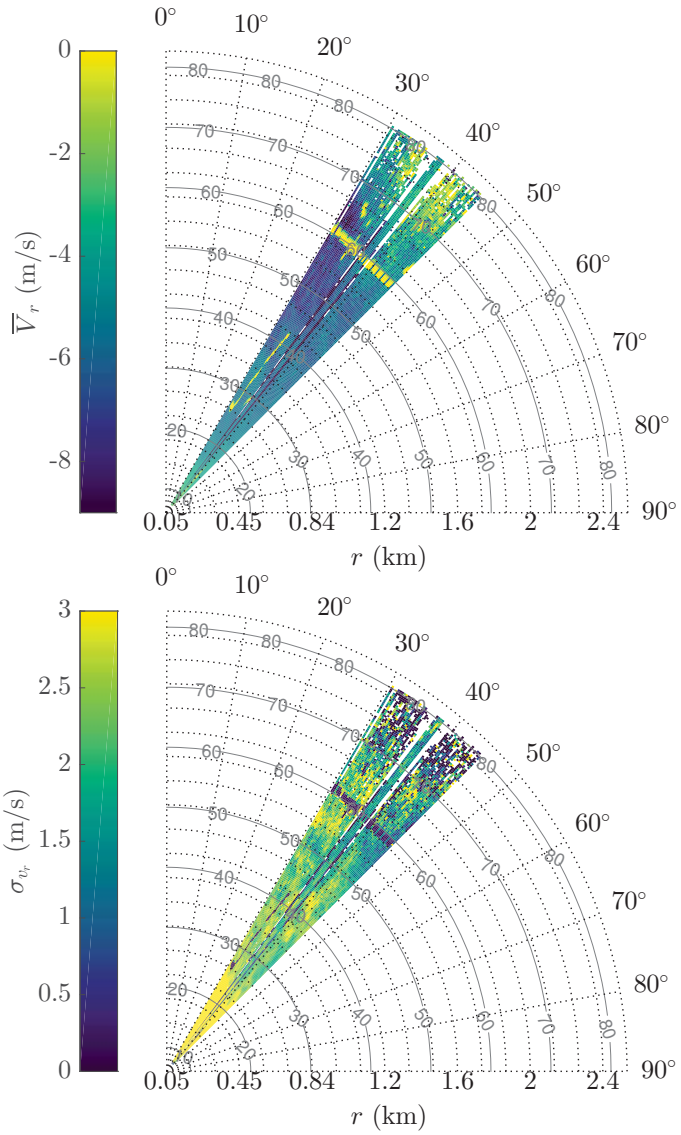

Figure 4.20 Mean (left) and standard deviation (right) of the along-beam wind velocity derived from the PPI scan recorded on 22/05/2014 between 08:30:03 and 9:13:16, with an elevation of 1.8°. The wind was blowing from N-NE with $\overline{V}_x = 6.0\ \mathrm{m\,s^{-1}}$ at the bridge centre. The radial grey contours indicate the altitude (in meters) above the sea level.

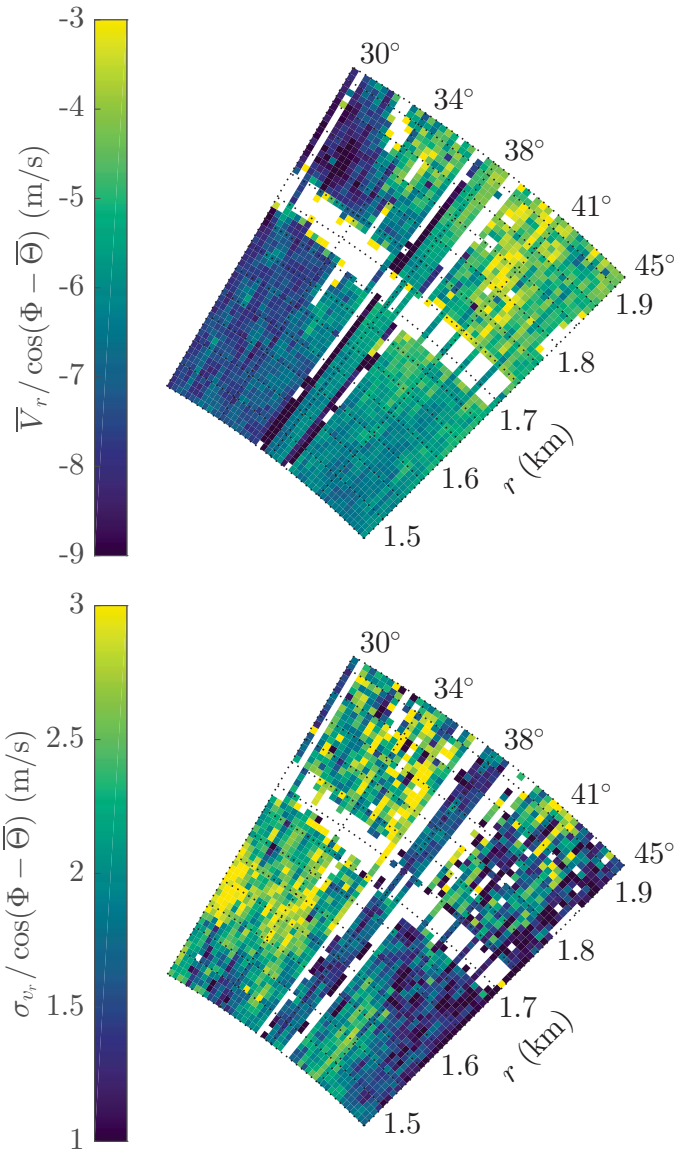

Figure 4.21 Close-up of the PPI scan with an elevation angle of 1.8° for the mean (left) and standard deviation (right) of the corrected along-beam wind velocity on 22/05/2014 between 08:30:03 and 9:13:16. The deck is visible as a white strip for r = 1.7 km.

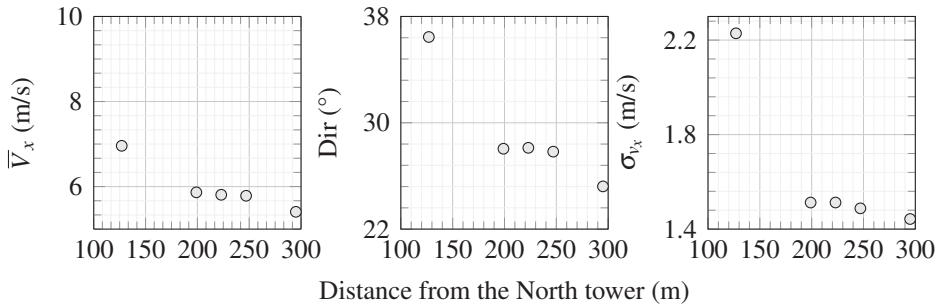

Figure 4.22 Mean wind velocity (left), mean wind direction (center) and RMS of the wind velocity (right) along the bridge, based on anemometer records between 09:30:00 and 10:10:00 on 22/05/2014.

The relatively good spatial resolution of the PPI scan shows its potential to study the effect of topography on the uniformity of the flow along a bridge deck. This can be particularly useful for longer spans and wider fjords, but such conditions require a lidar with a longer range than the one used in the present study.

Data from the WindScanners

On Figs. 4.23, the flow measured by the WindScanners downstream of the bridge appears quite homogeneous along the central part of the deck. The mean wind velocity measured by the lidar in the downstream flow is slightly lower than the one measured by the sonic anemometers, on average by 10 %, which agrees fairly well with the velocity deficit recorded in Cheynet et al. (2016c) for similar wind conditions. The integral length scales for the across and along-bridge axis components are almost identical with a value of about 40 m, i.e. an integral time scale of 8 s, except on H-10. Surprisingly, the WindScanner system does not show a similar overestimation of the integral length scales as for the S-SW wind case. The fact that the WindScanner system is monitoring the bridge wake may partly explain this difference. The values of σ_{v_x} and σ_{v_y} are almost identical, about 1 $\mathrm{m\,s^{-1}}$ and 1.1 $\mathrm{m\,s^{-1}}$

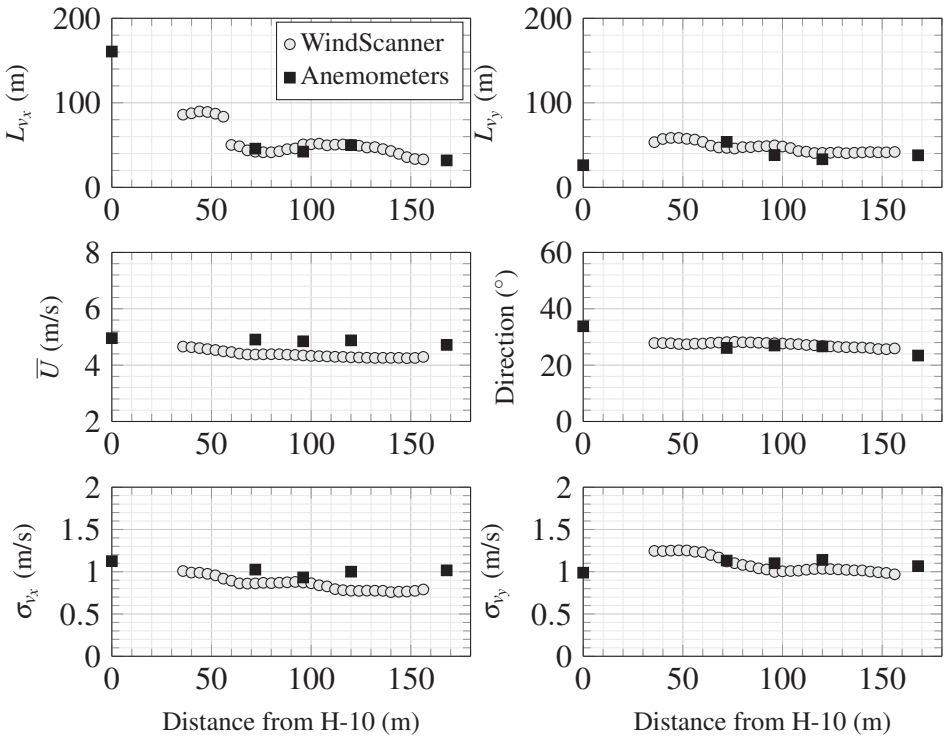

Figure 4.23 Single-point statistics of atmospheric turbulence measured by the WindScanners and the anemometers along the bridge deck on 22/05/2014 between 08:10 and 08:20.

respectively. The large yaw angle of about 30° and the disturbance of the flow by the bridge deck may explain why σ_{v_y} is larger than σ_{v_x}.

4.6 Single-point wind spectra

The single-point spectra are studied for the case of a S-SW wind, where the flow is assumed undisturbed by the bridge deck, and for the N-NE wind, where the wake of the bridge may be recorded.

Data from the WindCube 100S

The single-point wind spectrum of the along-beam wind velocity measured by the WindCube 100S using the LOS scanning mode is compared to the one measured by the sonic anemometers in Fig. 4.24. The spatial averaging effect is not easily visible which may be due to an increase of measurement noise for larger distance from the lidar and the low CNR threshold used in the present study. For the N-NE exposure, the spectra of the along-beam wind velocity measured by the WindCube 100S shows a satisfactory agreement with the spectra from the anemometers. however, the influence of the wake on the spectra is not clearly visible for the range of wavenumbers covered by the long-range lidar.

Data from the WindScanners

The spectra of the along-wind and across-wind components measured by the WindScanners and the sonic anemometers are directly compared in Fig. 4.25 and Fig. 4.26 for the S-SW and N-NE exposure respectively. Results from

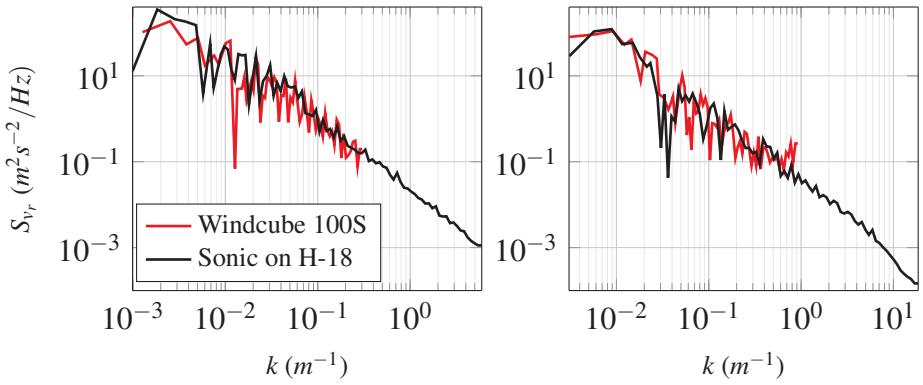

Figure 4.24 Power spectral densities of the along-beam wind velocity based on wind data recorded with the LOS scan for the S-SW exposure (left, from 15:12 to 15:20) and the N-NE exposure (right, from 11:10 to 11:20) on 22/05/2014.

the S-SW wind case are consistent with the study of Angelou et al. (2012), who compared the along-wind spectra between the WindScanner system and one sonic anemometer located 67.5 m away. They observed a clear spatial averaging effect for wavenumbers above $0.1\,\mathrm{m}^{-1}$.

For the flow from N-NE, the spatial averaging effect is not clearly noticeable for wavenumbers below $0.3\,\mathrm{m}^{-1}$. The wind spectra measured by the WindScanners are affected by the bridge wake and a larger measurement noise is expected, given the relatively low wind velocity recorded ($\overline{U} \leq 5\,\mathrm{m\,s}^{-1}$).

The bottom-panels of Figs. 4.25-4.26 show a comparison between the two wind components for the anemometers (bottom-left) and the WindScanners (bottom-right). According to the Kolmogorov hypothesis for the inertial subrange, a ratio of spectral values S_v/S_u close to 4/3 is expected. Wyngaard (1973) and Kaimal et al. (1972) observed such a ratio as well as its dependency on the atmospheric stability for flat and homogeneous terrain, conditions which the Lysefjord site does not generally fulfil.

For the time series selected, a value for the ratio S_v/S_u close to 4/3 can be observed by using the sonic anemometers data only. This ratio is visible on the bottom-left panel of Fig. 4.25 (S-SW exposure) for wavenumbers above $0.1\ \mathrm{m}^{-1}$ and in Fig. 4.26 (N-NE exposure) for wavenumbers above $1\,\mathrm{m}^{-1}$. In the present case, the wind spectra recorded by the WindScanners did not allow the observation of such a ratio because the sampling frequency was not large enough. Even if a larger sampling frequency is used, the spatial averaging effect may become predominant in the inertial subrange, preventing any observation of the ratio S_v/S_u close to 4/3.

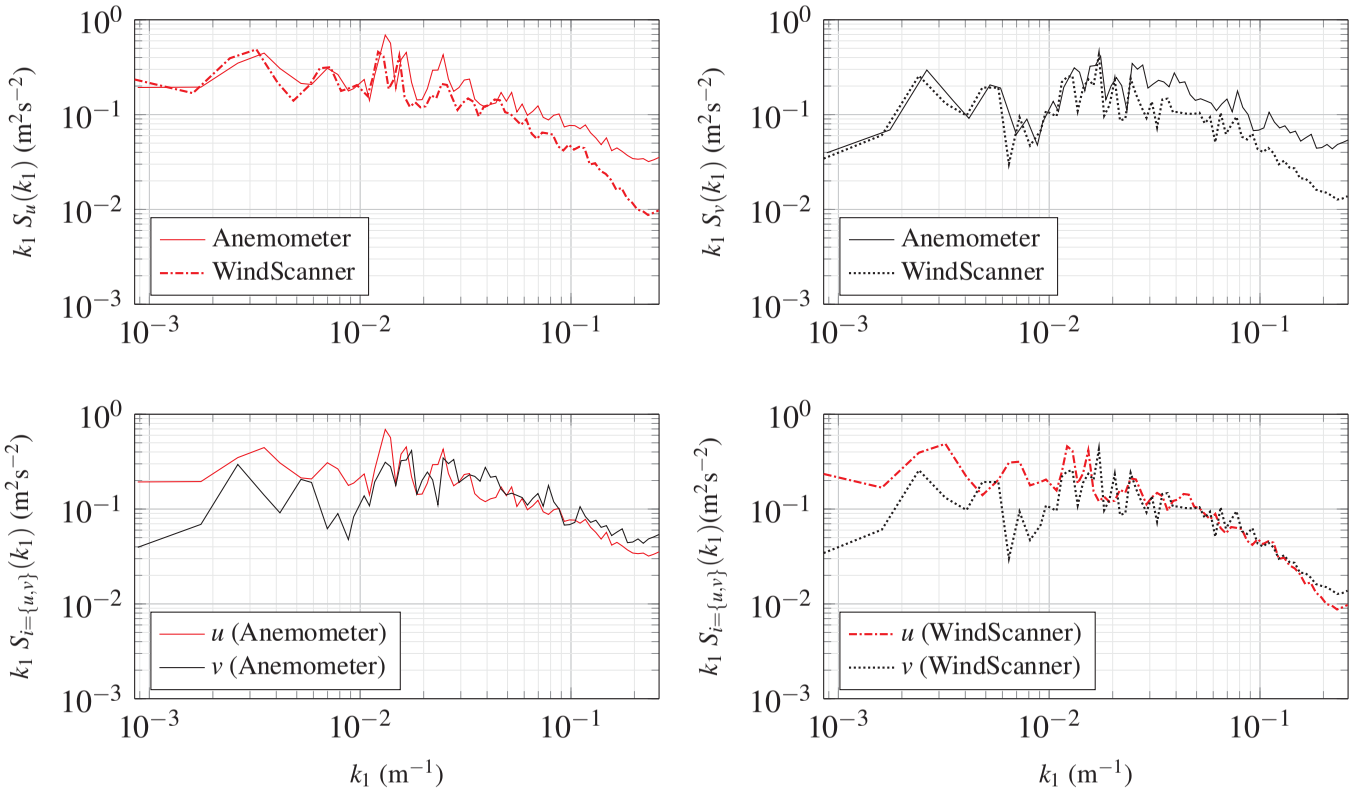

Figure 4.25 Power spectral density of the along (top-left) and across-wind components (top-right) measured by the WindScanners and the anemometers, and direct comparison between S_u and S_v for the anemometers (bottom left) and the WindScanners (bottom-right) is done using data recorded on 22/05/2014 between 16:20 and 16:40 (S-SW flow), $\overline{U} = 12\ \mathrm{m\,s^{-1}}$.

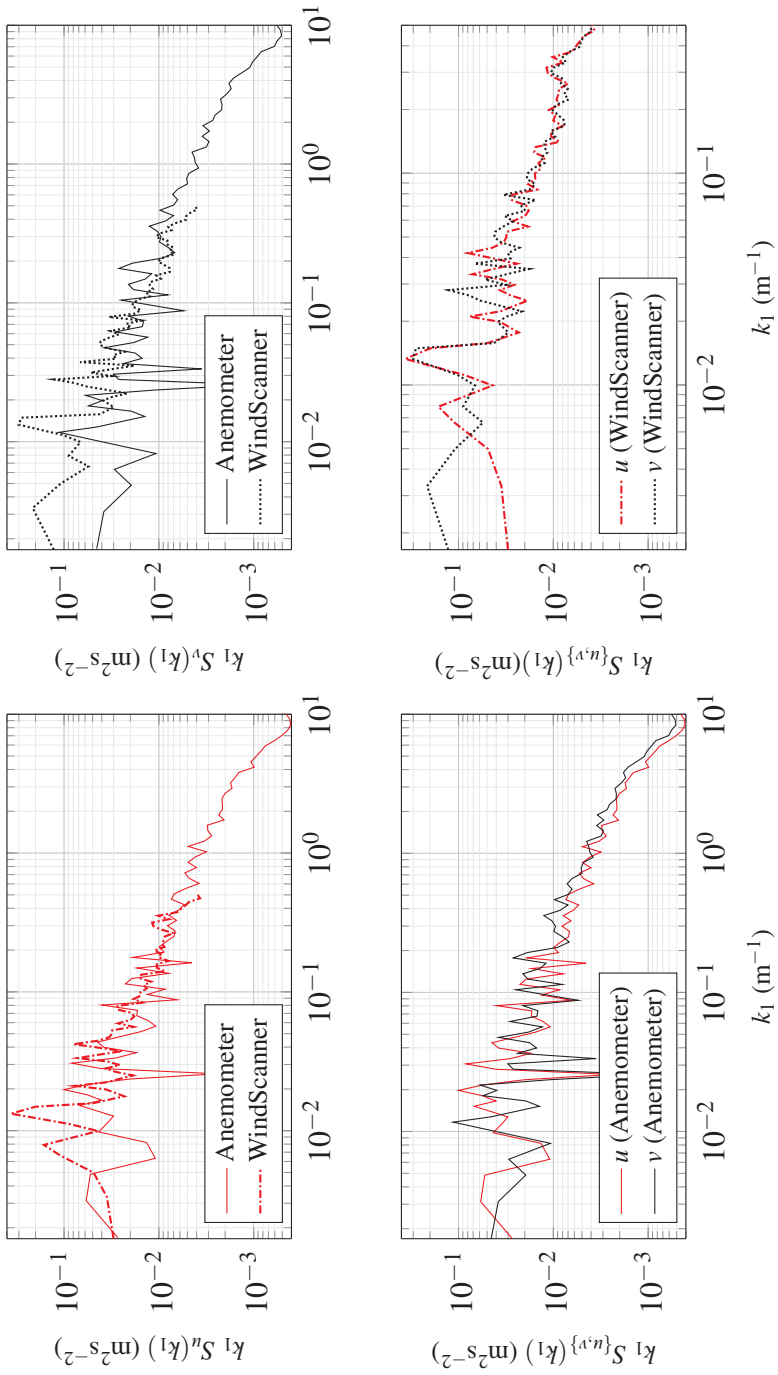

Figure 4.26 Power spectral density of the wind components normal and along the bridge deck measured by the WindScanners and the anemometers, based on data recorded on 22/05/2014 between 08:10 and 08:20 (N-NE flow), $\overline{U} = 4.9$ ms^{-1}.

4.7 Wind coherence

Wind coherence is among the key parameters used to estimate wind loads on large civil engineering structures. In this section, only wind data recorded by the WindScanner system between 16:20 and 16:40 (S-SW exposure) is used.

4.7.1 Co-coherence

The measured coherence is fitted using the four-parameter exponential decay function presented in Chapter 2. The fitted coefficients are presented in Table 4.2 for both the WindScanners and the anemometers. The coherence is calculated by using samples of 10 min duration and Welch's overlapped segment averaging estimator (Welch, 1967). To reduce the measurement noise and the bias of the coherence estimate, segments of 60 s are used with 50% overlapping as suggested by Carter et al. (1973) and Saranyasoontorn et al. (2004).

The measured co-coherence for the wind component V_x is displayed in Fig. 4.27 for three along-span separations d_y ranging from 24 m to 96 m. The fitted analytical coherence model approximates well the measured co-coherence. The negative part of the co-coherence is properly captured, which justifies the use of the four-parameter exponential decay function. A larger discrepancy is measured between the fitted and measured co-coherence for wavenumbers between $0.1\,\mathrm{m}^{-1}$ and $0.15\,\mathrm{m}^{-1}$ for the v_y-component and $d_y = 72$ m. This may come from the fitting procedure which considers data up to 0.1 Hz, i.e. wavenumbers below $0.05\,\mathrm{m}^{-1}$ only, as a larger measurement noise is often measured for higher frequencies, especially for large spatial separations.

Despite the limited length of data used, the good agreement between the WindScanner records and the anemometer data suggests that the WindScanners can properly capture the co-coherence of the horizontal wind components, the mean velocity and the turbulence intensities. Larger data set should however be analysed to evaluate the statistical significance of such a conclusion.

Table 4.2 Coefficients obtained with the four-parameter function fitted to wind data on 22/05/2014 between 16:25 and 16:35.

	c_1	c_2	c_3	c_4
Co_{v_x} (WindScanner)	1.9	0.02	1.3	4.4
Co_{v_x} (Anemometers)	1.4	0.02	1.4	4.0
Co_{v_y} (WindScanner)	1.6	0.02	1.4	2.3
Co_{v_y} (Anemometers)	1.8	0.02	1.3	2.9

4.7.2 Root-coherence

The root-coherence for the horizontal wind components is displayed for lateral separations ranging from ca. 18 m to 73 m in Fig. 4.28.

It is expressed as a function of the non-dimensional wavenumber obtained by multiplying the wavenumber k with the cross-wind separation D. The results based on the measured root-coherence from the WindScanners and the anemometers (scatter plot) are compared to theoretical root-coherence calculated with the von Kármán model and the ESDU model.

The anemometers data and the WindScanners data agree fairly well for the different lateral separations presented and for $kD \leq 2$. For the along-wind component, the von Kármán model gives larger values than the theoretical models for $kD > 2$. For the across-wind component, the measured root-coherence decreases faster than predicted for $kD > 1$. These discrepancies may be due to the existence of a significant yaw angle in the wind data.

4.7.3 Spatial averaging effect and coherence

Table 4.2 shows that the volume averaging effect seems to affect to a limited degree the coherence measured by the WindScanner. This may be explained by the normalization of the cross-spectra that reduces the influence of spatial averaging. In the general case, realization of an explicit relation between the coherence and the spatial transfer functions $\boldsymbol{H}$ is cumbersome, because the

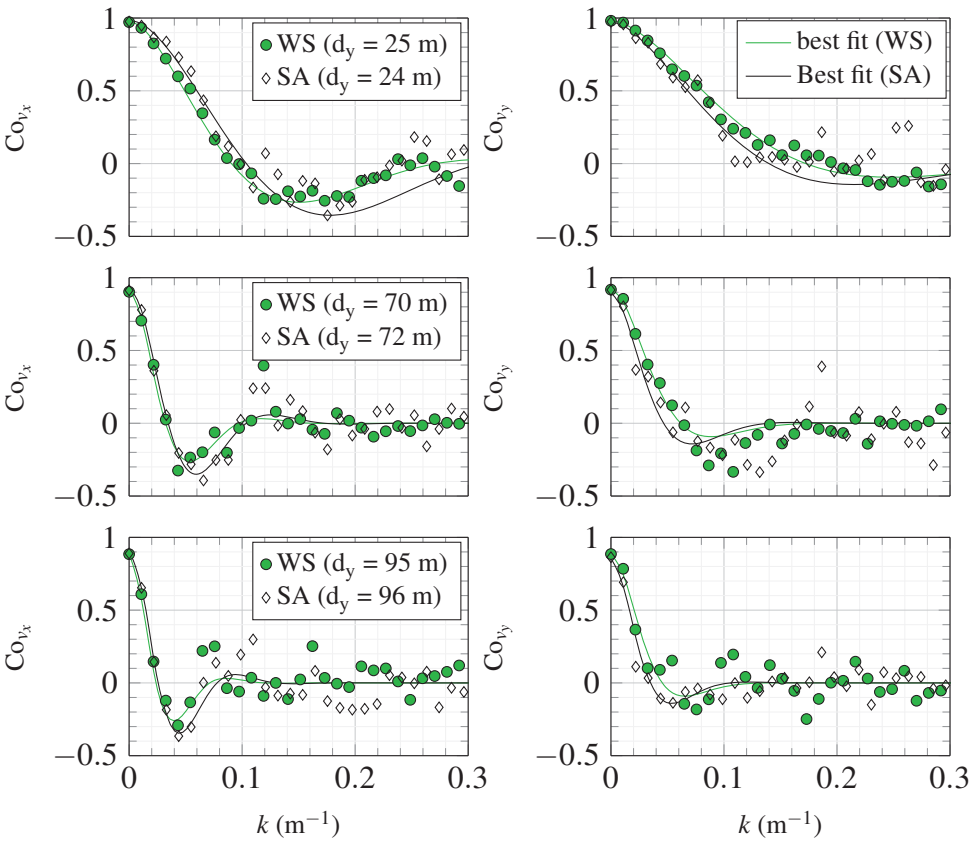

Figure 4.27 Measured (solid lines) and fitted (dashed lines) co-coherence, for the v_x-component (left) and the v_y-component (right), based on sonic anemometers (SA) and WindScanners (WS) wind records on 22/05/2014 from 16:25 to 16:35.

latter depends both on the radial distance r and the angle Ω between the beam and the wind direction. The spatial averaging effect can however be cancelled in a particular case, where two lidar beams are aligned with the flow, and monitor the wind field at two points y_1 and y_2, located at distances r_1 and r_2 from each lidar respectively. Under these conditions, analytic expressions of the single and two-point spectral densities of the wind components are much simpler, because they are not expressed as a linear combination of the

different radial velocities:

$$\boldsymbol{S_u}(k,y_1) = |\boldsymbol{H}(k,r_1)|^2 \cdot \boldsymbol{S_u^0}(k,y_1) \tag{4.1}$$

$$\boldsymbol{S_u}(k,y_2) = |\boldsymbol{H}(k,r_2)|^2 \cdot \boldsymbol{S_u^0}(k,y_2) \tag{4.2}$$

$$\boldsymbol{S_u}(k,y_1,y_2) = \boldsymbol{H}^*(k,r_2) \cdot \boldsymbol{H}(k,r_1) \cdot \boldsymbol{S_u^0}(k,y_1,y_2) \tag{4.3}$$

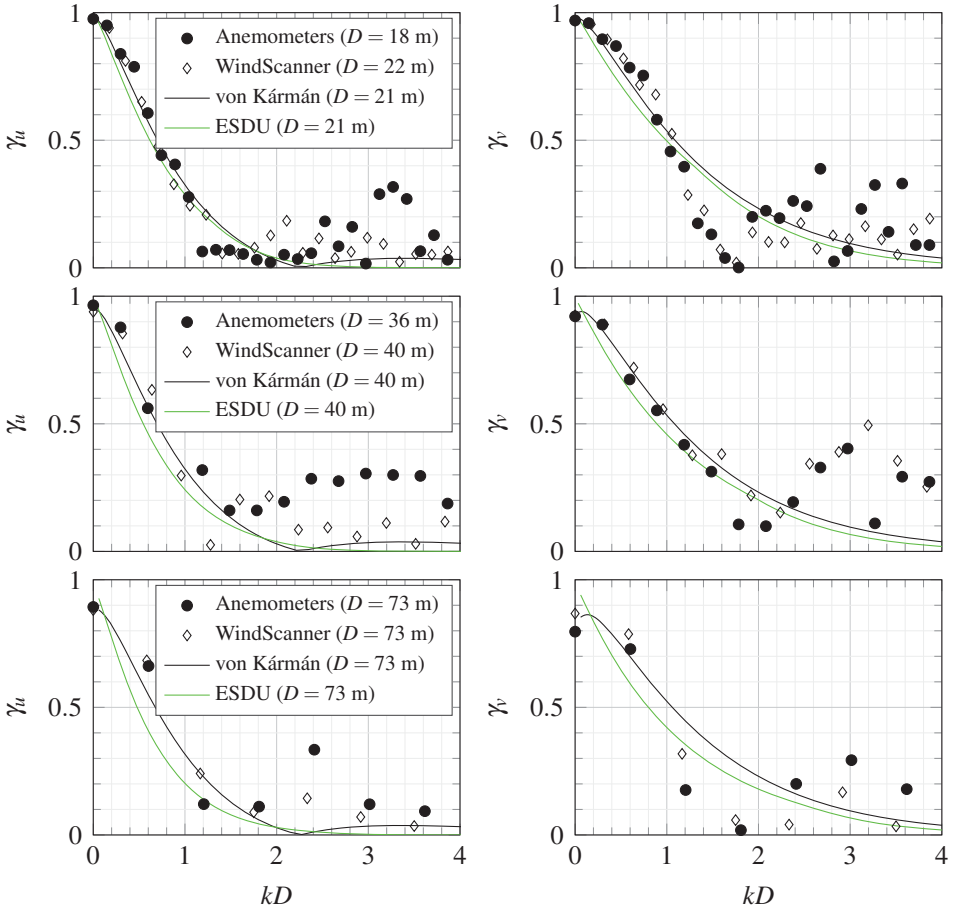

Figure 4.28 Root-coherence for the along-wind (left) and across-wind components (right) based on wind measurements on 22/05/2014 between 16:25:00 and 16:35:00.

where $\boldsymbol{H}^*$ is the conjugate of the spectral transfer function.

If $r_1 = r_2 = r$, then $\boldsymbol{H}$ becomes identical for the two along-beam wind velocities, and the root-coherence function becomes independent of $\boldsymbol{H}$:

$$\boldsymbol{\gamma_u}(y_1, y_2, k) = \frac{|\boldsymbol{S_u}(k, y_1, y_2)|}{\sqrt{\boldsymbol{S_u}(k, y_1) \cdot \boldsymbol{S_u}(k, y_2)}} \tag{4.4}$$

$$= \frac{\left|\boldsymbol{S_u^0}(k, y_1, y_2)\right|}{\sqrt{\boldsymbol{S_u^0}(k, y_1) \cdot \boldsymbol{S_u^0}(k, y_2)}} \tag{4.5}$$

The second reason that may explain why the averaging effect is hardly visible for the measured coherence is linked to the frequency range of interest. In Fig. 4.25, the spatial averaging effect is rather low for $k < 0.1$ m^{-1}, which is precisely the domain where the coherence is significantly high.

4.8 Summary

The WindScanners and the WindCube 100S showed the ability to perform at least a complementary role in wind field monitoring. The former was relevant for characterizing the flow with a high spatial resolution along a relatively small portion of the bridge deck, whereas the latter was useful in describing the wind field at a much larger scale. When a single lidar is used, the interpretation of the wind data can be a bit tricky because the along-beam wind component depends on both the elevation angle, the azimuth angle and the wind direction. Both the WindScanners and the WindCube 100S may provide good estimations of the first two statistical moments of the wind velocity, providing that high enough sampling frequency is used. It is already a well established fact that the mean wind velocity retrieved with the VAD scanning mode agrees well with the one from sonic anemometers (Peña et al., 2009; Sathe et al., 2011). This is however less evident for other scanning modes, especially at distances larger than 1 km and in complex terrain.

In this chapter, wind lidar data was used for the first time to study higher order wind statistics, such as turbulence length scales and wind coherence. The low sampling frequency of the WindCube 100S prevented coherence analysis using the pulsed lidar data. However, the WindScanners showed a promising potential in measuring wind coherence. In general, the short-range WindScanner system provided good quality data with a sufficiently high time and spatial resolution. However, statistical significance was not achieved in the present case because of the limited amount of data available.

More complex wind conditions were monitored for the N-NE wind direction. The WindCube 100S captured low wind velocities and high turbulence intensities with a satisfying accuracy. Because of the low wind velocity recorded for the N-NE exposure, a larger measurement noise was recorded by the short-range WindScanner system, which considerably reduced the amount of available data. An additional analysis conducted with a larger wind velocity from N-NE (Cheynet et al., 2016c) showed that the WindScanners can measure the flow in the wake of a bridge deck with a good spatial and temporal resolution.

For future application in bridge engineering, the low effective range of the short-range WindScanner system is the largest limiting factor. This is especially the case for future super-long span suspension bridges, where scanning distances of interest reach several kilometres without available infrastructure to support any sensors. On the other side, the limited amount of available data for WindCube 100S used here is another limiting factor. The ability of such a system in providing reliable and exploitable data remains a challenge to overcome for future deployments in complex terrains. One possibility to improve the reliability of the WindCube 100S is to develop new scanning configurations specifically suited for bridge engineering applications. Such a configuration was tested in offshore environment at the end of 2015 and provided encouraging results for the measurements of lateral and vertical wind coherence for the along-wind component (Cheynet et al., 2016b).

Chapter 5

Modal Analysis

5.1 Introduction

Direct measurements of the Free Decay Response (FDR) of a civil engineering structure enables the study of its modal parameters. This includes the identification of eigen-frequencies, mode shapes, modal damping ratios, and the study of their variations with different environmental conditions. For a long-span suspension bridge in full-scale, the FDR is rarely directly measured. One notable example is the study of Cunha et al. (2001), who suspended and released a mass of 60 t from one point fixed near the section 1/3 span of a cable-stayed bridge to obtain the free vibration response. Operational Modal Analysis (OMA), also called Ambient vibrations testing (AVT), is often more convenient and has actually become the "default procedure" (Brownjohn et al., 2010).

In this thesis, a Covariance-Driven Time-Domain (CDTD) method is applied to carry out an OMA on the Lysefjord bridge. The CDTD methods rely on the computation of the FDR or the output covariance of the system, followed by the extraction of the modal parameters using techniques that are usually applied using the free-decay response. To obtain the FDR, the Random Decrement Technique (RDT) (Chen et al., 2004; Ibrahim, 1977;

Siringoringo and Fujino, 2008) or the Natural Excitation Technique (NExT) (Juang and Pappa, 1985) are traditionally used. In the frequency domain, the peak-picking method allows a straightforward but less accurate identification of the eigen-frequencies, which remains advantageous at the early stages of the System identification process.

The first step of CDTD methods is based on the assumption of excitation by white noise. Under these conditions, the time series obtained from the RDT is equivalent to the free-decay response, providing that the velocity or displacement response is used (Huang and Yeh, 1999). If the acceleration response is used, the random decrement signature is not equivalent to the free-decay response due to the existence of a Dirac delta function at $t = 0$ (Huang and Yeh, 1999). Similarly, the decaying harmonic function obtained from the NExT procedure has the same properties as the directly measured counterpart (Bogunović Jakobsen, 1995; Farrar and James III, 1997). When a decaying harmonic function is obtained, the modal parameters can be retrieved by using The Ibrahim Time Domain (ITD) (Ibrahim, 1977), the Eigen-Realization Algorithm (ERA) (Juang and Pappa, 1985), or Covariance-Driven Stochastic Subspace Identification (SSI-COV) methods (van Overschee and de Moor, 1996). In the present study, only the automatic SSI-COV procedure developed by Magalhães et al. (2009) is studied in detail. Brownjohn et al. (2010) compared this method to the ERA (Juang and Pappa, 1985) and the p-LSCF algorithm (Peeters et al., 2004) and concluded that the SSI-COV method was well suited for application of SHM to long-span suspension bridges.

Siringoringo and Fujino (2008) and Brownjohn et al. (2010) are among the few who applied the SSI procedure to identify the modal parameters of a long-span bridge. Such procedure may become necessary for super-long span bridges, where eigen-frequencies are closely spaced, and cannot be efficiently studied with more traditional techniques such as the Time Domain Decomposition (TDD) (Kim et al., 2005) or Frequency Domain Decomposition (FDD) (Brincker et al., 2001). The reason is that these methods are

based on the analysis of the spectral peaks which are overlapping for closely-spaced modes. Siringoringo and Fujino (2008) and Brownjohn et al. (2010) compared different system identifications algorithms using 3 and 5 days long data set respectively. The amount of data they gathered may be statistically significant to assess the applicability of different algorithms, but it is unfortunately insufficient to evaluate the influence of environmental conditions on the bridge modal parameters as several months of data are required for that purpose.

The influence of environmental conditions on the bridge modal parameters is the main subject of this chapter. An automatic SSI-COV procedure was therefore applied to a considerable amount of 10 min acceleration response, wind velocity and temperature records acquired on the Lysefjord bridge during 6 months, from July 2015 to December 2015. Time efficiency is a governing factor in the present system identification since tens of thousands of acceleration records have to be analysed.

The theoretical background for the OMA procedure used here is first summarized. The influence of the environmental conditions on the identified eigen-frequency of the Lysefjord Bridge is then investigated. Furthermore, a brief presentation of the identified mode shapes is done. The measured modal damping ratios are afterwards studied more in detail as well as their dependency on the mean wind velocity and the temperature fluctuations. Finally, challenges and prospects of the application of an automatic SSI-COV procedure to future long-span bridges are discussed.

5.2 Free decay response from ambient vibrations

5.2.1 Random decrement technique

The RDT relies on the assumption that the dynamic response of the structure can be split into a deterministic and random part with zero mean. The FDR can be retrieved by removing the random part, which is done by splitting the

recorded response into multiple sub-samples and by averaging them. Each sub-sample is characterized by a given length and a triggering value. The length has to be large enough to capture the FDR and short enough so that the averaging of the sub-samples removes the random part. The triggering values are the initial value and/or the slope of the sub-sample. It has to be the same for every sub-sample so that the averaging process does not affect the deterministic part. Following the notations of Ibrahim (1977), the FDR x obtained with the RDT from an acceleration response s is:

$$x(\tau) = \frac{1}{N}\sum_{j=1}^{N} s(t_j + \tau) \tag{5.1}$$

where t_j is the starting time corresponding the triggering values.

5.2.2 NExT

The cross-covariance function between two acceleration records s_p and s_q is:

$$R_i(p,q) = \frac{1}{N}\sum_{j=1}^{N} s_p(j)s_q(j+i) \tag{5.2}$$

In the present case, the NExT was preferred to the RDT, because it requires only one parameter (the maximum time-lag) instead of two for the RDT (the triggering amplitude and the segment length). The construction of the cross-covariance matrix is also the strategy chosen by Magalhães et al. (2009) for the application of the automatic SSI-COV procedure. The cross-covariance can be obtained by using the inverse Fourier transform of the cross-power spectra between the different measured responses (Brownjohn et al., 2010; Farrar and James III, 1997; Siringoringo and Fujino, 2008), or by a direct calculation in the time domain. Here, the calculation using the inverse Fourier transform was adopted as it was computationally more efficient.

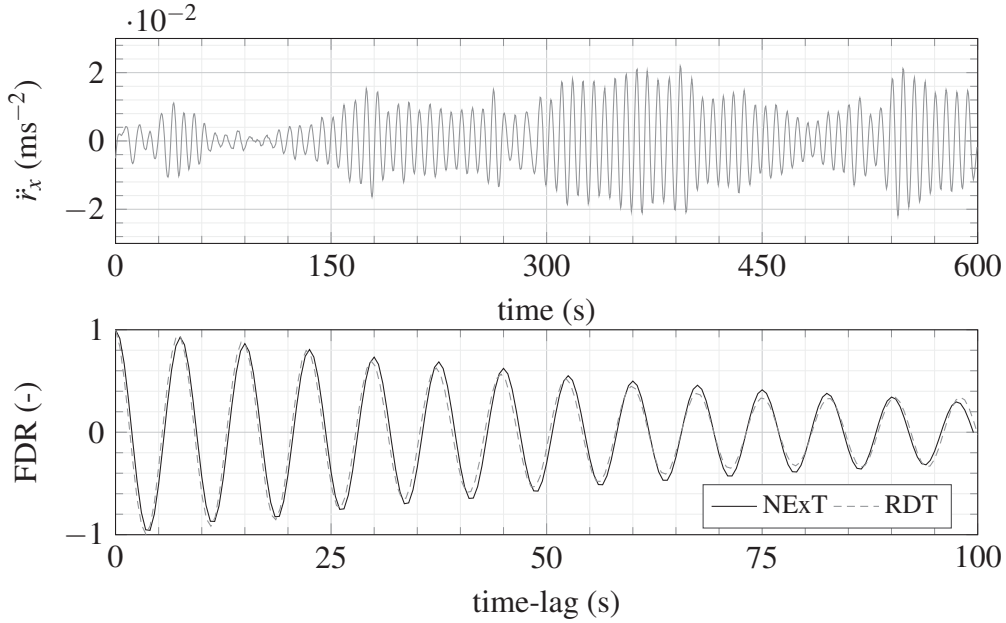

Figure 5.1 Random decrement signature (bottom: ----) and auto-covariance (bottom: ——) computed from the resonant lateral displacement response (top) recorded at mid-span on 26/10/2014 from 22:10.

The NExT and RDT are illustrated in Fig. 5.1 where the random decrement signature and the auto-covariance function are calculated using ambient vibrations data corresponding to the lateral bridge displacement at mid span (top panel of Fig. 5.1). The displacement data was high-pass filtered with a cut-off frequency of 0.08 Hz to conserve only the resonant bridge response. The two decaying harmonic functions displayed in the bottom panel of Fig. 5.1 have the same properties as the free-decay response. The lateral resonant displacement at mid-span is dominated by the first symmetric mode and can therefore be modelled as a single degree-of-freedom (SDOF) system.

By fitting an exponential decay to the envelop of the decaying harmonic functions, the modal-damping ratio can be retrieved [1]. In the present example,

[1] cf. File ID: #55557 on the MATLAB ® Central File Exchange website for a fully illustrated example.

if the first 50 s of the decay functions are considered, then a modal damping ratio of 0.74% is obtained with NExT and 0.67% with RDT. If the first 100 s are used, then a modal damping ratio of 0.94% and 1.1% is found with NExT and RDT respectively. These discrepancies illustrate the decisive influence of the maximum time-lag on the estimation of the modal damping ratio. The design structural modal damping ratios of the Lysefjord Bridge are of the order of 0.5% for every mode. Although the structural damping is likely to be different for every mode, the value of 0.5% can be considered as satisfactory at an initial stage. Given that the mean wind velocity was slightly below 13 $\mathrm{m\,s^{-1}}$ on 26/10/2014 from 22:10 to 22:20, the estimated total modal damping ratio for the first mode of the lateral acceleration response displayed in Fig. 5.1 is realistic.

The example given here is limited to the SDOF systems. For a modal identification procedure involving multiple sensors, large amount of data and multiple modes, more complex methods are required, such as e.g. the automated SSI-COV procedure used by Magalhães et al. (2009).

5.3 Automated SSI-COV procedure

When M acceleration records are simultaneously available, the cross-covariance function $\boldsymbol{R}_i$ calculated at a given time-lag i in Eq. 5.2 is a $M \times M$ cross-covariance matrix. The block-Toeplitz matrices $\boldsymbol{T_1}$ is then built as:

$$\boldsymbol{T_1} = \begin{bmatrix} \boldsymbol{R}_i & \boldsymbol{R}_{i-1} & \cdots & \boldsymbol{R}_1 \\ \boldsymbol{R}_{i+1} & \boldsymbol{R}_i & \cdots & \boldsymbol{R}_2 \\ \vdots & & \ddots & \vdots \\ \boldsymbol{R}_{2k-1} & \boldsymbol{R}_{2k-2} & \cdots & \boldsymbol{R}_i \end{bmatrix} \tag{5.3}$$

The size of the block-Toeplitz matrix is proportional to i (Fig. 5.2). The maximal time-lag plays therefore a central role in the system identification procedure. A longer time-lag implies a larger computation time and tends

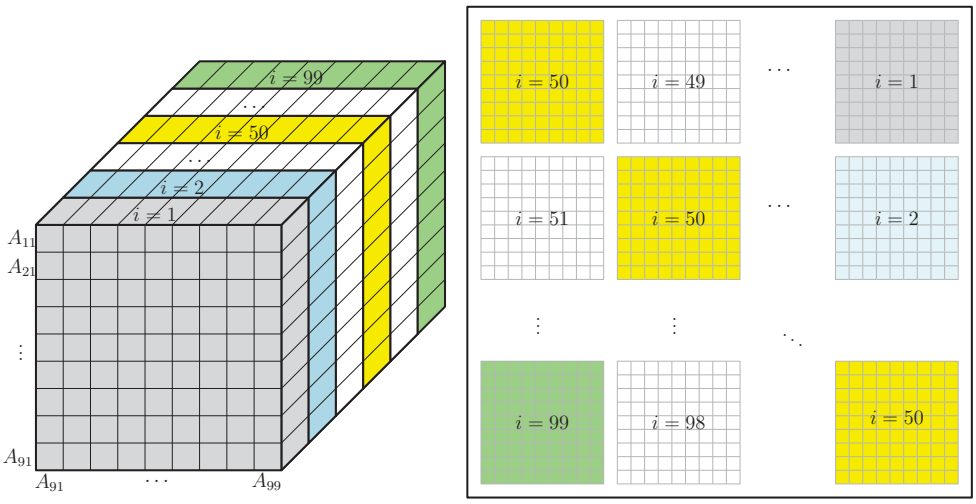

$9 \times 9 \times 99$ covariance matrix 450×450 Toeplitz matrix

Figure 5.2 Schematic of the 3D-cross correlation matrix, and the corresponding Toeplitz matrix, inspired from Magalhães and Cunha (2011), where the cross-covariance matrix is calculated for the first 99 time steps, based on 9 acceleration records (the numbers used here only serve an illustrative purpose).

to introduce an additional measurement error if the response of the system is non-stationary. On the other hand, if the time-lag is too short, then the numerical procedure may fail to identify the system properties. The choice of the time-lag seems to be mostly empirical. It depends on the system considered as well as its dependency on the environmental conditions. For example, Brownjohn et al. (2010) used a maximal time-lag corresponding to 2.23 times the longest natural period, whereas Magalhães et al. (2009) used a time-lag corresponding to 6.4 times the largest eigen-period. For the Lysefjord bridge, a time-lag between 2 and 3.25 time the largest eigen-period led to satisfying results. The low value of the time-lag for suspension bridges underlines how sensitive such structures are to the environmental conditions. This may explain why Magalhães et al. (2009) used a longer time-lag for the "Infante D. Henrique" Bridge, which is considerably less sensitive to wind excitation than the Humber Bridge or the Lysefjord Bridge.

The so-called extended observability and reversed extended controllability matrix, respectively denoted $\boldsymbol{O}$ and $\boldsymbol{\Gamma}$, are calculated using the output of the singular value decomposition of the block-Toeplitz matrix:

$$\boldsymbol{T_1} = \boldsymbol{U}\boldsymbol{\Lambda}\boldsymbol{V}^\top \tag{5.4}$$

$$\boldsymbol{O} = \boldsymbol{U}\boldsymbol{\Lambda}^{1/2} \tag{5.5}$$

$$\boldsymbol{\Gamma} = \boldsymbol{\Lambda}^{1/2}\boldsymbol{V}^\top \tag{5.6}$$

The state-space matrix is obtained by using the Moore–Penrose pseudo-inverse operator † (van Overschee and de Moor, 1996):

$$\boldsymbol{\Sigma} = \boldsymbol{O}_t^\dagger \boldsymbol{O}_b^\dagger \tag{5.7}$$

where $\boldsymbol{O}_t$ and $\boldsymbol{O}_b$ are obtained by considering the first and last $M \cdot (i-1)$ rows of $\boldsymbol{O}$ respectively.

The eigen-value decomposition of $\boldsymbol{\Sigma}$ leads to a diagonal matrix with elements λ_i, $i = \{1, 2, \cdots, m\}$. The matrix of mode shapes is denoted $\boldsymbol{\psi}$. The eigen-frequencies f_i, modal damping ratio ζ_i and mode shapes ψ_i are written by using the poles of the continuous time-model Ω_i:

$$\Omega_i = \frac{ln(\lambda_i)}{\mathrm{d}t} \tag{5.8}$$

$$f_i = \frac{|\Omega_i|}{2\pi} \tag{5.9}$$

$$\zeta_i = -\frac{\mathrm{Re}(\Omega_i)}{\mathrm{Im}(\Omega_i)} \tag{5.10}$$

$$\psi_i = \mathrm{Re}(\boldsymbol{C}_m) \cdot \boldsymbol{\psi} \tag{5.11}$$

where $\boldsymbol{C}_m$ is the matrix containing the first m rows of $\boldsymbol{O}$.

5.3.1 Stabilization diagram

The optimal number of singular values, i.e. the model order extracted from the block Toeplitz matrix in Eq. 5.4 is unknown. Acceleration data are contaminated by measurement noise and when the model order is larger than the maximal number of modes that can be extracted, spurious modes are identified. The stabilization diagram is an effective tool to detect and eliminate spurious modes. Such a diagram displays each identified mode for increasing model orders. For the same mode and two successive model orders i and j, the mode stability is studied by using accuracy tests, presented in Eq. 5.12 to Eq. 5.14:

$$\varepsilon_{\text{fn}} \geq \left| 1 - \frac{f_i}{f_j} \right| \tag{5.12}$$

$$\varepsilon_{\zeta} \geq \left| 1 - \frac{\zeta_i}{\zeta_j} \right| \tag{5.13}$$

$$\varepsilon_{\text{MAC}} \geq \left| 1 - \frac{\left(\psi_i \psi_j\right)^2}{\left(\psi_i^{\top} \psi_i\right)\left(\psi_j^{\top} \psi_j\right)} \right| \tag{5.14}$$

where ε_{fn}, ε_{ζ} and ε_{MAC} are arbitrary threshold values. The threshold ε_{MAC} is calculated based on the modal assurance criterion (MAC) introduced first by Allemang and Brown (1982) to simplify the identification of modes shapes by ignoring the possible scaling factor between them. Some values found in the literature are summarized in Table 5.1.

If the calculated accuracy is above the threshold value, then the test has "failed". Therefore, five types of pole stability can be defined:

- Stable pole if every accuracy test is passed.
- Pole with stable frequency if only the frequency test is passed.

- Pole with stable frequency and damping if only the MAC test has failed.
- Pole with stable frequency and MAC if only the damping test has failed.
- New pole if every accuracy test has failed.

Fig. 5.3 shows a stabilization diagram built for 10 min of nocturnal acceleration data recorded on the Lysefjord bridge on 07/10/2014 from 00:00, with both stable and spurious poles. Eight modes are clearly identified for model orders increasing from 4 to 40. No mode related to the lateral or torsional bridge motion were identified. The higher modes are not detected until the number of poles becomes high enough. An increasing model order is associated with a larger amount of spurious poles for the lower modes. In the case of the Lysefjord Bridge, a maximal model order of 30 was observed to be sufficient to identify the first 6 lateral and vertical modes and the first two torsional modes.

Seen from this angle, the stabilization diagram is also a powerful tool for the calibration stage of the automated SSI-COV algorithm. If one of the accuracy thresholds is poorly designed, the amount of identified "stable poles" may drop and another type of pole will be dominant. For example, if the number of poles with a stable frequency and MAC is prevailing, this may indicate the value of ε_ζ is too low. On the other hand, if the amount of "stable poles" is doubtfully large, this may indicate that at the value of at least one of the accuracy thresholds is too large.

Table 5.1 Accuracy test thresholds found in the literature.

source	ε_{fn}	ε_ζ	ε_{MAC}
Magalhães et al. (2009)	0.01	0.02	0.01
Siringoringo and Fujino (2008)	0.1	?	0.2
Chang and Pakzad (2013)	0.05	0.1	0.05
Bakir (2011)	0.01	0.05	0.02

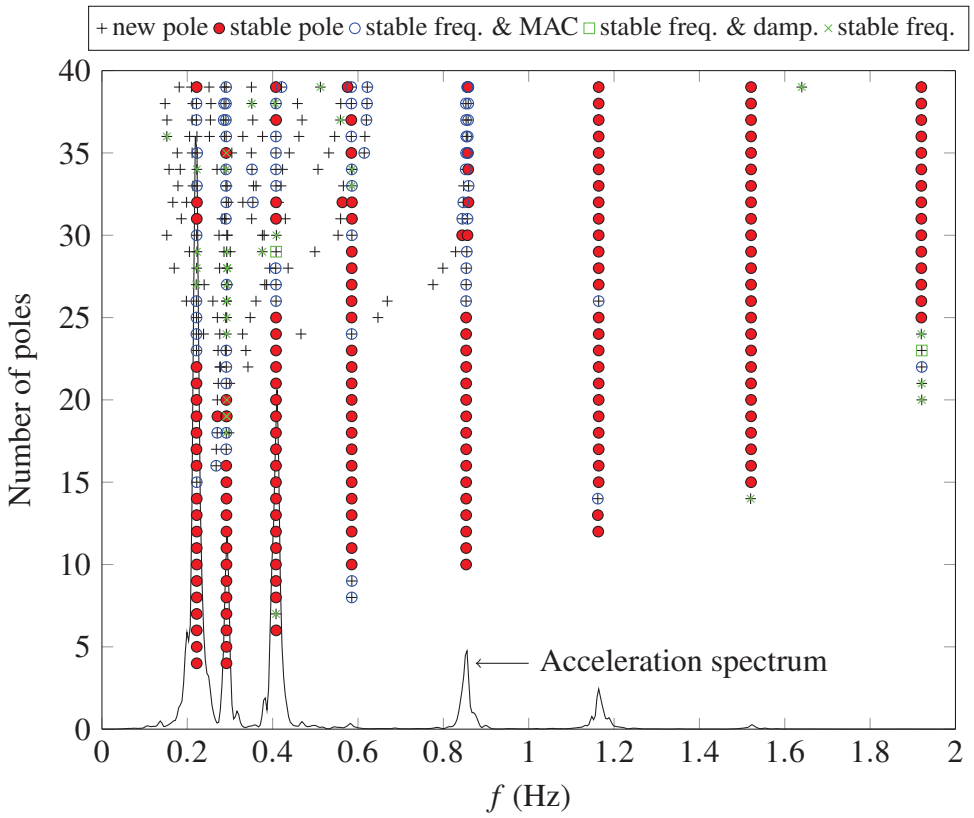

Figure 5.3 Stabilization diagram calculated for the vertical acceleration response of the Lysefjord bridge, near H-20, on 07/10/2014 from 00:00 to 00:10.

5.3.2 Cluster algorithm

The automatic selection of stable poles is a major challenge when it comes to use the SSI-COV method with the stabilization diagrams. The method used in the present study is directly inspired from Magalhães et al. (2009) where a cluster analysis is carried out. A cluster analysis aims to partition scattered data into groups. At the scale of a single group, data are homogeneous, whereas at the scale of multiple clusters, a strong heterogeneity is visible. In other words, objects inside the same cluster share the same properties.

Once stable poles are selected, they can be displayed as a function of the frequency and the modal damping ratio ζ. Poles that belong to the same mode tend to be close to each others, creating clusters as illustrated on Fig. 5.4. The purpose of cluster analysis is the automatic reliable detection of each modal parameter.

The number of clusters is unknown prior to the analysis, which prevents the use of non-hierarchical clustering methods. First, a hierarchical cluster tree is built, based on the single linkage algorithm, using Euclidean distance between elements i and j, in a similar fashion as in Magalhães et al. (2009):

$$d_{i,j} = \left| 1 - \frac{f_i}{f_j} \right| + 1 - \mathrm{MAC}_{i,j} \tag{5.15}$$

where $\mathrm{MAC}_{i,j}$ is the Modal Assurance Criterion (Allemang and Brown, 1982). Two elements belong to the same cluster if they are separated by less than a distance denoted ε_d, which could be considered as a fourth accuracy criterion in addition to those presented by Eqs. 5.12 to 5.14. Although the term

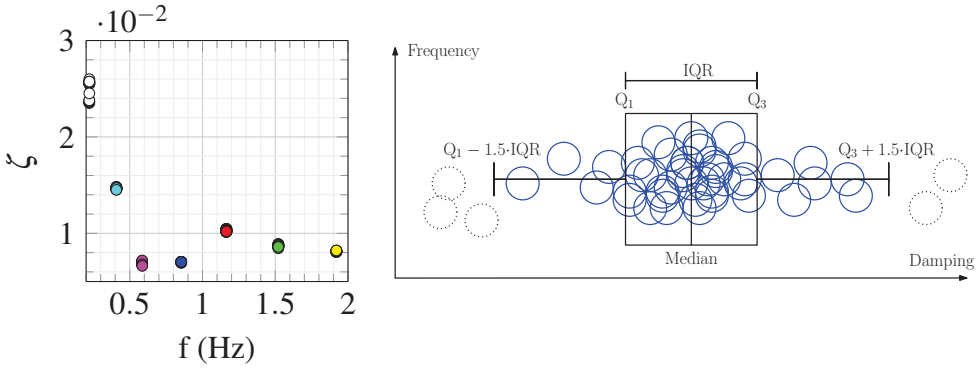

Figure 5.4 Left: damping ratios estimated for the vertical acceleration response of the Lysefjord bridge on 07/10/2014 from 00:00 to 00:10. Right: schematic of one cluster in a frequency vs damping diagram. Dotted circles refer to dismissed elements as they lay outside the line segment defined by $\mathrm{Q}_1 - 1.5{\cdot}\mathrm{IQR}$ and $\mathrm{Q}_3 + 1.5{\cdot}\mathrm{IQR}$, where IQR, Q_1 and Q_2 designates the interquartile range, the lower quartile and the upper quartile respectively.

"distance" is used, Eq. 5.15 is actually based on a deviation in terms of frequencies. The scatter of the modal damping ratios could also have been used in the cluster algorithm. In the present case, this is not a reliable criterion as this scatter is naturally large. The value of ε_d was chosen as 0.02 by Magalhães et al. (2009), but the value of ε_d actually depends on the signal to noise ratio of the output.

The dispersion of the elements in a cluster can still be important, especially for the modal damping ratios. An averaged value of the cluster may therefore be biased. To reduce this bias, the scatter of the elements is diminished by considering only data located between the first and the third quartile (Fig. 5.4). A similar procedure was done by e.g. Magalhães et al. (2009).

5.3.3 Summary

In this chapter, the parameters used in the SSI-COV analysis of the Lysefjord bridge acceleration data are summarized in Table 5.2.

The implementation of the automated SSI-COV to identify the modal parameters of a large civil engineering structure such as a suspension bridge can be done by defining a limited number of parameters:

1. The maximal time-lag $\tau_{\max}$ when computing the cross-covariance matrix.
2. The minimal and maximal order of the system for the calculation of the stabilization diagram, denoted $N_{\min}$ and $N_{\max}$ respectively.
3. The three accuracy thresholds (ε_{fn}, ε_ζ, ε_{MAC}).

Table 5.2 Parameters used in the SSI-COV method applied on Lysefjord bridge acceleration data.

$\tau_{\max}$ (s)	$N_{\min}$	$N_{\max}$	ε_{fn}	ε_ζ	ε_{MAC}	ε_{d}
15	3	30	5e − 3	3e − 2	5e − 3	2e − 2

4. The threshold accuracy ε_d for the cluster analysis.

5.4 Computational model estimation of modal parameters

Although the application of the automated SSI-COV to the acceleration data in full scale is the primary interest of this chapter, comparison of the identified modal parameters with those obtained from a computational model is also relevant. One of the objectives of this thesis is indeed to establish the bases of a systematic validation of the buffeting theory in full-scale and the present modal identification procedure is a required step in that process.

The Finite Element (FE) based software Alvsat developed by the Norwegian Public Road Administration (NPRA) has been used to evaluate a numerical prediction of the mode shapes and eigen-frequencies of the Lysefjord Bridge. The eigen-frequencies and the mode shapes of the Lysefjord Bridge were approximated by using harmonic series expansions following Sigbjörnsson and Hjorth-Hansen (1981) for the lateral motion and Strømmen (2014) for the vertical and torsional ones. In the following, this method is referred to as the "Simplified Bridge Model" denoted SBM [2]. An alternative and maybe more elegant approach to get the vertical mode shapes and eigen-frequencies is based on the classical theory from Bleich (1950) which was further developed by Luco and Turmo (2010). The mode shapes obtained with this model were however almost identical to those calculated with the SBM.

The mode shapes from the SBM and Alvsat model were found to be identical, except for the first two symmetrical mode shapes. The structural modal damping ratios are set to 0.5% for every mode. The total modal damping ratio, defined as the sum of the aerodynamic and structural modal

[2]The source code of the SBM is freely available at MATLAB Central File Exchange (cf. File ID: #54649 and #51815)

damping ratio, can be obtained assuming uncoupled modes, which is in general observed for the Lysefjord Bridge (cf. Chapter 7). Following the quasi-steady theory, the total modal damping ratio for the i^{th} mode is:

$$\zeta_i^{\text{tot}} = \zeta_i^{\text{struct}} + \frac{\tilde{C}_{\text{ae}i}}{4\pi f_i \tilde{M}_i} \tag{5.16}$$

where f_i is the eigen-frequency for the i^{th} mode. $\tilde{M}_i$ is the i^{th} diagonal element of the matrix of modal mass $\tilde{\boldsymbol{M}}$ defined in Eq. 2.55. Similarly, $\tilde{C}_{\text{ae}i}$ is the i^{th} diagonal element of the matrix of modal aerodynamic damping $\tilde{\boldsymbol{C}}_{\boldsymbol{ae}}$ defined in Eq. 2.59.

5.5 Full scale measurements

An OMA based on the automated SSI-COV method presented previously was applied to the Lysefjord bridge data acquired during 6 months, between 01/07/2015 and 31/12/2016. Continuous records from three pairs of accelerometers located near hangers 9, 18 and 24 (Fig. 3.4) were used for that purpose. One of the accelerometers near H-30 was defective during the study period and the acceleration records from H-30 were therefore disregarded. To benefit from high quality data from the entire set of accelerometers, data from the year 2014 was used to identify the mode shapes. The mode-shapes were therefore identified using a data set containing 144 samples, recorded on 26/10/2014. The considerable amount of available data offers a unique occasion to investigate the variations of the eigen-frequencies with temperature and wind velocity fluctuations as well as traffic-induced loads. This allows also a detailed analysis of the evolution of the modal damping ratios with the mean wind velocity.

5.5.1 Overview of the measured bridge response

Using the Lysefjord Bridge as a case study can be considered as a first step in developing and validating a methodology that may be applied to longer span bridges. For example, the eigen-frequencies of a medium-span suspension bridge are usually well separated which reduces the occurrence of modal coupling. This is illustrated on Fig. 5.5 where 120 s of the Lysefjord bridge acceleration record at mid-span are displayed.

Fig. 5.5 suggests that only a small number of modes is necessary to properly model the acceleration response of the Lysefjord bridge. The dominant eigen-frequency for the lateral motion is 0.13 Hz whereas it is 1.24 Hz for the torsional motion, i.e. a value almost ten times larger than for the lateral motion. A review of Fujino and Siringoringo (2013) showed for example that the first eigen-frequencies of the lateral, vertical and torsional motion are all located below 0.2 Hz for a main span of 2 km, and below 0.1 Hz for a main span of 3 km. In Fig. 5.5, the lateral acceleration response is dominated by only two modes with eigen-frequencies around 0.13 Hz and 0.45 Hz. For the vertical acceleration response at mid-span, only the first two symmetric modes with frequencies around 0.3 Hz and 0.4 Hz are clearly perceptible. For the torsional acceleration response, only the first torsional mode, at about 1.2 Hz is well defined. Since Fig. 5.5 displays the acceleration response at mid-span only, the asymmetric modes are not captured, but they have to be included to study the complete bridge response. To briefly assess the applicability of the present automated SSI-COV procedure on larger suspension bridges, a similar OMA was successfully conducted on 10 min of acceleration data recorded on the Hardanger Bridge at the end of the year 2013 (Appendix B).

Compared to a long-span suspension bridge, the response of a medium-span suspension bridge is relatively limited in amplitude, which is often associated with a lower signal-to-noise ratio. Consequently, the identification of the modal parameters of the Lysefjord bridge may be contaminated

by measurement noise, which justifies the statistical approach used in the following.

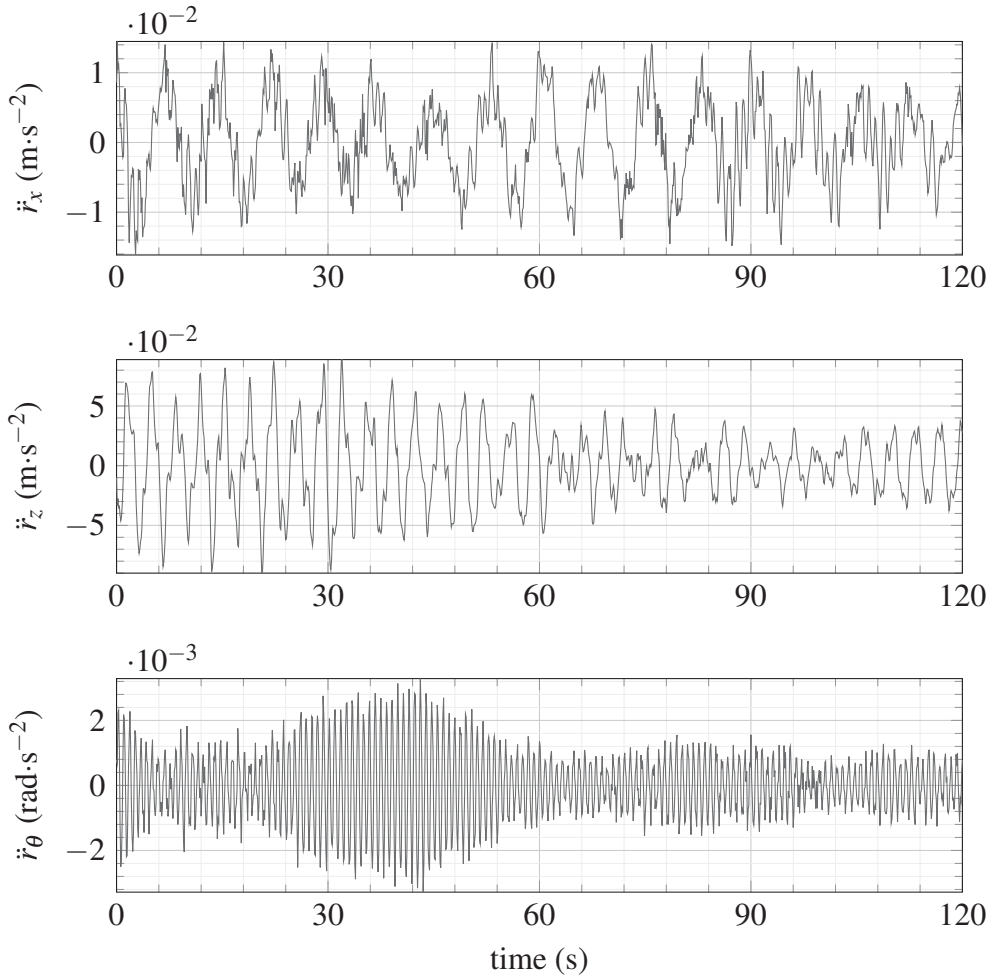

Figure 5.5 Lateral (top), vertical (middle) and torsional (bottom) acceleration response of the Lysefjord bridge (26/10/2014 from 01:00 to 01:02) near H-18 for a sampling frequency of 10 Hz.

5.5.2 Eigen-frequencies

The evolution of eigen-frequencies with time can be studied at different scales: long term fluctuations (several years), seasonal fluctuations (several months) or daily fluctuations (several days). The Humber Bridge modal analysis, carried out for the first time in 1985 (Brownjohn et al., 1987) and the second time in 2008 (Brownjohn et al., 2010) may be the most prominent example of long term operational modal analysis. Long term analysis may be particularly useful to detect damage, even if such an application remains challenging (Brownjohn et al., 2011). In the following, only seasonal and daily fluctuations of the bridge modal parameters are studied.

A study of Xia et al. (2012) suggests that the variations of eigen-frequencies of a suspension bridge due to temperature fluctuations may be less visible than for a concrete bridge such as the one studied by Magalhães and Cunha (2011). For this bridge, Magalhães and Cunha (2011) observed that the eigen-frequencies clearly followed a seasonal pattern. In the present case, environmental effects on the eigen-frequencies of the Lysefjord bridge are still expected to be detected by the SSI-COV algorithm, although the peak-picking method was not able to find any seasonal or daily fluctuations. The unsuitability of the peak-picking method to study the daily fluctuations of the eigen-frequencies has been underlined in previous studies such as e.g. Ding and Li (2011).

The eigen-frequencies identified over the 6 months period are displayed in Fig. 5.6. The modal parameters are hereby defined using the code XYZ, where $X = \{H, V, T\}$ represents the lateral (H), vertical (V) and torsional (T) bridge motion. $Y = \{S, A\}$ is the symmetric (S) or asymmetric (A) mode shape, and Z the mode number. For example HS1 refers to the first symmetric horizontal mode shape, and TA2 refers to the second asymmetric torsional mode shape. To increase the identification speed of the lower modes, the sampling frequency of the lateral and vertical acceleration records were reduced to 2 Hz. The sampling frequency of the torsional acceleration

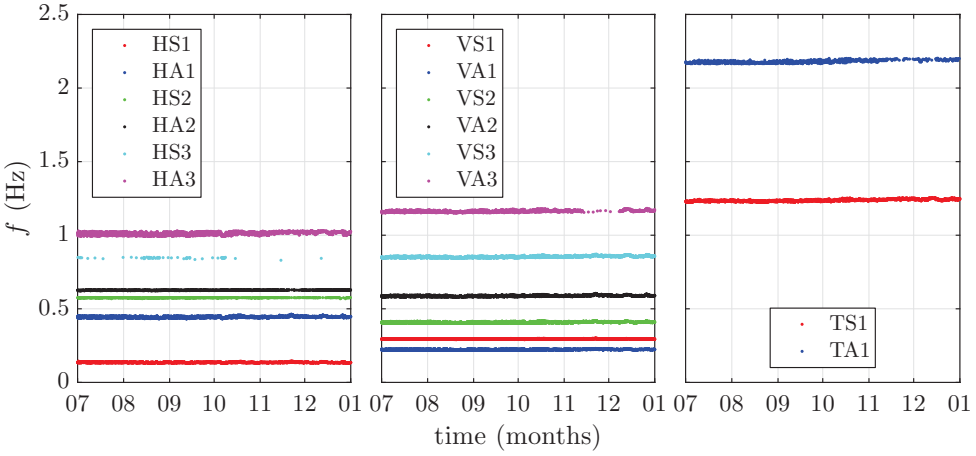

Figure 5.6 First six lateral and vertical and first two torsional eigen-frequencies identified during the 6 months period in 2015 at the Lysefjord bridge

response remained at 20 Hz. This allowed the SSI-COV algorithm to be applied to more than 50 000 acceleration records of 10 min duration in less than half a day.

The automated SSI-COV method managed to clearly identify the first five lateral modes, the first six vertical modes and the first two torsional modes. The sixth lateral mode (HS3), around 0.85 Hz, was more challenging to capture. The second mode of the bridge towers in the along-span direction is located near 0.85 Hz and was probably interfering with HS3. For the torsional motion, modes characterized with a frequency above 3 Hz had an amplitude too small to be detected with a high reliability.

A comparison between the predicted and measured eigen-frequencies (averaged over the period of study) is summarized in Table 5.3. For the lateral motion, the difference between the measured and computed eigen-frequencies is below 5% except for HS3. For the vertical motion, the difference is below 10 %, although the largest error is obtained for the dominant modes, i.e. VA1, VS1 and VS2. For the torsional motion, the discrepancy between the eigen-frequencies predicted by the SBM and the measured ones is between

Table 5.3 Comparison of the eigen-frequencies calculated using the SSI-COV method with the values calculated using the FEM code Alvsat, and the SBM.

Modes	SSI-COV	Alvsat		SBM	
	Hz	Hz	%	Hz	%
HS1	0.136	0.130	-4.35	0.130	-4.41
HA1	0.444	0.442	-0.43	0.442	-0.45
HS2	0.577	0.557	-3.45	0.556	-3.51
HA2	0.626	0.598	-4.51	0.597	-4.61
HS3	0.742	0.831	12.01	0.830	11.90
HA3	1.011	1.002	-0.89	1.000	-1.03
VA1	0.223	0.213	-4.30	0.205	-8.10
VS1	0.294	0.286	-2.69	0.319	8.35
VS2	0.408	0.400	-1.87	0.439	7.63
VA2	0.587	0.589	0.28	0.585	-0.39
VS3	0.853	0.867	1.59	0.864	1.31
VA3	1.163	1.198	3.06	1.194	2.72
TS1	1.237	1.154	-6.64	1.067	-13.69
TA1	2.184	2.125	-2.73	1.920	-12.09

12% and 14 %. This may be because the flexibility of the towers, hangers and backstay cables is ignored in the SBM. Only the Alvsat model manages to give acceptable prediction of the first two torsional eigen-frequencies.

Influence of temperature and traffic

The temperature-dependency of the eigen-frequencies of a bridge can be studied at the scale of some days or several months. Such studies are not well documented for suspension bridges, but are more common for concrete bridges (Magalhães et al., 2009; Sohn et al., 1999). Magalhães et al. (2009) recorded for example significantly higher eigen-frequencies of a concrete bridge during Winter than during Summer. The effects of seasonal temperature fluctuations on the static displacement of a suspension bridge were

investigated by Xu et al. (2010), but without focusing on the modal parameters. More efforts have been dedicated to model the thermal behaviour of suspension bridges (de Battista et al., 2015; Westgate et al., 2014; Zhou et al., 2016), which is a different topic.

Koo et al. (2013) observed a daily periodicity of the eigen-frequencies for the Tamar suspension bridge, but did not give any interpretation. Ding and Li (2011) briefly pointed out that the temperature fluctuations may actually cause daily variations of the eigen-frequencies. Actually, daily variations of the eigen-frequencies may be due to temperature fluctuations, traffic loading over the day, or both. The visualization of daily fluctuations of the eigen-frequencies of the Lysefjord bridge is therefore one of the objectives of this section.

As stated by Xia et al. (2012), a higher temperature leads in general to a decrease of vibration frequencies, which is mainly due to the temperature dependency of the materials Young's modulus. This variation of the eigen-frequencies are visible in Fig. 5.7 , except for temperatures over 20 °C where the amount of samples was probably too low to provide reliable results. Another possibility is a non-linear variation of the eigen-frequencies with the temperature and a stabilization of the eigen-frequencies for temperatures over 20 °C. The influence of temperature variations on the first lateral mode HS1 is rather small. The frequency drops from 0.137 to 0.134 Hz when the temperature increases from 0 °C to 20 °C. For a similar temperature change, the frequency associated with VA1 decreases from 0.226 Hz to 0.219 Hz. The most dramatic frequency change occurs for the mode TS1 where the frequency decreases from 1.25 Hz to 1.23 Hz. The scatter of the eigen-frequencies observed on Fig. 5.7 is due to the influence of other parameters such as traffic, the mean wind velocity and maybe wind turbulence.

The duration of the present study (6 months) suggests that the eigen-modes HS1, VA1, and TS1 display a "seasonal trend" rather than a "seasonal periodicity". This trend was slightly visible for TS1 but not for HS1 nor VA1

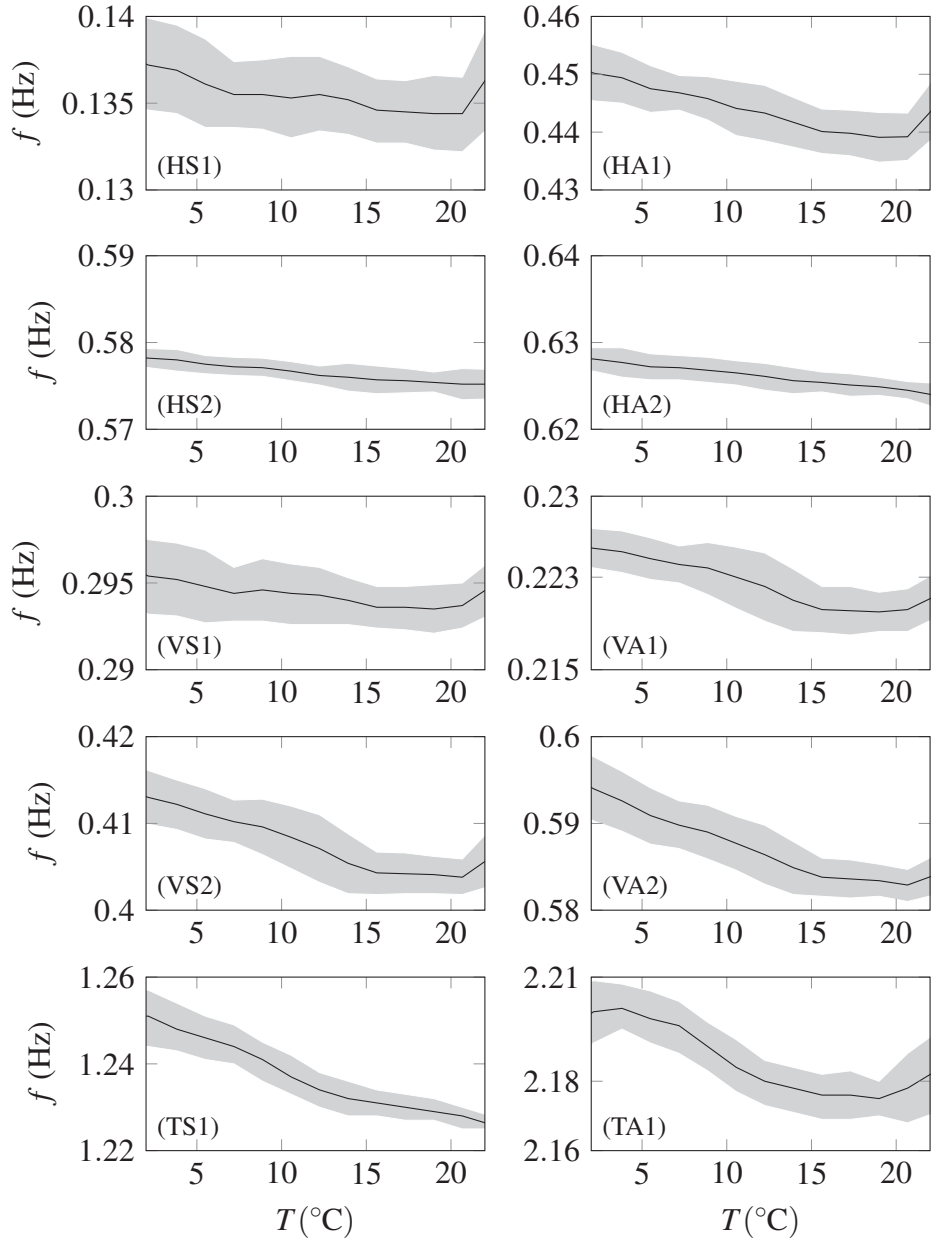

Figure 5.7 Evolution of the first four lateral and vertical and the first two torsional eigen-frequencies with the temperature. The data set comprises six months of acceleration and temperature records (July to December 2015).

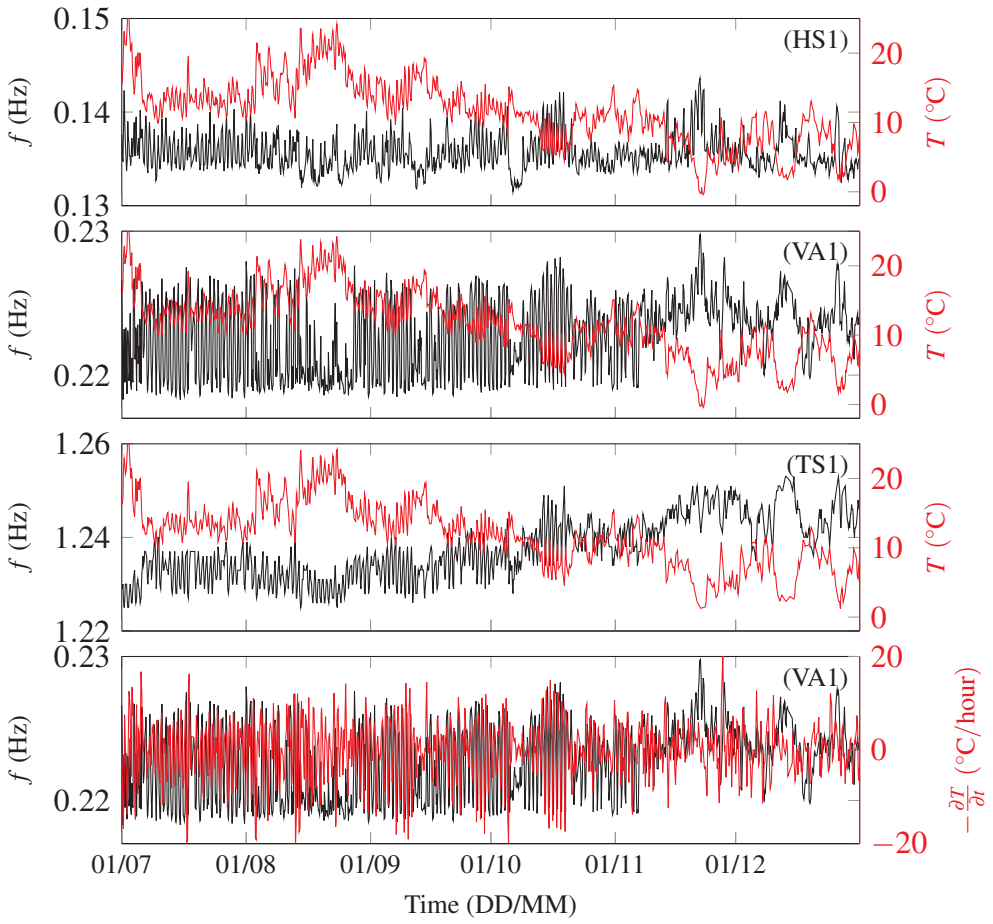

Figure 5.8 Evolution of the frequencies for HS1, VA1 and TS1 from July 2015 to December 2015 as a function of the temperature (T) (top three panels) and the negative temperature rate of change (bottom panel).

(Fig. 5.8). Clear daily variations of the lateral and vertical eigen-frequencies were however visible. On the bottom panel of Fig. 5.8, the temperature rate of change and the eigen-frequency fluctuations are almost in phase, suggesting a high correlation between the variations of the temperature and the bridge eigen-frequencies. These fluctuations reduce from the end of October to become more irregular in December. In the South-West part of Norway the

reduction of daylight becomes significant from the beginning of November, and daily temperature fluctuations are therefore attenuated, leading to an irregular temperature and eigen-frequency patterns, which are clearly visible in December. Between the 07/12 and the 15/12 for example, the temperature smoothly decreased from 10 °C to 0 °C before increasing back to 10 °C. This was associated with a clear increase of TS1 from 1.238 Hz to 1.253 Hz then a reduction back to 1.240 Hz.

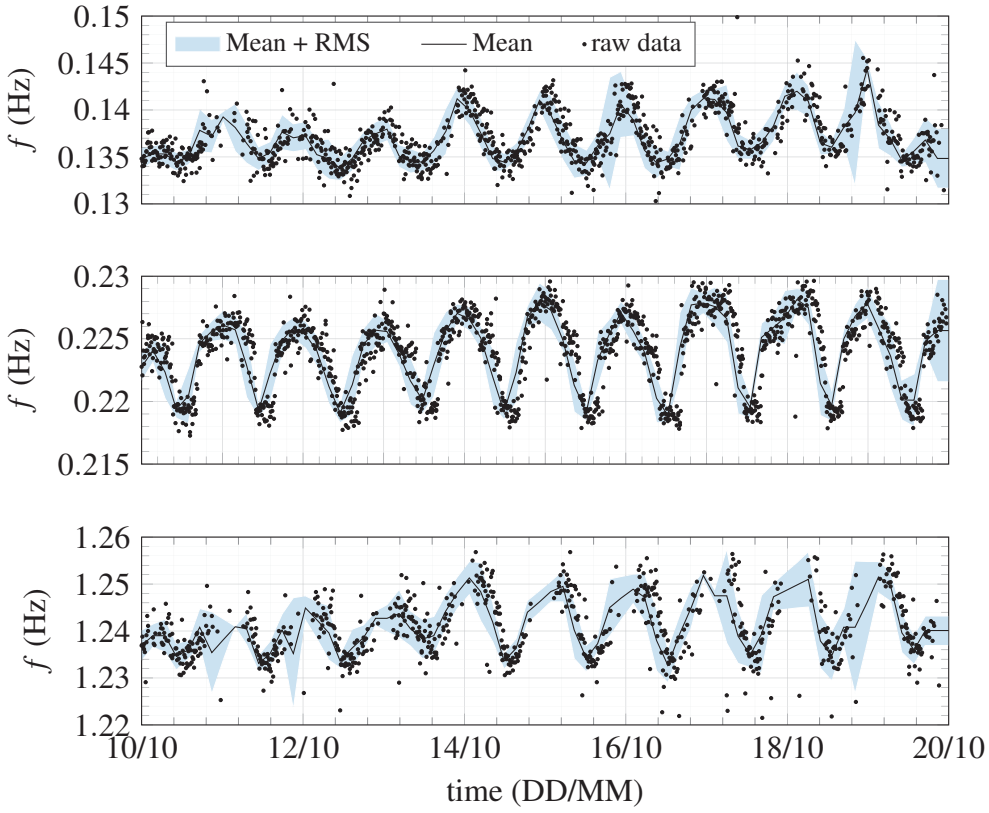

Figure 5.9 Evolution of the lowest eigen-mode for the lateral, vertical and torsional bridge motion, between the 20/09/2015 and 30/09/2015. Data binning has been applied to better estimate the fluctuating mean value and RMS of the eigen-frequencies.

The daily fluctuations of the eigen-frequencies can be visualized by studying few days worth of data. This is done in Fig. 5.9, where ten days of data recorded in October 2015 are displayed. The first lateral eigen-frequency HS1 fluctuates between 0.132 Hz for diurnal data and 0.145 Hz for nocturnal data. These fluctuations are relatively small compared to those from VA1 which ranges from 0.217 Hz at day time to almost 0.23 Hz during the night. For the torsional motion, TS1 fluctuates between 1.23 Hz up to 1.255 Hz. Such variations may not be explained by temperature fluctuations only. As underlined by Kim et al. (2003), heavy traffic is likely to be responsible for a reduction of the eigen-frequencies of the bridge deck.

The effects of the temperature and traffic variations on the bridge eigen-frequencies are therefore expected to superimpose and be responsible for larger frequency variations. At night time, the lower temperature and the reduced traffic leads to higher eigen-frequencies whereas at day time, the increase of the temperature and traffic leads to lower eigen-frequencies. This appears clearly on Fig. 5.9, where a pseudo-period of 24 hours is visible. Whereas the periodical pattern is clearly visible for the vertical bridge motion, it is more noisy for the lateral and torsional motions. This can be partly explained by the higher signal to noise ratio measured for the vertical motion.

The relative influence of traffic on the variation of the eigen-frequencies may be less than the influence of temperature fluctuations. The attenuation of the daily periodicity of the eigen-frequency in November and December cannot simply be explained by a reduction of heavy traffic for example. The periodicity pattern appears to be almost entirely modulated by temperature changes. For example, it can be observed that the sinusoid pattern highlighted in Fig. 5.9 is flatter on its bottom in July (longer day), and on its top in October (shorter day), without strong variations of the amplitude of the fluctuations.

Influence of wind velocity

The amplitude of excitations and thereby the amplitude of vibrations is known to affect the eigen-frequencies and damping ratios of long period structures (Tamura and Suganuma, 1996). For suspension bridges, an increasing wind velocity is known to result in a decrease in the torsional eigen-frequencies but an increase in the vertical eigen-frequencies (Macdonald and Daniell, 2005; Namini et al., 1992). At the same time, the lateral eigen-frequencies are usually assumed to remain constant. The data set investigated in this chapter offers an unique occasion to examine these predictions.

On Fig. 5.10, the first four lateral eigen-frequencies are actually fluctuating with the mean wind velocity. HS1 is slightly decreasing, whereas HA1 remain more or less constant, although its dependency on the mean wind velocity is not linear. For HS1 the maximal difference is about 0.03 Hz. The eigen-frequencies of HS2 and HA2 increase slightly when the mean wind velocity component normal to the deck becomes larger than 10 $\mathrm{m\,s^{-1}}$. The eigen-frequencies corresponding to the vertical and torsional motions are observed to hardly fluctuate with the mean wind velocity. For the period of study, the mean wind velocity and temperature cannot be considered as fully independent variables, because higher wind velocities are usually recorded at the end of Autumn, i.e. when the average temperature is much lower than in Summer.

Fig. 5.10 shows that the averaged value of TS1 is bounded between 1.23 Hz and 1.24 Hz. On Fig. 5.7, a significant portion of the value of TS1 is outside this interval. Yet, the same data sets is used in Fig. 5.7 and Fig. 5.10. The amount of data gathered is actually not uniformly distributed within the temperature interval displayed in Fig. 5.7. The majority of acceleration data have been recorded for a temperature from 10 °C to 12 °C. Consequently, the average value of TS1 is more or less constant when plotted against wind velocity, but the scatter is greater than seen in Fig. 5.7.

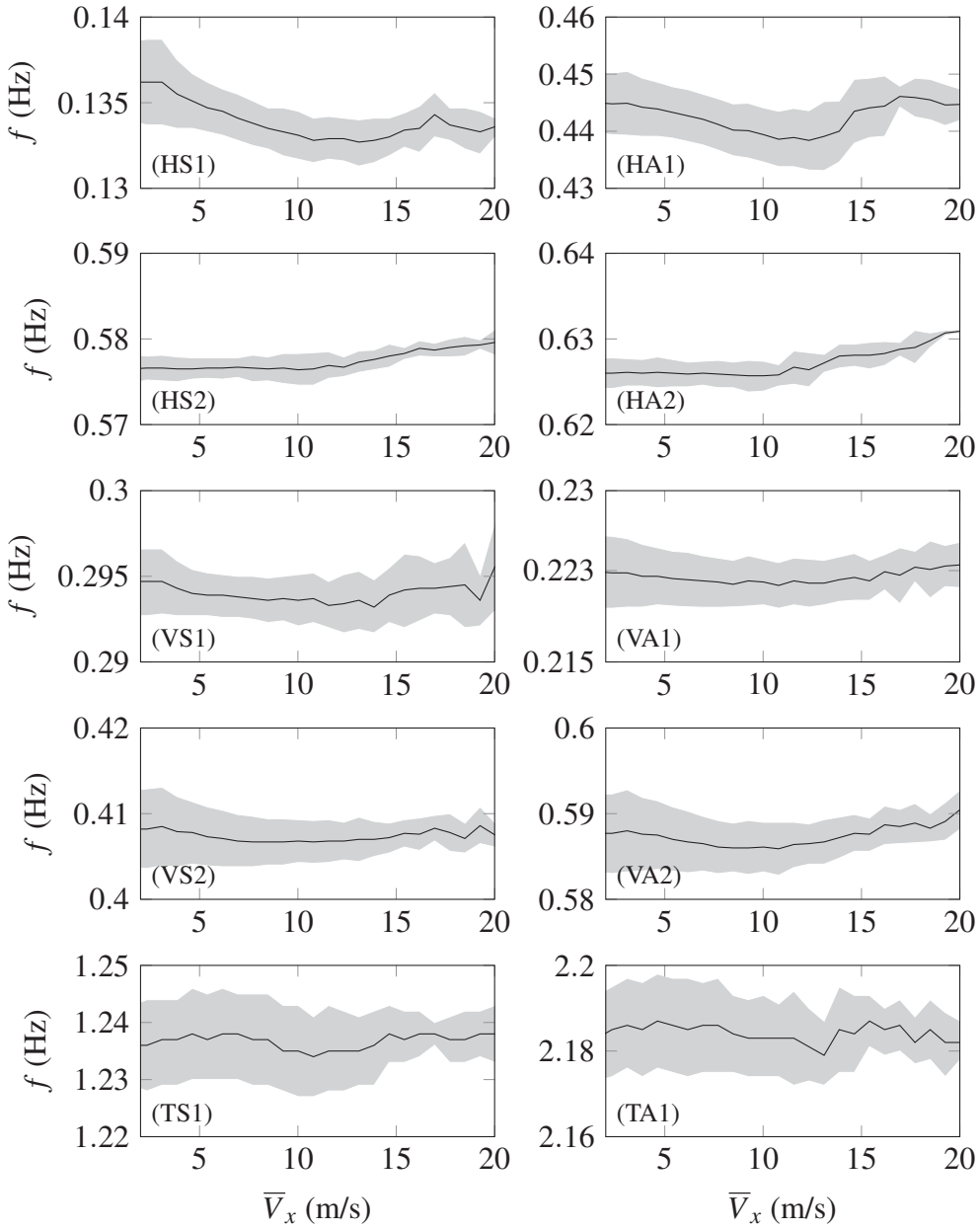

Figure 5.10 Evolution of the first four vertical eigen-frequencies with the mean wind velocity.

5.5.3 Modes shapes

The mode shapes identified using data from a single day (26/10/2014) are directly compared to those calculated with Alvsat and the SBM. The averaged mode shapes and their standard deviation, shown as error bars, are superimposed on Fig. 5.11. The standard deviation is however small enough so that the error bar is almost invisible, indicating that the mode shapes are identified with good accuracy.

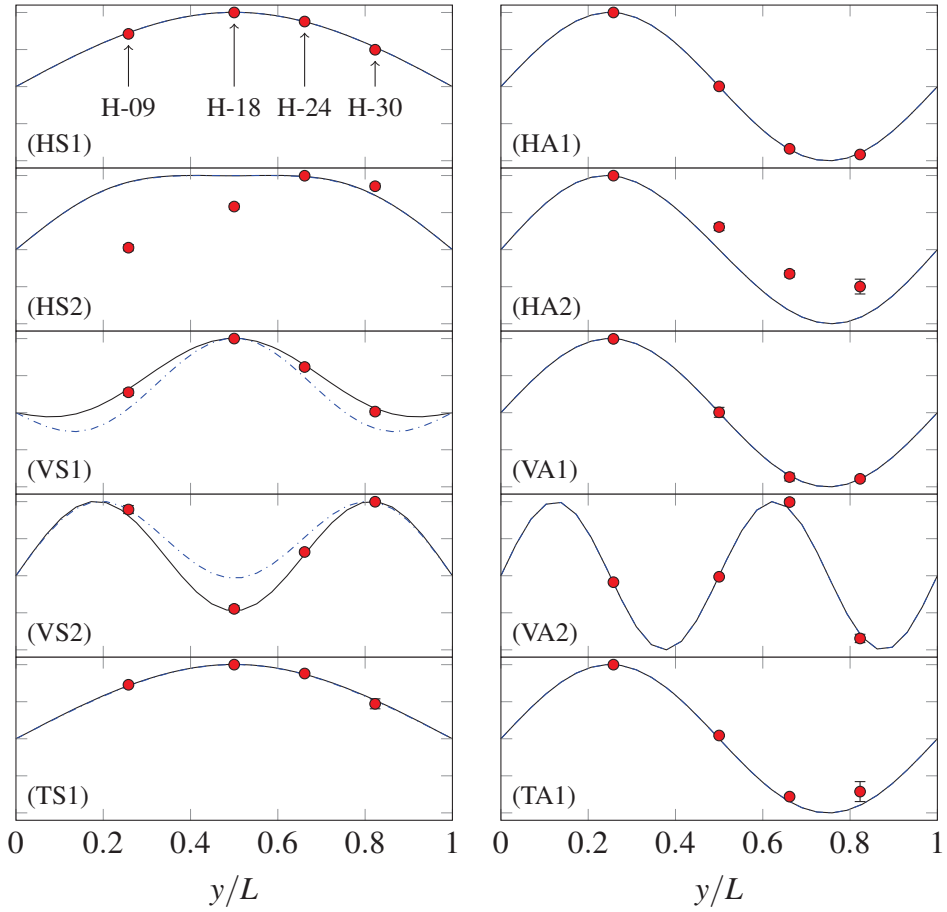

Figure 5.11 Normalized mode shapes identified for the first four lateral eigenfrequencies (measured: •; Alvsat model: ——; SBM: - - -).

A good agreement is observed between the measured mode shapes and those computed with the Alvsat model. The SBM appears to miscalculate the mode shapes VS1 and VS2. The Alvsat modal and the SBM provide however identical torsional and lateral mode shapes. The measured lateral mode shapes HS2 and HA2 show larger discrepancies from the theoretical ones. The FE models used by e.g. Steigen (2011) or Tveiten (2012) show that these discrepancies are due to the fact the software Alvsat and the SBM do not account for the asymmetry of the bridge geometry, e.g. in terms of different hanger lengths in the Northern and Southern span.

5.5.4 Modal damping ratios

The estimation of the modal damping ratios is one of the most crucial step in studying accurately the buffeting response of a suspension bridge. Unfortunately, such studies are a rarity in full scale. In general, the aerodynamic damping ratios are obtained with a large dispersion in full-scale (Brownjohn et al., 1987; Siringoringo and Fujino, 2008). This calls for a statistical approach, which is hardly documented in the literature, as the amount of available data is usually low. In this subsection, the total damping is considered for various wind conditions and for a considerable amount of samples. Similarly to subsection 5.5.2, the averaged damping ratios are presented together with a shaded area representing the standard deviation, and compared to estimates based on the quasi-steady theory.

Assuming stationary wind conditions, no traffic induced vibrations and no significant temperature effects on the bridge modal parameters, the quasi-steady theory predicts a linear dependency of the modal damping ratios on the wind velocity. If samples detected as non-stationary by using the reverse arrangement test (Bendat and Piersol, 2011) or characterized by a turbulence intensity larger than 30% are disregarded, then the shaded area representing the dispersion of the modal damping ratios becomes narrower. However, this

censuring of the data has minimal effect on the overall evolution of the modal damping ratios.

In general, wind-structure interaction including the aerodynamic damping is expected to be quasi-steady at high reduced velocities (Bogunović Jakobsen, 1995; Øiseth et al., 2010). For the vertical and torsional response, a non-linear dependency of the aerodynamic damping on the mean wind velocity is expected in the present case since the reduced velocity may not be large enough to fulfil this assumption. Another source of non-linearity may also be a change of structural and aerodynamic damping with the vibration amplitude.

There have been relatively few studies dealing with this subject in full-scale. A slightly non-linear evolution of the total damping ratios was observed by Macdonald and Daniell (2005) for a cable-stayed bridge with a main span almost equal to the one of the Lysefjord Bridge. Traffic induced vibrations should have a limited impact on the bridge modal parameters at wind velocity above 12 $\mathrm{m\,s^{-1}}$ (Cheynet et al., 2015b; Macdonald, 2003), but that might not be the case for lower wind velocities.

Influence of mean wind velocity

The evolution of the measured modal damping ratios with the wind velocity is compared to the predictions from the quasi-steady theory in Fig. 5.12. The dispersion of the identified damping ratio for the mode HS1 is particularity large and a systematic discrepancy is visible for all wind velocities, which suggests an erroneous estimation of the structural damping ratio (1.3% instead of the assumed value of 0.5%). Both the large dispersion and the discrepancy between the estimated and measured structural damping ratios may be due to the sample duration, fixed to 10 min, which is relatively short compared to the eigen period of HS1 (7 s). A more accurate estimation of the damping ratios may be obtained by increasing the record duration. However, a duration too large may lead to a misinterpretation of the velocity-dependency of the damping ratio due to the increasing occurrence of non-stationary wind records.

This issue needs to be further investigated, but is outside the scope of the present chapter. If the measured value of the structural damping ratio is correct, then the value of 0.5% structural damping assumed for HS1 is too low, leading to a computed response that is too large. A similar conclusion applies for HA1, whereas for HS2 and HA2, the modal damping ratios hardly change with the wind velocity and remains in agreement with the fixed value of 0.5% for the structural damping ratio. More generally, the evolution of the total damping ratios for the lateral modes is linear and tends to agree well with the theoretical predictions.

For the vertical modes VS1, VA1 and VS2, the measured structural damping ratios are in the overall agreement with the predicted ones. However the total modal damping ratios measured do not increase linearly with the mean wind velocity and are lower than the predicted ones. This may lead to a computed response lower than expected. The damping for the fourth mode shows a lower dependency with the wind velocity than predicted. In general, there is a good agreement between the measured and predicted values. For the torsional bridge motion, the value of 0.5% for the structural modal damping ratios corresponding to TS1 and TA1 appear to be realistic. The variation of the total damping with the mean wind velocity agrees rather well with the predicted values. This indicates that the value $k_\theta = 0.25$ for the torsional aerodynamic damping was a pertinent choice.

The increase of the damping ratios with the mean wind velocity is particularly notable for the vertical motion. For a mean wind velocity of 20 $\mathrm{m\,s^{-1}}$, the measured modal damping ratio is around 1% for TS1, 0.8% for TA1 and 0.8% for HA1, whereas for VA1 and VS1 it is equal to 2.5% and 1.9% respectively. This justifies the need to properly evaluate the aerodynamic damping for the vertical motion. Incorrect estimation of the aerodynamic damping may therefore lead to a large error of the computed vertical bridge displacement.

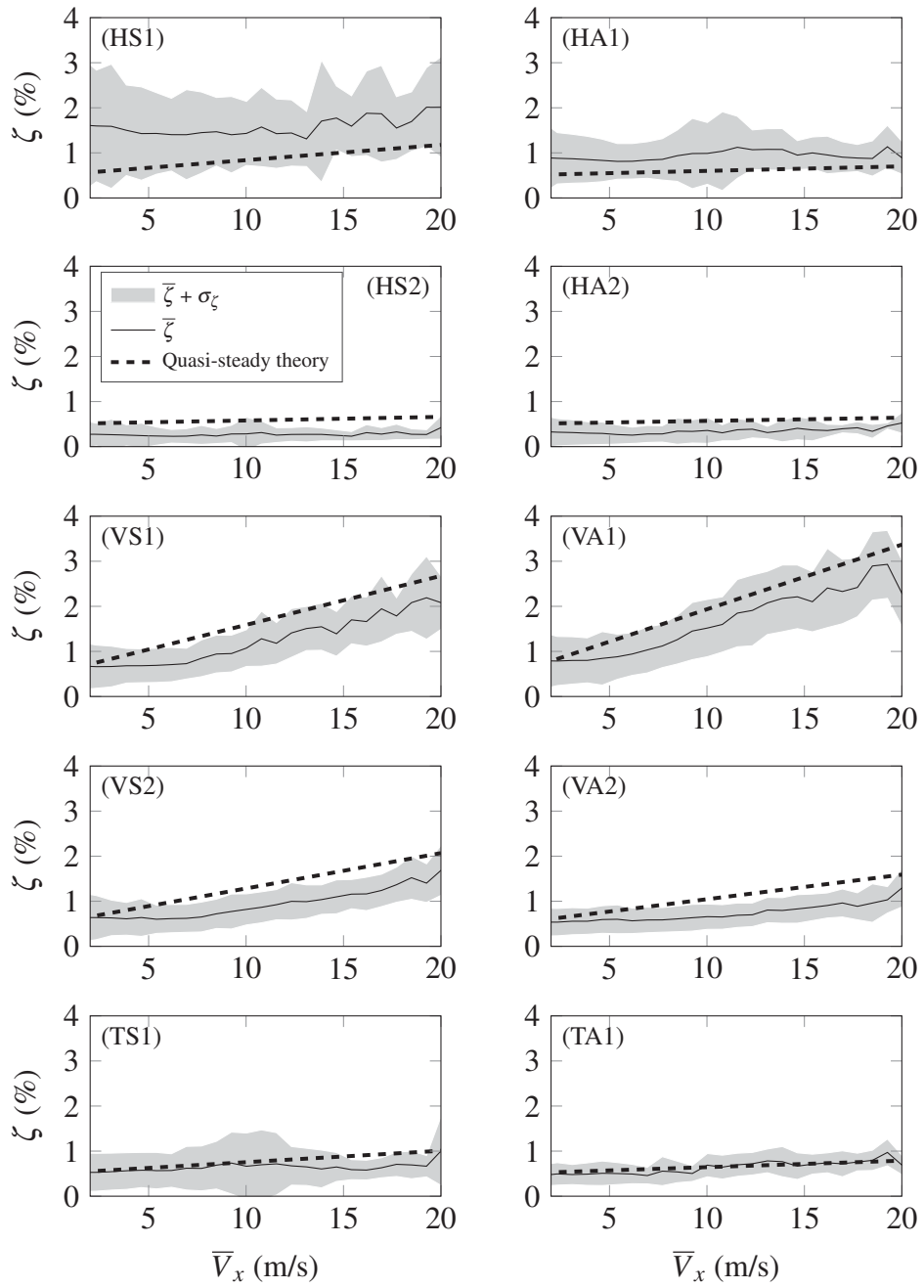

Figure 5.12 Total modal damping ratios (structural + aerodynamic) expressed as a function of the mean wind velocity for the first four lateral and vertical modes and the first two torsional modes.

Influence of temperature fluctuations

To the author's knowledge, temperature effects on the modal damping ratios remains unexplored and are therefore briefly investigated in the following. The variation of the modal damping ratios with the temperature for the first four lateral and vertical modes and the first two torsional modes is displayed in Fig. 5.13.

As expected, the damping ratios for HS1, HS2, HA2, VS1, VA1 and TA1 fluctuate little with the temperature. For a given temperature, multiple wind velocities are recorded. Because the total modal damping ratios increase with the wind velocity, a large variety of total modal damping ratios is recorded for a given temperature. Consequently, a large dispersion is expected when the modal damping ratios are expressed as a function of the temperature alone. On Fig. 5.13, VS1 and VA1 have an averaged modal damping ratios of about 0.75% and 1% respectively and are characterized by a considerable spreading. This is not surprising given that the modal damping ratios associated with VS1 and VA1 are highly affected by the wind velocity (Fig. 5.12). The distribution of the wind velocity is not uniform and the majority of wind records are characterized by a wind velocity lower than 8 $\mathrm{m\,s^{-1}}$. For this reason, the high values of the modal damping ratios observed in Fig. 5.12 for VS1 and VA1 have a limited influence on the averaged value of the modal damping ratios displayed in Fig. 5.13.

More surprising is the decrease of the damping ratios of VS2, VA2 and TS1 for increasing temperatures. The average damping ratio for the mode VS2 decreases by 0.3% when the temperature increases from 5 °C to 20 °C. However, this may be explained by the higher probability of strong wind conditions at low temperatures (Winter time). In other words, temperature and wind velocity cannot be considered as independent variables in the data set used. However, this dependency does not explain the decrease of TS1 from 0.7% at 5 °C at 0.3% at 20 °C. The dependency of the damping ratio of TS1 with the wind velocity is indeed rather weak (Fig. 5.12). To improve

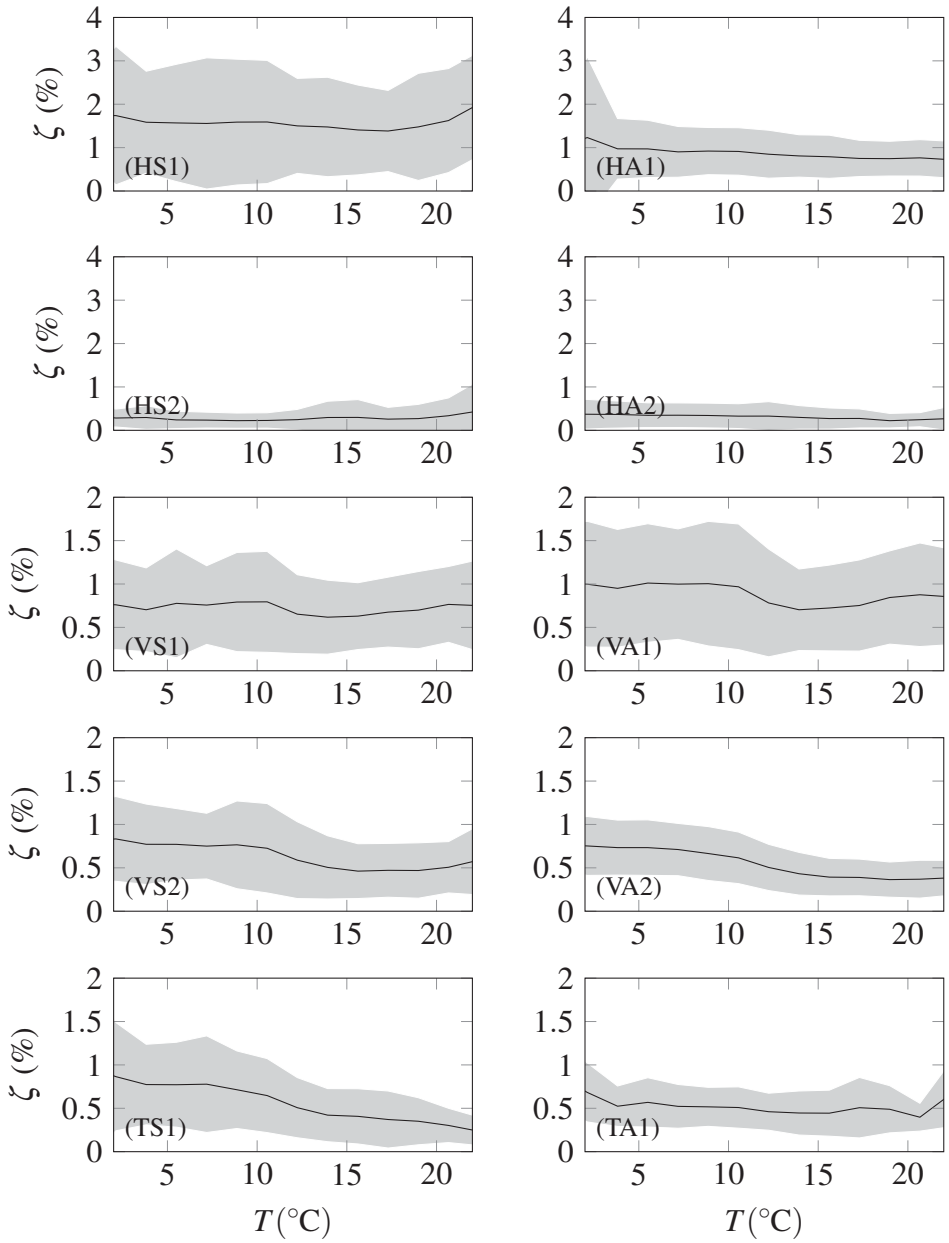

Figure 5.13 Modal damping ratios expressed as a function of the temperature for the first four lateral and vertical modes and the first two torsional modes.

the reliability of these results, at least one year of temperature, velocity and acceleration data is required.

5.5.5 Summary

The focus of this chapter was on modal parameter identification of a full-scale suspension bridge by the use of an automated SSI-COV procedure. It complements and expands the works of Magalhães et al. (2009) and Brownjohn et al. (2010) by using several months of continuous acceleration records. Environmental effects were observed with a level of details that is hardly available in the literature. In particular, the daily fluctuations of eigen-frequencies and seasonal effects, typical for Northern Europe, were remarkably well captured as was the possible temperature-dependency of the modal damping ratios. A relatively large amount of acceleration data was accumulated, so that a statistical description of the influence of the mean wind velocity on the modal damping ratios could be achieved. Application of OMA using the automated SSI-COV method on other suspension bridge in Norway, such as the Hardanger Bridge (Appendix B) may provide a better understanding of environmental loads on the modal parameters of long-span suspension bridges.

The relatively good agreement between the computed modal parameters and the measured ones is encouraging to proceed further with the investigation of the buffeting theory from full-scale measurement data. The overall good agreement between the quasi-steady theory and the velocity-dependency of the measured damping ratios is also one of the key results from this chapter. This modal analysis also documented the non-linearity of the modal damping ratios and a possible non-negligible role of temperature effects on the bridge response. Further analysis will consider at least one year of full-scale measurements, and a more severe segregations of wind samples characterized by unusually high turbulence intensity or non-stationary wind fluctuations.

Chapter 6

Structural response

6.1 Introduction

The displacement response of the Lysefjord Bridge is studied in details by considering two days of continuous wind and acceleration records (07/10/2014 and 26/10/2014). These two days are assumed to represent well the two dominant wind conditions observed on the bridge site during stormy weather. On 07/10/2014, the flow was coming from N-NE, with a mean wind direction of 22° and a standard deviation of almost 9° (left panel of Fig. 6.1). On 26/10/2014 the dominant wind direction was S-SW with a mean value of 211° and a standard deviation of 6° (right panel of Fig. 6.1). The two wind conditions had different characteristics. The wind-induced bridge response was therefore studied separately for the two main wind directions.

The differences between the S-SW flow and N-NE flow are illustrated on Fig. 6.2 where 10 min of wind record with a mean wind velocity of 12 $\mathrm{m\,s^{-1}}$ are selected for both the S-SW and N-NE flow. The along-wind and vertical wind components are superimposed to better underline the different features of the flow. For the along-wind component, the turbulence intensity is 14% and 42% for the flow from S-SW and N-NE respectively. Although the N-NE wind data displayed in Fig. 6.2 challenges the assumption of flow stationarity,

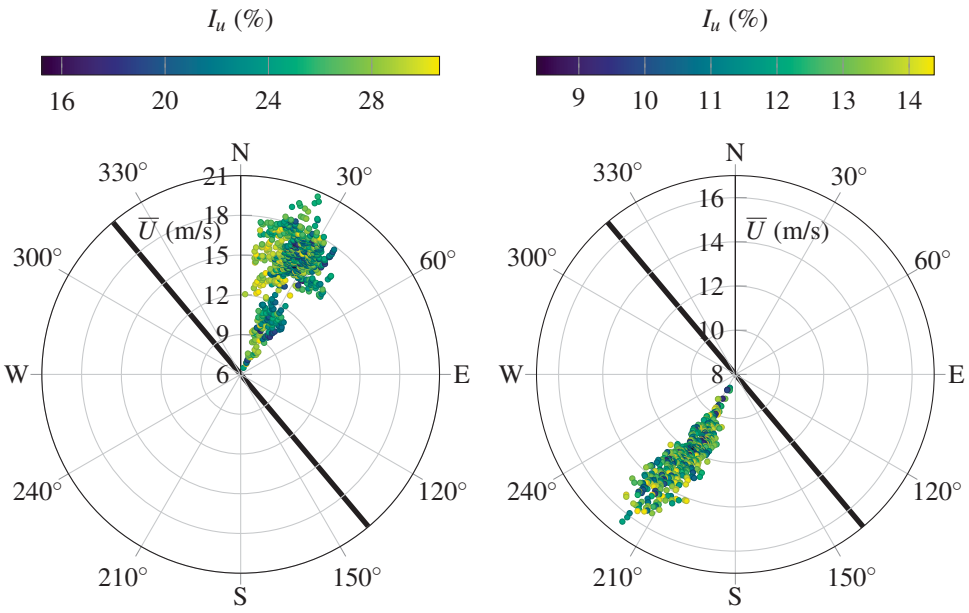

Figure 6.1 Two dominant wind conditions usually observed at Lysefjord Bridge: 07/10/2014 to the left and 26/10/2014 to the right. The thick black line indicates the bridge orientation. Each dot represents 10 min of averaged wind data.

it does not display any particular linear trend. This flow does not fit with the non-stationary wind model from e.g Chen et al. (2007) which assume the existence of a slowly "time-varying" mean velocity. On the contrary, the wind velocity shows rapid increases and decreases in Fig. 6.2, especially near 240 s and 570 s. These large fluctuations are, however, too short and too close to each other to be considered as "ramp-up events" which are commonly observed during thunderstorms (Lombardo et al., 2014).

For the vertical wind component, the turbulence intensity is equal to 16% and 7% for the flow from N-NE and S-SW respectively. Although the turbulence intensity for the N-NE flow is particularly large, the ratio I_w/I_u is lower than 0.4, which is lower than usually observed (Solari and Piccardo,

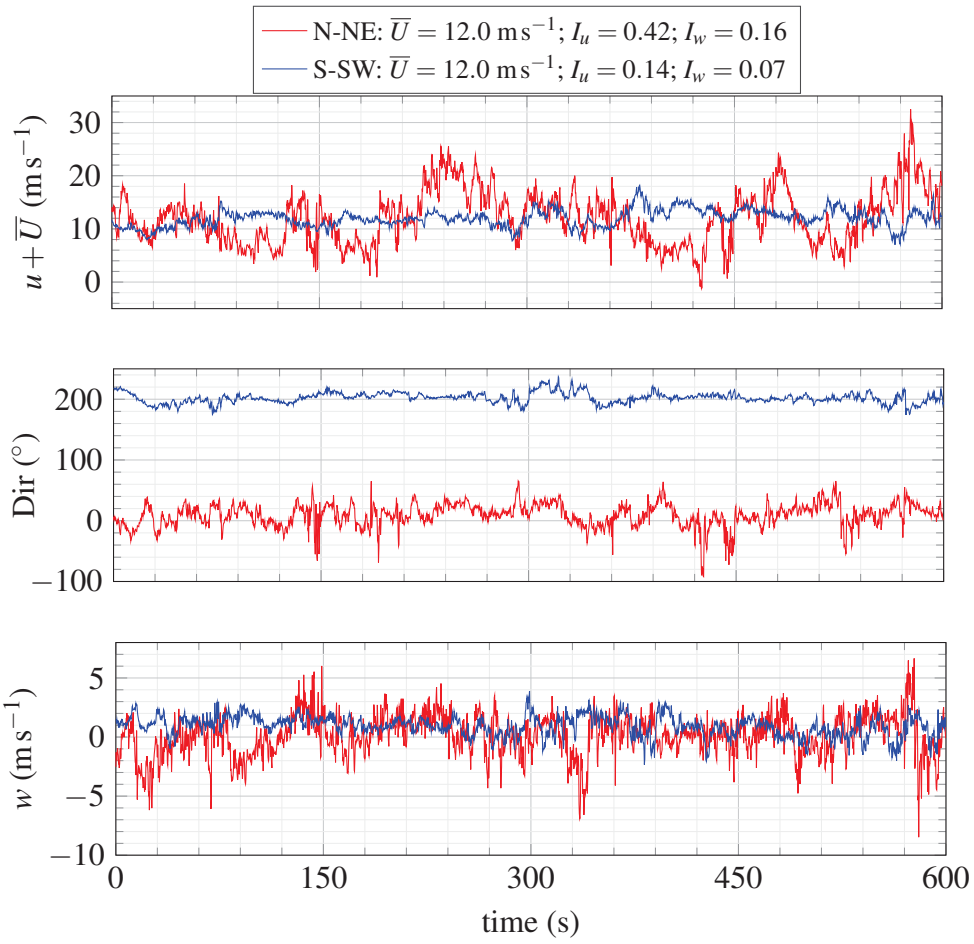

Figure 6.2 Wind velocity and direction recorded on 26/10/2014 from 09:50 (S-SW wind) and on 07/10/2014 from 07:30 (N-NE wind).

2001). In the two examples displayed in Fig. 6.2, the wind direction was relatively stable, but the flow from N-NE was characterized by a mean wind direction of 9°. This direction corresponds to a flow descending from the mountains, over the hilly landscape on the North side of the bridge.

In this chapter, the flow properties are described first. Then the bridge model is introduced, followed by a sensitivity analysis to identify the relative importance of key parameters influencing the bridge response. Finally,

the buffeting response is studied based on an empirical approach and by a computational model.

6.2 Flow statistics

The statistics of the wind turbulence are analysed in the bridge-based coordinate system and used directly to estimate the buffeting load. This is equivalent to applying the "cosine rule" to account for the yaw angle effect, but more straightforward. The wind spectra and turbulence intensities are also investigated in the wind-based coordinate system to provide data comparable to those available in the literature.

6.2.1 Single-point statistics

The flow coming from the inside of the fjord (N-NE exposure) was characterized by a large turbulence intensity. This may be due to a possible partial flow descending from the mountains and/or a variable wind direction. The average ratio between I_w and I_u is equal to 0.41 and 0.57 for the N-NE and S-SW wind respectively, while a value of 0.55 is suggested by Holmes (2007). The low ratio observed in the case of the flow from N-NE is uncommon considering previous studies (Solari and Piccardo, 2001). This may be due to complex topographic effects, the influence of the bridge deck on the measured vertical turbulence, or a combination of both.

One day of continuous wind monitoring provides 144 samples of 10 min duration. The wind spectra are calculated for the data from the anemometers at hangers 16, 18 and 20 in the wind-based coordinate system for every sample, and then normalized. For each component, an average normalized spectrum is calculated as the average of all 10 min spectra, and displayed as a

function of the wavenumber k, defined as:

$$k = \frac{2\pi f}{\overline{U}} \tag{6.1}$$

If the wind component V_x is used instead, then the modified wavenumber is used:

$$k_x = \frac{2\pi f}{\overline{V}_x} \tag{6.2}$$

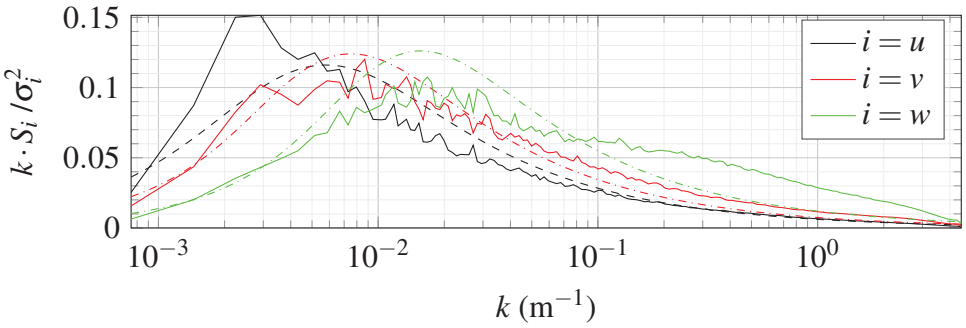

Figure 6.3 Average normalized wind spectra recorded on 07/10/2014 (N-NE wind).

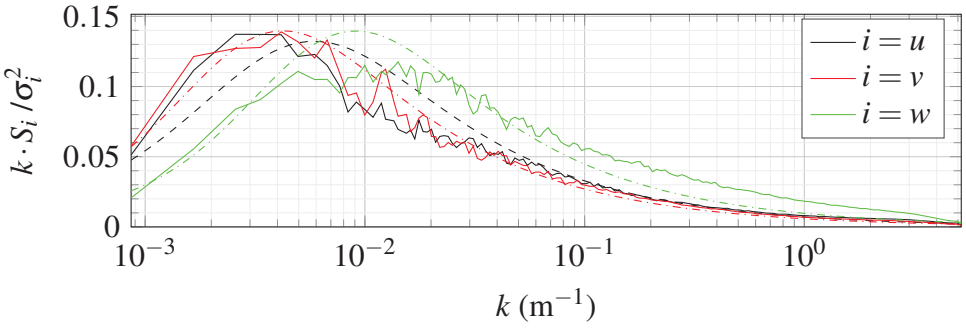

Figure 6.4 Average normalized wind spectra recorded on 26/10/2014 (S-SW wind).

The measured spectrum is then compared to the von Kármán spectrum (Morfiadakis et al., 1996), which requires the calculation of the along-wind turbulence length scales, the mean wind velocity and the turbulence intensities. In Figs. 6.3-6.4, the von Kármán spectrum is seen to agree reasonably well with the measured spectra for the along-wind and across-wind components, both for a wind from N-NE and S-SW, at least for the resonant response, i.e. for $k > 0.04$ m^{-1}. The measured vertical spectra is however larger than the computed one for $k > 0.1$ m^{-1}.

6.2.2 Two-point statistics

The co-coherence has been calculated in the bridge-based coordinate system, using Welch's spectral estimate (Welch, 1967), based on data of 10 min that are divided into two blocks of 5 min each, a Hamming Window and 50% overlapping, as suggested by Carter et al. (1973) and Saranyasoontorn et al. (2004). For a given frequency and a given spatial separation, the co-coherence is averaged for every sample recorded during one day, i.e. 144 samples. The coefficients for the co-coherence function used in Eq. 2.16 are calculated using curve fitting techniques for the along-span distances ranging from 24 m to 168 m. The coefficients evaluated during the least-square fitting procedure, by referring to the bridge-based coordinate system, are presented in Table

Table 6.1 Decay coefficients measured on 26/10/2014 (S-SW flow) and 07/10/2014 (N-NE flow) for lateral separations along the span.

		Decay coefficients			
Exposure	component	c_1	c_2	c_3	c_4
N-NE	v_x	5.0	0.07	1.1	3.3
	w	4.7	0.08	1.2	2.0
S-SW	v_x	6.5	0.02	0.9	6.7
	w	7.9	0.1	1.1	5.4

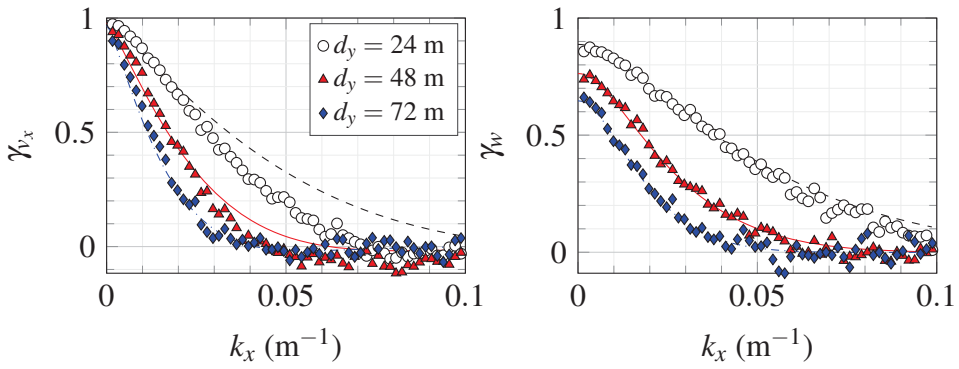

Figure 6.5 Measured (scatter plot) and fitted co-coherence (solid and dashed lines) for the v_x- and w-components, based on all wind data recorded on 07/10/2014 (N-NE exposure), with $\overline{V}_x = 12.6$ m s^{-1} for the whole day.

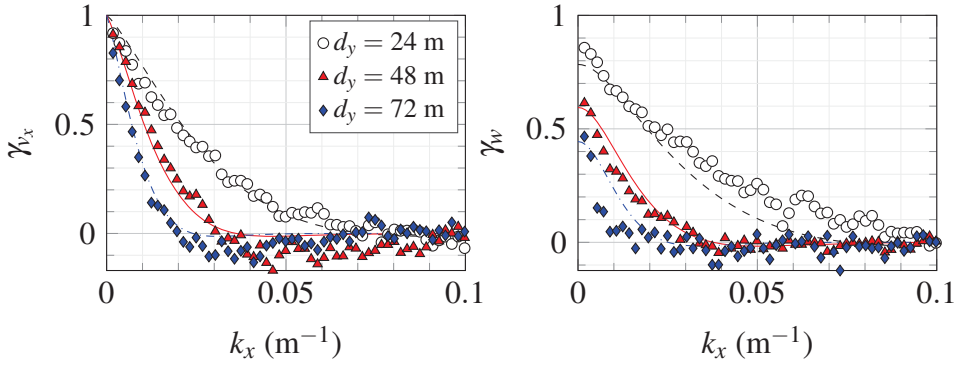

Figure 6.6 Measured (scatter plot) and fitted co-coherence (solid and dashed lines) for the v_x- and w-components, based on all wind data recorded on 26/10/2014 (S-SW exposure), with $\overline{V}_x = 11.8$ m s^{-1}.

6.1. The measured and fitted co-coherence are presented as a function of the modified wavenumber k which is expressed as a function of $\overline{V}_x$ instead of $\overline{U}$. The co-coherence is displayed for three different lateral separations on Fig. 6.5 and Fig. 6.6.

The overall surface-fitting process shows satisfying results, but some discrepancies are observed for the wind component V_x in the N-NE flow

above wavenumbers of $0.03\,\mathrm{m}^{-1}$. As highlighted by the coefficient c_1, the co-coherence is higher for a wind from N-NE than for a wind from S-SW. For small distances and wavenumbers above $0.02\ \mathrm{m}^{-1}$, the fitted co-coherence for the v_x-component of N-NE wind did not compare well with the measured co-coherence. The negative part of the co-coherence is taken into account but has little consequence on the overall shape of the fitted function. The values of the coefficients in Table 6.1 are used in section 6.4.2 and 6.4.3 for the computation of the buffeting response of the Lysefjord Bridge.

6.3 The computational bridge models

The structural response can be studied using three numerical models of increasing complexity:

1. "Empirical model": An empirical model can be obtained by expressing the root mean square (RMS) of the bridge acceleration or displacement response as a function of the wind velocity. Such models have been studied by e.g. Hay (1984) and Macdonald (2003, 2004) who observed that the RMS of the acceleration response and the mean wind velocity are connected by a power law.

2. "Simplified Bridge Model" (SBM): the SBM is based on the computation of the modal parameters of a suspension bridge using the mathematical model developed by e.g. Sigbjörnsson and Hjorth-Hansen (1981). They do not require FE software, which allows a fast computation time, and facilitates reproducibility of the results. However, the mode shapes and eigen frequencies produced are not always adequate.

3. Finite Element (FE) model: Such models are more accurate but require a dedicated software. In addition, the computation of the bridge response is more time consuming and the reproducibility of the results is

Table 6.2 Key structural parameters of the Lysefjord Bridge.

Structural parameters	Symbols	Value
Main span length (m)	L	446
Girder mass (kg/m)	m_g	5350
Main cables mass (kg/m)	m_c	408
Mass moment of inertia (girder + cables) (kg m^2/m)	I_θ	82430
Girder height (m)	D	2.76
Girder width (m)	B	12.3
Drag coefficient	C_D	1.0
Lift coefficient	C_L	0.1
Pitching moment	C_M	0.02
$\frac{\partial C_D}{\partial \alpha}$	C'_D	0.0
$\frac{\partial C_L}{\partial \alpha}$	C'_L	3.0
$\frac{\partial C_M}{\partial \alpha}$	C'_M	1.12

more difficult to obtain between different researchers, because of the uniqueness of the various details of each FE model.

In the present study, the empirical model is used for a preliminary analysis of the buffeting response of the Lysefjord Bridge. Results from this analysis are compared to those obtained by Hay (1984) and Macdonald (2004). The buffeting response of the Lysefjord Bridge is computed based on the mode shapes provided by the software Alvsat and the eigen frequencies estimated with the operational modal analysis presented in Chapter 5. Since no FE software is used, the bridge deck is modelled as an horizontal line. The deck dimensions, mechanical properties and its static aerodynamic coefficients are summarized in Table 6.2.

6.3.1 Background and resonant response

The wind-induced bridge response can be split into a resonant part and a background part. The background part corresponds to the frequency domain well below the first eigen frequency, whereas the resonant part includes the first eigen frequency and the higher modes. In the present study, the power spectral density (PSD) of the buffeting response is computed for the resonant part only since most accelerometers are not designed to measure accurately vibrations with frequencies below 0.1 Hz (Xu and Xia, 2011). The background part is usually negligible when the acceleration response is studied, but not longer if the displacement response is considered. If the measured response is not high-pass filtered, erroneous displacements are measured in the background frequency range. A high-pass Butterworth filter of order 8 with a cut-off frequency of 0.08 Hz was therefore applied to the displacement response of the Lysefjord Bridge. The cut-off frequency is chosen so that only the resonant response is considered, since the lowest eigen-frequency of the bridge is about 0.13 Hz.

6.3.2 Sensitivity analysis

The large amount of parameters involved in the computation of the buffeting response of a suspension bridge justifies the analysis of the relative influence of each parameter on the bridge response. A sensitivity analysis requires the computation of the buffeting response multiple times. For example, if the influence of ten parameters is evaluated by using ten different values for each of them, the buffeting response must be computed 100 times. For a numerical model based on the finite element method, such a repeated analysis would have a high computational cost. Here, the application of the simplified bridge model, constructed based on the reference parameters displayed in Table 6.2-6.3, reduces the computation time to a couple of minutes when using a personal computer (2.5 GHz processor with 8 GB of RAM).

Table 6.3 Initial values of the wind parameters used for the sensitivity analysis.

$\overline{U}$	L_u	L_w	I_u	C_u^y	C_u^y
10	100	25	0.1	3	3

For the sensitivity analysis, the structural modal damping ratio is taken equal to 0.2% for every mode. It is a low value compared to the design value of 0.5%, but is justified by the need to gradually increase the damping value for the sensitivity analysis, up to 0.8% in a consistent manner with the other parameters. Finally, the wind coherence is computed using the model proposed by Davenport (1961b).

The sensitivity analysis is conducted by using the RMS of the resonant bridge displacement response computed for frequencies above 0.08 Hz. The relative difference (expressed in percent) between the reference bridge response and the one computed after modification of one of the parameters is denoted $\hat{\sigma}_i$, where $i = \{r_x, r_z, r_\theta\}$ refers to the bridge lateral, vertical and torsional response.

Every parameter is kept constant except one that is progressively increased by using a multiplicative coefficient denoted c ranging from 1 to 1.3, except for the modal damping ratios where c ranges from 1 to 3. When the maximal value of c is reached, a new parameter is selected as the former one retrieves its initial value. Results from the sensitivity analysis are presented in Fig. 6.7, where the normalized RMS of the bridge displacement is expressed as a function of c.

From Fig. 6.7, several remarkable observations are done:

- As expected, the bridge response is most sensitive to the mean wind velocity and the turbulence intensity. If the measured flow is disturbed by the bridge deck or the main cables, large discrepancies between the computed and measured response are expected.

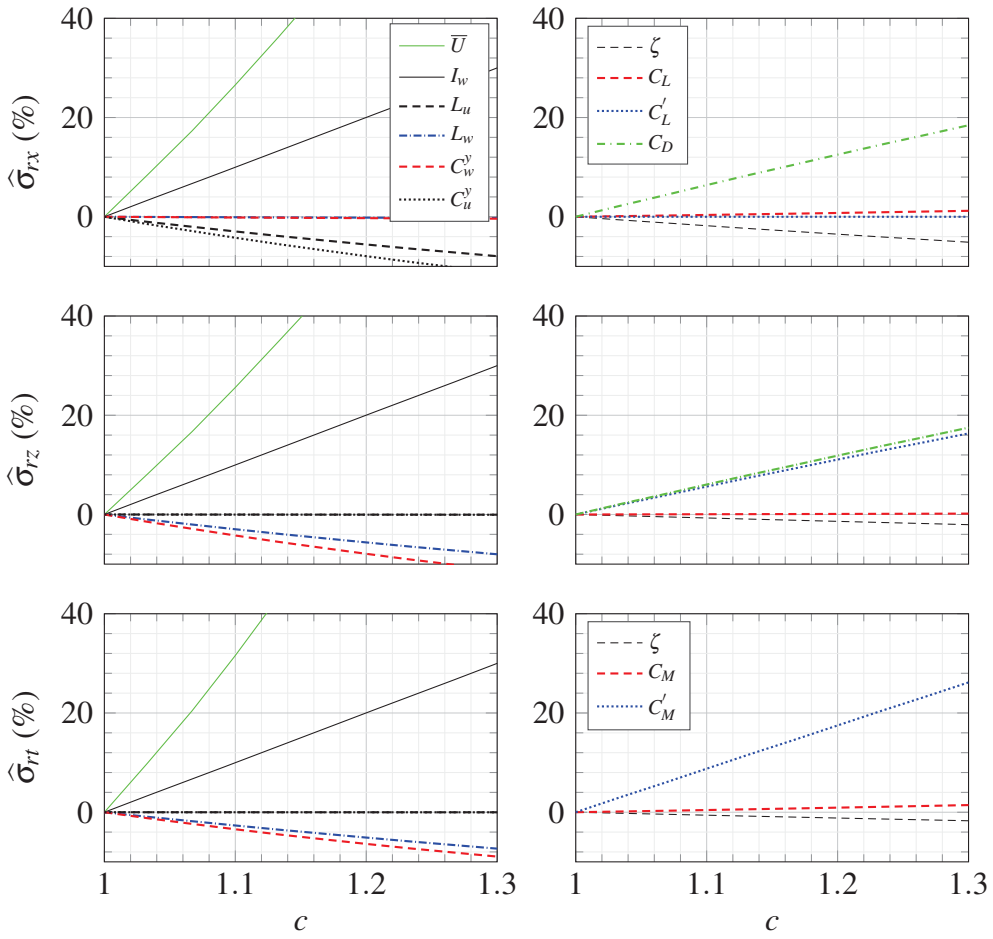

Figure 6.7 Sensitivity of the computed bridge response on different parameters, for the lateral (top), vertical (middle) and torsional motion (bottom).

- The influence of L_u and C_u^y on the vertical and torsional response is negligible. Similarly, L_w and C_w^y do not have any significant role on the lateral bridge response. This justifies the simplified expression of the matrix of linearised dynamic buffeting load coefficients that is occasionally found in the literature, e.g. Bogunović Jakobsen (1995, subsection 2.3.4).

- The decay coefficients C_u^y and C_w^y are the third most significant wind parameters on the lateral and vertical bridge response respectively. For example $\widehat{\sigma}_{r_z}$ decreases by 10% when C_w^y increases by 30%.

- The measure of L_u is highly sensitive to the wind conditions. Therefore, overestimation up to 100% is not unusual in full scale. In Fig. 6.7, the computed lateral response is 8% lower if the value of L_u increases by 30%. This indicates that in the case of the Lysefjord Bridge, if the turbulence length scales are overestimated, then the computed lateral response can be considerably lower than the measured one. The same conclusion applies to the vertical and torsional motions. This is an unexpected result coming from the fact that the length scale in the present analysis influences only the wind spectra but not the span-wise coherence. For the spectrum used here, the value of the integral length scale governs the location of the spectral peak. An increase of the value

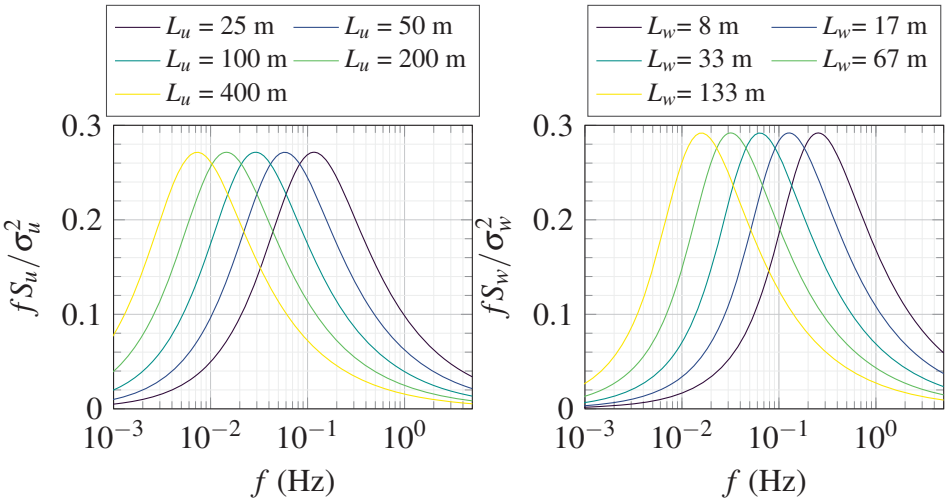

Figure 6.8 Relocation of the von Kármán spectral peak toward the low frequencies for increasing values of L_u and L_w. The spectra displayed here have been computed using $\overline{U} = 20\ \mathrm{m\,s^{-1}}$, $\sigma_u = 2\ \mathrm{m\,s^{-1}}$, $\sigma_w = 1\ \mathrm{m\,s^{-1}}$, which are chosen for illustrative purpose only.

of L_u or L_w leads to a relocation of the spectral peak towards the low frequency domain (Fig. 6.8). In the case of the Lysefjord Bridge, the relocation of the spectral peak is associated with a reduction of the dynamic wind load and an increase of the quasi-static one.

- Variations of C_L and C_M due to skew winds for example, have negligible consequences on the bridge response. Influence of the variations of C_D on the computed lateral and vertical bridge response are more significant. Decreasing values of C_D due to a large yaw angle are however possible, and would imply a reduced response.

- An error in the estimation of C'_L may also translate into an error of the buffeting response of the bridge. If the value of C'_L increases by 10% then the computed vertical bridge response is increased by 5%.

- If the structural modal damping ratio is estimated to be 0.8% instead of 0.2%, i.e. if $c = 4$, then the computed lateral displacement is only 13% lower. The same conclusion applies to the vertical and torsional response estimation where an overestimation by 30% of the structural damping ratios leads to a reduction of the displacement response by less than 4%. In general, large uncertainties are associated with the measured modal damping ratios, especially for low frequencies, but an overestimation of the modal damping ratio by 30% does not have as dramatic consequences for the vertical bridge response estimation. This is often because the aerodynamic damping dominates the total damping.

6.4 Results

6.4.1 Empirical approach

The analysis of the buffeting response is done here in a similar fashion as by Macdonald (2003), i.e. by expressing the RMS of the bridge acceleration response normalized by the turbulence intensity as a function of $\overline{V}_x$. Hay (1984) carried out a similar study with three short-span suspension bridges, i.e. for main span length less than 300 m. One of the goals of these studies was to estimate the empirical relationship between the bridge response and the wind velocity. A power law can be fitted to this normalized response relation, where the exponents a_x, a_z and a_θ are the relevant parameters to identify, whereas the scaling coefficients b_x, b_z and b_θ are less important:

$$\frac{\sigma_{\ddot{r}_x}}{I_u} = b_x \cdot \left(\overline{V}_x\right)^{a_x} \tag{6.3}$$

$$\frac{\sigma_{\ddot{z}_z}}{I_w} = b_z \cdot \left(\overline{V}_x\right)^{a_z} \tag{6.4}$$

$$\frac{\sigma_{\ddot{r}_\theta}}{I_w} = b_\theta \cdot \left(\overline{V}_x\right)^{a_\theta} \tag{6.5}$$

Hay (1984) found for example a value for a_z between 1.42 and 2.45 for the vertical bridge motion. He calculated the theoretical coefficient, and found a value of 2.83. According to Macdonald (2004), the value of a_z can actually fluctuate between 2.33 and 3.33. In addition, Macdonald (2004) carried out similar analysis for the torsional response and found a similar coefficient to the one estimated for the vertical response. Neither Macdonald (2004) nor Hay (1984) seems to have tried to determine a coefficient for the exponent a_x, describing the lateral bridge acceleration response.

In this section, a similar analysis is performed by using the data set recorded on the 07/10/2014 and 26/10/2014 (Fig. 6.9 and Table 6.4). For the S-SW exposure, the vertical and torsional responses agrees fairly well with the observations of Macdonald (2004) and Hay (1984). The coefficients found

Table 6.4 Empirical coefficients a_i, $i = \{x, z, \theta\}$ found for the acceleration bridge response (Fig. 6.9).

Day	a_x	a_z	a_θ
07/10/2014	1.80	1.32	1.63
26/10/2014	0.87	1.5	2.28

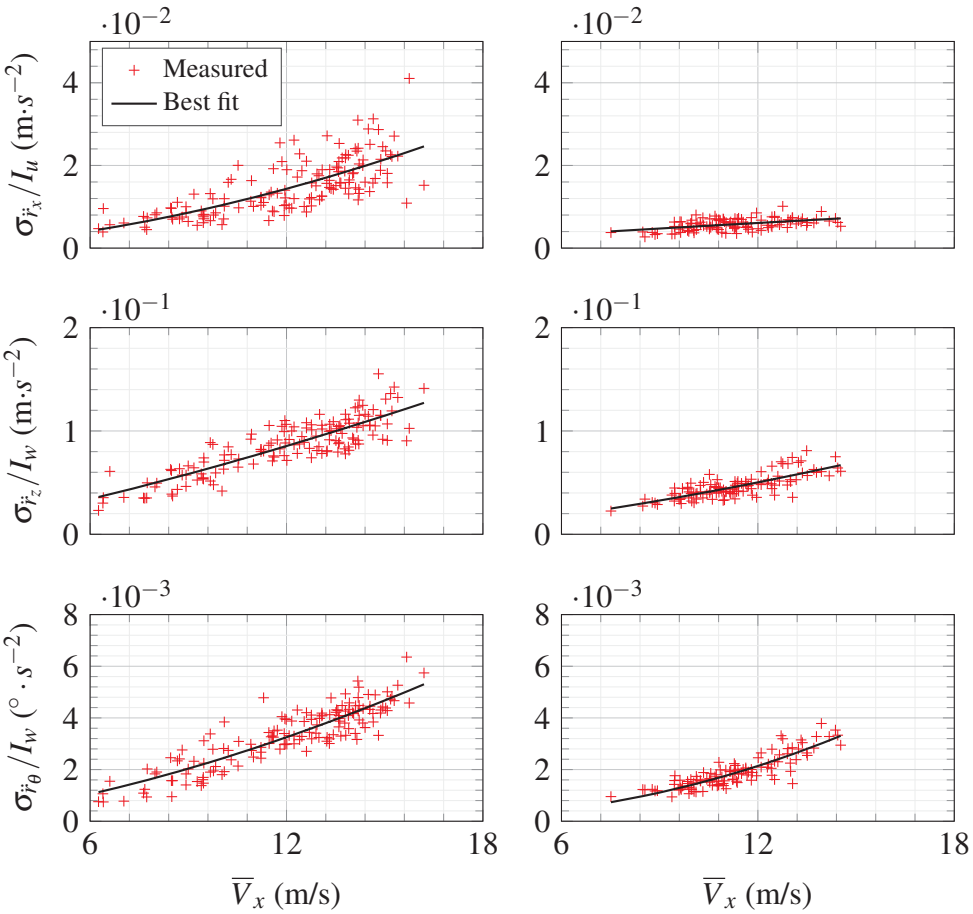

Figure 6.9 RMS of the bridge acceleration response near H-18, for the N-NE flow on 07/10/2014 (left panels) and the S-SW flow on 26/10/2014 (right panels).

for the N-NE wind case in Table 6.4 are lower than observed by Macdonald (2003, 2004) and Hay (1984). A much larger number of samples should be used for a more rigorous comparison. In addition, the method used to calculate the RMS of the displacement should be the same. In the present study, the RMS of the bridge response is based on 10 min of data. Hay used much shorter records, corresponding to 40 to 105 bridge oscillations, i.e. a couple of minutes, and Macdonald used 1 h of data. The scatter of the data is expected to be lower as the duration of the wind records increases. The lower values of the exponents found for the Lysefjord Bridge may also be due to the large yaw angles recorded. Macdonald (2003) considered only yaw angles close to 0°. On the other hand, Hay (1984) observed a reduction of the exponent when the component normal to the bridge was used instead of the along-wind component.

6.4.2 Buffeting response at the middle of the bridge-span for several wind records

The buffeting response is evaluated based on 144 samples of 10 min wind data and displacement response recorded on 26/10/2014 and on 07/10/2014 (Fig 6.10). The wind field is assumed homogeneous along the span, and therefore, the mean wind speed and wind spectra measured near the bridge centre at H-18 and H-20 are averaged. The standard deviation of the measured and computed bridge displacement are expressed as functions of the mean wind speed normal to the bridge deck. The RMS of the displacement has been normalized by the corresponding turbulence intensity to reduce the spreading of the data.

A good overall agreement is found between the measured and computed RMS values for the S-SW exposure. The computed RMS values underestimate the normalized RMS response for N-NE wind for the lateral and vertical motions. For a given wind velocity, the RMS of the bridge displacement is generally higher for a N-NE wind than for a S-SW wind.

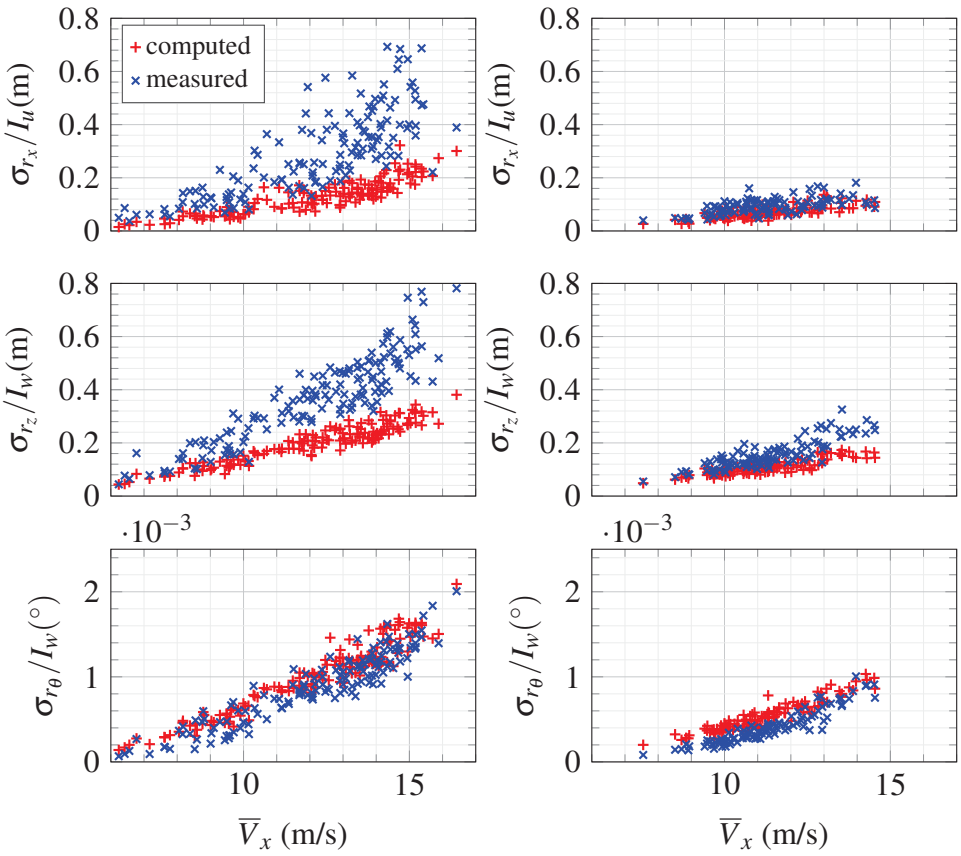

Figure 6.10 RMS of the bridge deck response for a N-NE wind on 07/10/2014 (left panels) and a S-SW wind on 26/10/2014 (right panels).

6.4.3 Bridge response for multiple positions along the span

To study the bridge response for multiple positions along the span, a single sample is selected out of all the before mentioned wind records. Its stationarity is assessed by using the RA test from Bendat and Piersol (2011), and its mean wind velocity is chosen as large as possible, so that the bridge response can be assumed to be mainly due to wind turbulence rather than traffic (Cheynet et al., 2015b). For the sake of simplicity, the co-coherence coefficients and cross-sectional aerodynamic admittance functions are the same as in

subsection 6.4.2. The measured wind spectra at the different hangers are directly used as input to compute the buffeting response of the bridge. For the wind conditions considered, mode coupling induced by the wind load is found to be insignificant for the structure, which is consistent with e.g. Jain et al. (1996a) and Thorbek and Hansen (1998), and is therefore neglected. The shear centre of the bridge cross-section is located 0.4 m below the neutral axis (Tveiten, 2012), which induces an additional structural coupling between the lateral and torsional motions of the bridge deck. However, it has small effects on the overall response and was therefore neglected. The properties of the wind sample selected for each wind exposure are displayed in Table 6.5.

The RMS of the computed bridge response at H-09, H-18, H-24 and H-30 is compared to the measured one on Fig. 6.11. The computed RMS of the bridge response agrees well with the one measured for the S-SW wind exposure but underestimates the one measured for the N-NE flow. The simulated response displays a symmetry with respect to the mid-span, which is not the case for the measured response. The bridge deck is indeed not symmetric: the Northern end and the middle part of the span are respectively 8 and 13 m higher than the Southern end. In addition, the wind field is assumed homogeneous along the deck, whereas the wind spectra may display non-

Table 6.5 Properties of the selected wind sample for the computation of the buffeting response on Fig. 6.11).

Exposure	NNE	SSW
$\overline{U}$ (m s^{-1})	17.7	13.9
$\overline{V}_x$ (m s^{-1})	14.7	12.9
I_u	0.26	0.15
I_v	0.21	0.15
I_w	0.11	0.08
L_u (m)	220	202
L_v (m)	83	120
L_w (m)	41	73

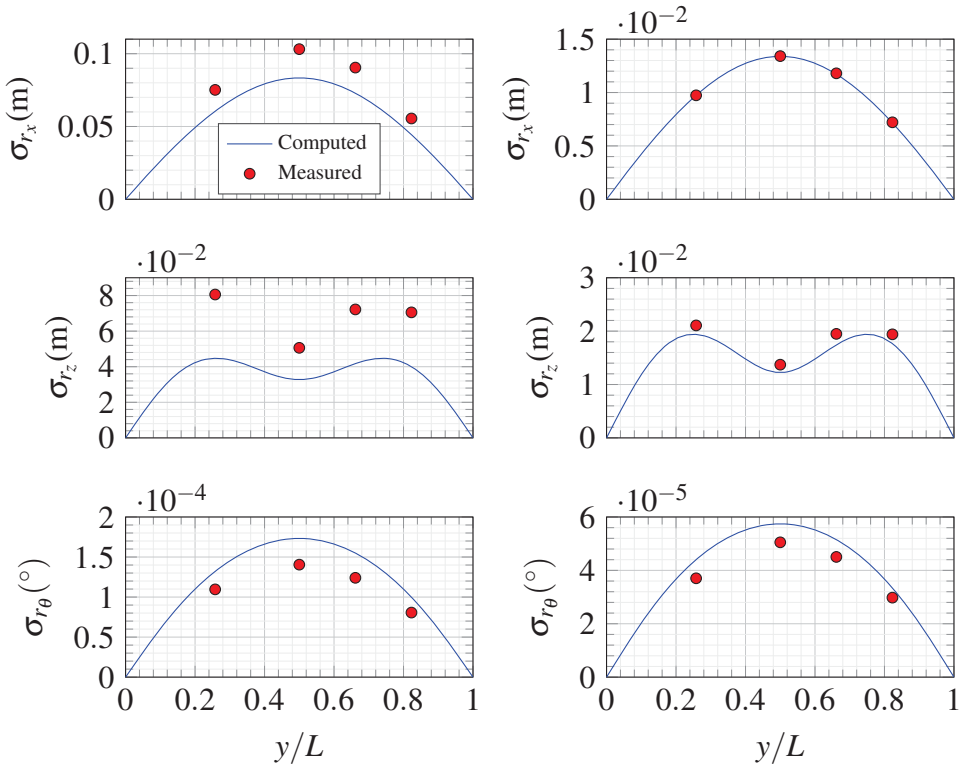

Figure 6.11 RMS of the deck response for a N-NE wind (left panels, on 07/10/2014 at 09:20) and a S-SW-wind (right panels, on 26/10/2014 at 08:50), see Table 6.5.

negligible variations along the span. The approach based on using averaged spectra to compute the wind load may therefore not be satisfactory. The assumption of homogeneity may be acceptable for a S-SW wind, but is unlikely to be valid for the N-NE wind direction, where a higher mean wind speed is often observed towards the North tower.

A more detailed description of the bridge response near H-24 is shown in Fig. 6.12. The main sources of discrepancies are the computed resonant peaks that sometimes disagree with the measured ones in terms of broadness and/or amplitude. Different possibilities for these discrepancies are investigated in the next chapter. Beyond the third or fourth mode for each direction, these

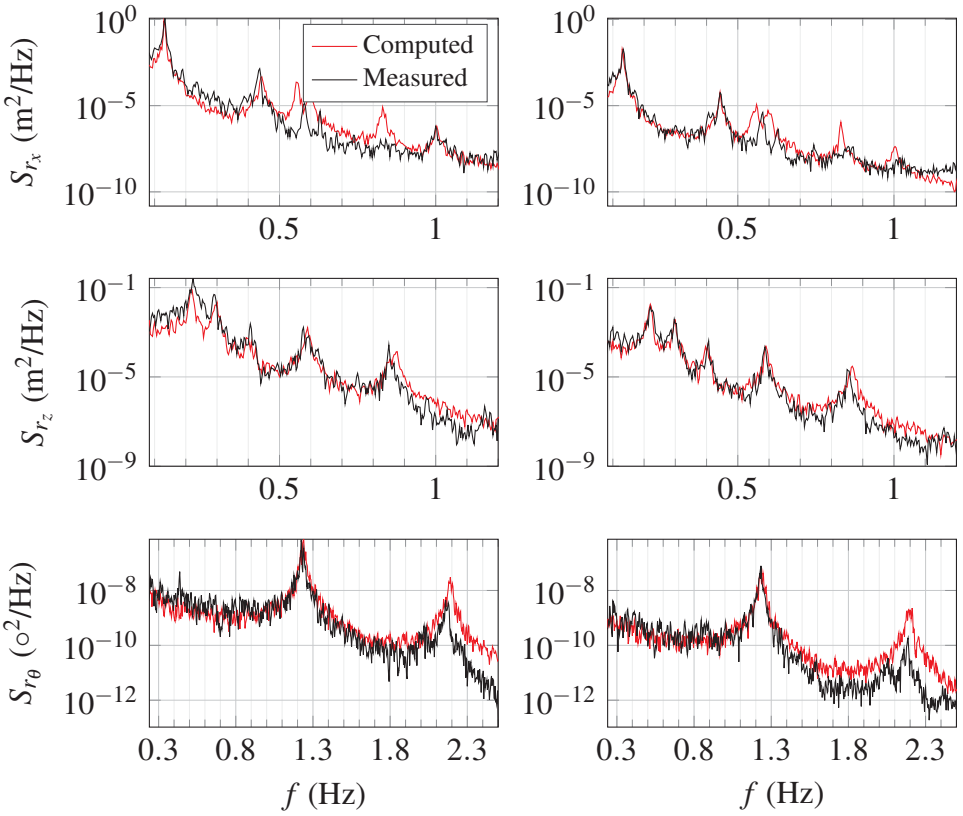

Figure 6.12 PSD the deck displacement response near H-24, for the N-NE wind case (left panels, on 07/10/2014 at 09:20) and a S-SW-wind case (right panels, on 26/10/2014 at 08:50) described in subsection 6.4.3.

discrepancies have a negligible influence on the overall response of the bridge. As seen in Fig. 6.12, the resonant torsional response of the bridge at mid-span is governed by the mode TS1 only. The overestimation of the computed spectral response near the mode TA1 is likely due to the choice of the cross-sectional aerodynamic admittance function that did not fit well with the one obtained from the recorded data at frequencies larger than 1.8 Hz.

6.5 Summary

The present study compared the theoretically estimated buffeting response and the measured response of a long span bridge in a complex terrain. Two unique sets of 24-h of continuous data were used for this purpose. The first data set was made of wind records from a stable S-SW direction, with wind velocities ranging from 8 $\mathrm{m\,s^{-1}}$ to almost 17 $\mathrm{m\,s^{-1}}$. The second data set corresponded to flow from N-NE with velocities data ranging from 6 $\mathrm{m\,s^{-1}}$ to 21 $\mathrm{m\,s^{-1}}$. A large turbulence intensity for the N-NE wind was detected, suggesting a non-negligible influence of the topography on the flow. The different wind conditions observed showed that a separate response analyse for the two wind directions was desirable.

The analysis was carried out based on the information provided by the modal analysis conducted in Chapter 5. The buffeting response of the bridge deck was studied first at the middle of the span for multiple wind records, and then along the whole span for two particular wind records. To improve the response estimate based on the quasi-steady theory, the use of a cross-sectional aerodynamic admittance function for the torsional motion was found necessary. The Liepmann's approximation of the Sears' function was observed to be an applicable choice.

For a mean wind velocity normal to the deck between 13 $\mathrm{m\,s^{-1}}$ and 14 $\mathrm{m\,s^{-1}}$, the ratio between $(\sigma_{\dot{r}_x}/I_u)_{\mathrm{NNE}}$ and $(\sigma_{\dot{r}_x}/I_u)_{\mathrm{SSW}}$ was about 2.9 at mid-span. This ratio was about 1.7 and 1.5 for the vertical and torsional displacement responses. The main reasons of such discrepancies may be the influence of the topography on the turbulent wind properties and possible distortion of the observed flow by the bridge deck for N-NE flow direction, due to the fact that the anemometers are all installed on the West side of the bridge deck.

Chapter 7

Challenges in the buffeting response prediction

Chapter 6 has shown that the measured buffeting bridge response is in general larger for a flow from N-NE than from S-SW. This discrepancy could not be simply explained by the larger wind coherence and the larger turbulence intensity observed fro the N-NE exposure. The sources of discrepancies explored in this chapter are:

- The connection between the yaw angle, the topography and the bridge response.
- The possible disturbance of the recorded velocities by the bridge deck.
- The validity of the assumption of homogeneous flow.
- The role of modal coupling on the buffeting response.
- The non-stationarity of the wind fluctuations.
- The influence of the quadratic terms of the wind load on the total load.
- The role of traffic-induced vibrations on the measured RMS response.

7.1 Skew winds and the "cosine rule"

The effects of the wind directionality on structural response have been studied since the 80's as they may lead to unexpected large structural responses (Barnard, 1981; Diana et al., 1995). The most common approach to describe skew wind conditions is often called the "cosine rule". It is based on a decomposition of the horizontal wind field into a component normal to the bridge deck, and another parallel to it. Then, only the normal component is considered to estimate the horizontal wind load, whereas the vertical wind component remains unchanged. This method has been used previously by e.g. Kimura and Tanaka (1992); Scanlan (1993); Tanaka and Davenport (1982); Xie et al. (1991), and appears to apply well for low turbulence intensities and relatively small yaw angles.

Although the cosine rule is simple, it does not take into account the variation of the aerodynamic coefficients with the yaw angle. This may lead to an inaccurate estimation of the buffeting response (Zhu et al., 2002). Deviations from the cosine rule have been previously observed in wind tunnel tests, in particular at large yaw angles (Diana et al., 1995; Zhu et al., 2007). To include the dependency of the aerodynamic coefficients with the yaw angle, Zhu et al. (2002) have used oblique cross sections in wind tunnel tests. This avoids the decomposition of the wind field into the across-deck and along-deck components. Zhu et al. (2007) observed the largest bridge deck response may be expected for yaw angles ranging from 5° to 30°. Full-scale measurements of bridge response to skew-wind have also been conducted to validate these predictions (Wang et al., 2011; Xu and Zhu, 2005). For a complex terrain characterized by sea-land transitions, steep hills, high cliffs or large buildings, any change in the wind direction is associated with modifications of the flow properties. Although this aspect has been little mentioned in previous studies, it may have considerable consequences on the connection between yaw angle and displacement response of wind-sensitive civil engineering structures.

In Fig. 7.3, the bridge deck acceleration data for an entire year (2015) is presented for different wind yaw angles, to further investigate possible validation of the cosine rule in full-scale. For the S-SW exposure, the response data is consistent with the cosine rule, as a clear decrease of the bridge

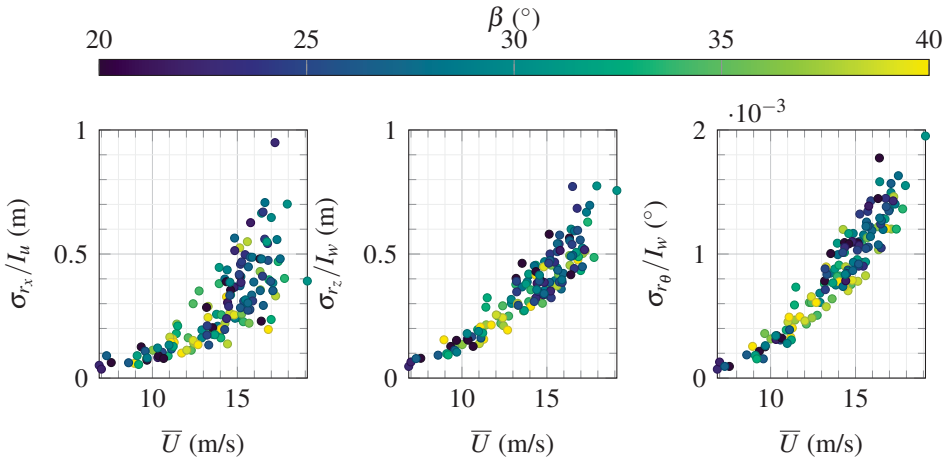

Figure 7.1 Evolution of the rms response of the Lysefjord Bridge on H-18 with the mean wind velocity and the yaw angle on 2014-10-07 (N-NE exposure).

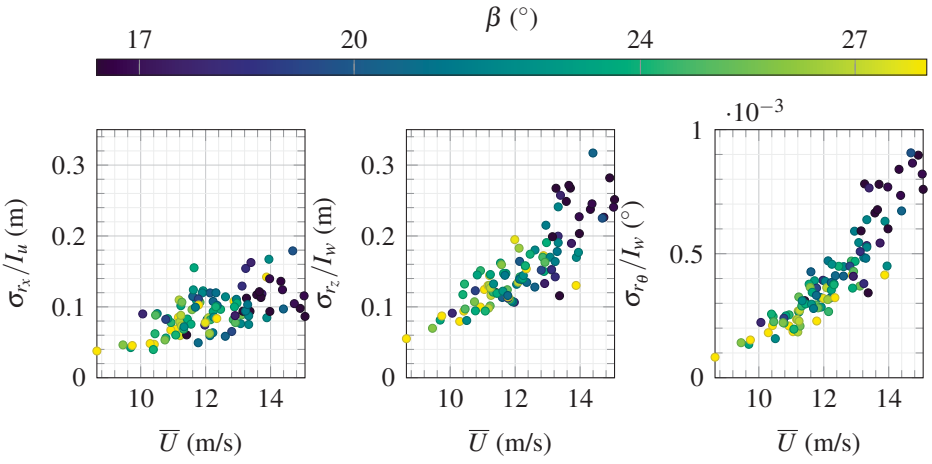

Figure 7.2 Evolution of the rms response of the Lysefjord Bridge on H-18 with the mean wind velocity and the yaw angle on 2014-10-26 (S-SW exposure).

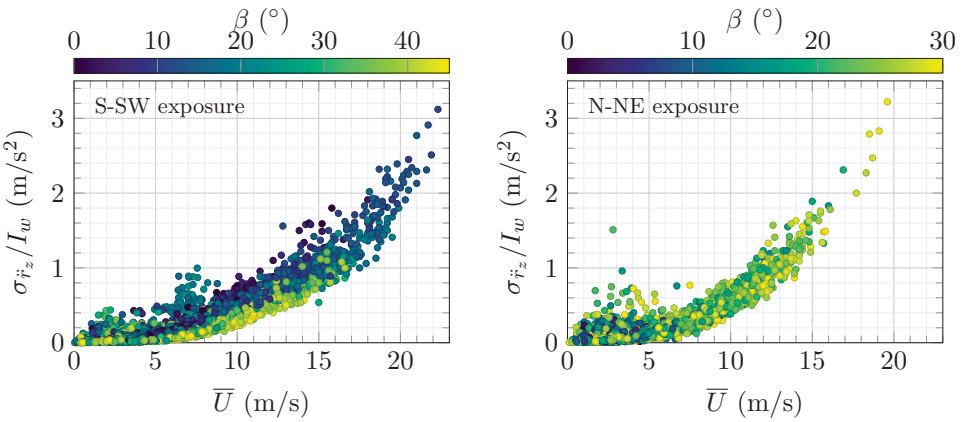

Figure 7.3 RMS of the vertical acceleration bridge response for the year 2015 for a yaw angle up to 45° for the S-SW exposure (8.8×10^3 samples) and 30° for the N-NE exposure (5.3×10^3 samples).

acceleration response is observed for increasing yaw angles. For the N-NE exposure, the relationship is not that obvious, partly because low yaw angles are associated with low wind speeds only. In general, the complex topography further to the N-NE of the bridge creates correspondingly complex flow characteristics and their dependency on the local wind direction.

If the yaw angle is between 0° and 25°, then the flow passes over the island of Bergsholmen, located 1 km on the East of the bridge reaches an altitude of 54 m, i.e. almost equal to the deck altitude at mid-span. If the yaw angle ranges from 25° to 40°, the wind flows between the Northern edge of the fjord and Bergsholmen. Under such conditions, it may be accelerated by the sudden narrowing of the fjord 1 km upstream of the bridge. Abrupt topographical changes may consequently modify both the wind profile and the spectral content of the wind. To better estimate the bridge response to skew winds, the computational model that is used in this thesis may also be improved using yaw-angle dependent aerodynamic coefficients as done previously by Zhu et al. (2002).

In conclusion, a somewhat larger bridge response at large yaw angle may be due to a more turbulent flow due to an increasing terrain roughness and cannot be predicted simply using the cosine rule. At least, the discrepancies between the measured response for the two wind directions studied cannot be explained solely by the influence of the yaw angle on the bridge response.

7.2 Influence of the bridge deck on the flow

The preliminary wind field analysis suggests that the bridge deck may affect the observed turbulence, especially for the N-NE flow. On 07/10/2001 (N-NE flow), the ratio I_w/I_u was lower than observed in most of previous studies (Solari, 1987). The possible influence of a bridge deck on the mean flow recorded by anemometers has been investigated by Kristensen and Jensen (1979) and Frandsen (2001a). Kristensen and Jensen (1979) used sonic anemometers mounted 3 m above the deck of the Sotra Bridge (truss-type girder), whereas Frandsen (2001a) used cup anemometers installed 2 m above the deck of the Great belt Bridge (closed-box girder with $H = 4$ m and $B = 31$ m). They did not find any significant influence of the deck on the mean flow, and assumed therefore that the measured flow was representative of the upstream one.

In the case of the Lysefjord Bridge, all the anemometers are installed on the West side of the deck. By using the two anemometers installed on the same hanger at 6 m (H-08b) and 10 m (H-08t) above the 2.76 m high girder, the influence on the bridge deck on the recorded flow was investigated. On 07/10/2014 (N-NE flow), the sonic on H-08t measured a mean wind velocity on average 2.3% lower than at H-08b, whereas on 26/10/2014 (S-SW flow) the difference was less than 1%. Although the velocity reduction is relatively small, this may indicate that the mean flow measured at 6 m above the deck is slightly speeded up when passing the bridge obstacle. Similarly, a slightly larger coherence for the N-NE may reflect an influence of the bridge deck on

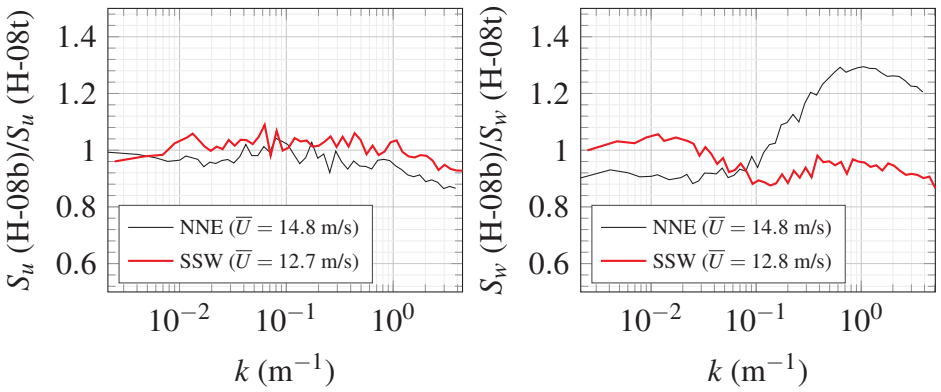

Figure 7.4 Bridge deck influence on the along-wind (left) and vertical wind component (right).

the recorded velocity data. Such details will be scrutinized in a future study, by introducing additional sonic anemometers on the East side of the bridge.

The ratio between the wind spectra recorded on H-08b over H-08t is in addition calculated and directly compared in Fig. 7.4. For both the flow from S-SW and N-NE, the along-wind component appears to be affected by the deck to a limited degree only. For the vertical wind component and if the flow comes from N-NE, this ratio increases up to 1.3 for $k = 1\text{m}^{-1}$. For $\overline{U} = 14.8$ m s^{-1}, $k = 0.1$ m^{-1} corresponds to $f = 0.24$ Hz. The amplified spectral content in the higher frequency range for the N-NE direction is likely due to the bridge signature turbulence recorded by the anemometers.

No particular relation was observed between the incidence angle and the bridge response. Larger incidence angles were observed for the wind from S-SW but may be due to the influence of the deck on the measured vertical flow. This may also explain the somewhat untraditional values measured for the ratio S_w/S_u and S_v/S_u in the inertial subrange which differ from the expected value of $4/3$.

7.3 The homogeneous flow assumption

The assumption of non-homogeneous flow can be introduced in the present computational model by defining a non-uniform mean wind profile along the span. This leads to a non-uniform wind spectrum and coherence, although the exponential decays for the coherence can remain unchanged in a first approximation. The matrix of buffeting load, the aerodynamic damping and stiffness are also affected by the non-uniformity. When the wind load is calculated in the modal base, the non-uniformity of the load is "weighted" by the mode shapes during the integration process corresponding to the transformation of the wind load from the physical base to the modal base.

To the author's knowledge, the buffeting response of a suspension bridge associated with a horizontal non-uniform mean wind velocity profile has not been studied before. Prior to the evaluation the non-uniformity of the mean flow using wind data in full-scale, a purely arbitrary non-uniform profile is studied. It is modelled by considering a Gaussian function:

$$G(y,a,b) = \overline{U}_0 \exp\left[\frac{-(y-a)^2}{2b^2}\right] \tag{7.1}$$

where $\overline{U}_0$ is the maximal mean wind velocity along the span, a is the normalized position of the centre of the peak, and b controls the width of the profile.

This profile is chosen in the present case because it can represent in a simple way the smooth variations of the mean wind velocity along the span. It can be used to model the reduction of the mean flow towards the bridge towers (Fig. 7.5) or the increasing mean velocity on the North side of the deck (Fig. 7.6). These examples are simplified cases where the non-uniformity is entirely defined by the function G, which is unlikely to be the case for a real flow. In both examples, a larger bridge response is observed when the flow is

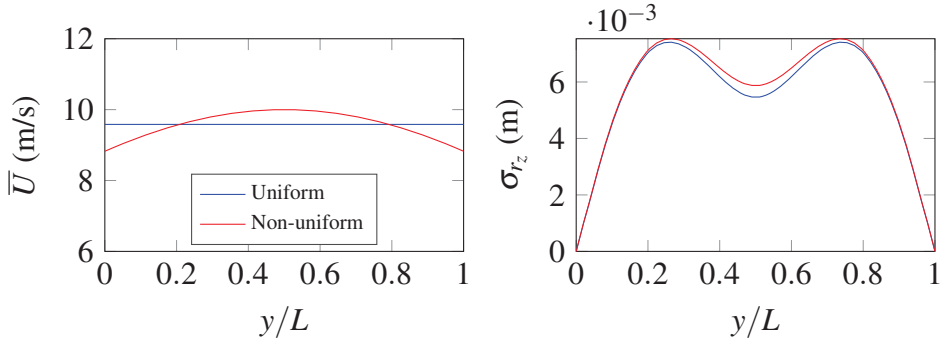

Figure 7.5 RMS of the vertical bridge response (right) for a non-uniform and uniform along-span mean wind velocity profile (left), generated using Eq. 7.1 with $a = 0.5$, $b = 1$ and $\overline{U}_0 = 10\,\mathrm{m\,s^{-1}}$.

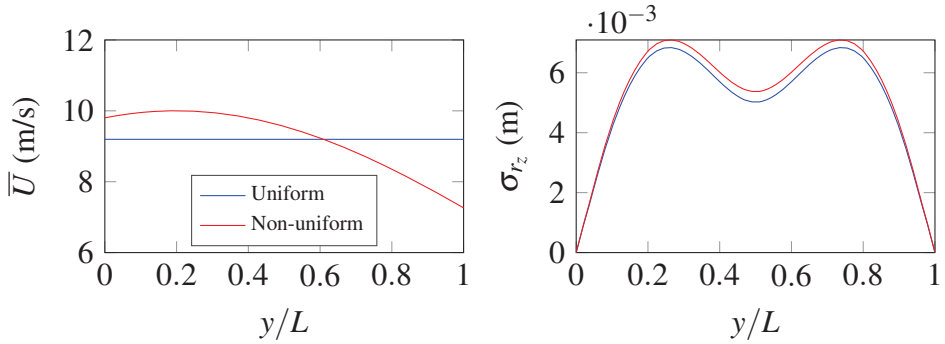

Figure 7.6 RMS of the vertical bridge response (right) for a non-uniform and uniform along-span mean wind velocity profile (left), generated using Eq. 7.1 with $a = 0.2$, $b = 1$ and $\overline{U}_0 = 10\,\mathrm{m\,s^{-1}}$.

non-uniform. However, the discrepancies observed in Figs. 7.5-7.6 may be small enough to assume the flow as homogeneous.

In the case of the Lysefjord Bridge, the anemometers located on H-16, H-18 and H-20 provide relatively consistent wind statistics. For a N-NE flow, the anemometers on H-08 record wind velocities different than the anemometers clustered in the central part of the bridge span. In Chapter 6, single-point statistics of wind turbulence were averaged based on data measured on H-16, H-18 and H-20 only. If wind statistics are now picked from the anemometers

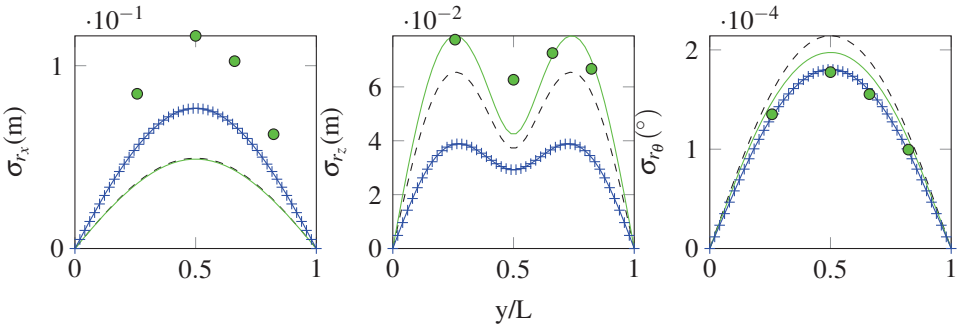

Figure 7.7 Measured (•) and computed displacement response, the input of which is based on different reference sonic anemometers (H-08t: ——; H-08b: - - -; H-18: —+—). Data set: 07/10/2014 at 03:50:00 (N-NE exposure).

located one on H-08b (bottom), H-08t (top) or H-18 and individually used as representative of the entire span, large discrepancies in the resulting buffeting response are observed (Fig. 7.7), highlighting the lack of flow uniformity.

7.4 Role of modal coupling

Modal coupling was introduced more than 25 years ago in the buffeting analysis of suspension bridges (Bucher and Lin, 1988; Namini et al., 1992). Jain et al. (1996a,b) proposed a numerical method to study both the buffeting response and coupled-flutter of a suspension bridge by computing simultaneously the lateral, vertical and torsional displacements and using a multi-mode analysis. Katsuchi et al. (1998, 1999) applied this numerical method to study the response of the full model of Akashi-Kaikyō Bridge in wind tunnel and observed a good agreement between the predicted and measured response. The formulation of the multi-mode coupled buffeting response for a finite element model was introduced by Sun et al. (1999) and Xu et al. (2000a) in the case of the Tsing Ma Bridge. In the beginning of the 2000's, Chen et al. (2000b) presented a similar work to the one from Jain et al. (1996a),

but applied it later to a time domain analysis (Chen and Kareem, 2002; Chen et al., 2000a).

Few investigations related to coupled buffeting response of suspension bridges have been performed in full-scale (Jakobsen and Larose, 1999; Nikitas et al., 2011). This is partly due to the difficulties in instrumenting a suspension bridge for WASHM purposes, but also the fact that modal coupling is challenging to detect for short and medium-span suspension bridges (Jain et al., 1996b). In this section, the numerical implementation of modal coupling is first investigated. Then, the possibility to detect modal coupling from full-scale measurement data is studied.

7.4.1 Numerical implementation of modal coupling

For a suspension bridge, modal coupling is mostly induced by wind load but can also be structural. In the present study, structural coupling is disregarded. Consequently, modal coupling is simply introduced by taking into account the off-diagonal terms in the matrix of aerodynamic damping $\boldsymbol{C_{ae}}$ and aerodynamic stiffness $\boldsymbol{K_{ae}}$:

$$\boldsymbol{C_{ae}} = -\frac{1}{2}\rho\overline{U}B\begin{bmatrix} 2\frac{D}{B}C_D & \frac{D}{B}C'_D - C_L & k_\theta B(\frac{D}{B}C'_D - C_L) \\ 2C_L & C'_L + \frac{D}{B}C_D & k_\theta B(C'_L + \frac{D}{B}C_D) \\ 2BC_M & BC'_M & k_\theta B^2 C'_M \end{bmatrix} \tag{7.2}$$

$$\boldsymbol{K_{ae}} = -\frac{1}{2}\rho\overline{U}^2 B\begin{bmatrix} 0 & 0 & (\frac{D}{B}C'_D - C_L) \\ 0 & 0 & (C'_L + \frac{D}{B}C_D) \\ 0 & 0 & BC'_M \end{bmatrix} \tag{7.3}$$

where all the notations are the same as in Chapter 2. The terms written in red in Eqs. 7.2-7.3 quantify the modal coupling. The computation of the lat-

Table 7.1 Modes taken into account into the 6-modes, 12-modes or 18-modes configuration (included: ✓; not included: ×).

Modes	6-modes	12-modes	18-modes
HS1	✓	✓	✓
HA1	✓	✓	✓
HS2	×	✓	✓
HA2	×	✓	✓
HS3	×	×	✓
HA3	×	×	✓
VS1	✓	✓	✓
VA1	✓	✓	✓
VS2	×	✓	✓
VA2	×	✓	✓
VS3	×	×	✓
VA3	×	×	✓
TS1	✓	✓	✓
TA1	✓	✓	✓
TS2	×	✓	✓
TA2	×	✓	✓
TS3	×	×	✓
TA3	×	×	✓

eral, vertical and torsional bridge displacement is carried out simultaneously, increasing the computational cost. In the following, the multi-mode analysis adopted consists of three possible mode combinations, called 6-modes configuration, 12-modes configuration and 18-modes configuration (Table 7.1). Here, the notations used to identify the eigen-modes are the same as in Chapter 5.

7.4.2 Modal coupling from full-scale measurements

Jain et al. (1996a,b) analysed the buffeting response of a hypothetical medium-span and long-span suspension bridge to assess the influence of modal cou-

pling. In the present case, a similar analysis is done, using this time full-scale wind and bridge displacement records. The Lysefjord Bridge is used as the "medium-span study case" whereas the Hardanger Bridge is used as the "long-span bridge study case".

Case study: The Lysefjord Bridge

For the Lysefjord Bridge, the ratio between the eigen-frequencies TS1 and VS1 is about 4, and the ratio between the eigen-frequencies TS1 and VS2 is 3. For a ratio between the eigen-frequencies TS1-VS1 and/or TS1-VS2 ranging

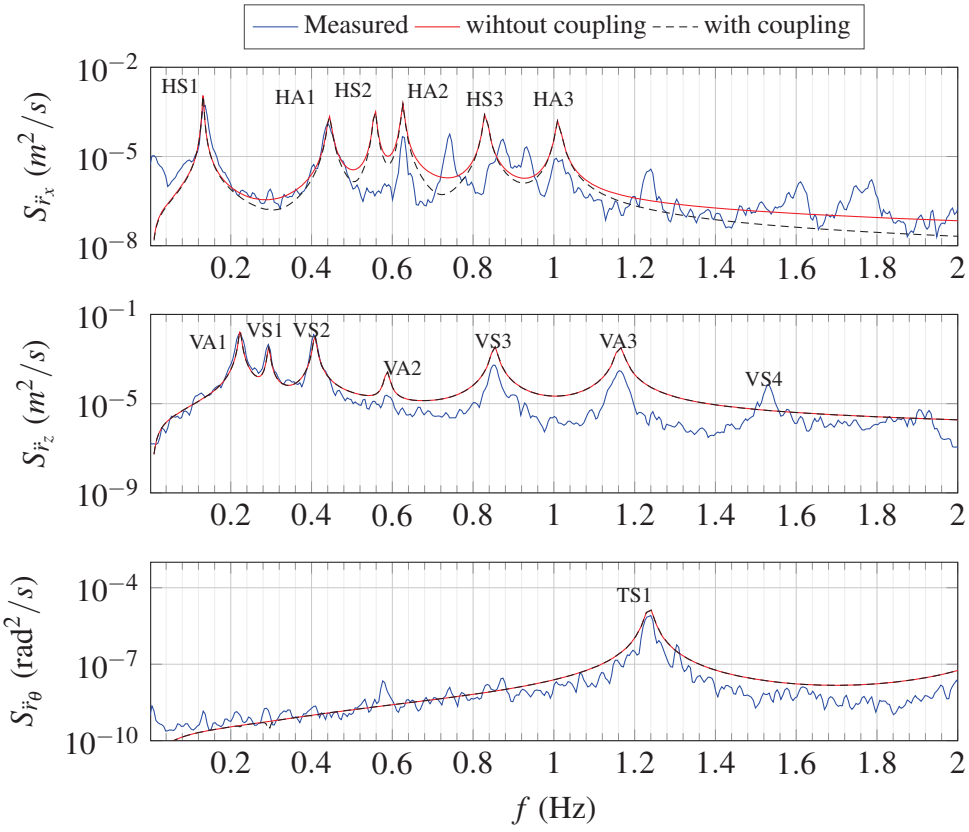

Figure 7.8 Computed and measured PSD of the Lysefjord Bridge acceleration response near H-09 on 26/10/2014 (S-SW flow) at 00:10, with $\overline{U} = 9.7\ \mathrm{m\,s^{-1}}$.

from 2 and 3, Thorbek and Hansen (1998) suggest that modal coupling has to be taken into consideration when the mean wind velocity reaches 60% of the critical velocity for the coupled flutter. The critical velocity for the Lysefjord Bridge is ca. 166 $\mathrm{m\,s^{-1}}$ according to the Selberg's formula (Selberg, 1961). Consequently, modal coupling is likely to be negligible for the Lysefjord Bridge, even if large wind velocities are recorded.

Modal coupling is implemented in the Lysefjord Bridge computational model and its influence on the PSD of the buffeting response of the bridge is shown in Fig. 7.8. As expected, modal coupling has a negligible contribution to the response. The coupled modes TS1-VS1 and TS1-VS2 are hardly visible in the PSD of the computed torsional response in the bottom panel of Fig. **??**. Although the PSD of the computed lateral acceleration response seems to be affected by modal coupling, the resonant peaks are almost unchanged leading to a RMS of the lateral acceleration response that is almost the same with and without modal coupling.

In Fig. 7.8, the acceleration response computed using the von Kármán spectra associated with a fitted four-parameter coherence function is compared to the measured one. Both the vertical and torsional motions show a negligible modal coupling. For the measured lateral motion, a peak at 1.24 Hz, corresponding to TS1 is visible. Its amplitude is minor compared to HS1, and is due to structural coupling as shown in e.g. Steigen (2011); Tveiten (2012). The peak at 0.74 Hz corresponds to the first mode of vibrations of the towers along axis x, i.e. perpendicular to the span. As stated in Chapter 5, the absence of measured resonant peak at 0.58 Hz is due an oversimplification of the bridge response by the SBM (Tveiten, 2012). Finally, the peaks at 0.87 Hz and 0.93 Hz are also linked to the interaction between the towers, the main cables and the bride deck.

Case study: The Hardanger Bridge

Similarly to the case of the Lysefjord Bridge, the buffeting response of the Hardanger Bridge is computed with and without modal coupling. 30 min of wind and acceleration data recorded on 06/12/2013 from 13:25:13 (Appendix B) have been used for this purpose. The wind records were clearly non-stationary which made the estimation of the buffeting load challenging. The computed response agrees however fairly well with the measured acceleration response (Fig. 7.9).

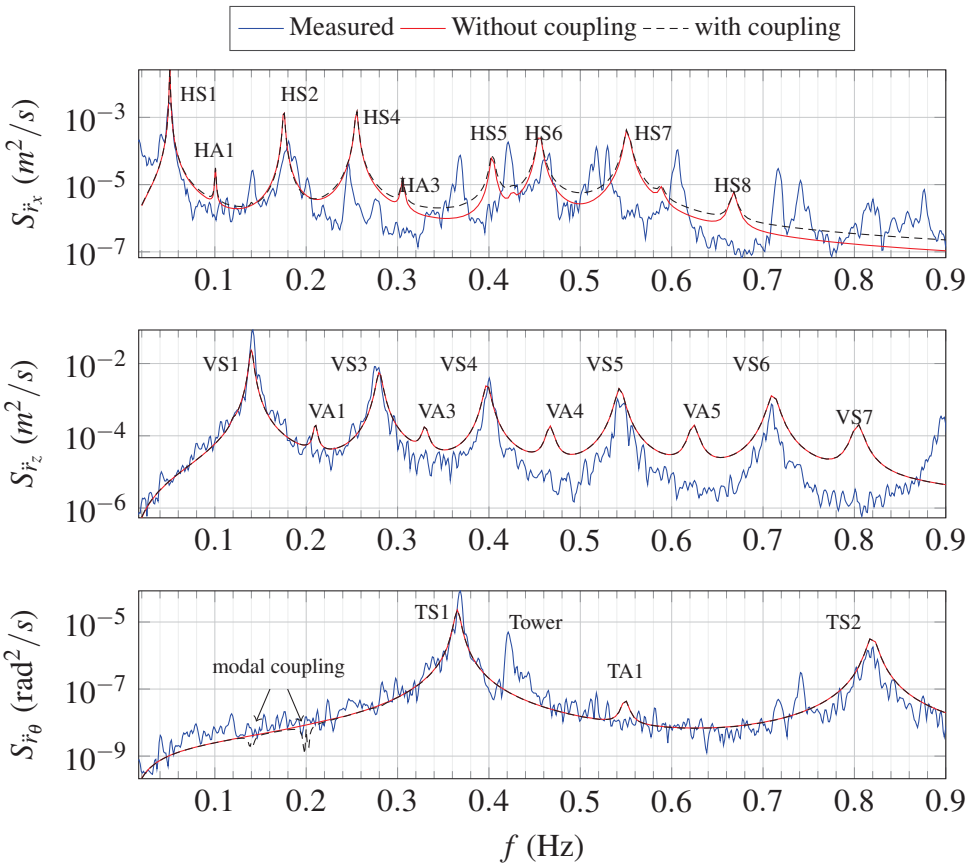

Figure 7.9 Computed and measured PSD of the Hardanger Bridge acceleration response at mid-span, with $\overline{U} = 11.9\ \mathrm{m\,s^{-1}}$ on 06/12/2016 from 13:25:13.

Aerodynamic-induced modal coupling is not clearly observed for the measured response. The torsional response computed by including modal coupling differs from the one without modal coupling near 0.14 Hz and 0.2 Hz, which corresponds to a coupling VS1-TS1 and VS2-TS1. Because of the rather low wind velocity recorded, the spectral response corresponding to the coupled-modes may have an amplitude too low, compared to the ambient noise, to be easily observed from the measurement data.

For the lateral motion, a larger amount of resonant peaks are measured than computed. The peaks at 0.14 Hz, 0.2 Hz, 0.27 Hz correspond to the modes VS1, VS2 and VS3 respectively and may result from a misalignment between the two accelerometers installed on each side of the deck. The peak at 0.37 Hz, visible in the PSD of the lateral acceleration response, corresponds to TS1. Its relatively large amplitude documents the structural coupling, i.e. a horizontal component of the TS1 mode (Mikkelsen, 2013). The resonant peak at 0.42 Hz visible in both the lateral and torsional motion and corresponds likely to the first eigen-frequency of the towers. The large number of measured peaks in the top panel of Fig. 7.9 that are not predicted by the SBM suggests that the towers, main cables and backstay cables play a more important role on the lateral bridge response in the case of the Hardanger Bridge than in the case of the Lysefjord Bridge.

7.5 Quadratic terms of the wind load

As presented in Chapter 2, the buffeting theory is traditional based on the linearised aerodynamic forces, by applying Taylor's expansion series up to the first order to the relative wind incidence and the relative wind velocity. Kareem et al. (1998) developed the Taylor's expansion series of the aerodynamic drag up to the second order to include the quadratic terms of the wind load, and to evaluate the consequences on the peak response of a SDOF model. By using Taylor's series expansion for higher order, Denoël (2005)

proposed polynomial expressions for the aerodynamic forces. In addition, Denoël and Degée (2006) showed that the second derivatives of the aerodynamic coefficients may be important for the quadratic terms of the wind load. However, these forces were not expressed in the bridge coordinate system, i.e. the drag and lift were assumed to be equal to the horizontal and vertical wind forces respectively.

In this section, the quadratic terms of the aerodynamic forces are taken into account for the buffeting load only. In other words, the self excited forces remain linear. By using the same notations as in Chapter 2, the instantaneous total wind incidence angle is:

$$\alpha_f - r_\theta = \arctan\left(\frac{w - \dot{r}_z - k_\theta B \dot{r}_\theta}{\overline{U} + u - \dot{r}_x}\right) \tag{7.4}$$

Taylor's series up to order 2 of the total instantaneous wind incidence angle $\alpha_f - r_\theta$, the instantaneous wind relative velocity V_{rel} and the quasi steady terms of the aerodynamic coefficients C_D, C_L and C_M are:

$$\alpha_f - r_\theta = \left(\frac{w - \dot{r}_z - k_\theta B \dot{r}_\theta}{\overline{U}} - \frac{uw}{\overline{U}^2}\right) + \mathscr{O}\left(\frac{1}{\overline{U}}\right)^3 \tag{7.5}$$

$$\cos(\alpha_f - r_\theta) = 1 - \frac{w^2}{2\overline{U}^2} + \mathscr{O}\left(\frac{1}{\overline{U}}\right)^3 \tag{7.6}$$

$$\sin(\alpha_f - r_\theta) = \alpha_f - r_\theta + \mathscr{O}\left(\frac{1}{\overline{U}}\right)^3 \tag{7.7}$$

$$|V_{rel}|^2 = \overline{U}^2 + 2\overline{U}u - 2\overline{U}\dot{r}_x + u^2 + w^2 + \mathscr{O}\left(\frac{1}{\overline{U}}\right)^3 \tag{7.8}$$

$$C_D(\alpha) = C_D + \alpha_f \cdot C_D^{'} + \frac{1}{2}\alpha_f^2 \cdot C_D^{''} + \mathscr{O}\left(\alpha^3\right) \tag{7.9}$$

$$C_L(\alpha) = C_L + \alpha_f \cdot C_L^{'} + \frac{1}{2}\alpha_f^2 \cdot C_L^{''} + \mathscr{O}\left(\alpha^3\right) \tag{7.10}$$

$$C_M(\alpha) = C_M + \alpha_f \cdot C_M^{'} + \frac{1}{2}\alpha_f^2 \cdot C_M^{''} + \mathscr{O}\left(\alpha^3\right) \tag{7.11}$$

The second derivative of the drag, lift and moment coefficients with respect to the angle of attack are denoted C_D'', C_L'' and C_M'' respectively. Their value is not experimentally available for the Lysefjord Bridge. The horizontal, vertical and torsional forces are denoted F_x, F_z and F_t respectively:

$$\begin{bmatrix} F_x \\ F_z \\ F_\theta \end{bmatrix} = \frac{1}{2}\rho B V_{rel}^2 \begin{bmatrix} \frac{D}{B}C_D \cdot \cos(\alpha_f - r_\theta) - C_L \cdot \sin(\alpha_f - r_\theta) \\ \frac{D}{B}C_D \cdot \sin(\alpha_f - r_\theta) + C_L \cdot \cos(\alpha_f - r_\theta) \\ BC_M \end{bmatrix} \tag{7.12}$$

Combining equations 7.5-7.12 leads to the calculation of the total non-linear wind force matrix $\boldsymbol{F_{nl}}$ of the static and buffeting loads, the non dimensional form of which is:

$$\widehat{\boldsymbol{F}}_{\boldsymbol{nl}} = \frac{2}{\rho \overline{U}^2 B} \cdot \begin{bmatrix} F_x & F_z & F_\theta \end{bmatrix}^\top \tag{7.13}$$

For a zero yaw angle, $\widehat{\boldsymbol{F}}_{\boldsymbol{nl}}$ is expressed as a function of u, w and $\overline{U}$:

$$\widehat{\boldsymbol{F}}_{\boldsymbol{nl}} = \widehat{\boldsymbol{A}}_{\boldsymbol{0}} \begin{bmatrix} 1 \end{bmatrix} + \widehat{\boldsymbol{A}}_{\boldsymbol{1}} \begin{bmatrix} u/\overline{U} \\ w/\overline{U} \end{bmatrix} + \widehat{\boldsymbol{A}}_{\boldsymbol{2}} \begin{bmatrix} u^2/\overline{U}^2 \\ w^2/\overline{U}^2 \end{bmatrix} + \widehat{\boldsymbol{A}}_{\boldsymbol{uw}} \begin{bmatrix} uw/\overline{U}^2 \end{bmatrix} \tag{7.14}$$

where :

$$\widehat{\boldsymbol{A}}_{\boldsymbol{0}} = \begin{bmatrix} D/B \cdot C_D \\ C_L \\ BC_M \end{bmatrix} \tag{7.15}$$

$$\widehat{\boldsymbol{A}}_{\boldsymbol{1}} = \begin{bmatrix} 2\frac{D}{B}C_D \cdot \chi_{ux} & \left(\frac{D}{B}C_D' - C_L\right) \cdot \chi_{wx} \\ 2C_L \cdot \chi_{uz} & \left(C_L' + \frac{D}{B}C_D\right) \cdot \chi_{wz} \\ 2BC_M \cdot \chi_{u\theta} & BC_M' \cdot \chi_{w\theta} \end{bmatrix} \tag{7.16}$$

$$\widehat{\boldsymbol{A}}_{\mathbf{2}} = \begin{bmatrix} \frac{D}{B} \cdot C_D & \frac{D}{2B} \cdot (C_D + C_D^{''}) - C_L^{'} \\ C_L & \frac{1}{2}(C_L + C_L^{''}) + \frac{D}{B} C_D^{'} \\ BC_M & B(C_M + \frac{C_M^{''}}{2}) \end{bmatrix} \tag{7.17}$$

$$\widehat{\boldsymbol{A}}_{\boldsymbol{uw}} = \begin{bmatrix} -C_L + \frac{D}{B} \cdot C_D^{'} \\ C_L^{'} + \frac{D}{B} \cdot C_D \\ BC_M^{'} \end{bmatrix} \tag{7.18}$$

In a first approximation, the matrix $\widehat{\boldsymbol{A}}_{\boldsymbol{uw}}$ can be omitted if the components u and w are assumed uncorrelated. The components u and w are assumed to be Gaussian variables with zero mean. Therefore u^2 and w^2 follow a Chi-squared distribution with one degree of freedom. The variance of u^2 and w^2 are therefore equal to $2\sigma_u^4$ and $2\sigma_w^4$ respectively. The variance of the linearised and quadratic buffeting wind load are denoted σ_{l}^2 and σ_{nl}^2 respectively:

$$\boldsymbol{\sigma}_{\mathbf{l}}^{\mathbf{2}} = \widehat{\boldsymbol{A}}_{\mathbf{1}}{}^2 \begin{bmatrix} I_u^2 \\ I_w^2 \end{bmatrix} \tag{7.19}$$

$$\boldsymbol{\sigma}_{\mathbf{nL}}{}^2 = \widehat{\boldsymbol{A}}_{\mathbf{2}}{}^2 \begin{bmatrix} 2I_u^4 \\ 2I_w^4 \end{bmatrix} \tag{7.20}$$

By assuming uncoupled motions of the bridge deck, the relative weight of the variance of the total buffeting load over the variance of the linearised buffeting load is:

$$\boldsymbol{\varepsilon} = \frac{\boldsymbol{\sigma}_{\mathbf{nL}}{}^2 + \boldsymbol{\sigma}_{\mathbf{L}}{}^2}{\boldsymbol{\sigma}_{\mathbf{L}}{}^2} \tag{7.21}$$

By introducing Eqs. 7.19-7.20 into Eq. 7.21:

$$\boldsymbol{\varepsilon}^2 = \boldsymbol{I} + \boldsymbol{C}^2 \begin{bmatrix} 2I_u^2 \\ 2I_w^2 \end{bmatrix} \tag{7.22}$$

where:

$$\boldsymbol{C} = \frac{1}{2} \begin{bmatrix} 1 & \left(\frac{D}{B}(C_D + C_D^{''}) - 2C_L^{'}\right) / \left(\frac{D}{B}C_D^{'} - C_L\right) \\ 1 & \left(C_L + C_L^{''} + 2\frac{D}{B}C_D^{'}\right) / \left(C_L^{'} + \frac{D}{B}C_D\right) \\ 1 & (2C_M + C_M^{''}) / \left(C_M^{'}\right) \end{bmatrix} \tag{7.23}$$

For a streamlined closed bridge girder like the one of the Lysefjord Bridge, $C_D^{'} \simeq 0$ and $C_M \ll C_M^{'}$. Assuming that the vertical turbulence intensity follows $I_w = \delta I_u$, where $\delta < 1$, and that $C_D^{''} = C_L^{''} = C_M^{''} \simeq 0$, Eq. 7.22 becomes:

$$\boldsymbol{\varepsilon}^2 = \boldsymbol{I} + \frac{I_u^2}{2} \begin{bmatrix} 1 + \left[\delta \cdot \left(-\frac{D}{B}C_D + 2C_L^{'}\right) / C_L\right]^2 \\ 1 + \left[\delta \cdot C_L / \left(C_L^{'} + \frac{D}{B}C_D\right)\right]^2 \\ 1 + \left[\delta \cdot C_M / C_M^{'}\right]^2 \end{bmatrix} \tag{7.24}$$

$$\simeq \boldsymbol{I} + \frac{I_u^2}{2} \begin{bmatrix} 1 + \delta^2 \left(-\frac{D}{B}C_D + 2C_L^{'}\right)^2 / (C_L)^2 \\ 1 \\ 1 \end{bmatrix} \tag{7.25}$$

By expressing $\boldsymbol{\varepsilon}$ as:

$$\boldsymbol{\varepsilon} = \begin{bmatrix} \varepsilon_x & \varepsilon_z & \varepsilon_\theta \end{bmatrix}^\intercal \tag{7.26}$$

Eq. 7.25 can be re-written:

$$\varepsilon_x = \sqrt{1 + \frac{I_u^2}{2} + \frac{I_u^2}{2}\frac{\delta^2}{(C_L)^2}\left(-\frac{D}{B}C_D + 2C_L'\right)^2} \tag{7.27}$$

$$\varepsilon_z = \varepsilon_\theta = \sqrt{1 + \frac{I_u^2}{2}} \simeq 1 + \frac{I_u^2}{4} \tag{7.28}$$

A similar result for the vertical and torsional motions have been found by Denoël (2005). For a turbulent intensity of 30 %, the STD of the vertical wind force is larger by only 2.2% is the quadratic terms of the wind load are included. For the measured vertical bridge displacement response, the large difference between the S-SW and the N-NE wind case cannot be explained by the non-linearity of the wind load only. For the lateral motion, the quadratic terms of the wind load may not be neglected. For the Lysefjord bridge, if $\delta = 0.5$ and $I_u = 30$ %, then the STD of the lateral load is increased by 200 % when the Taylor's series expansion up to order 2 is used. It should be noted that in the N-NE flow, the measured lateral response in the top left panel of Fig. 6.10 was in average 150 % larger than predicted.

If the vertical wind component is neglected in the calculation of the horizontal force, or if the drag F_D is used instead of F_x, then ε_x becomes equal to ε_z. Further computation of the bridge response in the time domain is required to better estimate the influence of the quadratic terms of the wind load on the lateral bridge response.

7.6 Non-stationarity of the flow

A wind record is considered as non-stationary when its statistics, such as mean wind velocity, standard deviation and/or wind spectra change with time. Under these circumstances, the traditional statistical tools to describe wind turbulence become inappropriate (Lombardo et al., 2014). In full scale, every

wind record is actually more or less non-stationary. For analysed wind records of 1 h duration, Chen and Letchford (2004) and Xu and Xia (2011) sorted non-stationary flows into two categories. The first one corresponds to wind records with a mean value slowly fluctuating with time. If the "fluctuating mean" is removed, then the time series display stationary statistics. The second category is more challenging to deal with since the entire spectral content of the time series evolves with the time, requiring e.g. a time-frequency domain analysis (Chen et al., 2007).

Since the beginning of the 2000s, non-stationary flow modelling has become particularly popular, especially to model downbursts (Chen and Letchford, 2004; Lombardo et al., 2014; Su et al., 2015) or typhoon winds (Chen et al., 2007; Hu et al., 2013; Wang et al., 2016). In this thesis, only stationary flows are studied. Possible non-stationary data have to be corrected for or removed from the data population analysed. The linear trend of every time series is removed prior to the study of its fluctuations. This linear trend may be the most common type of "fluctuating mean" when time series of 10 min duration are used. If 1 h of wind data are used, more complex fluctuating mean may be observed and captured by applying a moving average method, a kernel regression method or the empirical modal decomposition (Chen et al., 2007; Huang et al., 1998; Su et al., 2015).

The flow stationarity is usually assessed using the reverse arrangement test from Bendat and Piersol (2011). This test has been previously applied to wind velocity data (Wang et al., 2016; Xu, 2013) and more generally to a variety of random processes, see e.g. Aryan et al. (2013); Beck et al. (2006). According to Bendat and Piersol (2011), the RA test is a "non-parametric and distribution-free procedure where no assumption is made concerning the probability distribution of the data being evaluated" used to detect non-negligible trends in random data set. By paraphrasing Siegel and Castellan (1988), the null hypothesis for this test is that the wind sample considered is

made of independent observations. The alternative hypothesis is that the data points are not random because of the existence of an underlying trend.

Consider a sample $X = \{X_1, X_2, ...X_N\}$ made of N data-points corresponding to the along-wind velocity component. According to Bendat and Piersol (2011), a reverse arrangement is defined as the number of times that $X_i > X_j$ for $i < j$. For a number A of reverse arrangements, the mean and standard deviation of A are:

$$\mu_a = \frac{N(N-1)}{4} \tag{7.29}$$

$$\sigma_a = \frac{N(2N+5)(N-1)}{72} \tag{7.30}$$

Following Siegel and Castellan (1988), a z-score is calculated as:

$$z = \frac{A - \mu_a}{\sqrt{\sigma_a}} \tag{7.31}$$

In the following, the null hypothesis is verified at 5% significance level if $-1.96 \leq z \leq 1.96$.

Although the RA test is recognized as efficient, its performance has not been assessed in details for wind records. A rigorous application of this test requires increasing values of the reverse arrangements, which may have a heavy computational cost when thousands of wind samples have to be tested. This may limit its applicability for large data sets.

The goal of this section is to investigate the possible causes for non-stationary wind conditions at the Lysefjord Bridge site, as well as the alternative stationarity tests that could complement the reverse arrangement test. In the following, a first stationarity test based on the measurement of abrupt changes in the wind direction is first studied. Then the reverse arrangement test is compared to an alternative test which is based on the calculation of the integral time scale.

7.6.1 Directional non-stationarity

Chen et al. (2007) mentioned the possibility of non-zero mean values for the across-wind and vertical wind components. However, they did not discuss their origin, as their objective was only to remove the "fluctuating mean" of the different wind records to retrieve a stationary wind model. For the sake of simplicity, only the horizontal flow is investigated in the following. For a stationary flow, the relationship between the northern V_n, eastern V_e, along-wind U, across-wind component V and the mean wind direction $\overline{\Theta}$ is:

$$\begin{bmatrix} V_n \\ V_e \end{bmatrix} = \begin{bmatrix} \cos(\overline{\Theta}) & \sin(\overline{\Theta}) \\ \sin(\overline{\Theta}) & -\cos(\overline{\Theta}) \end{bmatrix} \times \begin{bmatrix} U \\ V \end{bmatrix} \tag{7.32}$$

Eq. 7.32 shows that the along-wind and across-wind components can be retrieved from the eastern and northern ones by applying a rotation matrix. To retrieve the components U and V from V_n and V_e, the wind direction must be calculated first as:

$$\Theta = \arctan\left(\frac{V_e}{V_n}\right) \tag{7.33}$$

For a stationary wind record, a singular value decomposition (SVD) can be applied to the left term of Eq. 7.32 to directly retrieve the U and V components without first calculating the wind direction:

$$\boldsymbol{B}\boldsymbol{\Sigma}\boldsymbol{E} = \begin{bmatrix} V_n \\ V_e \end{bmatrix} \tag{7.34}$$

$$\begin{bmatrix} U \\ V \end{bmatrix} = \boldsymbol{\Sigma}\boldsymbol{E} \tag{7.35}$$

where $\boldsymbol{B}$ is the matrix of left singular vectors, $\boldsymbol{\Sigma}$ is the matrix of singular values and $\boldsymbol{E}$ is the matrix of right singular vectors.

The SVD can be seen as a factorization of the matrix $\begin{bmatrix} V_n & V_e \end{bmatrix}^\top$ to find the optimal rotation so that one of the components has the largest mean value and the other component the smallest value, i.e. as close as possible to 0 $\mathrm{m\,s^{-1}}$.

In a more general case, Eqs. 7.34-7.35 can be used to retrieve the along-wind and across-wind components from any matrix $\begin{bmatrix} V_x & V_y \end{bmatrix}^\top$ where V_x and V_y are two orthogonal wind components. For the Lysefjord Bridge, the components V_x and V_y correspond to the across-deck and along-deck wind components. If Eq. 7.32 is used, then the mean wind direction Θ is calculated with respect to the bridge span which makes an angle 40° with the North. The method involving the SVD does not require any knowledge of the bridge orientation to retrieve the components U and V from V_x and V_y.

Fig. 7.10 illustrates this method for 10 min of wind data recorded on 09/08/2014 from 18:40 to 18:50 and displayed in Fig. 7.11. The application of Eq. 7.32 is referred to as the "traditional method" in Fig. 7.10. There is an almost perfect agreement between the different wind components retrieved by the two methods used above. The good agreement is due to the stationary fluctuations of the wind direction, even though the along-wind velocity may not be stationary.

However, if the non-stationarity of the flow is induced by abrupt modifications of the wind direction, larger discrepancies appear between the results based on the SVD analysis and those based on Eq. 7.32. This is illustrated in Fig. 7.12 and Fig. 7.13 where the wind direction changed multiple times from S-SW to N-NE at the Lysefjord Bridge site on the afternoon of 09/08/2014.

Figs. 7.10-7.12 shows therefore that a stationarity test can be created by evaluating the correlation coefficient between the along-wind component retrieved from Eqs. 7.34-7.35 and Eq. 7.32. A correlation coefficient lower than 0.8 or 0.9 may for example indicate that a non-stationary flow induced by a non-stationary wind direction is recorded. The number of samples

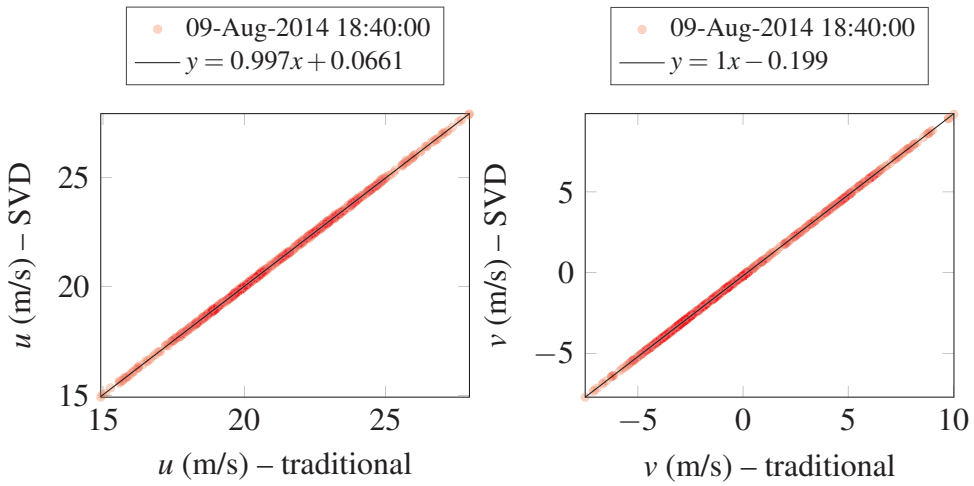

Figure 7.10 Application of Eq. 7.32 and Eqs. 7.34-7.35 to retrieve the horizontal wind components from the across-deck and along-deck wind component for a stationary wind direction.

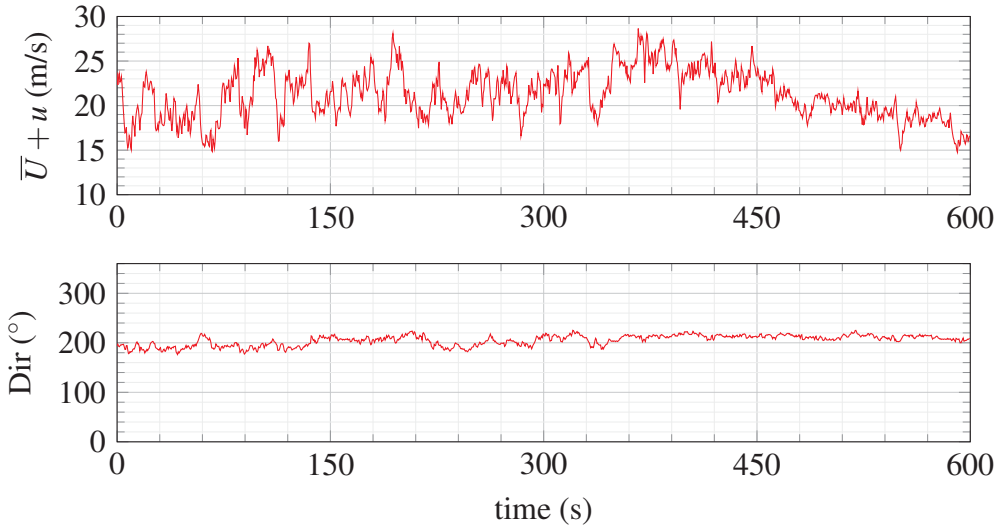

Figure 7.11 Along-wind component (top) and wind direction (bottom) recorded on 09/08/2014 from 18:40 to 18:50 on the Lysefjord bridge.

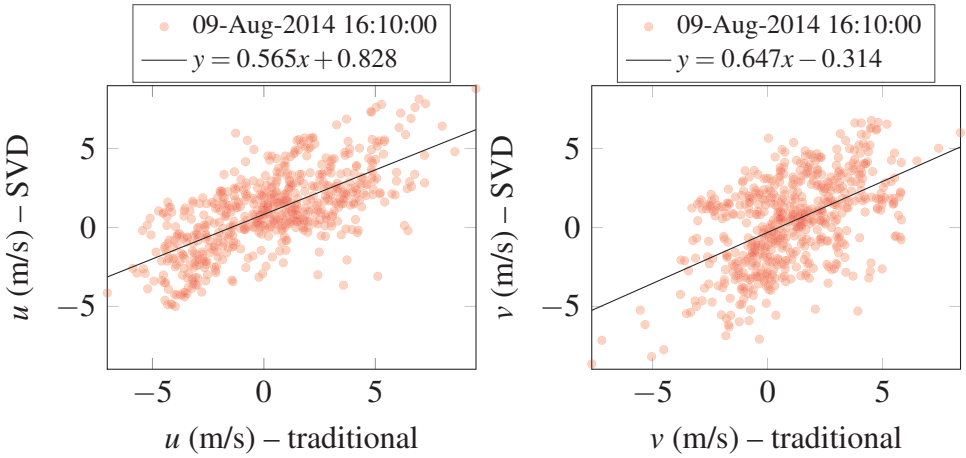

Figure 7.12 Comparison of the application of Eq. 7.32 and a SVD to retrieve the horizontal wind components from the components normal and along the bridge deck, for a flow with abrupt changes in the wind direction.

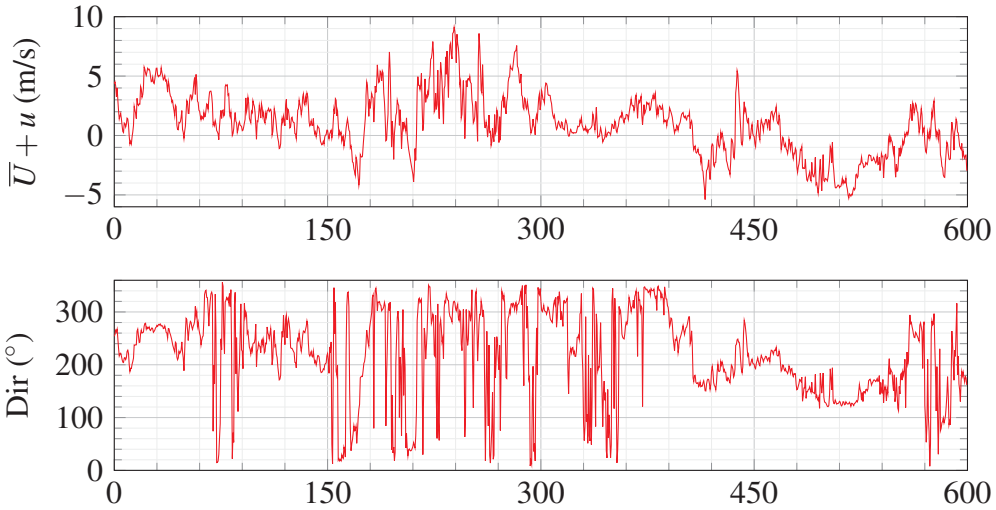

Figure 7.13 Along-wind component (top) and wind direction (bottom) recorded on 09/08/2014 from 16:10 to 16:20 on the Lysefjord bridge.

characterized by flow changing from S-SW to N-NE or vice versa remains however small, and are often associated with low wind velocities.

7.6.2 An alternative stationarity test

To evaluate the stationarity of wind fluctuations, the reverse arrangement (RA) test (Bendat and Piersol, 2011) is traditionally used (Chen et al., 2007; Xu and Chen, 2004). The outcome of the RA test depends on the number of observations, i.e. the number of data points constituting one wind record. The sampling frequency corresponding to the number of observations is referred to as the "test sampling frequency". In Fig. 7.14, the stationarity of the wind data recorded on 07/10/2014 (N-NE flow) was assessed using the RA test and time series of 10 min duration with decreasing test sampling frequencies. Fig. 7.14 shows that when the test sampling frequency decreases, the percentage of sample detected as non-stationary is dropping.

The integral time scale for the along-wind component can be used as a criterion to evaluate the stationarity of the flow:

$$T_u = \int_{t=0}^{t(R_u(t)=0)} R_u(t)\,\mathrm{d}t \tag{7.36}$$

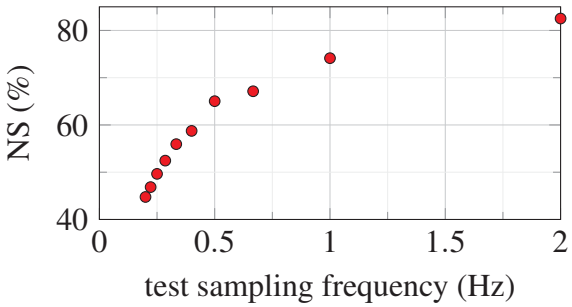

Figure 7.14 Percentage of samples detected as non-stationary (NS) with the RA test, based on wind data recorded on 07/10/2014 (N-NE flow).

where R_i is the single-sided auto-covariance function of the fluctuating wind velocity. The integral time scale has the advantage to show little dependency on the sampling frequency, but depends on the sample duration, which is here equal to the standard value of 10 min. To study non-stationary flows, several authors (Chen et al., 2007; Hu et al., 2013; Xu and Chen, 2004) used a duration of 1 h, and Su et al. (2015) used 30 min. Although the averaging time of such studies do not comply with most of the standards, it permits an efficient use of the empirical modal decomposition (EMD) (Huang et al., 1998) to extract the time-varying mean. This is because an efficient application of the EMD requires a fluctuating mean that evolves slowly with time. If 10 min of wind records are considered, this is not necessarily true as "ramp-up" events can be recorded (Lombardo et al., 2014) and the extraction of the time-varying mean becomes therefore more challenging.

In this subsection, the integral time scale is chosen as the determining criterion to evaluate the flow stationarity, rather than the integral length scale because the latter depends on the mean wind velocity. A large integral length scale may indeed results from a non-stationary flow, but also a large mean wind velocity, which would lead to a misinterpretation of the flow stationarity.

If the integral time scale calculated with Eq. 7.36 is based on unmodified wind data, it is denoted T_u^{nd}. If the linear trend of the time series is removed, the integral time scale is denoted T_u^{d}. If a time series is not affected by any trend, then T_u^{nd} and T_u^{d} should be equal, otherwise large differences are expected as the outcome of Eq. 7.36 is highly sensitive to any trend or abrupt variation of the velocity.

The relative difference between T_u^{nd} and T_u^{d} is:

$$\varepsilon_{T_u} = \frac{T_u^{\mathrm{d}} - T_u^{\mathrm{nd}}}{T_u^{\mathrm{nd}}} \tag{7.37}$$

The alternative stationarity test proposed here is based on two steps. First, the wind data are de-trended, then T_u is calculated for each sample. Any data

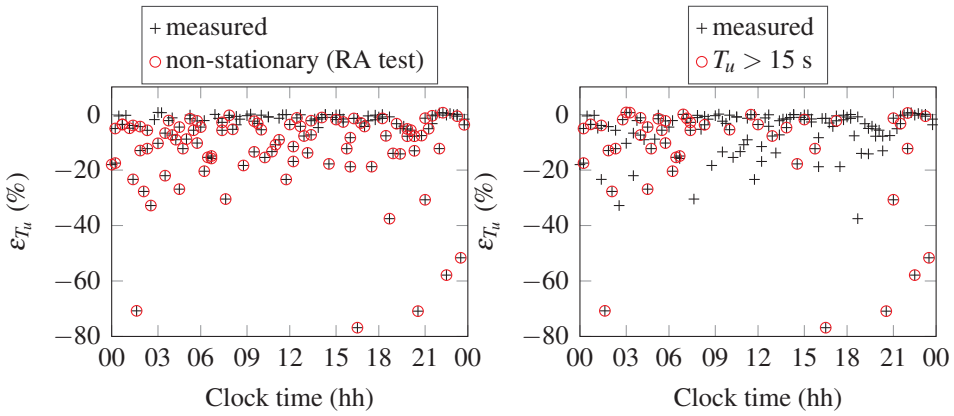

Figure 7.15 Influence of the trend on the estimation of the integral time-scales, and comparison of the RA test with the alternative stationarity test based on a threshold integral time scale (data recorded on 07/10/2014 for a N-NE flow).

with a value of T_u above a threshold value is considered as non-stationary. Here, the threshold value was set to 15 s, i.e. about the third quartile of the distribution of the integral time scales for the year 2015, which corresponds to an integral length scale of 300 m for a mean wind velocity of 20 m s^{-1}.

A decreasing value of ε_{T_u} in Fig. 7.15 is not surprising. Chen et al. (2007) observed also a reduction of the integral length scales after they had removed the fluctuating mean of the time series they were studying. In the left panel of Fig. 7.15, every sample characterized by an absolute value $|\varepsilon_{T_u}|$ larger than 5% is detected as non-stationary, i.e. 65% of the entire set. The alternative stationarity test, based on a threshold value for ε_{T_u} is displayed on the right panel of Fig. 7.15. The number of samples detected as non-stationary is much lower (32%), and the largest absolute value of ε_{T_u} for a stationary sample is 37%. For this sample, $T_u^{\mathrm{nd}} = 8$ s, $I_u = 20\%$ and the trend was quasi-negligible. This underlines the high sensitivity of the integral time scale calculated with Eq. 7.36 to any trend present in the data set.

Compared to the RA test, this alternative stationarity test is less sensitive to the sampling frequency, can be directly related to the wind load, has

a lower computational cost and does not produce a large amount of false-positives. This stationarity test can also be combined with the one based on the non-stationary fluctuations of the wind direction so that the sources of non-stationarity can be identified. Alternatively, both a threshold value for ε_{T_u} and T_u can be used.

7.7 Traffic-induced vibrations

At low wind velocities, the motion of a suspension bridge may be dominated by traffic-induced vibrations rather than by wind. When examining the validity of the buffeting theory in full scale, acceleration records dominated by traffic-induced vibrations have to be removed. A simple test can be conducted to check if a sample of the bridge acceleration response is dominated by wind or traffic. Traffic loads mainly excite the higher modes of vibration of the bridge. Consequently, if the variance of the acceleration response is mainly due to the higher modes, then traffic load is likely to be dominant. The main difficulty is to find a proper frequency threshold f_t separating the domain of "low frequencies" from the "high frequencies" one. The contribution of the high frequency content to the overall bridge response is evaluated using a ratio λ defined as:

$$\lambda = \frac{\sigma_{\mathrm{HF}}}{\sigma_{\mathrm{LF}}} \tag{7.38}$$

where:

$$\sigma_{\mathrm{HF}} = \sqrt{\int_{f_t}^{f_c} S_{\ddot{r}_z}(f)\, df} \tag{7.39}$$

$$\sigma_{\mathrm{LF}} = \sqrt{\int_{f_0}^{f_t} S_{\ddot{r}_z}(f)\, df} \tag{7.40}$$

where f_0 is the lowest frequency recorded and f_c is the Nyquist frequency. The frequency threshold is arbitrary set to 2 Hz in the present case, such as the domain of the "high frequencies" is defined between f_t and f_c. This threshold is good enough for the vertical motion of the Lysefjord Bridge, as the first 8 vertical eigen-frequencies are below 2 Hz, and the vertical acceleration response is usually dominated by the first four modes. Alternative methods can be found in Cheynet et al. (2015b). A frequency threshold limited at 1 Hz may be another possibility. Rare cases where traffic excites mostly the low eigen-frequencies have been monitored, and are associated with low wind velocity, low turbulence and a single vehicle crossing the bridge.

Figure 7.16 illustrates the method briefly described here to detect vibrations dominated by traffic. A high-resolution time-frequency distribution called Zhao–Atlas–Marks distribution (Fulop, 2011) is used to describe the development of the bridge acceleration response both in the time and frequency domain. A spectrogram could have been used, but a lower frequency and/or time resolution would have been obtained despite a good signal-to-noise ratio. Similarly, the evolutionary spectrum from Priestley (1966) could have been used, but the frequency resolution was still relatively low compared to the ZAM distribution.

At $t = 180$ s and $t = 380$ s, the accelerometers monitor an unknown number of vehicles crossing the bridge, leading to multiple resonant peaks at 0.4 Hz, 0.86 Hz, 1.5 Hz and 3.3 Hz that fade away after a couple of minutes. The only eigen-frequency that remains visible during the whole record corresponds to the first vertical symmetric mode, at 0.3 Hz.

According to the data collected during the year 2015, the influence of traffic-induced vibrations can be considered as insignificant for wind velocities above 12 $\mathrm{m\,s^{-1}}$ (Fig. 7.17). For lower wind velocities, unexpected large

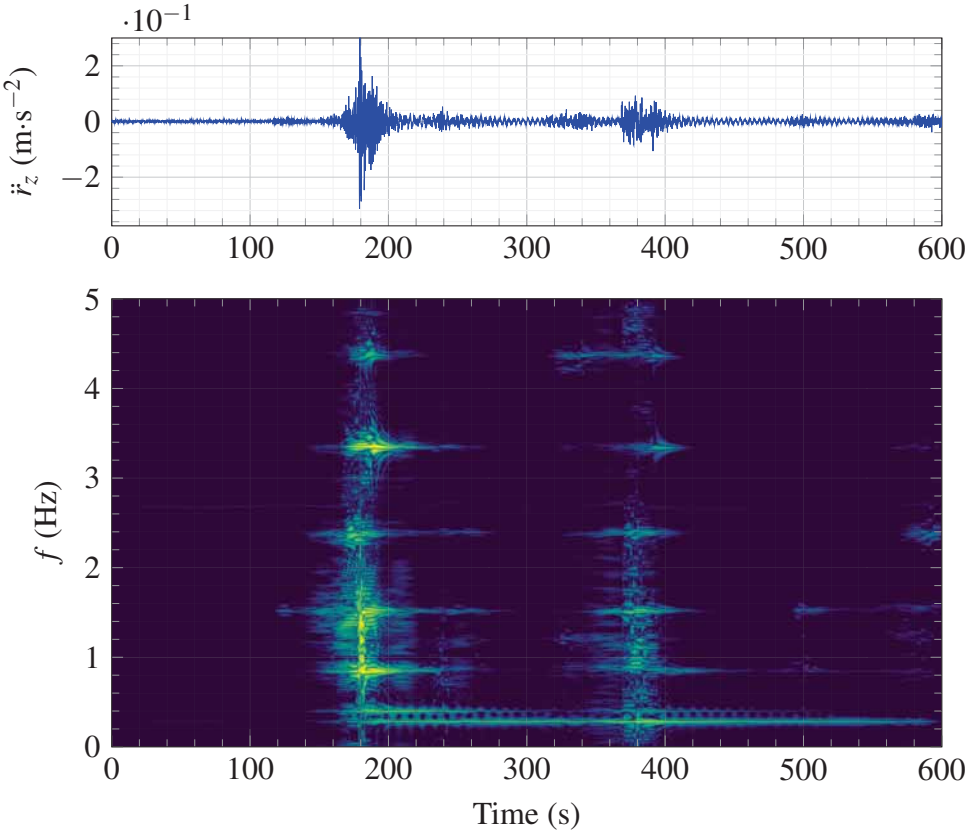

Figure 7.16 Time-frequency analysis of the vertical acceleration response of the Lysefjord Bridge on 12/02/2015 at 12:20.

amplitudes of vibration are often due to heavy traffic, leading to a measured response larger than predicted by the buffeting theory. For the data studied on 07/10/2014 and 26/10/2014, the variance of the measured bridge displacement did not display any sudden variation at lower wind velocities. This indicates that the large displacements measured for the flow from N-NE are unlikely to be due to heavy traffic. In Fig. 7.17, the large amount of samples detected as “dominated by traffic” suggests that traffic-induced vibrations may have to be systematically included in structural health monitoring of long-span suspension bridges, even in a relatively remote area such as the Lysefjord.

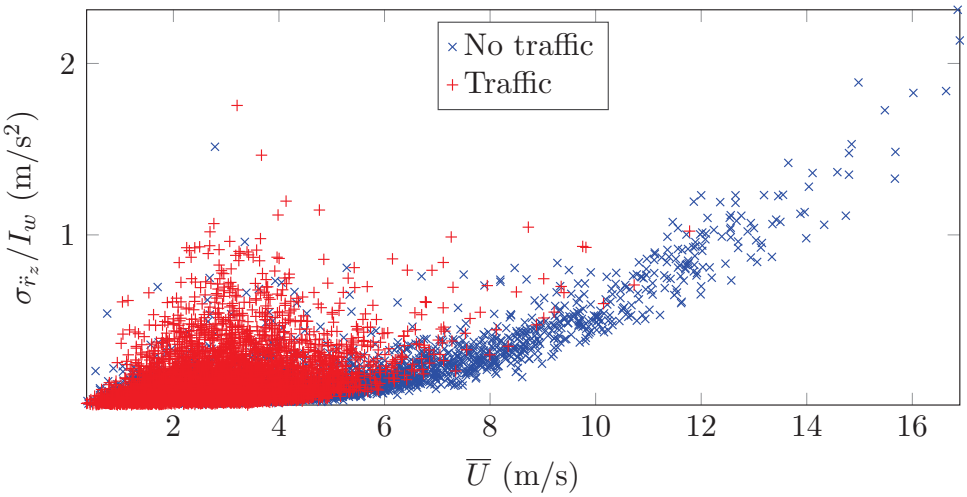

Figure 7.17 RMS of the vertical acceleration of the Lysefjord Bridge measured during the year 2015, at mid-span, for a wind from N-NE and $I_u < 20\%$. The "No traffic" and "Traffic" data set are made of 5154 samples and 2826 samples respectively.

7.8 Other source of discrepancies

7.8.1 Influence of the *u*–*w* cross-spectral densities

The in-phase co-spectrum S_{uw} of wind fluctuations was not included in the present discussion of the buffeting response of the Lysefjord Bridge. The contribution of S_{uw} on the bridge response was found to be lower than 0.3% on average. This is in agreement with Øiseth et al. (2013) who observed that the contribution of the co-spectrum to the dynamic response of a suspension bridge is low compared to the uncertainties related to the modelling of the bridge and wind turbulence properties.

7.8.2 Bridge cables and towers

The estimation of the bridge response has been performed by accounting for the wind load on the bridge deck only. For the Tsing Ma Bridge, Xu

et al. (2000b) observed an increase up to 15% of the computed buffeting lateral response at mid-span when the buffeting load was applied to the whole structure (deck, tower and main cables). For the Lysefjord Bridge, the main cables consist of 6 individual cables installed next to each other, each with the 0.1 m diameter. With the drag coefficient of 2 applied to the whole cable group, the mean drag load on the main cable accounts for 7% of the total one on the bridge. Large discrepancies between the computed and measured lateral displacement response are therefore unlikely to be due to the influence of the bridge towers and main cables on the deck lateral motion.

7.9 Summary

For a given mean wind velocity and a given turbulence intensity, a much larger bridge response is measured for the N-NE exposure than from the S-SW one. This observation is undoubtedly the most important result from Chapter 6 and may be partially explained by topographic effects. The latter are indeed much stronger in the N-NE wind case and their influence on the wind field is visible through non-stationary wind fluctuations, large yaw angles, large turbulence intensities and the non-uniformity of the flow. However, wind data may be affected by the deck, what would partly explain the discrepancies observed between the computed and measured response in the N-NE wind case. Additional flow measurements on the East side of the bridge deck with sonic anemometer will provide data to evaluate this hypothesis.

The limits of the simple bridge model used for the buffeting analysis were highlighted here by its inability in modelling in details the influence of the towers, backstay cables and main cables on the buffeting response. However, it is uncertain whether the influence of traffic loads on the acceleration response of super-long span suspension bridges will be the same as for a medium-span suspension bridges.

Chapter 8

Conclusions

8.1 Summary

This thesis has focused on different aspects of a procedure applied to analyse wind-induced vibrations of a suspension bridge in full-scale. This was done by using the Lysefjord Bridge located in South-West Norway as a study case. Each of the chapters covering the data analysis, i.e. Chapters 3-7, contain summaries of results. The present summary will therefore only give a short review of the main aspects that were investigated.

The first aspect studied is wind turbulence, which was examined for the bridge site at different scales by using traditional sensors (sonic anemometers) and less common ones (wind lidars). The complexity of the terrain surrounding the bridge had considerable effects on the flow so that a case-by-case approach was required to study the buffeting response of the bridge. A similar approach may have to be included to study wind-induced vibrations of future super-long span suspension bridges in fjords. In this thesis, lidar data complemented the sonic anemometers records, e.g. for the evaluation of the flow homogeneity along the bridge span or the wind coherence. Remote sensing technology may become central in wind monitoring over large distances, or for sites that are not easily accessible, such as in the middle of a wide fjord.

Until now, wind lidars have been mainly used for wind energy applications or in the field of meteorology. Their application in the field of wind engineering requires new configurations to find a balance between temporal and spatial resolution good enough to provide reliable estimates of the single and two-point statistics of wind turbulence.

The second aspect is the application of a time-efficient method to identify the suspension bridge modal properties. The method used is an automatic SSI-COV procedure that was observed to properly identify the modal parameters of the Lysefjord Bridge. The time required to analyse one full year of wind and acceleration record was less than half a day by using a personal computer, which was satisfactory. Additional challenges in ambient vibration testing may arise for future bridges characterized with long natural periods. For example, the modal damping ratios of modes with a low eigen-frequency are usually identified with a poor accuracy, which requires the use of longer acceleration records. For wind-sensitive structures, this may become challenging as the modal damping ratios evolve with the mean wind velocity. Another issue is the inability of accelerometers to accurately record signals with low frequency content. This challenge may however be overcome by the use of GNSS sensors, the popularity of which is increasing when it comes to monitor structures with long natural periods (Appendix A).

The third aspect is the analysis of the structural response of the Lysefjord Bridge to wind turbulence. It requires an analysis of the flow properties and bridge modal parameters beforehand. A systematic investigation of this kind in full scale remains a rarity. The data selected corresponds to strong winds that were recorded in the same month of 2014, and that were assumed to represent well the main wind directions recorded at the bridge site (N-NE and S-SW). For each set, 24 hours of high wind velocities with a stable wind direction were available, fulfilling the conditions of statistical significance for the study of wind-induced vibrations of suspension bridges.

The lateral and vertical bridge displacement responses were observed to be considerably larger for the N-NE exposure than for the S-SW one. Consequently, the vertical and lateral computed buffeting responses of the bridge was lower than expected in the N-NE wind situation. The flow from N-NE is characterized by a strong dependency of the yaw angle on the topography making the application of the "cosine rule" challenging. The assumption of flow stationarity and flow uniformity were not fully validated, increasing the inaccuracies of the computed bridge response. Finally, the influence of the bridge deck on the vertical wind turbulent component may not be negligible despite the relatively high position of the sensor above the deck (6 m) . The experience gained from this measurement campaign may therefore be useful for the application of Wind and Structural health Monitoring Systems on other long-span suspension bridges in the world.

8.2 Future works

This thesis investigated the applicability of the buffeting theory to a suspension bridge in full-scale. The estimation of turbulence statistics, the identification of the bridge modal properties and the measurement of the structural response were presented as the central steps of this validation procedure. The estimation of the aerodynamic admittance function was however not much discussed. In the present thesis, only the computed torsional motion required the use of a cross-sectional aerodynamic admittance function. For a wider bridge deck, a more in-depth study of the aerodynamic admittance functions may be required. For a streamlined closed box girder with a geometry close to the one used for the Lysefjord Bridge, Larose (1997) proposed an aerodynamic admittance function based on a series of investigated section models in wind tunnel test. In the past, pressure sensors have been applied in full-scale on suspension bridges with some success (Frandsen, 2001b; Isaksen, 2008). In a near future, the deployment of improved pressure sensors on the bridge deck

may give the opportunity to evaluate the aerodynamic admittance functions in full-scale.

The large amount of data recorded during this thesis offers the possibility to focus on a probabilistic description of the buffeting response of the Lysefjord Bridge. The large dispersion of the RMS of the recorded bridge response motivates such an investigation. In addition, some turbulent statistics such as the integral length scales or the wind coherence may not be estimated accurately by a currently deterministic formulation (Solari, 1987; Solari and Piccardo, 2001). A probabilistic buffeting analysis may lead to a more comprehensive description of the bridge response to wind turbulence in full-scale. This may also help to generalize the properties of the flow recorded in other fjords and characterize wind turbulence in mountainous terrain. When it comes to flow measurements, future works should also focus on the applicability of long-range wind lidars to measure wind turbulence and coherence over cross-wind distances up to several hundreds of meters, which is currently not feasible by using classical sonic anemometers, especially not in the middle of wide fjords.

A time-domain buffeting analysis, conducted using an improved FE model in Abaqus, may allow a more detailed assessment of the influence of the quadratic terms of the wind load or non-stationary flows on the bridge displacement response. A refined response analysis making direct use of the motion-dependant forces from the OMA can also be adopted.

References

Allemang, R. J. and Brown, D. L. (1982). A correlation coefficient for modal vector analysis. In *Proceedings of the 1st international modal analysis conference*, volume 1, pages 110–116. SEM, Orlando.

Angelou, N., Mann, J., Sjöholm, M., and Courtney, M. (2012). Direct measurement of the spectral transfer function of a laser based anemometer. *Review of Scientific Instruments*, 83(3):–.

Antonia, R. A. and Luxton, R. E. (1972). The response of a turbulent boundary layer to a step change in surface roughness. Part 2. Rough-to-smooth. *Journal of Fluid Mechanics*, 53.

Aryan, H., Boynton, R. J., and Walker, S. N. (2013). Analysis of trends between solar wind velocity and energetic electron fluxes at geostationary orbit using the reverse arrangement test. *Journal of Geophysical Research: Space Physics*, 118(2):636–641.

Ashkenazi, V. and Roberts, G. (1997). Experimental monitoring of the Humber Bridge using GPS. In *Proceedings of the Institution of Civil Engineers-Civil Engineering*, volume 120, pages 177–182. London: Published for the Institution of Civil Engineers by Thomas Telford Services, c1992-.

Bakir, P. G. (2011). Automation of the stabilization diagrams for subspace based system identification. *Expert Systems with Applications*, 38(12):14390 – 14397.

Banta, R. M., Darby, L. S., Fast, J. D., Pinto, J. O., Whiteman, C. D., Shaw, W. J., and Orr, B. W. (2004). Nocturnal low-level jet in a mountain basin complex. part I: Evolution and effects on local flows. *Journal of applied meteorology*, 43(10):1348–1365.

Barkwith, A. and Collier, C. G. (2011). Lidar observations of flow variability over complex terrain. *Meteorological Applications*, 18(3):372–382.

Barnard, R. (1981). Wind loads on cantilevered roof structures. *Journal of Wind Engineering and Industrial Aerodynamics*, 8(1–2):21 – 30.

Beck, T. W., Housh, T. J., Weir, J. P., Cramer, J. T., Vardaxis, V., Johnson, G. O., Coburn, J. W., Malek, M. H., and Mielke, M. (2006). An examination of the runs test, reverse arrangements test, and modified reverse arrangements test for assessing surface EMG signal stationarity. *Journal of neuroscience methods*, 156(1):242–248.

Bendat, J. and Piersol, A. (2011). *Random Data: Analysis and Measurement Procedures*. Wiley Series in Probability and Statistics. Wiley.

Bietry, J., Delaunay, D., and Conti, E. (1995). Comparison of full-scale measurement and computation of wind effects on a cable-stayed bridge. *Journal of wind engineering and industrial aerodynamics*, 57(2):225–235.

Bleich, F. (1950). *The mathematical theory of vibration in suspension bridges*. US Government Printing Office.

Bogunović Jakobsen, J. (1995). *Fluctuating wind load and response of a line-like engineering structure with emphasis on motion-induced wind forces*. PhD thesis, Universitetet i Trondheim.

Bogunović Jakobsen, J. (1997). Span-wise structure of lift and overturning moment on a motionless bridge girder. *Journal of wind engineering and industrial aerodynamics*, 69:795–805.

Breuer, P., Chmielewski, T., Górski, P., and Konopka, E. (2002). Application of GPS technology to measurements of displacements of high-rise structures due to weak winds. *Journal of Wind Engineering and Industrial Aerodynamics*, 90(3):223–230.

Brincker, R., Zhang, L., and Andersen, P. (2001). Modal identification of output-only systems using frequency domain decomposition. *Smart materials and structures*, 10(3):441.

Brownjohn, J., Bocciolone, M., Curami, A., Falco, M., and Zasso, A. (1994). Humber Bridge full-scale measurement campaigns 1990–1991. *Journal of Wind Engineering and Industrial Aerodynamics*, 52:185–218.

Brownjohn, J., Dumanoglu, A., Severn, R., and Taylor, C. (1987). Ambient vibration measurements of the Humber suspension bridge and comparison with calculated characteristics. *Proceedings of the Institution of Civil Engineers*, 83(3):561–600.

Brownjohn, J., Magalhaes, F., Caetano, E., and Cunha, A. (2010). Ambient vibration re-testing and operational modal analysis of the Humber Bridge. *Engineering Structures*, 32(8):2003–2018.

Brownjohn, J. M., De Stefano, A., Xu, Y.-L., Wenzel, H., and Aktan, A. E. (2011). Vibration-based monitoring of civil infrastructure: challenges and successes. *Journal of Civil Structural Health Monitoring*, 1(3-4):79–95.

Bucher, C. G. and Lin, Y. K. (1988). Stochastic stability of bridges considering coupled modes. *Journal of Engineering Mechanics*, 114(12):2055–2071.

Calhoun, R., Heap, R., Princevac, M., Newsom, R., Fernando, H., and Ligon, D. (2006). Virtual towers using coherent Doppler lidar during the joint urban 2003 dispersion experiment. *Journal of Applied meteorology and climatology*, 45(8):1116–1126.

Cao, S. (2013). *Strong Winds and Their Characteristics*, pages 1–25. Springer Japan, Tokyo.

Carter, G., Knapp, C., and Nuttall, A. H. (1973). Estimation of the magnitude-squared coherence function via overlapped fast fourier transform processing. *Audio and Electroacoustics, IEEE Transactions on*, 21(4):337–344.

Chan, W., Xu, Y., Ding, X., and Dai, W. (2006a). An integrated GPS–accelerometer data processing technique for structural deformation monitoring. *Journal of Geodesy*, 80(12):705–719.

Chan, W.-S., Xu, Y.-L., Ding, X.-L., Xiong, Y.-L., and Dai, W.-J. (2006b). Assessment of dynamic measurement accuracy of GPS in three directions. *Journal of Surveying Engineering*, 132(3):108–117.

Chang, M. and Pakzad, S. N. (2013). Modified natural excitation technique for stochastic modal identification. *Journal of Structural Engineering*, 139(10):1753–1762.

Chen, J., Hui, M., and Xu, Y. (2007). A comparative study of stationary and non-stationary wind models using field measurements. *Boundary-layer meteorology*, 122(1):105–121.

Chen, J., Xu, Y., and Zhang, R. (2004). Modal parameter identification of Tsing Ma suspension bridge under Typhoon Victor: EMD-HT method. *Journal of Wind Engineering and Industrial Aerodynamics*, 92(10):805 – 827.

Chen, L. and Letchford, C. W. (2004). A deterministic–stochastic hybrid model of downbursts and its impact on a cantilevered structure. *Engineering structures*, 26(5):619–629.

Chen, X. and Kareem, A. (2002). Advanced analysis of coupled buffeting response of bridges: a complex modal decomposition approach. *Probabilistic Engineering Mechanics*, 17(2):201–213.

Chen, X., Matsumoto, M., and Kareem, A. (2000a). Aerodynamic coupling effects on flutter and buffeting of bridges. *Journal of Engineering Mechanics*, 126(1):17–26.

Chen, X., Matsumoto, M., and Kareem, A. (2000b). Time domain flutter and buffeting response analysis of bridges. *Journal of Engineering Mechanics*, 126(1):7–16.

Cheynet, E., Bogunović Jakobsen, J., and Snæbjörnsson, J. (2015a). Buffeting response of a bridge at the inlet of a fjord. In *ICWE14: 14th International Conference on Wind Engineering*.

Cheynet, E., Bogunović Jakobsen, J., and Snæbjörnsson, J. (2016a). Wind-induced vibrations monitoring with satellite navigation. In *19th IABSE Congress Stockholm, 21-23 September 2016*.

Cheynet, E., Bogunović Jakobsen, J., and Snæbjörnsson, J. T. (2015b). Full scale monitoring of wind and traffic induced response of a suspension bridge. In *Proc. 6th International Conference on Experimental Vibration Analysis for Civil Engineering Structures (EVACES)*.

Cheynet, E., Bogunović Jakobsen, J., Svardal, B., Reuder, J., and Kumer, V. (2016b). Wind coherence measurement by a single pulsed Doppler wind lidar. *Energy Procedia*, 94:462 – 477. 13th Deep Sea Offshore Wind R&D Conference, EERA DeepWind'2016.

Cheynet, E., Jakobsen, J. B., Snæbjörnsson, J., Angelou, N., Mikkelsen, T., Mikael, S., and Svardal, B. (2016c). Full-scale observation of the flow downstream of a suspension bridge deck. In *BBAA VIII: 8th International Colloquium on Bluff Body Aerodynamics and Applications*.

Courtney, M., Wagner, R., and Lindelöw, P. (2008). Testing and comparison of lidars for profile and turbulence measurements in wind energy. In *IOP Conference Series: Earth and Environmental Science*, volume 1. IOP Publishing.

Cunha, A., Caetano, E., and Delgado, R. (2001). Dynamic tests on large cable-stayed bridge. *Journal of Bridge Engineering*, 6(1):54–62.

Davenport, A. (1963). *The Relationship of Wind Structure to Wind Loading*. National Physical Laboratory.

Davenport, A. (1975). Perspectives on the full-scale measurement of wind effects. *Journal of Wind Engineering and Industrial Aerodynamics*, 1:23 – 54.

Davenport, A. G. (1961a). The application of statistical concepts to the wind loading of structures. In *ICE Proceedings*, volume 19, pages 449–472.

Davenport, A. G. (1961b). The spectrum of horizontal gustiness near the ground in high winds. *Quarterly Journal of the Royal Meteorological Society*, 87(372):194–211.

Davenport, A. G. (1962). The response of slender, line-like structures to a gusty wind. *Proceedings of the Institution of Civil Engineers*, 23(3):389–408.

de Battista, N., Brownjohn, J. M., Tan, H. P., and Koo, K.-Y. (2015). Measuring and modelling the thermal performance of the Tamar Suspension Bridge using a wireless sensor network. *Structure and Infrastructure Engineering*, 11(2):176–193.

Denoël, V. (2005). *Application des méthodes d'analyse stochastique à l' étude des effets du vent sur les structures du génie civil*. Phd thesis, University of Liège.

Denoël, V. and Degée, H. (2006). A simplified method to account for the non linearity of aerodynamic coefficients in the analysis of wind-loaded bridges. In *NCTAM, 7th National Congres on Theoretical and Applied Mechanics*, page 7.

Diana, G., Falco, M., Bruni, S., Cigada, A., Larose, G., Darnsgaard, A., and Collina, A. (1995). Third asian-pacific symposium on wind engineering comparisons between wind tunnel tests on a full aeroelastic model of the

proposed bridge over stretto di messina and numerical results. *Journal of Wind Engineering and Industrial Aerodynamics*, 54:101 – 113.

Ding, Y. and Li, A. (2011). Temperature-induced variations of measured modal frequencies of steel box girder for a long-span suspension bridge. *International Journal of Steel Structures*, 11(2):145–155.

Drew, D. R., Barlow, J. F., and Lane, S. E. (2013). Observations of wind speed profiles over greater london, uk, using a Doppler lidar. *Journal of Wind Engineering and Industrial Aerodynamics*, 121(0):98 – 105.

EN 1991-1-4 (1991). 1-4: 2005 Eurocode 1: Actions on structures – General actions – Wind actions.

ESA (2012). Galileo fact sheet. http://download.esa.int/docs/Galileo_IOV_Launch/Galileo_factsheet_2012.pdf. Accessed: 2013-02-15.

ESDU 86010 (2001). Characteristics of atmospheric turbulence near the ground part iii: variations in space and time for strong winds (neutral atmosphere).

Farrar, C. and James III, G. (1997). System identification from ambient vibration measurements on a bridge. *Journal of Sound and Vibration*, 205(1):1 – 18.

Frandsen, J. (2001a). Simultaneous pressures and accelerations measured full-scale on the great belt east suspension bridge. *Journal of Wind Engineering and Industrial Aerodynamics*, 89(1):95 – 129.

Frandsen, J. (2001b). Simultaneous pressures and accelerations measured full-scale on the Great Belt East suspension bridge. *Journal of Wind Engineering and Industrial Aerodynamics*, 89(1):95 – 129.

Friedrich, K., Lundquist, J. K., Aitken, M., Kalina, E. A., and Marshall, R. F. (2012). Stability and turbulence in the atmospheric boundary layer: A comparison of remote sensing and tower observations. *Geophysical Research Letters*, 39.

Fuertes, F. C., Iungo, G. V., and Porté-Agel, F. (2014). 3D turbulence measurements using three synchronous wind lidars: validation against sonic anemometry. *Journal of Atmospheric and Oceanic Technology*, 31(7):1549–1556.

Fujino, Y., Murata, M., Okano, S., and Takeguchi, M. (2000). Monitoring system of the Akashi Kaikyō Bridge and displacement measurement using GPS. In *SPIE's 5th Annual International Symposium on Nondestructive Evaluation and Health Monitoring of Aging Infrastructure*, pages 229–236. International Society for Optics and Photonics.

Fujino, Y. and Siringoringo, D. (2013). Vibration mechanisms and controls of long-span bridges: a review. *Structural Engineering International*, 23(3):248–268.

Fulop, S. (2011). *Speech Spectrum Analysis*. Signals and Communication Technology. Springer Berlin Heidelberg.

Garnier, S. (2015). viridis: Matplotlib default color map. *R package version 0.2*.

Harris, R. (1975). Editorial. *Journal of Wind Engineering and Industrial Aerodynamics*, 1:1 – 2.

Hay, J. (1984). Analyses of wind and response data from the Wye and Erskine Bridges and comparison with theory. *Journal of wind engineering and industrial aerodynamics*, 17(1):31–49.

Hjorth-Hansen, E. (1993a). Fluctuating drag, lift anf overturning moment for a line-like structure predicted (primarily) from static, mean loads. *Wind Engineering, Lecture note no*, 2.

Hjorth-Hansen, E. (1993b). Fluctuating drag,lift and overturning moment for a line-like structure predicted (primarily) from static, mean loads. Technical report, Norges Tekniske Høgskole.

Hjorth-Hansen, E., Jakobsen, A., and Strømmen, E. (1992). Wind buffeting of a rectangular box girder bridge. *Journal of Wind Engineering and Industrial Aerodynamics*, 42(1):1215–1226.

Hofmann-Wellenhof, B., Lichtenegger, H., and Wasle, E. (2007). *GNSS – Global Navigation Satellite Systems: GPS, GLONASS, Galileo, and more*. Springer Vienna.

Holmes, J. (1975). Prediction of the response of a cable-stayed bridge to turbulence. In *Proceedings of 4th International Conference on Buildings and Structures London, England. Cambridge: Cambridge University Press*, pages 187–198.

Holmes, J. (2007). *Wind Loading of Structures*. CRC Press.

Hu, L., Xu, Y.-L., and Huang, W.-F. (2013). Typhoon-induced non-stationary buffeting response of long-span bridges in complex terrain. *Engineering Structures*, 57:406 – 415.

Huang, C. and Yeh, C. (1999). Some properties of randomdec signatures. *Mechanical Systems and Signal Processing*, 13(3):491–507.

Huang, N. E., Shen, Z., Long, S. R., Wu, M. C., Shih, H. H., Zheng, Q., Yen, N.-C., Tung, C. C., and Liu, H. H. (1998). The empirical mode decomposition and the Hilbert spectrum for nonlinear and non-stationary time series analysis. In *Proceedings of the Royal Society of London A: Mathematical, Physical and Engineering Sciences*, volume 454, pages 903–995. The Royal Society.

Hui, M., Larsen, A., and Xiang, H. (2009a). Wind turbulence characteristics study at the Stonecutters Bridge site: Part II: Wind power spectra, integral length scales and coherences. *Journal of Wind Engineering and Industrial Aerodynamics*, 97(1):48 – 59.

Hui, M., Larsen, A., and Xiang, H. (2009b). Wind turbulence characteristics study at the Stonecutters Bridge site: Part I:mean wind and turbulence intensities. *Journal of Wind Engineering and Industrial Aerodynamics*, 97(1):22 – 36.

Ibrahim, S. (1977). Random decrement technique for modal identification of structures. *Journal of Spacecraft and Rockets*, 14(11):696–700.

IEC 61400-1 (2005). *IEC 61400-1 Wind turbines –Part 1: Design requirements*.

Im, S. B., Hurlebaus, S., and Kang, Y. J. (2011a). Summary review of GPS technology for structural health monitoring. *Journal of Structural Engineering*, 139(10):1653–1664.

Im, S. B., Hurlebaus, S., and Kang, Y. J. (2011b). Summary review of GPS technology for structural health monitoring. *Journal of Structural Engineering*, 139(10):1653–1664.

Irwin, H. and Wardlaw, R. (1976). Wind tunnel and analytical investigations of the response of Lions' Gate Bridge to turbulent wind. National Research Council of Canada. Technical report, NAE LTR-LA-210.

Isaksen, B. (2008). *Experimental Investigations of Wind Loading on a Suspension Bridge Girder*. Phd thesis, NTNU.

Jain, A., Jones, N. P., and Scanlan, R. H. (1996a). Coupled aeroelastic and aerodynamic response analysis of long-span bridges. *Journal of Wind Engineering and Industrial Aerodynamics*, 60:69–80.

Jain, A., Jones, N. P., and Scanlan, R. H. (1996b). Coupled flutter and buffeting analysis of long-span bridges. *Journal of Structural Engineering*, 122(7):716–725.

Jakobsen, J. B. and Larose, G. (1999). Estimation of aerodynamic derivatives from ambient vibration data. In *Wind Engineering into the 21st Century, Proceedings of the Tenth International Conference on Wind Engineering, Balkema, Rotterdam*, pages 837–844.

Juang, J.-N. and Pappa, R. S. (1985). An eigensystem realization algorithm for modal parameter identification and model reduction. *Journal of guidance, control, and dynamics*, 8(5):620–627.

Kaimal, J., Wyngaard, J., Izumi, Y., and Coté, O. (1972). Spectral characteristics of surface-layer turbulence. Technical report, DTIC Document.

Kareem, A. a., Tognarelli, M., and Gurley, K. (1998). Modeling and analysis of quadratic term in the wind effects on structures. *Journal of Wind Engineering and Industrial Aerodynamics*, 74:1101–1110.

Karlsson, C. J., Olsson, F. Å., Letalick, D., and Harris, M. (2000). All-fiber multifunction continuous-wave coherent laser radar at 1.55 μm for range, speed, vibration, and wind measurements. *Applied optics*, 39(21):3716–3726.

Katsuchi, H., Jones, N., Scanlan, R., and Akiyama, H. (1998). Multi-mode flutter and buffeting analysis of the akashi-kaikyo bridge. *Journal of Wind Engineering and Industrial Aerodynamics*, 77:431–441.

Katsuchi, H., Jones, N. P., and Scanlan, R. H. (1999). Multimode coupled flutter and buffeting analysis of the akashi-kaikyo bridge. *Journal of Structural Engineering*, 125(1):60–70.

Kijewski-Correa, T., Kareem, A., and Kochly, M. (2006). Experimental verification and full-scale deployment of global positioning systems to monitor the dynamic response of tall buildings. *Journal of Structural Engineering*, 132(8):1242–1253.

Kim, B. H., Stubbs, N., and Park, T. (2005). A new method to extract modal parameters using output-only responses. *Journal of Sound and Vibration*, 282(1):215–230.

Kim, C.-Y., Jung, D.-S., Kim, N.-S., Kwon, S.-D., and Feng, M. Q. (2003). Effect of vehicle weight on natural frequencies of bridges measured from traffic-induced vibration. *Earthquake Engineering and Engineering Vibration*, 2(1):109–115.

Kimura, K. and Tanaka, H. (1992). Bridge buffeting due to wind with yaw angles. *Journal of Wind Engineering and Industrial Aerodynamics*, 42(1):1309 – 1320.

Koo, K., Brownjohn, J., List, D., and Cole, R. (2013). Structural health monitoring of the Tamar suspension bridge. *Structural Control and Health Monitoring*, 20(4):609–625.

Krenk, S. (1996). Wind field coherence and dynamic wind forces. In *IUTAM symposium on advances in nonlinear stochastic mechanics*, pages 269–278. Springer.

Kristensen, L. and Jensen, N. O. (1979). Lateral coherence in isotropic turbulence and in the natural wind. *Boundary-Layer Meteorology*, 17(3):353–373.

Kristensen, L. and Kirkegaard, P. (1986). *Sampling problems with spectral coherence*. Risø National Laboratory.

Kristensen, L., Kirkegaard, P., Mann, J., Mikkelsen, T., Nielsen, M., and Sjöholm, M. (2010). Spectral coherence along a lidar-anemometer beam. Technical report, Danmarks Tekniske Universitet, Risø Nationallaboratoriet for Bæredygtig Energi.

Kristensen, L., Kirkegaard, P., and Mikkelsen, T. (2011). *Determining the velocity fine structure by a laser anemometer with fixed orientation*. Danmarks Tekniske Universitet, Risø Nationallaboratoriet for Bæredygtig Energi.

Kumer, V.-M., Reuder, J., and Furevik, B. R. (2014). A comparison of lidar and radiosonde wind measurements. *Energy Procedia*, 53(0):214 – 220.

Kumer, V.-M., Reuder, J., Svardal, B., Sætre, C., and Eecen, P. (2015). Characterisation of single wind turbine wakes with static and scanning wintwex-w lidar data. *Energy Procedia*, 80:245 – 254. 12th Deep Sea Offshore Wind R&D Conference, EERA DeepWind'2015.

Lane, S., Barlow, J., and Wood, C. (2013). An assessment of a three-beam Doppler lidar wind profiling method for use in urban areas. *Journal of Wind Engineering and Industrial Aerodynamics*, 119(0):53 – 59.

Lange, J., Mann, J., Angelou, N., Berg, J., Sjöholm, M., and Mikkelsen, T. (2015). Variations of the wake height over the Bolund escarpment measured by a scanning lidar. *Boundary-Layer Meteorology*, pages 1–13.

Larose, G. (1997). *The dynamic action of gusty winds on long-span bridges*. Technical University of Denmark.

Larose, G., Tanaka, H., Gimsing, N., and Dyrbye, C. (1998). Direct measurements of buffeting wind forces on bridge decks. *Journal of Wind Engineering and Industrial Aerodynamics*, 74–76:809 – 818.

Larsén, X. G. and Mann, J. (2006). The effects of disjunct sampling and averaging time on maximum mean wind speeds. *Journal of Wind Engineering and Industrial Aerodynamics*, 94(8):581 – 602.

Lenschow, D., Lothon, M., Mayor, S., Sullivan, P., and Canut, G. (2012). A comparison of higher-order vertical velocity moments in the convective boundary layer from lidar with in situ measurements and large-eddy simulation. *Boundary-Layer Meteorology*, 143(1):107–123.

Lenschow, D. H. and B. Stankov, B. (1986). Length scales in the convective boundary layer. *Journal of Atmospheric Sciences*, 43:1198–1209.

Liepmann, H. (1952). On the application of statistical concepts to the buffeting problem. *Journal of the Aeronautical Science*, 19(2):793–800.

Lombardo, F. T., Smith, D. A., Schroeder, J. L., and Mehta, K. C. (2014). Thunderstorm characteristics of importance to wind engineering. *Journal of Wind Engineering and Industrial Aerodynamics*, 125:121–132.

Lothon, M., Lenschow, D., and Mayor, S. (2006). Coherence and scale of vertical velocity in the convective boundary layer from a Doppler lidar. *Boundary-Layer Meteorology*, 121(3):521–536.

Lothon, M., Lenschow, D. H., and Mayor, S. D. (2009). Doppler lidar measurements of vertical velocity spectra in the convective planetary boundary layer. *Boundary-Layer Meteorology*, 132(2):205–226.

Lovse, J., Teskey, W., Lachapelle, G., and Cannon, M. (1995). Dynamic deformation monitoring of tall structure using GPS technology. *Journal of surveying engineering*, 121(1):35–40.

Luco, J. E. and Turmo, J. (2010). Linear vertical vibrations of suspension bridges: A review of continuum models and some new results. *Soil Dynamics and Earthquake Engineering*, 30(9):769–781.

Luke, Y. L. (1962). *Integrals of Bessel functions*. McGraw-Hill.

Macdonald, J. H. (2003). Evaluation of buffeting predictions of a cable-stayed bridge from full-scale measurements. *Journal of Wind Engineering and Industrial Aerodynamics*, 91(12–15):1465 – 1483.

Macdonald, J. H. (2004). Dynamic behaviour of the Clifton suspension bridge: response to wind loading. Technical report, Bristol Earthquake and Engineering Laboratory Ltd.

Macdonald, J. H. and Daniell, W. E. (2005). Variation of modal parameters of a cable-stayed bridge identified from ambient vibration measurements and {FE} modelling. *Engineering Structures*, 27(13):1916 – 1930.

Magalhães, F. and Cunha, A. (2011). Explaining operational modal analysis with data from an arch bridge. *Mechanical Systems and Signal Processing*, 25(5):1431 – 1450.

Magalhães, F., Cunha, A., and Caetano, E. (2009). Online automatic identification of the modal parameters of a long span arch bridge. *Mechanical Systems and Signal Processing*, 23(2):316 – 329.

Mann, J. (2000). The spectral velocity tensor in moderately complex terrain. *Journal of Wind Engineering and Industrial Aerodynamics*, 88(2–3):153 – 169. International Conference on wind Engineering.

Mann, J., Cariou, J.-P. C., Parmentier, R. M., Wagner, R., Lindelöw, P., Sjöholm, M., and Enevoldsen, K. (2009). Comparison of 3D turbulence measurements using three staring wind lidars and a sonic anemometer. *Meteorologische Zeitschrift*, 18(2):135–140.

Matsuda, K., Hikami, Y., Fujiwara, T., and Moriyama, A. (1999). Aerodynamic admittance and the 'strip theory' for horizontal buffeting forces on a bridge deck. *Journal of Wind Engineering and Industrial Aerodynamics*, 83(1–3):337 – 346.

Meng, X., Dodson, A., and Roberts, G. (2007). Detecting bridge dynamics with GPS and triaxial accelerometers. *Engineering Structures*, 29(11):3178–3184.

Mikkelsen, O. (2013). *Modelling of wind loads and wind-induced response of a long-span bridge in time–domain.* PhD thesis, Universitetet i Stavanger.

Mikkelsen, T., Courtney, M., Antoniou, I., and Mann, J. (2008a). *Wind scanner: A full-scale laser facility for wind and turbulence measurements around large wind turbines*. European Wind Energy Association (EWEA).

Mikkelsen, T., Mann, J., Courtney, M., and Sjöholm, M. (2008b). Windscanner: 3-D wind and turbulence measurements from three steerable Doppler lidars. In *IOP conference series: Earth and Environmental Science*, volume 1. IOP Publishing.

Miyata, T., Yamada, H., Katsuchi, H., and Kitagawa, M. (2002). Full-scale measurement of Akashi–Kaikyō Bridge during typhoon. *Journal of wind engineering and industrial aerodynamics*, 90(12):1517–1527.

Morfiadakis, E., Glinou, G., and Koulouvari, M. (1996). The suitability of the von Kármán spectrum for the structure of turbulence in a complex terrain wind farm. *Journal of Wind Engineering and Industrial Aerodynamics*, 62(2):237–257.

Moschas, F. and Stiros, S. (2014). Dynamic multipath in structural bridge monitoring: an experimental approach. *GPS solutions*, 18(2):209–218.

Nagayama, T., Abe, M., Fujino, Y., and Ikeda, K. (2005). Structural identification of a nonproportionally damped system and its application to a full-scale suspension bridge. *Journal of structural engineering*, 131(10):1536–1545.

Nakamura, S. (2000). GPS measurement of wind-induced suspension bridge girder displacements. *Journal of Structural Engineering*, 126(12):1413–1419.

Namini, A., Albrecht, P., and Bosch, H. (1992). Finite element-based flutter analysis of cable-suspended bridges. *Journal of Structural Engineering*, 118(6):1509–1526.

Newsom, R., Calhoun, R., Ligon, D., and Allwine, J. (2008). Linearly organized turbulence structures observed over a suburban area by dual-Doppler lidar. *Boundary-Layer Meteorology*, 127(1):111–130.

Newsom, R. K., Berg, L. K., Shaw, W. J., and Fischer, M. L. (2015). Turbine-scale wind field measurements using dual-Doppler lidar. *Wind Energy*, 18(2):219–235.

Nickitopoulou, A., Protopsalti, K., and Stiros, S. (2006). Monitoring dynamic and quasi-static deformations of large flexible engineering structures with GPS: accuracy, limitations and promises. *Engineering Structures*, 28(10):1471–1482.

Nikitas, N., Macdonald, J. H., and Jakobsen, J. B. (2011). Identification of flutter derivatives from full-scale ambient vibration measurements of the Clifton Suspension Bridge. *Wind and Structures*, 14(3):221–238.

Norwegian Ministry of Transport and Communication (2013). National transport plan 2014 – 2023. report to storting (white paper) summary. Technical report, Meld. St. 26 (2012–2013).

Øiseth, O., Rönnquist, A., and Sigbjörnsson, R. (2010). Simplified prediction of wind-induced response and stability limit of slender long-span suspension bridges, based on modified quasi-steady theory: a case study. *Journal of wind engineering and industrial aerodynamics*, 98(12):730–741.

Øiseth, O., Rönnquist, A., and Sigbjörnsson, R. (2013). Effects of co-spectral densities of atmospheric turbulence on the dynamic response of cable-supported bridges: A case study. *Journal of Wind Engineering and Industrial Aerodynamics*, 116:83 – 93.

Panofsky, H. A., Brier, G. W., and Best, W. H. (1958). *Some application of statistics to meteorology*. Earth and Mineral Sciences Continuing Education, College of Earth and Mineral Sciences, Pennsylvania State University.

Peña, A., Hasager, C. B., Gryning, S.-E., Courtney, M., Antoniou, I., and Mikkelsen, T. (2009). Offshore wind profiling using light detection and ranging measurements. *Wind Energy*, 12(2):105–124.

Pearson, G., Davies, F., and Collier, C. (2009). An analysis of the performance of the ufam pulsed Doppler lidar for observing the boundary layer. *Journal of Atmospheric and Oceanic Technology*, 26(2):240–250.

Peeters, B., Van der Auweraer, H., Guillaume, P., and Leuridan, J. (2004). The PolyMAX frequency-domain method: a new standard for modal parameter estimation? *Shock and Vibration*, 11(3-4):395–409.

Priestley, M. B. (1966). Design relations for non-stationary processes. *Journal of the Royal Statistical Society. Series B (Methodological)*, 28(1):228–240.

Reitebuch, O. (2012). Wind lidar for atmospheric research. In Schumann, U., editor, *Atmospheric Physics*, Research Topics in Aerospace, pages 487–507. Springer Berlin Heidelberg.

Roberts, G., Meng, X., and Dodson, A. (2004). Integrating a global positioning system and accelerometers to monitor the deflection of bridges. *Journal of Surveying Engineering*, 130(2):65–72.

Saranyasoontorn, K., Manuel, L., and Veers, P. S. (2004). A comparison of standard coherence models for inflow turbulence with estimates from field measurements. *Journal of Solar Energy Engineering*, 126(4):1069–1082.

Sathe, A. and Mann, J. (2013). A review of turbulence measurements using ground-based wind lidars. *Atmospheric Measurement Techniques*, 6.

Sathe, A., Mann, J., Gottschall, J., and Courtney, M. (2011). Can wind lidars measure turbulence? *Journal of Atmospheric and Oceanic Technology*, 28(7):853–868.

Sathe, A., Mann, J., Vasiljevic, N., and Lea, G. (2015). A six-beam method to measure turbulence statistics using ground-based wind lidars. *Atmospheric Measurement Techniques*, 8(2):729–740.

Scanlan, R. (1975). The action of flexible bridges under wind, II: Buffeting theory. *Journal of Sound and Vibration*, 60(2):201 – 211.

Scanlan, R. H. (1993). Bridge buffeting by skew winds in erection stages. *Journal of Engineering Mechanics*, 119(2):251–269.

Schneemann, J., Trabucchi, D., Trujillo, J. J., and Kühn, M. (2014). Comparing measurements of the horizontal wind speed of a 2D multi-lidar and a cup anemometer. In *Journal of Physics: Conference Series*, volume 555, page 012091. IOP Publishing.

Selberg, A. (1961). *Oscillation and aerodynamic stability of suspension bridges*. Acta polytechnica Scandinavica.Civil engineering and building construction series. Norges Teknisk-Naturvitenskapelige Forskningsrad.

Siegel, S. and Castellan, N. (1988). *Nonparametric Statistics for the Behavioral Sciences*. McGraw-Hill international editions. Statistics series. McGraw-Hill.

Sigbjörnsson, R. and Hjorth-Hansen, E. (1981). Along-wind response of suspension bridges with special reference to stiffening by horizontal cables. *Engineering Structures*, 3(1):27–37.

Simiu, E. and Scanlan, R. H. (1996). *Wind effects on structures*. Wiley.

Simley, E., Angelou, N., Mikkelsen, T., Sjöholm, M., Mann, J., and Pao, L. Y. (2016). Characterization of wind velocities in the upstream induction zone of a wind turbine using scanning continuous-wave lidars. *Journal of Renewable and Sustainable Energy*, 8(1).

Siringoringo, D. M. and Fujino, Y. (2008). System identification of suspension bridge from ambient vibration response. *Engineering Structures*, 30(2):462–477.

Sjöholm, M., Angelou, N., Hansen, P., Hansen, K. H., Mikkelsen, T., Haga, S., Silgjerd, J. A., and Starsmore, N. (2014). Two-dimensional rotorcraft downwash flow field measurements by lidar-based wind scanners with agile beam steering. *Journal of Atmospheric & Oceanic Technology*, 31(4):930 – 937.

Sjöholm, M., Kapp, S., Kristensen, L., and Mikkelsen, T. (2011). Experimental evaluation of a model for the influence of coherent wind lidars on their remote measurements of atmospheric boundary-layer turbulence. In *SPIE Remote Sensing*. International Society for Optics and Photonics.

Sjöholm, M., Mikkelsen, T., Mann, J., Enevoldsen, K., and Courtney, M. (2008). Time series analysis of continuous-wave coherent Doppler lidar wind measurements. *IOP Conference Series: Earth and Environmental Science*, 1(1):012051.

Sjöholm, M., Mikkelsen, T., Mann, J., Enevoldsen, K., and Courtney, M. (2009). Spatial averaging-effects on turbulence measured by a continuous-wave coherent lidar. *Meteorologische Zeitschrift*, 18(3):281–287.

Smalikho, I. (1995). On measurement of the dissipation rate of the turbulent energy with a cw Doppler lidar. *Atmospheric and Ocean Optics*, 8:788–793.

Smith, D. A., Harris, M., Coffey, A. S., Mikkelsen, T., Jørgensen, H. E., Mann, J., and Danielian, R. (2006). Wind lidar evaluation at the Danish wind test site in Høvsøre. *Wind Energy*, 9(1-2):87–93.

Sohn, H., Dzwonczyk, M., Straser, E. G., Kiremidjian, A. S., Law, K. H., and Meng, T. (1999). An experimental study of temperature effect on modal parameters of the Alamosa Canyon Bridge. *Earthquake Engineering & Structural Dynamics*, 28(8):879–897.

Solari, G. (1987). Turbulence modeling for gust loading. *Journal of Structural Engineering*, 113(7):1550–1569.

Solari, G. and Piccardo, G. (2001). Probabilistic 3-D turbulence modeling for gust buffeting of structures. *Probabilistic Engineering Mechanics*, 16(1):73–86.

Sonnenschein, C. M. and Horrigan, F. A. (1971). Signal-to-noise relationships for coaxial systems that heterodyne backscatter from the atmosphere. *Appl. Opt.*, 10(7):1600–1604.

SRTM, N. (2014). Shuttle Radar Topography Mission. *Jet Propulsion Laboratory, California Institute of Technology*, page 236.

Stawiarski, C., Träumner, K., Kottmeier, C., Knigge, C., and Raasch, S. (2015). Assessment of surface-layer coherent structure detection in dual-Doppler lidar data based on virtual measurements. *Boundary-Layer Meteorology*, 156(3):371–393.

Steigen, R. O. (2011). Modeling and analyzing a suspension bridge in light of deterioration of the main cable wires. Master's thesis, University of Stavanger.

Strømmen, E. N. (2014). *Structural Dynamics*, chapter Eigenvalue Calculations of Continuous Systems, pages 89–159. Springer International Publishing, Cham.

Su, Y., Huang, G., and Xu, Y.-l. (2015). Derivation of time-varying mean for non-stationary downburst winds. *Journal of Wind Engineering and Industrial Aerodynamics*, 141:39–48.

Sun, D., Xu, Y., Ko, J., and Lin, J. (1999). Fully coupled buffeting analysis of long-span cable-supported bridges: formulation. *Journal of Sound and Vibration*, 228(3):569–588.

Tamura, Y., Matsui, M., Pagnini, L.-C., Ishibashi, R., and Yoshida, A. (2002). Measurement of wind-induced response of buildings using RTK-GPS. *Journal of Wind Engineering and Industrial Aerodynamics*, 90(12):1783–1793.

Tamura, Y. and Suganuma, S.-y. (1996). Evaluation of amplitude-dependent damping and natural frequency of buildings during strong winds. *Journal of wind engineering and industrial aerodynamics*, 59(2):115–130.

Tanaka, H. and Davenport, A. G. (1982). Response of taut strip models to turbulent wind. *Journal of the Engineering Mechanics Division*, 108(1):33–49.

Teunissen, H. (1980). Structure of mean winds and turbulence in the planetary boundary layer over rural terrain. *Boundary-Layer Meteorology*, 19(2):187–221.

Thorbek, L. and Hansen, S. (1998). Coupled buffeting response of suspension bridges. *Journal of Wind Engineering and Industrial Aerodynamics*, 74:839–847.

Toriumi, R., Katsuchi, H., and Furuya, N. (2000). A study on spatial correlation of natural wind. *Journal of Wind Engineering and Industrial Aerodynamics*, 87(2):203–216.

Trabucchi, D., Steinfeld, G., Bastine, D., Trujillo, J.-J., Schneemann, J., and Kühn, M. (2015). Study of wake meandering by means of fixed point lidar measurements: Spectral analysis of line-of-sight wind component. *Journal of Physics: Conference Series*, 625(1):012016.

Tveiten, J. (2012). Dynamic analysis of a suspension bridge. Master's thesis, University of Stavanger.

van Overschee, P. and de Moor, B. (1996). *Subspace Identification for Linear Systems: Theory — Implementation — Applications*. Springer.

Vickery, B. J. (1970). On the reliability of gust loading factors. In *Proc., Technical Meeting Concerning Wind Loads on Buildings and Structures, Building Science Series*, volume 30, pages 296–312.

von Kármán, T. (1948). Progress in the statistical theory of turbulence. *Proceedings of the National Academy of Sciences*, 34(11):530–539.

Wang, H., Li, A., and Hu, R. (2011). Comparison of ambient vibration response of the Runyang Suspension Bridge under skew winds with time-domain numerical predictions. *Journal of Bridge Engineering*, 16(4):513–526.

Wang, H., Li, A., Niu, J., Zong, Z., and Li, J. (2013). Long-term monitoring of wind characteristics at Sutong Bridge site. *Journal of Wind Engineering and Industrial Aerodynamics*, 115:39–47.

Wang, H., Wu, T., Tao, T., Li, A., and Kareem, A. (2016). Measurements and analysis of non-stationary wind characteristics at sutong bridge in typhoon damrey. *Journal of Wind Engineering and Industrial Aerodynamics*, 151:100 – 106.

Weitkamp, C. (2005). *Lidar: Range-Resolved Optical Remote Sensing of the Atmosphere*. Springer Series in Optical Sciences. Springer.

Welch, P. D. (1967). The use of fast fourier transform for the estimation of power spectra: A method based on time averaging over short, modified periodograms. *IEEE Trans. Audio Electroacoustics*, 15:70–73.

Westgate, R., Koo, K.-Y., and Brownjohn, J. (2014). Effect of solar radiation on suspension bridge performance. *Journal of Bridge Engineering*, 20(5):04014077.

Wyngaard, J. (2010). *Turbulence in the Atmosphere*. Turbulence in the Atmosphere. Cambridge University Press.

Wyngaard, J. C. (1973). On surface layer turbulence. In *Workshop on micrometeorology*, pages 101–149. Am. Meteorol. Soc.

Xia, Y., Chen, B., Weng, S., Ni, Y.-Q., and Xu, Y.-L. (2012). Temperature effect on vibration properties of civil structures: a literature review and case studies. *Journal of civil structural health monitoring*, 2(1):29–46.

Xie, J., Tanaka, H., Wardlaw, R., and Savage, M. (1991). Buffeting analysis of long span bridges to turbulent wind with yaw angle. *Journal of Wind Engineering and Industrial Aerodynamics*, 37(1):65 – 77.

Xu, L., Guo, J., and Jiang, J. (2002). Time–frequency analysis of a suspension bridge based on GPS. *Journal of Sound and Vibration*, 254(1):105–116.

Xu, Y. (2013). *Wind Effects on Cable-Supported Bridges*. Wiley.

Xu, Y. and Chan, W. (2009). Wind and structural monitoring of long span cable-supported bridges with GPS. In *Proceedings of the 7th Asia-Pacific Conference on Wind Engineering (APCWE'09)*.

Xu, Y., Chen, B., Ng, C., Wong, K., and Chan, W. (2010). Monitoring temperature effect on a long suspension bridge. *Structural Control and Health Monitoring*, 17(6):632–653.

Xu, Y., Sun, D., Ko, J., and Lin, J. (2000a). Fully coupled buffeting analysis of tsing ma suspension bridge. *Journal of Wind Engineering and Industrial Aerodynamics*, 85(1):97–117.

Xu, Y. and Xia, Y. (2011). *Structural Health Monitoring of Long-Span Suspension Bridges*. CRC Press.

Xu, Y. and Zhu, L. (2005). Buffeting response of long-span cable-supported bridges under skew winds. part II: case study. *Journal of Sound and Vibration*, 281(3–5):675 – 697.

Xu, Y., Zhu, L., Wong, K., and Chan, K. (2000b). Field measurement results of Tsing Ma suspension bridge during typhoon Victor. *Structural Engineering and Mechanics*, 10(6):545–559.

Xu, Y. L. and Chen, J. (2004). Characterizing nonstationary wind speed using empirical mode decomposition. *Journal of Structural Engineering*, 130(6):912–920.

Yu, J., Meng, X., Shao, X., Yan, B., and Yang, L. (2014). Identification of dynamic displacements and modal frequencies of a medium-span suspension bridge using multimode GNSS processing. *Engineering Structures*, 81:432–443.

Zhou, L., Xia, Y., Brownjohn, J. M., and Koo, K. Y. (2016). Temperature analysis of a long-span suspension bridge based on field monitoring and numerical simulation. *Journal of Bridge Engineering*, 21(1):04015027.

Zhu, L., Wang, M., Wang, D., Guo, Z., and Cao, F. (2007). Flutter and buffeting performances of third Nanjing Bridge over Yangtze River under yaw wind via aeroelastic model test. *Journal of Wind Engineering and Industrial Aerodynamics*, 95(9–11):1579 – 1606. The Fourth European and African Conference on Wind Engineering.

Zhu, L., Xu, Y., Zhang, F., and Xiang, H. (2002). Tsing Ma bridge deck under skew winds – part I: Aerodynamic coefficients. *Journal of Wind Engineering and Industrial Aerodynamics*, 90(7):781 – 805.

Appendix A

Wind-induced vibrations monitoring with satellite navigation

Etienne Cheynet[a], Jasna Bogunović jakobsen[a], Jónas Snæbjörnsson[a,b]

[a] Department of Mechanical and Structural Engineering and Materials Science, University of Stavanger, N-4036 Stavanger, Norway.

[b] School of Science and Engineering, Reykjavik University, Menntavegur 1, 101 Reykjavík, Iceland.

Appendix A was presented at 19th IABSE Congress Stockholm, 21-23 September 2016: Challenges in Design and Construction of an Innovative and Sustainable Built Environment.

Introduction

Accelerometers are widely used to measure the dynamic response of civil engineering structures, although their accuracy at low frequencies is not always adequate (Xu and Xia, 2011). For large structures such as future super-long span suspension bridges, the resonant part of the displacement is likely to be located close to or below the operating limit of most accelerometers. During the last two decades, Global Navigation Satellite Systems (GNSS) have been promising tools to monitor the static and quasi-static displacements of civil engineering structures (Im et al., 2011b; Lovse et al., 1995). Until now, the focus has mainly been on the development of methodologies and algorithms to assess the accuracy of GNSS measurement technology (Chan et al., 2006a,b; Nickitopoulou et al., 2006), as well as on testing its capabilities in comparison to accelerometers (Meng et al., 2007; Yu et al., 2014). Early applications of GPS technology on suspension bridges started at the end of the 90's (Ashkenazi and Roberts, 1997; Fujino et al., 2000), and have been expanding since 2000. In particular, applications to identify modal parameters (Meng et al., 2007; Roberts et al., 2004; Yu et al., 2014), and for wind-induced vibration analysis of both suspension bridges (Nakamura, 2000; Xu and Chan, 2009) and tall-buildings (Kijewski-Correa et al., 2006; Tamura et al., 2002) have become increasingly popular. Still there are many uncertainties about the complementary role of GNSS and accelerometers in monitoring wind-induced vibrations of long-span suspension bridges. During the summer of 2015, a GNSS base-rover monitoring system was installed at midspan on the deck of the Lysefjord Bridge in Norway. The data sampling is synchronized to previously installed accelerometers and anemometers (Cheynet et al., 2015a).

Bridge site and instrumentation

The Lysefjord Bridge

The Lysefjord Bridge, located at the narrow inlet of a fjord in the South-West part of the Norwegian coast, is used as a study case. Its main span is 446 m, and at midspan the bridge deck is 55 m above the sea level. It is oriented from North-West to South-East in a mountainous environment (Fig. A.1). It is entrenched between two steep hills with slopes ranging from 30° to 45° and a maximum altitude of 350 m to the North and 600 m to the South. Its East side is exposed to winds that may descent from the mountains nearby or follow the fjord over a longer path. To the West, the bridge is exposed to a more open and levelled area, where the wind may be accelerated in the vicinity of the bridge because of the narrowing effect of the fjord

Figure A.1 South view of the Lysefjord Bridge.

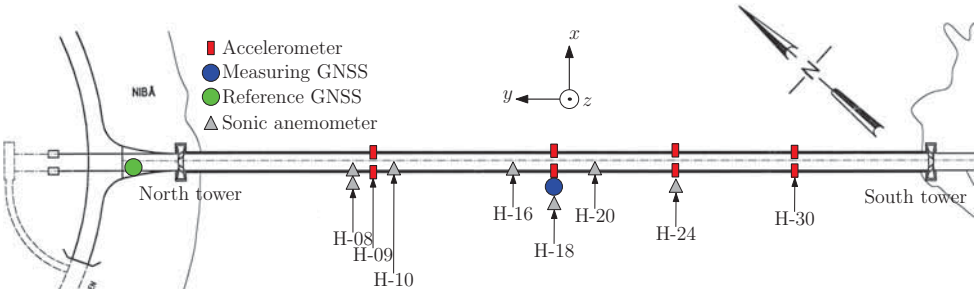

Figure A.2 Sensors installed along the bridge deck. Anemometers are represented by grey triangles; GNSS sensors are visible as one blue and green dot; accelerometers are depicted as red rectangles.

Accelerometers and anemometers

Between 2013 and 2014, the Lysefjord Bridge has been instrumented with seven sonic anemometers and four pairs of accelerometers placed along the span (Fig. A.2). Two anemometers are located on hanger 8, denoted H-08, and the others are installed near hangers H-10, H-16, H-18, H-20 and H-24, on the west side of the deck, about six metres above the girder. The distance between each hanger is 12 m, leading to a distance between the anemometers ranging from 24 m to 168 m. The anemometers are 3D WindMaster Pro sonic anemometers, except the one installed on hanger 10, which is a Vaisala weather transmitter WXT520. Wind and acceleration data are synchronized using GPS timing, and continuously transferred to a server via mobile net. The records are filtered and re-sampled at 20 Hz. The displacement data is obtained by transforming the acceleration data into the frequency domain and applying a multiplication scheme, instead of direct integration in the time domain.

GNSS data

A Real-Time Kinematic-Global Positioning System is used to measure the displacement of the Lysefjord Bridge. Similar systems have previously been

used by e.g. Tamura et al. (2002) to study wind-induced vibrations of a tall tower. In the present study, a set of Trimble BD930 GNSS receivers are coupled to Trimble AV33 GNSS antennas. These sensors can handle data sampling at a frequency of 20 Hz, with an accuracy of $\pm$ 8 mm+1ppm for the horizontal displacement and $\pm$ 15 mm+1ppm for the vertical displacements. The base-rover combination may increase measurement accuracy, as it is the relative displacement between a "fixed" base station and a "moving" rover station that is monitored.

The GNSS base-rover monitoring system measures the displacement at mid-span in the East, North and vertical directions. Therefore, the lateral and vertical bridge displacement can be directly obtained using Eq. A.1, where θ is the bridge orientation with respect to North, equal to 40.5°.

$$\begin{bmatrix} r_x \\ r_y \\ r_z \end{bmatrix} = \begin{bmatrix} \cos(\theta) & \sin(\theta) & 0 \\ -\sin(\theta) & \cos(\theta) & 0 \\ 0 & 0 & 1 \end{bmatrix} \times \begin{bmatrix} r_E \\ r_N \\ r_z \end{bmatrix} \tag{A.1}$$

Results and discussion

Wind data from N-NE that is recorded on 07/10/2015 is used for both the static and the dynamic analysis. The analysis relies on calculations in the modal base, assuming homogeneous and stationary flow. Modal coupling is neglected, and only the vertical and lateral displacements are investigated. The first four lateral and vertical modes are taken into account, and are provided by a finite element model. To improve the accuracy of the computed response, slight discrepancies between the computed and measured eigen-frequencies were corrected. In the present study, the static displacement is computed for the lateral direction only, and is obtained using a multimodal approach:

$$\bar{\boldsymbol{r}}_{\boldsymbol{x}} = \boldsymbol{\Phi}^{\top} \boldsymbol{K}^{-1} \boldsymbol{F}_{\boldsymbol{x}} \tag{A.2}$$

where $\mathbf{\Phi}$ is a N_m by N_y matrix of mode shapes, where N_m is the number of modes and N_y is the number of integrations points along the suspension bridge modelled as a line segment. The matrix of modal stiffness $\boldsymbol{K}$ is a N_m by N_m matrix, and $\boldsymbol{F_x}$ is a N_m by 1 vector of the static modal load. The dynamic response to wind turbulence is undertaken in the frequency domain, based on the buffeting theory (Scanlan, 1975), and the quasi-steady theory (Holmes, 2007), using the same numerical model as in Cheynet et al. (2015a). The single point wind spectrum is obtained by averaging the measured wind spectra on hangers 16, 18 and 20. The co-coherence is approximated by a simple exponential decay function as used by Davenport (1961b). The spectral densities are computed using Welch's overlapped segment averaging estimator, based on 10 min long data series divided into blocks of 300 seconds, using shorter blocks of 60 seconds to reduce the aleatory variability and the bias error in the estimate (Kristensen and Kirkegaard, 1986).

Static analysis

Nakamura (2000) observed a good agreement between the static lateral displacement computed with a finite element model of a suspension bridge and the one measured from a wind tunnel model using GPS technology. For a full-scale bridge, he noted a considerable scatter, which might have been due to multipath effects, signal distortion due to ionosphere and troposphere delays, cycle slips, high noise to signal ratio, non-stationary wind conditions, or temperature variations.

For data recorded on 07/10/2015, we observed that high number of samples were affected by cycle slips (Hofmann-Wellenhof et al., 2007). Cycle slips are discontinuities in the recorded signal due to temporary signal loss, which were here probably due to bad satellite coverage, caused by high latitude location, mountainous terrain surrounding the bridge and possibly some shadowing effects from the bridge North tower. Because the measurement of the static displacement requires stationary wind conditions, the reverse

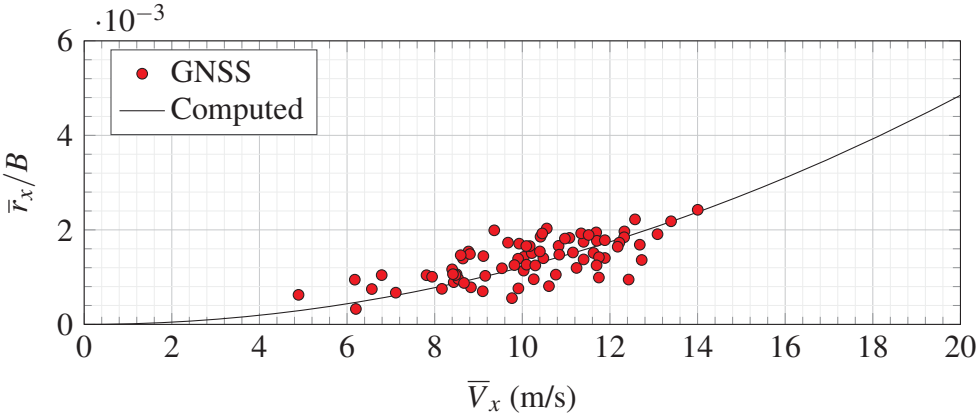

Figure A.3 Lateral static displacement measured at midspan, on 07/10/2015, based on 10-min averaged displacement data from the GNSS.

arrangement test (Bendat and Piersol, 2011) was applied to select only stationary displacement records. This led to a significant reduction of the scatter of measured static displacement, because both cycle slips and non-stationary bridge records were eliminated. The measured static displacements are divided by the deck width, denoted B, and expressed as a function of the mean wind component normal to the deck, V_x in Fig. A.3. A satisfying agreement was then observed, between the measured and computed lateral static displacement in Fig. A.3.

Dynamic analysis

Single sample

The time histories and the power spectral density (PSD) of the bridge displacement response recorded on 07/10/2015 between 05:20 and 05:30 is used as a study case. A stationary flow from the N-NE was monitored, with a mean wind velocity at mid span of 11.7 $\mathrm{m\,s^{-1}}$, and turbulence intensities I_u = 31 % and I_w = 12 %. The along-wind integral length scales L_u and L_w were equal to 110 m and 37 m respectively. In the present study, the measured

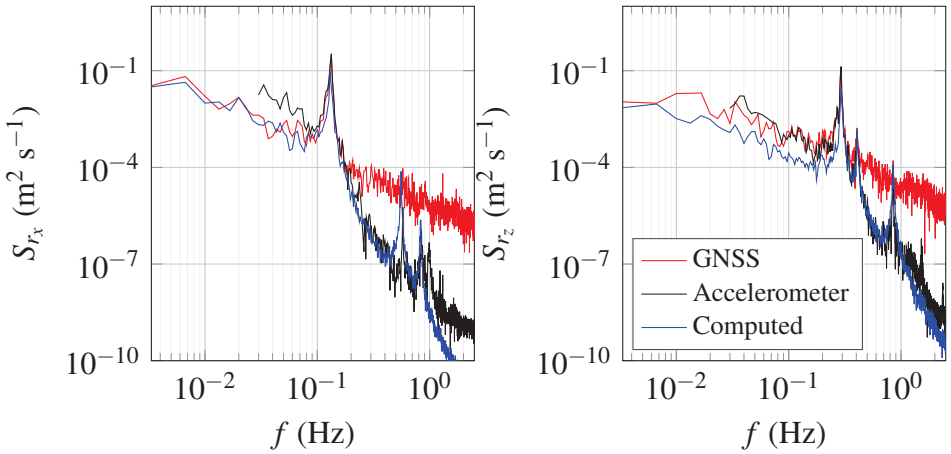

Figure A.4 PSD of the lateral (top) and vertical (bottom) bridge displacement responses recorded near H-18, on 07/10/2015 between 05:20 and 05:30.

co-coherence was fairly well approximated by the single exponential decay. The decays coefficients C_u^y and C_w^y were found to be equal to 8.4 and 5.7 respectively. As highlighted by e.g. Moschas and Stiros (2014); Xu and Xia (2011), accelerometers usually show limited capabilities in monitoring vibrations below a given frequency threshold, which is here observed to range from 0.06 Hz to 0.1 Hz.

A direct comparison between the PSD of the accelerometers and the GNSS system in Fig. A.4 shows that more measurement noise is present in the GNSS record than in the accelerometer data for frequencies above 0.5 Hz. Both sensors capture properly the first eigen-frequency, which is located around 0.30 Hz for the vertical direction and 0.13 Hz for the lateral one. Below frequencies corresponding to the first resonant peak, the accelerometer indicates somewhat larger displacement response although The GNSS and accelerometers data agree well down to 0.1 Hz. Below 0.1 Hz the difference between the two measurement techniques becomes non-negligible, and illustrates the limitations of accelerometers in monitoring displacement responses at low frequencies.

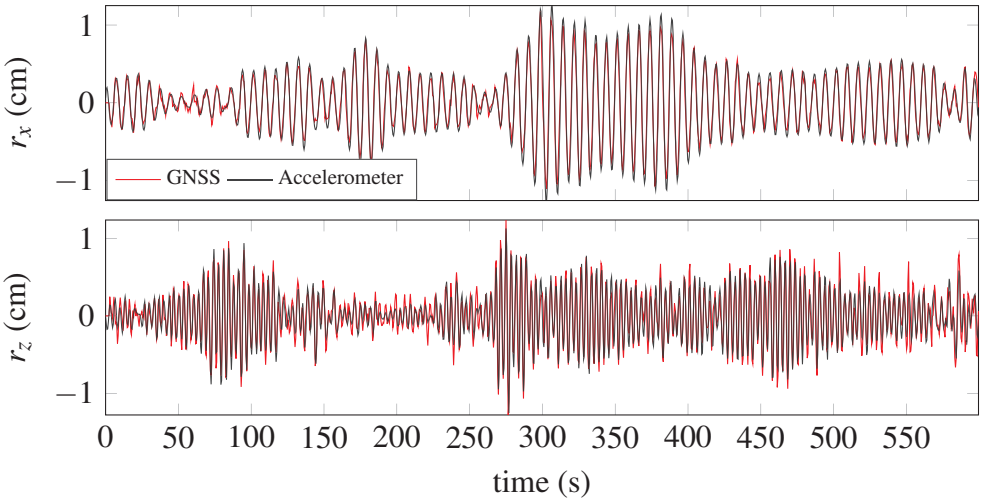

Figure A.5 Lateral (top) and vertical (bottom) resonant wind-induced bridge response near H-18, on 07/10/2015 between 05:20 and 05:30.

The PSD of the computed vertical displacement is lower than the one measured by the GNSS at low frequencies (Fig. A.4). For the lateral displacement, the computed and measured quasi static response show however a good agreement. The limiting resolution of the vertical displacement results in a more or less constant measurement noise over the whole frequency range. However, this noise does not explain the discrepancy between the quasi-static part of the measured and computed PSD for the vertical response. The influence of the torsional angle of the bridge deck, which cannot be removed if the displacement is monitored at one point only, may be responsible for this discrepancy. The coherence model we used in the present study may also underestimate wind coherence at low frequencies. The application of the 3-parameter exponential decay model (Cheynet et al., 2015a) did not improve the estimated vertical PSD. Better estimation of wind coherence at low frequencies requires analysis using wind data of duration larger than 10 min.

In Fig. A.5, the direct comparison in the time domain between the GNSS and the accelerometer data shows a good agreement for both the lateral and the vertical direction. A slightly higher noise is visible for the vertical direction, which is expected given the technical specifications of the GNSS. A lower measurement accuracy is generally observed for the vertical displacements compared to the horizontal ones (Im et al., 2011b). Sub-centimetre down to a millimetre level accuracy can be achieved by modern GNSS technology. By using a motion simulation table, Chan et al. (2006b) measured horizontal and vertical displacements with an accuracy up to 5 mm and 10 mm respectively. By simulating harmonic displacement with a rotating GPS antenna, Nickitopoulou et al. (2006) observed that an accuracy of 15 mm for the horizontal displacements and 35 mm for the vertical ones was permitted at 1.5 % outlier level. More recently, a sub-millimetre accuracy was achieved by Yu et al. (2014) by using a higher number of GNSS antenna. In the present study, the standard deviation for the lateral and vertical dynamic displacement are 5 mm and 4 mm respectively. This indicates that the vertical displacements recorded are close to the operative limits of the GNSS used.

Multiple samples

For a full day of records, the dynamic displacement at mid-span was obtained by applying a band-pass filter with an upper and lower cut-off frequency of 1 Hz and 0.1 Hz to the total measured deck displacement. The lower boundary is chosen so that the accelerometer data provides a reliable comparison. The upper boundary is chosen so that the first four eigen-modes in each direction are taken into account, providing a good overview of the resonant response. In addition, this procedure allows removing possible torsional resonant responses at around 1.2 Hz, which might complicate the interpretation of the displacement data.

Fig. A.6 compares the RMS of the dynamic displacements measured by the GNSS with those obtained with the accelerometer on H-18. We

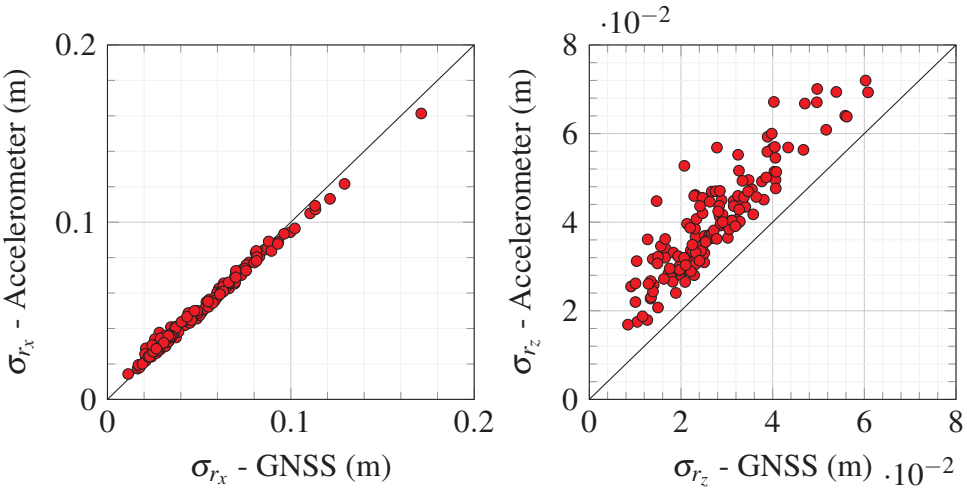

Figure A.6 Standard deviation of the dynamic displacements measured by the GNSS sensor compared to the accelerometers data at mid-span, in the range [0.1-2.5 Hz] on 07/10/2015. The continuous line refers to the ideal case of a perfect correlation between the accelerometers and GNSS measurements.

observed a good agreement for the lateral displacement, but for the vertical one, the GNSS instruments provide systematically higher values of resonant displacement response than the accelerometer data, which is consistent with Fig. A.4 and Fig. A.5. The presence of measurement noise associated by the combination of vertical and torsional displacement may be responsible for the overestimation of the vertical resonant response measured by the GNSS. A higher noise is generally observed in the GNSS data. At low wind velocities, the data quality may be too poor to accurately monitor the Lysefjord Bridge displacement. For larger suspension bridges, the influence of measurement noise should be mitigated because larger displacements of the deck are expected. In addition, estimation of the GNSS measurement noise during a calibration procedure (Roberts et al., 2004) should reduce the systematic error between the accelerometers and the GNSS for the vertical displacement.

Some current large suspensions bridges in Norway have already natural frequencies close or below the operative limit of most accelerometers. For example, the first symmetrical lateral eigen-frequency of the Hardanger Bridge is 0.05 Hz, and its first asymmetric vertical eigen-frequency is 0.11 Hz. For future super-long span suspension bridges, even lower eigen-frequencies are expected as highlighted by Fujino and Siringoringo (2013), meaning that GNSS sensors may play a central role in structural health monitoring. The static and dynamic displacements are likely to be much larger than those recorded at Lysefjord Bridge, which should increase the amount of high-quality data obtained with GNSS systems. However, the latitude of Norway is well above 50°, which is the limit beyond which the availability of satellite constellations start reducing (Breuer et al., 2002; Nickitopoulou et al., 2006). Consequently, the quality of results is expected to be poorer than for mid-latitudes. In the present study, the amplitude of wind-induced vibrations for wind from S-SW were for example often too low to be captured in details by the GNSS rover. Fortunately, the deployment of the Galileo system in 2020 (ESA, 2012) should improve the accuracy of GNSS positioning in Northern Europe.

Conclusions

Wind-induced vibrations of a suspension bridge have been investigated in details using GNSS base-rover devices. Comparisons with three-axial accelerometers have shown that GNSS observations play a complementary role that may become predominant for super-long span suspensions bridges. Because of the relative short span of the Lysefjord Bridge, the dynamic displacement for the vertical motion was close to the operative limit of the GNSS, for the wind velocities studied, and a non-negligible measurement noise was obtained. The GNSS and accelerometers showed however a good agreement for the dynamic and static lateral displacements. A good signal to

noise ratio was obtained for large bridge displacements only, which limited the quantity of available data. The high latitude of the Lysefjord Bridge may also at least partly be responsible for lack of data quality at low excitation levels. The deployment of the Galileo system should improve the accuracy of GNSS measurements in Europe and consequently strengthen the development of GNSS monitoring systems as a complementary tool for structural health monitoring of large civil engineering structures.

Acknowledgements

The authors would like to gratefully acknowledge the support of the Norwegian Public Roads Administration to the measurement campaign, as well as to the installation and maintenance of the monitoring system.

Appendix B

Hardanger Bridge properties

Introduction

Ten minutes of wind and acceleration data recorded on the Hardanger Bridge on 06/12/2013 from 13:25:13 have been used to evaluate the applicability of the automated SSI-COV algorithm to capture the mode shapes and eigen-frequencies of a long-span suspension bridge with closely spaced modes. The parameters used for the SSI-COV procedure are summarized in Table B.1.

The data set was provided by Aksel Fenerci (NTNU). The measured modal parameters are compared to those from the SBM the parameters of which are summarized in Table B.2. The parameters in Table B.2 come from a finite element model of the Hardanger Bridge using the software Alvsat and conducted on 28/11/2006. The quasi-steady aerodynamic coefficients used for the buffeting analysis of the Hardanger Bridge in Chapter 7 are summarized in Table B.3.

Eigen frequencies and mode shapes

The first nine eigen-frequencies for the lateral, vertical and torsional motion of the Hardanger Bridge are summarized in table B.4. A larger number of modes

Table B.1 Parameters used in the SSI-COV method applied on 10 min of Hardanger Bridge acceleration data on 06/12/2013 from 13:25:13.

Motion	τ_{max} (s)	N_{min}	N_{max}	ε_{fn}	ε_{ζ}	ε_{MAC}	ε_{d}
Lateral	60	3	60	$8{\cdot}10^{-3}$	$4{\cdot}10^{-2}$	$4{\cdot}10^{-3}$	$4{\cdot}10^{-2}$
Vertical	30	3	100	$5{\cdot}10^{-3}$	$4{\cdot}10^{-2}$	$4{\cdot}10^{-3}$	$4{\cdot}10^{-2}$
Torsional	15	3	50	$5{\cdot}10^{-3}$	$4{\cdot}10^{-2}$	$1{\cdot}10^{-3}$	$4{\cdot}10^{-2}$

Table B.2 Parameters of the SBM of the Hardanger Bridge.

Description	Value	Unit
Length of main span	1310	m
Deck width	18.3	m
Deck height	3.33	m
Young modulus of deck	2.1e+11;	Pa
Young modulus of cable	2.05e+11;	Pa
Cross section main cable	0.223	m^2
Lineic mass of girder	9111	$kg\,m^{-1}$
Lineic mass of cable	1901	$kg\,m^{-1}$
Sag	121	m
Hanger length at mid span	2.88	m
Distance from shear center to hanger attachment	1.669	m
Distance between main cables	14.5	m
Tension in one main cable	1.1266e+8	N
Moment of inertia w.r.t. bending about y-axis	16.877	m^4
Moment of inertia w.r.t. bending about z-axis	0.99	m^4
Moment of inertia w.r.t. torsion around y-axis	2.467;	m^4
Mass moment of inertia	4.26e+5;	$kg\ m^{-1}$
Shear modulus	80700e+6;	$N\ mm^{-2}$

Table B.3 Quasi-steady aerodynamic coefficients of the Hardanger Bridge.

Structural parameters	Symbols	Value
Drag coefficient	C_D	0.7
Lift coefficient	C_L	-0.25
Pitching moment	C_M	0.01
$\frac{\partial C_D}{\partial \alpha}$	C'_D	0.0
$\frac{\partial C_L}{\partial \alpha}$	C'_L	2.4
$\frac{\partial C_M}{\partial \alpha}$	C'_M	0.74

were identified but are not displayed in the following for the sake of brevity. The mode shapes associated with these eigen-frequencies are displayed in Fig. B.1-B.3.

A good agreement is observed between the SBM and the identified eigen-frequencies, except for VA1 and the first six torsional eigen-frequencies. For the latter, larger discrepancies were expected as the increasing height of the towers implies an increasing flexibility that is not modelled in the SBM. For the mode shapes, a good overall agreement is observed for every mode, except maybe for HS4 and HA4. For the modes HS4 and HA4, the discrepancies between the measured mode shapes and the computed ones echo the discrepancies observed for the modes HA2 and HS3 of the BSM of the Lysefjord Bridge. For the Hardanger Bridge, the mode HA4 and HS4 are closely spaced as well as the modes VS2 and VA2, but the automated SSI-COV procedure managed to properly identify them.

Table B.4 Eigen-frequencies identified using the SSI-COV method for the Hardanger Bridge acceleration data on 06/12/2013 from 13:25 to 13:35.

Modes	SSI-COV	SBM	Relative difference
	Hz	Hz	%
HS1	0.050	0.051	1.02
HA1	0.103	0.101	-2.28
HS2	0.181	0.175	-3.13
HA2	0.234	0.244	4.19
HS3	0.246	0.255	3.82
HA3	0.314	0.305	-2.77
HA4	0.411	0.404	-1.83
HS4	0.421	0.426	1.05
HS5	0.452	0.455	0.70
VA1	0.122	0.102	-16.22
VS1	0.142	0.143	0.94
VS2	0.204	0.210	2.97
VA2	0.213	0.224	5.45
VS3	0.276	0.278	0.57
VA3	0.333	0.330	-0.75
VS4	0.400	0.398	-0.57
VA4	0.468	0.467	-0.30
VS5	0.542	0.543	0.21
TS1	0.370	0.322	-12.87
TA1	0.547	0.453	-17.26
TS2	0.820	0.676	-17.63
TA2	1.050	0.891	-15.10
TS3	1.290	1.113	-13.73
TA3	1.510	1.333	-11.69
TS4	1.681	1.555	-7.42
TA4	1.810	1.777	-1.83
TS5	1.979	1.999	0.97

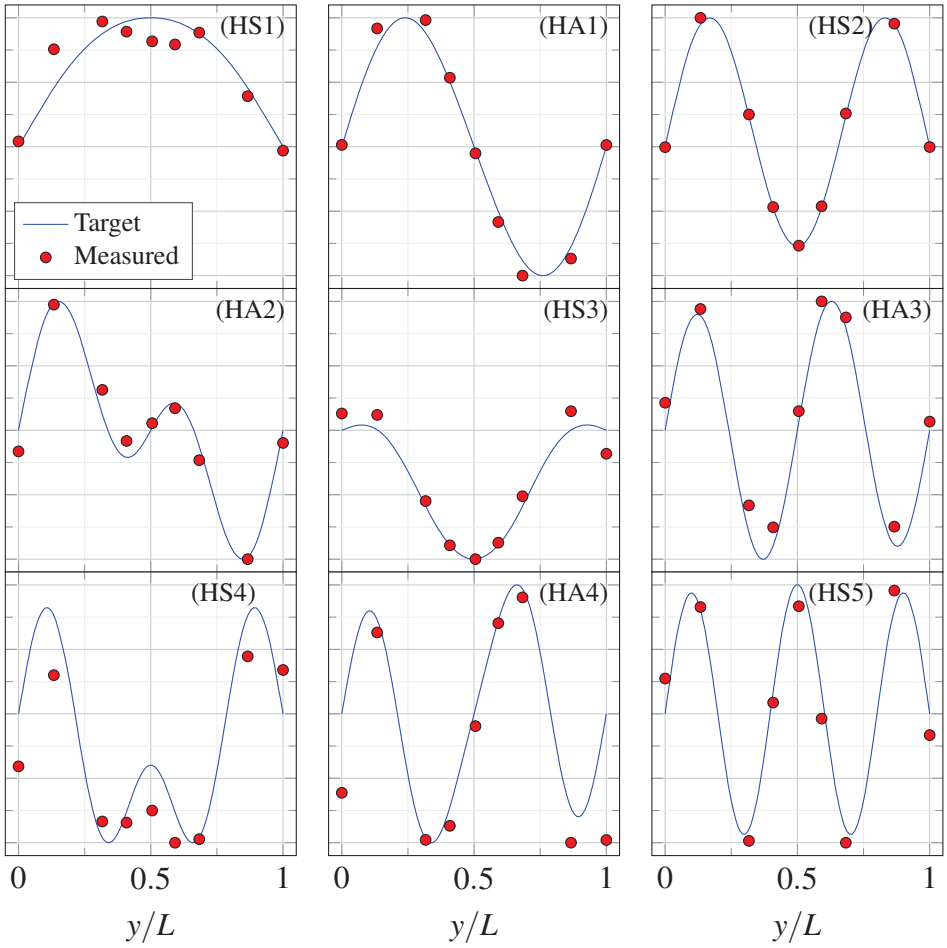

Figure B.1 First nine lateral eigen-frequencies of the Hardanger Bridge identified using the automated SSI-COV algorithm.

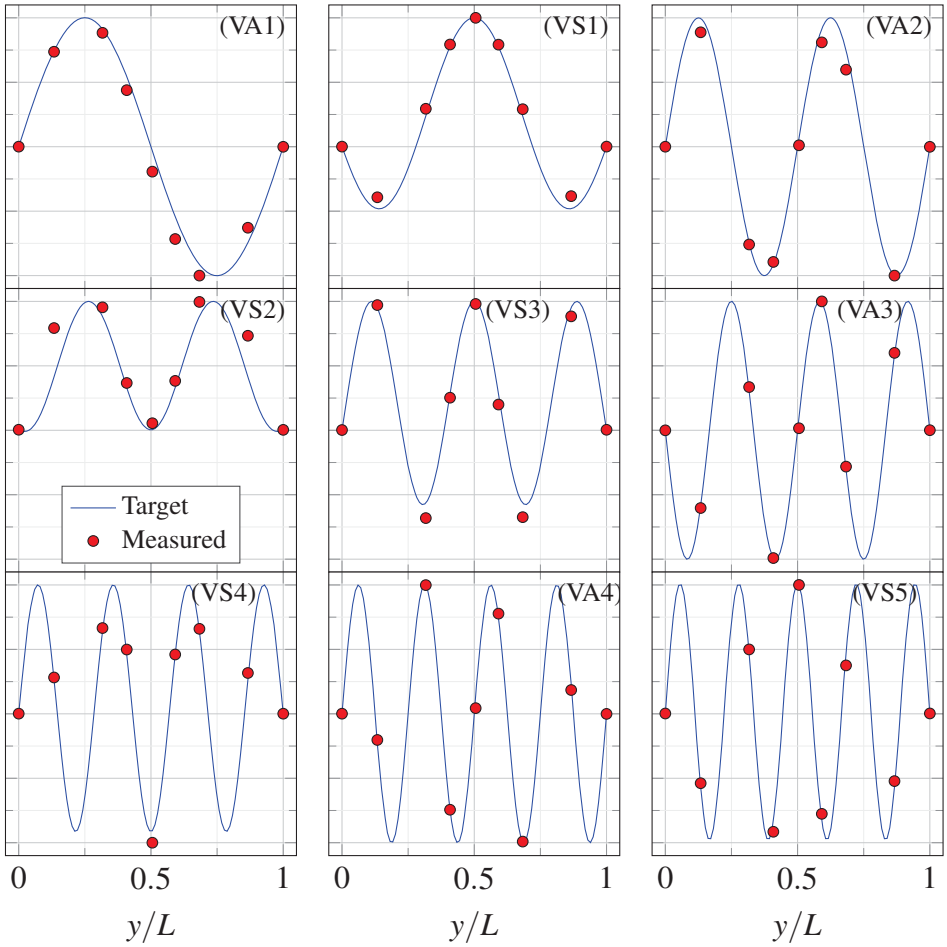

Figure B.2 First nine vertical eigen-frequencies of the Hardanger Bridge identified using the automated SSI-COV algorithm.

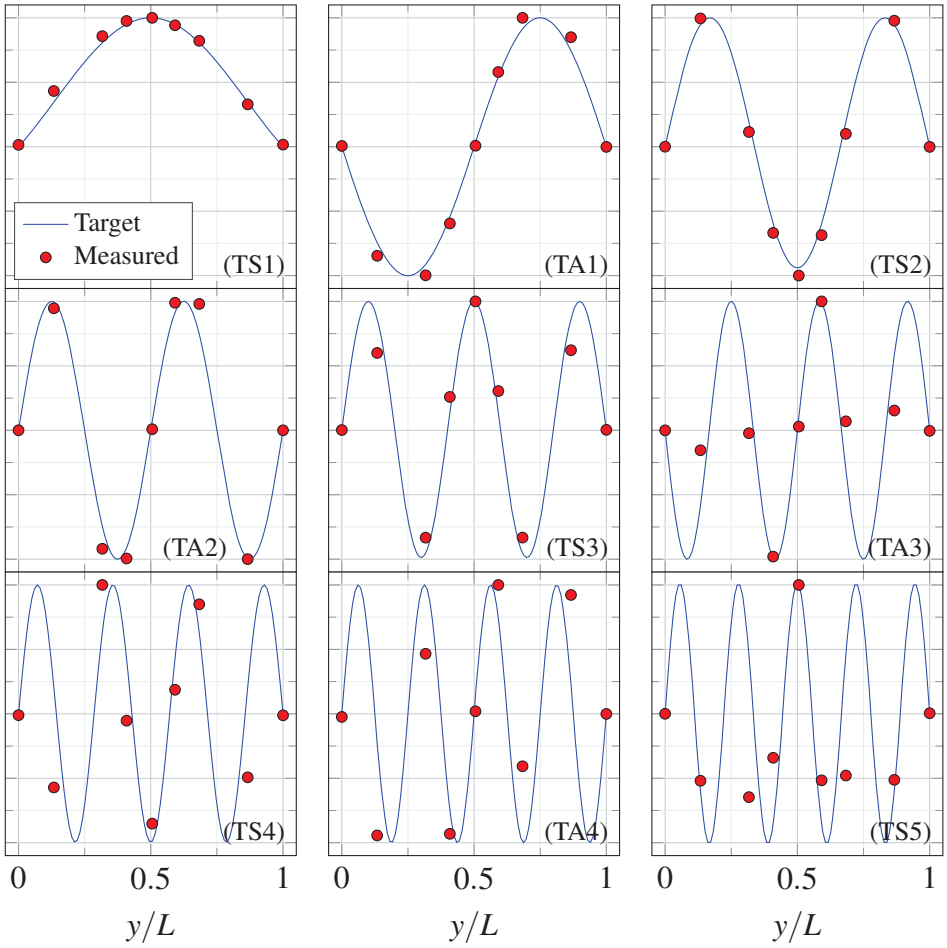

Figure B.3 First nine torsional eigen-frequencies of the Hardanger Bridge identified using the automated SSI-COV algorithm.

Appendix C

Publications related to the thesis

Journal papers

1. E. Cheynet, J. Bogunović Jakobsen, and J. Snæbjörnsson. Buffeting response of a suspension bridge in complex terrain. Engineering Structures, 128:474–487, 2016

2. E. Cheynet, J. Bogunović Jakobsen, J. Snæbjörnsson, J. Reuder, V. Kumer and B. Svardal. Wind characterisation by a pulsed lidar at a bridge site. Accepted for publication in Journal of Wind Engineering & Industrial Aerodynamics.

3. E. Cheynet, J. Bogunović Jakobsen, J. Snæbjörnsson, N. Angelou, T. Mikkelsen, M. Sjöholm and B. Svardal. Full-scale observation of the flow downstream of a suspension bridge deck. Submitted to Journal of Wind Engineering & Industrial Aerodynamics.

4. E. Cheynet, J. Bogunović Jakobsen, J. Snæbjörnsson, T. Mikkelsen, M. Sjöholm, J. Mann, P. Hansen, N. Angelou and B. Svardal. Application of short-range dual-Doppler lidars to evaluate the coherence of turbulence. Experiments in Fluids, 57(12), 184, 2016.

5. E. Cheynet, J. Bogunović Jakobsen, B. Svardal, J. Reuder, and V. Kumer. Wind coherence measurement by a single pulsed Doppler wind lidar. Energy Procedia, 94:462 – 477, 2016.

6. J. Bogunović Jakobsen, E. Cheynet, J. Snæbjörnsson, T. Mikkelsen, M. Sjöholm, N. Angelou, P. Hansen, J. Mann, B. Svardal, V. Kumer, et al. Assessment of wind conditions at a fjord inlet by complementary use of sonic anemometers and lidars. Energy Procedia, 80:411–421, 2015.

Conference papers

1. E. Cheynet, J. Bogunović Jakobsen, and J. Snæbjörnsson. Wind-induced vibrations monitoring with satellite navigation. In 19th IABSE Congress Stockholm, 21-23 September 2016, 2016.

2. J. Snæbjörnsson, E. Cheynet, and J. Bogunović Jakobsen. Performance evaluation of a suspension bridge excited by wind and traffic induced action. In 8th European Workshop On Structural Health Monitoring (EWSHM 2016), 2016.

3. E. Cheynet, J. Bogunović Jakobsen, J. Snæbjörnsson, N. Angelou, T. Mikkelsen, M. Sjöholm, and B. Svardal. Full-scale observation of the flow downstream of a suspension bridge deck. In BBAA VIII: 8th International Colloquium on Bluff Body Aerodynamics and Applications, 2016.

4. E. Cheynet, J. Bogunović Jakobsen, and J. Snæbjörnsson. Full scale monitoring of wind and traffic induced response of a suspension bridge. In MATEC Web of Conferences, volume 24, page 04003. EDP Sciences, 2015.

5. E. Cheynet, J. Bogunović Jakobsen, and J. Snæbjörnsson. Buffeting response of a bridge at the inlet of a fjord. In ICWE14: 14th International Conference on Wind Engineering, 2015.

6. J. Bogunović Jakobsen, E. Cheynet, J. Snæbjörnsson, T. Mikkelsen, M. Sjöholm, N. Angelou, P. Hansen, J. Mann, B. Svardal, V. Kumer, et al. Application of lidars for assessment of wind conditions on a bridge site. In ICWE14: 14th International Conference on Wind Engineering, 2015.

7. E. Cheynet, J. Bogunović Jakobsen, and J. Snæbjörnsson. Wind-induced response of a bridge at the inlet of a fjord. In WES 2014: Proceedings of the 11th UK conference on wind engineering , 2014.

8. E. Cheynet, J. Bogunović Jakobsen, and J. Snæbjörnsson. Wind characteristics on a suspension bridge at the inlet of a fjord. In IN-VENTO 2014: XIII Conference of the Italian Association for Wind Engineering, 2014.

Index

accelerometers, 9, 37
aerodynamic
    coefficients, 143
    forces, 27
Alvsat, 112, 143
atmospheric
    boundary layer, 12
    stability, 12
auto-covariance, 16
averaging period, 13
AVT, 99
azimuth angle, 40

Beam Sweeping, 50
Bridge
    Hardanger, 170
    Lysefjord, 35, 135, 168
bridge
    acceleration response, 11
    deck, 161
    displacement response, 135
bridge model
    empirical, 142
    Finite Element, 142
    SBM, 112, 142
bridge-based coordinate system, 14
buffeting response, 143
buffeting theory, 3, 10, 26

Carrier-to-Noise Ratio, 52
cluster analysis, 109
co-spectrum, 189
coherence, 20, 92
coherence model
    four-parameter, 22
    Krenk, 24
    von Kármán, 24
correlation coefficients, 20
cosine rule, 138, 158
coupling
    aerodynamic, 166
    structural, 153

design wind velocity, 63

eigen-frequency, 116
elevation angle, 40
excess coefficient, 61

flow homogeneity, 76, 163
frequency domain, 26

Global Navigation Satellite Systems, 9, 216

incidence angle, 13
integral length scales, 16, 63

kurtosis, 61

lidar, 39, 58
Line-Of-Sight, 40

MATLAB, 103, 112
mean wind velocity, 13
Modal Assurance Criterion, 110
modal coupling, 26, 165
modal damping ratio, 127
mode shape, 126

non-Gaussian, 63
non-stationary, 176

OMA, 99

Plan Position Indicator, 40

quasi-steady assumption, 26

random process, 12
Range Height Indicator, 40
reverse arrangement test, 127, 177
root-coherence, 21

sensitivity analysis, 144
skew wind, 13, 158
skewness, 60
spatial averaging effect, 82, 89
SSI-COV, 100
stabilization diagram, 107
statistical moments, 59
statistics
    single-point, 14
    two-point, 19
strip assumption, 27
structural Health Monitoring, 9
super-long span, 58

temperature effects, 118
time-frequency distribution, 187
traffic, 123
traffic-induced vibrations, 186
turbulence intensity, 14, 60
turbulence length scale
    cross-flow , 20
    streamwise, 16
typhoon, 15, 57

Viridis, 66
von Kármán spectrum, 17, 140

wind components, 13
wind load
    linearity, 26
    quadratic terms, 171
wind spectra, 17, 87, 139
wind-based coordinate system, 14

WindCube, 44
WindScanner, 44

yaw angle, 13